

Melanie Klein-Bösing

Development of a
Transition Radiation Detector
and Reconstruction of Photon Conversions
in the CBM Experiment

— 2009 —

Experimentelle Physik

Development of a
Transition Radiation Detector
and Reconstruction of Photon Conversions
in the CBM Experiment

Inauguraldissertation
zur Erlangung des Doktorgrades
der Naturwissenschaften im Fachbereich Physik
der Mathematisch-Naturwissenschaftlichen Fakultät
der Westfälischen Wilhelms-Universität Münster

vorgelegt von
Melanie Klein-Bösing
aus Telgte

— 2009 —

Dekan: Prof. Dr. J. P. Wessels
Erster Gutachter: Prof. Dr. J. P. Wessels
Zweiter Gutachter: PD Dr. A. Khoukaz

Tag der Disputation:
Tag der Promotion:

Contents

Introduction	5
1 Theoretical Overview	9
1.1 Particles and Forces	9
1.1.1 Leptons and Quarks	10
1.1.2 Hadrons	12
1.1.3 Interactions	12
1.2 Quark-Gluon Plasma and Hadron Gas	15
1.2.1 The Phase Diagram of Strongly Interacting Matter	15
1.2.2 Chiral-Symmetry Restoration	17
1.3 Relativistic Heavy-Ion Collisions	18
1.3.1 Exploration of the QCD Phase Diagram	20
1.3.2 Signatures for a Phase Transition	23
2 Probing Heavy-Ion Collisions with Dileptons and Photons	29
2.1 Dileptons	29
2.1.1 Previous Experimental Results on Dileptons	32
2.2 Direct Photons	37
2.2.1 Thermal Photons	38
2.2.2 Non-Thermal Photons	41
2.2.3 Previous Experimental Results on Direct Photons	41
3 Interaction of Charged Particles and Photons with Matter	47
3.1 Energy Loss of Charged Particles	47
3.2 Additional Mechanisms for Radiative Energy Loss of Charged Particles .	52
3.2.1 Cherenkov Radiation	52

3.2.2	Transition Radiation	54
3.3	Interaction of Photons with Matter	59
4	The CBM Experiment	65
4.1	The Future Facility for Antiproton and Ion Research (FAIR)	65
4.2	Physics Goals and Observables of the CBM Experiment	68
4.3	Detector Concept	70
4.3.1	The Silicon Tracking and Vertex Detection System	71
4.3.2	The Ring Imaging Cherenkov Detector	73
4.3.3	The Transition Radiation Detector	74
4.3.4	The Time-of-Flight Detector	75
4.3.5	The Electromagnetic Calorimeter	76
4.3.6	The Projectile Spectator Detector	77
4.3.7	Data Acquisition	77
4.3.8	The Muon Chamber System	77
4.4	Dilepton Spectroscopy in CBM	79
5	The Transition Radiation Detector	83
5.1	Radiator Material	84
5.2	Multiwire Proportional Chambers	85
5.2.1	Signals Induced on Cathode Pads	89
5.2.2	Gas Mixture	92
5.2.3	Signal Generation	92
5.3	Design of the MB-TRD Prototype	93
5.3.1	Absorption Efficiency of TR in the Gas Volume	95
5.3.2	Double-sided Pad Readout Electrode	97
5.3.3	Prototype Assembly	100
6	Performance of the MB-TRD Prototypes	103
6.1	^{55}Fe Source Measurements	103
6.2	In-Beam Test at GSI	106
6.3	Pulse Height Distribution	109
6.4	Electron/Pion Separation	110
6.4.1	Pion Efficiency	113

6.5	Simulation of Electron/Pion Separation	119
6.5.1	Simulation of Energy Loss by Ionization and Transition Radiation	119
6.5.2	Implementation of the New Detector Design	120
6.5.3	Particle Simulation	120
6.5.4	Comparison of Simulated and Measured Energy-Loss Spectra . .	120
6.5.5	Pion Efficiency in Simulation	124
6.6	Position Resolution	125
6.6.1	The Pad Response Function	126
6.6.2	Cluster Reconstruction	131
6.6.3	Position Resolution Along Wire Direction	131
6.6.4	Position Resolution Perpendicular to the Wire Direction	138
6.6.5	The Next Generation of CBM TRD Prototypes	141
7	Dielectron Reconstruction in CBM by Using the MB-TRD Geometry	147
7.1	The CbmRoot Simulation Framework	147
7.2	Track and Vertex Reconstruction	148
7.3	Electron Identification	149
7.3.1	Electron Identification in the RICH	150
7.3.2	Electron Identification in the TRD	151
7.3.3	Electron Identification in the TOF	154
7.4	Feasibility Study of Measuring Direct Photons via Conversion into e^+e^- Pairs	154
7.4.1	Photon Measurement in CBM	154
7.4.2	Reconstruction of Photon Conversions	157
7.5	Measurement of Neutral Pions	171
7.5.1	Extraction of the π^0 -Signal	173
	Summary	189
	Zusammenfassung	193
A	Run summary of the test beam in 2006 at GSI	199
B	Technical Drawings	205
	Danksagung	221

Introduction

The focus of this thesis is the development of a Transition Radiation Detector (TRD) for the Compressed Baryonic Matter (CBM) experiment at the future Facility for Antiproton and Ion Research (FAIR) in Darmstadt. In addition, the usage of the TRD in the measurement of direct photons is investigated. CBM will be a fixed-target heavy-ion experiment, which investigates collisions in the beam energy range of 5–35 AGeV.

The nature of nuclear matter at very high temperatures and/or densities is the focus of relativistic heavy-ion physics. In particular, the experimental program aims to study effects of a new phase of matter, the quark-gluon plasma (QGP). The QGP is a deconfined and thermalized form of strongly interacting matter, where individual quarks are liberated from the nucleons. Up to now the phase diagram of strongly interacting matter has not been explored in detail at high net baryon densities. Theoretically, at high baryon densities and low temperatures, a first-order phase transition between hadronic matter and the QGP is expected, but has not yet been experimentally confirmed. In addition, new interest is sparked since recent lattice quantum chromodynamics (QCD) calculations predict this phase boundary ending in a critical endpoint whose existence and exact position in the phase diagram is currently being debated. A large area of the phase diagram can be covered in nucleus-nucleus collisions in the energy range that will be provided at FAIR.

The CBM experiment aims to investigate the regime of high baryon densities where the phase transition is expected to be of first order. Moreover, the discovery of the critical endpoint would be a breakthrough in high-energy heavy-ion research since this observation would be the first measurement on the deconfinement phase-transition line. The goal of the CBM experiment is to look in particular for rare probes by taking advantage of high intensity heavy-ion beams delivered by FAIR. CBM will be a multipurpose experiment with the ability to measure leptons, hadrons, and photons. Therein, a TRD will provide the electron identification and – together with a Silicon Tracking System (STS) – the tracking of charged particles. In conjunction with a ring imaging Cherenkov (RICH) detector and a time-of-flight (TOF) measurement, the TRD is to provide a sufficient electron-identification for the measurements of charmonium and low-mass vector mesons. For the

TRD, the required pion suppression is a factor of about 100 at 90% electron efficiency, and the position resolution has to be of the order of 300 to 500 μm . Moreover, the material budget in terms of radiation length has to be kept at a minimum in order to minimize multiple scattering and conversions which would limit the precise measurement in following TRD stations and other detectors. The largest and up to now unrivaled challenge for the TRD design is that both (PID and tracking) have to be fulfilled in the context of very high particle rates (event rates of up to 10 MHz are envisaged) and at the same time large charged-particle multiplicities of up to 600 per event in the CBM detector acceptance. For the most central part of the TRD, this leads to particle rates of up to 100 kHz/cm².

Currently, the TRD system is envisaged to be subdivided into three stations consisting of three or four layers each. In order to fulfill the CBM requirements, small prototypes of the TRD based on multiwire proportional chambers (MWPC) with pad readout were developed and tested. The development and construction of the prototypes was performed in collaboration with the group of Prof. M. Petrovici from IFIN-HH, Bucharest, Romania. By using secondary beams of electrons, pions, and protons the tracking performance and the electron-pion separation were determined for particle rates of up to 200 kHz/cm².

The TRD layout and the detector responses measured in the test beam were implemented in the existing CBM simulation framework in order to perform realistic physics simulations. The implementation of the TRD layout as well as an analysis of photon conversions into dielectrons are further aspects of the work presented here. A feasibility study for the measurement of photons and neutral pions, decaying into photons, via photon conversions in the target is performed in simulations using the TRD layout developed in hardware.

For more than 20 years photons have been considered as one of the most valuable probes of the dynamics and the properties of matter formed in heavy-ion collisions. In contrast to hadronic particles, which have large interaction cross sections in nuclear matter, photons interact only electromagnetically and have a long mean free path. This path length is typically much larger than the transverse size of the hot dense matter created in nuclear collisions. Since photons can pass through the matter almost undistorted by final-state interactions, they carry information on the entire collision history, and thus provide an undistorted insight into the hot and dense phase in which they are produced.

In CBM, the ECAL is designated to provide photon identification. In addition, a complementary measurement of dielectrons from photon conversions can be used to increase the precision of the photon measurement: this method is very auspicious especially at low momenta due to the good momentum resolution of the electron tracking. The e^+e^- pairs from photon conversions in the target can be measured with the charged particle tracking (STS and TRD) and electron identification detectors (RICH, TRD, and TOF), and they

can subsequently be used for photon reconstruction. The measurement of direct photons requires precise knowledge of the photon contribution from decays (mainly $\pi^0 \rightarrow \gamma\gamma$) to the inclusive photon spectrum. The observation of an enhancement of photons as compared to the expectation from hadron decays can be directly attributed to a direct photon signal. The π^0 -signal is determined through an invariant mass analysis of reconstructed photon pairs.

1. Theoretical Overview

1.1 Particles and Forces

Elementary particle physics examines the fundamental laws of interactions and the origin of matter. In search of the fundamental components, physicists repeatedly penetrated to smaller constituents, which later proved to be divisible. The very first philosophical theories about this topic date back to 460 BC, when Democritus and his teacher Leucippus speculated that matter is composed of smallest indivisible units, the *atoms*. However, it was not until the nineteenth century that this idea was picked up again. In 1803, John Dalton of England introduced the atomic idea to chemistry. He proposed that all matter was composed of small indivisible particles termed atoms and suggested that atoms of a given element possess unique characteristics and weight. Dalton's theory identified chemical elements as a specific type of atom. He inferred proportions of elements in compounds by taking ratios of the weights of reactants. But even at that time, the atomic theory was not yet established and some still believed matter to be continuous with no smallest units of a given kind of matter. Only with Einstein's paper on Brownian motion was the atomic theory ultimately established [Ein05].

At that time the only known forces were electromagnetism and gravity. In the first quarter of the twentieth century, in particular due to experiments by Rutherford, one arrived at the modern idea of the atom, which was found to be composed of an electron shell and a positively charged nucleus containing most of the atomic mass. This can be regarded as the true beginning of elementary particle physics. With the discovery of the neutron in 1932, no doubt was left that the nucleus consists of neutrons and protons, the so-called nucleons. In addition to the electron, the proton, and the neutron, the neutrino was postulated in 1930 in order to reconcile the observations in β -decay with the conservation laws of energy, momentum, and angular momentum. Furthermore, in order to explain physical effects like nuclear decay and binding, new forces were postulated: the weak and strong interactions were introduced. Hence, in the 30s of the last century, four particles were established, by which the known phenomena of atomic and nuclear physics could be described. Nevertheless, this simple system was insufficient. In accelerator experiments carried out during the 50s and 60s of the 20th century, the proton and neutron were found to belong to the *hadrons*, which are a large family of non-fundamental particles that can be subdivided into groups with similar properties. Since the second half of

the 60s the *quark* model put order into the so-called hadron zoo. Using this model, all hadrons as well as their properties could be explained as combinations of two or three quarks. According to present knowledge, quarks are considered as elementary particles. So far, no substructure has been observed.

1.1.1 Leptons and Quarks

All known elementary particles are described by the Standard Model of particle interactions, which combines the elementary particles with three elementary forces: the electromagnetic force, the weak nuclear force, and the strong nuclear force. In this context, gravitation takes a special role. It is not included in the Standard Model and fitting gravity comfortably into the framework has proven to be a difficult challenge. However, for particle physics, when it comes to the small scale of particles, the effect of gravity is so weak that it can be neglected. The elementary particles are grouped into *matter constituents*, which include quarks and leptons, and *interaction quanta* or *gauge bosons*. The latter include particles mediating the force, e.g. the photon, which mediates the electromagnetic interaction. The matter constituents have spin $1/2$, obey Fermi-Dirac statistics, and are therefore called *fermions*. The fundamental fermions are considered as point-like particles. They are listed in Table 1.1. Each particle has a corresponding antiparticle, which is identical in mass, spin and lifetime, but which has opposite additive quantum numbers such as charge.

Leptons are unaffected by the strong interaction. Three leptons – the electron e^- , the muon μ^- , and the tau τ^- – have an electric charge equal to -1 ; they differ in their mass values. The other three leptons, the *neutrinos*, are electrically neutral and have a mass either vanishing (previous measurements cannot exclude that neutrinos of one flavor are mass-less) or very small with an absolute value yet to be determined. Each charged lepton is associated with a neutrino: they are forming a *family*. Lepton families are preserved in all interaction processes, which is tantamount to the conservation of three generalized charges, the electronic number L_e , the muonic number L_μ , and the tauonic number L_τ . This conservation is valid only at a reaction vertex but violated e.g. in the propagation of neutrinos by oscillation. The numbers are assigned to be $+1$ for the corresponding charged lepton and its neutrino, -1 for the corresponding antileptons, and 0 for every other particle.

The quarks are classified into six different types or *flavors*, called *up* (u), *down* (d), *charm* (c), *strange* (s), *top* (t), and *bottom* (b). They are arranged into three families according to their main modes of interactions: (u, d) , (c, s) , (t, b) . The quarks in the first family constitute the basic components of existing matter and the quarks of the other families

Leptons			Quarks		
	Charge (e)	Mass		Charge (e)	Mass
e^-	-1	$0.511 \text{ MeV}/c^2$	u	$+2/3$	$(2.55^{+0.75}_{-1.05}) \text{ MeV}/c^2$
ν_e	0	$< 2 \text{ eV}/c^2$	d	$-1/3$	$(5.04^{+0.96}_{-1.54}) \text{ MeV}/c^2$
μ^-	-1	$105.7 \text{ MeV}/c^2$	c	$+2/3$	$(1.27^{+0.07}_{-0.11}) \text{ GeV}/c^2$
ν_μ	0	$< 190 \text{ eV}/c^2$	s	$-1/3$	$(104^{+26}_{-34}) \text{ MeV}/c^2$
τ^-	-1	$1.777 \text{ GeV}/c^2$	t	$+2/3$	$(171.2 \pm 2.1) \text{ GeV}/c^2$
ν_τ	0	$< 182 \text{ eV}/c^2$	b	$-1/3$	$(4.2^{+0.17}_{-0.07}) \text{ GeV}/c^2$

Table 1.1: Properties of fundamental fermions [Ams08].

are the main components of unstable particles. Unlike leptons, quarks have a fractional electrical charge. The difference between the charges within one family is 1. In order to describe the empirical observation of conservation of baryonic matter, e.g. the stability of the lightest baryon, the proton, the baryonic number N_B was introduced, defined as being $+1/3$ for quarks, $-1/3$ for antiquarks, and 0 for all leptons and antileptons. Hence, the sum of quarks minus antiquarks is conserved and leptons minus antileptons are separately conserved within each family.

Quarks have a quantum number called *color* and come in three colors, which play the role of the charge for the strong interaction among quarks. Shortly after the existence of quarks was proposed for the first time in 1964, O.W. Greenberg introduced the notion of this color charge to explain how quarks could coexist inside some hadrons in otherwise identical quantum states without violating the Pauli exclusion principle. As leptons have no color they cannot couple to the strong force.

All observable particles are color-neutral. In quantum chromodynamics (QCD), a quark's color can take one of three values, called red, green, and blue, and an antiquark can take one of three anti-colors, called anti-red, anti-green, and anti-blue.

Quarks are bound by the elementary force of the strong interaction which results from exchanging particles with integer spin, the *gluons*. Gluons are mixtures of two colors, such as red and anti-green, which constitutes their color charge. QCD considers eight gluons of the possible nine color-anti-color combinations to be unique. There are eight

different gluons as there is no colorless one. Quarks cannot exist as free particles, but only as color-neutral objects confined with other quarks. For example, the proton can be described as $p = uud$, the neutron is $n = udd$, and the pion is $\pi^+ = u\bar{d}$.

1.1.2 Hadrons

Hadrons have an internal structure and thus they are not elementary particles. They can be classified into *mesons*, *baryons*, and their corresponding antiparticles. The mesons are composed of a quark and an antiquark. Consequently, they have spin 0 or 1. They obey Bose-Einstein statistics and are called *bosons*. Baryons consist predominately of three quarks, and thus are fermions of spin $1/2$ or $3/2$. According to QCD sum rules, more exotic states like the *pentaquark* ($qqqq\bar{q}$) are allowed but have not yet been experimentally confirmed although indications for their existence have been discussed recently. Table 1.2 shows a small selection of hadrons and their properties, which are important for this thesis. In fact, hundreds of states are known today (see Reference [Yao06]).

1.1.3 Interactions

Table 1.3 summarizes the four fundamental forces together with their coupling strengths and ranges as well as the masses of the interaction quanta, the particles carrying the force. These particles are called gauge bosons because their existence and physical behavior are predicted and studied in gauge theories. The strength of a force is measured by its coupling constant. At short distances, which are relevant for particle physics, the gravitation is the weakest of all forces and can be neglected. Gravitation and electromagnetism are known from experience to have a very long range, correspondingly the mass of the exchanged bosons is to be very small. At least for the photon the mass is known to be exactly zero. The range of weak interaction is extremely short which implies a large mass for the interaction quantum. Actually, there are three gauge bosons associated with the weak force: two of them, W^+ and W^- , are electrically charged and have a mass of about $80 \text{ GeV}/c^2$, and the other, Z^0 , is electrically neutral with a mass of about $91 \text{ GeV}/c^2$.

When going to electrodynamics, the theory is called quantum electrodynamics (QED), which is a relativistic quantum field theory. QED mathematically describes all phenomena involving electrically charged particles interacting via photon exchange. The electromagnetic and weak forces can be described in a unified way by the so-called electroweak theory. Analogously to QED, the theory of strongly interacting quarks was developed and is called quantum chromodynamics (QCD).

Mesons					
	$I(J^P)$	Mass (MeV/ c^2)	Full width (MeV/ c^2)	Mean lifetime (s)	Decay modes (BR)
π^\pm	$1(0^-)$	139.6		$2.6 \cdot 10^{-8}$	$\mu^\pm \nu$
π^0	$1(0^-)$	135.0		$0.83 \cdot 10^{-16}$	$\gamma\gamma, e^+e^-\gamma$ (1.2%)
η	$0(0^-)$	547.5		$0.8 \cdot 10^{-18}$	$\gamma\gamma, 3\pi^0, \pi^+\pi^-\pi^0$
K^\pm	$\frac{1}{2}(0^-)$	493.7		$1.2 \cdot 10^{-8}$	$\mu^\pm \nu, \pi^\pm \pi^0$
K^0, \bar{K}^0	$\frac{1}{2}(0^-)$	497.7			50% K_S^0 , 50% K_L^0
K_S^0				$0.9 \cdot 10^{-10}$	$\pi^+\pi^-, 2\pi^0$
K_L^0				$5.2 \cdot 10^{-8}$	$3\pi^0, \pi^+\pi^-\pi^0,$ $\pi^\pm e^\pm \nu, \pi^\pm \mu^\pm \nu$
ρ	$1(1^-)$	775.5	149.4		e^+e^- ($4.7 \cdot 10^{-5}$), $\mu^+\mu^-$ ($4.6 \cdot 10^{-5}$)
ω	$0(1^-)$	782.7	8.5		e^+e^- ($7.2 \cdot 10^{-5}$), $\mu^+\mu^-$ ($9.0 \cdot 10^{-5}$)
Φ	$0(1^-)$	1019.5	4.3		e^+e^- ($2.97 \cdot 10^{-4}$), $\mu^+\mu^-$ ($2.86 \cdot 10^{-4}$)
J/ψ	$0(1^-)$	3096.9	0.093		e^+e^- (5.94%), $\mu^+\mu^-$ (5.93%)
Baryons					
	$I(J^P)$	Mass (MeV/ c^2)		Mean lifetime (s)	Decay modes (BR)
p	$\frac{1}{2}(\frac{1}{2}^+)$	938.3		$>10^{31}$ a	stable
n	$\frac{1}{2}(\frac{1}{2}^+)$	939.6		917	$p e^- \bar{\nu}$
Λ^0	$0(\frac{1}{2}^+)$	1115.6		$2.6 \cdot 10^{-10}$	$p \pi^-, n \pi^0$
Σ^+	$1(\frac{1}{2}^+)$	1189.4		$0.8 \cdot 10^{-10}$	$p \pi^0, n \pi^+$
Σ^0	$1(\frac{1}{2}^+)$	1192.5		$7 \cdot 10^{-20}$	$\Lambda \gamma$
Σ^-	$1(\frac{1}{2}^+)$	1197.4		$1.5 \cdot 10^{-10}$	$n \pi^-$
Ξ^0	$\frac{1}{2}(\frac{1}{2}^+)$	1314.9		$2.9 \cdot 10^{-20}$	$\Lambda \pi^0$
Ξ^-	$\frac{1}{2}(\frac{1}{2}^+)$	1321.3		$1.6 \cdot 10^{-10}$	$\Lambda \pi^-$

Table 1.2: Properties of a selection of important, strongly interacting particles (I =Isospin, J =Spin, P =Parity, BR=Branching ratio) [Yao06].

Interaction	Physical phenomenon	Effective coupling	Gauge boson, mass	Range
Strong force	Nuclear binding	1	gluons, 0	10^{-13} cm
Electromagnetism	Electricity, magnetism, optics	1/137	photon, 0	∞
Weak force	Radioactive decay	10^{-5}	W^\pm, Z^0 , (80 – 91) GeV/ c^2	10^{-16} cm
Gravitation	Curved space-time continuum	10^{-39}	graviton	∞

Table 1.3: Characteristic properties of the fundamental interactions [Yao06].

An important feature of QCD, the quantum field theory of the interactions of quarks and gluons, which was discovered in 1973 by D. Gross and F. Wilczek [Gro73] and by D. Politzer [Pol73], is the *asymptotic freedom*. This means that the coupling between colored particles, such as quarks, becomes arbitrarily weak at very short distances, i.e. length scales that asymptotically converge to zero (or, equivalently, energy scales that become very large). Asymptotic freedom implies that in high-energy scattering the quarks move within nucleons, such as the neutron and proton, mostly as free, non-interacting particles. When the coupling approaches 0, asymptotic freedom allows to calculate the cross sections of processes involving large scales (momentum transfer Q^2 or masses) in particle physics reliably using perturbative techniques. In contrast, when the coupling becomes large, analytic or perturbative solutions in QCD are difficult or impossible due to the highly nonlinear nature of the strong force. If so, one uses *lattice QCD*, which is a theory of quarks and gluons formulated on a space-time lattice. It is a special case of a lattice gauge theory or lattice field theory. At the moment, this is the most established non-perturbative approach to QCD.

In first order QCD perturbation theory the strength of the coupling between quarks can be specified as function of the momentum transfer Q^2 of the interaction:

$$\alpha_s(Q^2) \approx \frac{12\pi}{(33 - 2N_f) \cdot \ln(Q^2/\Lambda^2)}, \quad (1.1)$$

where N_f is the number of participating quark flavors ($N_f \leq 6$) and Λ is the free scale constant of QCD [Roe96]. High momentum transfers are tantamount to small quark distances. As mentioned before, asymptotic freedom describes the behavior for $\alpha_s(Q^2) \rightarrow 0$ or $Q^2 \rightarrow \infty$, respectively.

Since no free color-charges are observed, it is postulated that the total color charge of quark combinations has to be color-neutral for measurable particles. This is true for baryons with the quark content (qqq) and mesons with the quark content ($q\bar{q}$). More exotic states have not yet been discovered. This property is called *confinement*. Although lattice QCD can already calculate confined objects to some degrees, the exact mechanisms of confinement are not yet fully understood. However, the confinement of quarks in hadrons can be illustrated by the phenomenological potential of a quark-antiquark system:

$$V_{q\bar{q}}(r) = -\frac{4}{3} \frac{\alpha_s(r)}{r} + k \cdot r. \quad (1.2)$$

The term $k \cdot r$ dominates at large distances and corresponds to a distance-independent, constant force. The k is often associated with string tension. Hence, in contrast to an atomic binding, the breakup of a quark-antiquark pair requires an infinite high energy transfer.

1.2 Quark-Gluon Plasma and Hadron Gas

A proton has a mass of about $1 \text{ GeV}/c^2$ and an average charge radius of about 0.875 fm [Ams08]. This corresponds to an energy density $\varepsilon = E/V$ of about $0.36 \text{ GeV}/\text{fm}^3$. If it is possible to produce nuclear matter with an energy density of this scale, one can imagine that the individual hadrons overlap in such a volume. Quarks and gluons can move throughout the volume which is large in comparison to a hadron volume. That means that the quark confinement in hadrons vanishes and individual, confined hadron-gas particles dissolve into a free gas of quarks and gluons, which is referred to as the quark-gluon plasma (QGP).

The QGP can be defined as thermalized many-particle system whose thermodynamic properties are dominated by the degrees of freedom of the quarks and gluons. In contrast to a simple hadron gas with only three pion degrees of freedom and without any color charge, the QGP has a larger number of thermodynamic degrees of freedom. The transition of hadron matter to a QGP at a critical temperature T_c is predicted by many simple models (e.g. the *bag model* [Cho74]) and also by lattice QCD calculations. The different phases of QCD are illustrated in the phase diagram of strongly interacting matter.

1.2.1 The Phase Diagram of Strongly Interacting Matter

A schematic phase diagram of QCD matter is shown in Fig. 1.1 in the plane of temperature T and baryo-chemical potential μ_B . Based on the fundamental property of asymptotic

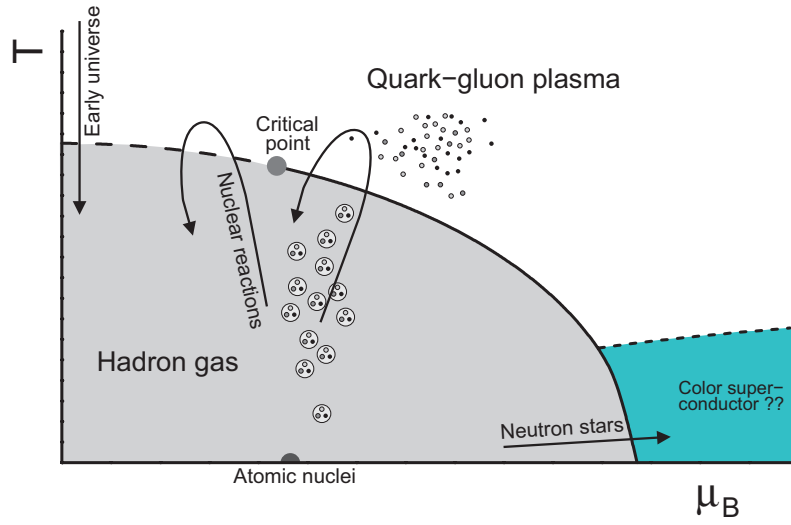


Figure 1.1: Schematic phase diagram of QCD [KB05]. The dot on the μ_B -axis denotes the baryon density of normal nuclear matter. Possible locations at which the various phases of QCD may exist include the hot plasma in the early universe, the dense plasma in the interior of neutron stars, and the hot/dense matter created in heavy-ion collisions.

freedom, one expects at least three different regions: the hadronic phase (at low μ_B and low T), the QGP (at high T) and the color-superconducting region (at high μ_B , low T). For high temperatures and/or high baryon densities, we expect a deconfined phase. Possible phases and the precise location of the phase transitions and critical points are currently studied also from a theoretical side. An overview of recent experimental results is given in Chapter 1.3.1. Theoretically, a first-order phase transition is expected at high baryon densities and low temperatures. In general, first-order phase transitions exhibit a discontinuity in the first derivative of the free energy with respect to a thermodynamic variable. The phase coexistence curve between the hadron gas and QGP may end in a critical point, in which the phase transition is of second order. The existence as well as the exact position of the critical point in the phase diagram are currently being debated. Recent lattice QCD calculations predict the phase transition in the region of highest temperature to be neither of first nor of second order. In this region, it is expected that variables like the energy density change quickly but continuously in the vicinity of T_c . Thus, a transition in this region is called *crossover* [Fod04]. Since the existence of the critical point and of a first-order phase transition are not yet confirmed, the phase transition may also remain a crossover all along. Depending on the curvature of the critical surface in the μ - m_u - m_d - m_s space (with the quark masses m_u , m_d , m_s and the quark density μ), a QCD chiral critical point may be

present or not [Phi08]. While the theoretical assumptions are still ambiguous, it is widely accepted that given the existence of a first-order phase transition at finite baryon density terminating in a critical endpoint, a crossover is expected at $\mu_B = 0$.

At very high densities and very low temperatures, correlated quark-quark pairs (Cooper pairs) are predicted to form a color superconductor [Alf01]. This color-superconductive phase has already been conjectured early in the study of quark matter [Bar77].

The transition from a hadron gas to a QGP is also interesting for cosmology and astrophysics. Today it is believed that in the Big Bang scenario for the origin of the universe the elementary particles were produced in the freeze-out from a QGP phase with high temperature and low baryon density around $1 \mu\text{s}$ after the Big Bang. Furthermore, it can be seen in the phase diagram that a phase transition to the QGP, or even to more exotic states of matter at zero temperature, is expected for large baryon densities. It is assumed that these densities are reached in the center of neutron stars. Here, the possible superconducting phase and the QGP can play an important role in the stability of neutron stars. In this context, it might even be possible to use astrophysical observations to rule out or confirm expected phases [Alf08].

Deconfinement can also be reached in nuclear-collision reactions. It ‘freezes’ back into the state containing confined hadrons during the temporal evolution of the small fireball, as indicated in the arrows in Fig. 1.1. Almost the entire μ_B region can be explored by varying the collision energy of the colliding nuclei (as discussed in Chapter 1.3.1).

1.2.2 Chiral-Symmetry Restoration

Besides confinement, QCD has another important property, which is associated to the fact that the masses of the u - and d -quarks are small compared to the relevant scales of QCD. Thus, these masses can be taken as zero for many practical applications. The theory assumes that a massless quark with its spin pointing into the direction of the momentum preserves its helicity for all times in spite of the interaction with other quarks and likewise for a mass-less quark with its spin opposite to the direction of motion. This symmetry is called chiral symmetry because the conserved spin alignment with the quark’s direction of motion can be associated with the right-, respectively left-handedness. They are so-called chiral partners under parity transformation. Chiral symmetry predicts for every particle the existence of a mirror reflected particle with same properties such as the mass. Hence, the spectrum of hadrons should group into parity partners with identical properties. This, however, is not observed in nature (see Chapter 1.1). Actually, the parity partners exhibit large differences in their masses. Hence, in nature chiral symmetry is observed to be

spontaneously broken. If chiral symmetry is spontaneously broken, zero mass excitation modes have to exist. These particles, the so-called Goldstone bosons, can be associated with the pions. Their small masses (on the scale of hadron masses) are an indication of “leftovers” of chiral symmetry. Pions are the lightest hadrons and they indeed have proper chiral properties. Their masses are not quite vanishing which results from the small but finite masses of the u - and d -quarks. These finite masses explicitly break chiral symmetry just like an externally applied magnetic field breaks the spin symmetry in a ferromagnet. The concept of chiral symmetry has turned out to be very powerful for the understanding and interpretation of the light hadrons and their structure.

At high temperatures and/or densities a transition to the chirally restored phase is expected. This fact would imply dramatic changes in the properties of certain hadrons in the medium in the vicinity of the phase transition. In the chirally restored phase each particle and its parity partner have to become alike. In particular, their masses have to become similar.

1.3 Relativistic Heavy-Ion Collisions

A challenging field of modern physics is the investigation of nuclear matter under extreme conditions and the exploration of the phase diagram of strongly interacting matter with high-energy nucleus-nucleus collisions.

Classical experiments for investigating the atomic structure, e.g. via excitation with electron collisions, require typical energies of a few eV. For the examination of the next smaller units, the atomic nuclei, already energies of some MeV are required. With increasing energies ever smaller dimensions can be explored. This relation can be understood through the uncertainty principle of Heisenberg:

$$\Delta p_x \cdot \Delta x \approx \hbar. \quad (1.3)$$

Consequently, probes with a minimum momentum of $p \approx \hbar/\Delta l$ are required to resolve the structures of the size Δl . Therefore, very high particle energies are necessary for elementary particle physics to resolve the structure of matter.

Dense matter with properties similar to those in nucleus-nucleus collisions is expected to have existed in the early universe until about $10 \mu\text{s}$ after the Big Bang. In order to study the bulk properties of that matter the largest possible volume of that matter is required. It is important to understand its collective behavior and not only point-like interactions. That is why the study of high-energy collisions of the heaviest nuclei is preferred to the investigation of more elementary systems like interactions of protons and leptons. Up

to now, the largest physical systems studied in the laboratory are collision systems of lead (Pb) and gold (Au). Besides Pb and Au, the future FAIR facility will also accelerate uranium (U) ions (see Chapter 4.1), which are even heavier, but the non-spherical shape of these ions exacerbates the production of central collisions and the determination of the collision centrality.

When atomic nuclei collide at very high energies, such that the kinetic energy exceeds significantly their rest energy, dense hadronic matter is produced. In such relativistic heavy-ion collisions the energy density of hadronic matter typically exceeds a value of $\epsilon = 1 \text{ GeV fm}^{-3} = 1.8 \times 10^{15} \text{ g cm}^{-3}$, and the corresponding relativistic matter pressure is $P \simeq \frac{1}{3}\epsilon = 0.52 \times 10^{30} \text{ bar}$ [Let02].

Although genuine phase transitions are not expected to develop in finite physical systems, it is possible to experimentally explore the properties of the phase transition involving the dissolving of hadronic particles. The reason for this is that relativistic systems are investigated in which the ability to produce particles from energy and the presence of virtual fluctuation effects greatly enhance the number of physical states accessible. Hence, it is possible to identify a phase transition from the nuclear, hadronic phase to a matter phase consisting of quarks and gluons in collisions of relativistic heavy-ions.

Experimental results have shown that in relativistic heavy-ion collisions a dense hadronic fireball can be formed, well localized in space, with an energy density exceeding 1 GeV/fm^3 [Let02]. Due to the high internal pressure, this fireball explodes rapidly: the lifetime is characterized by the size of the system $\tau \simeq 2R/c$. In relativistic heavy-ion reactions, the collision energy is shared among numerous newly produced hadronic particles. In the final state much more low-energy particles than high-energy particles are produced, the latter mainly stemming from hard, elementary interactions. The conversion of kinetic collision energy into high particle multiplicity can be examined using statistical mechanics. This description does not require a complete knowledge of the microscopic production and dynamics of particles.

It is also expected that very high baryon densities – which are comparable to those in the core of neutron stars – can be reached in heavy-ion collisions. Complementary to the activities at the Relativistic Heavy Ion Collider (RHIC) at BNL and at the Large Hadron Collider (LHC) at CERN, which concentrate on high temperatures and very low net baryon densities, the approach of the Compressed Baryonic Matter (CBM) experiment is the exploration of the phase diagram in the region of highest baryon densities. The CBM research program aims at the exploration of the structure of high-density matter, particularly the question of deconfinement and chiral phase transitions. Details about the CBM experiment can be found in Chapter 4.

1.3.1 Exploration of the QCD Phase Diagram

The current knowledge of the phase diagram of strongly interacting matter is shown in Fig. 1.2. This diagram presents the temperature T versus the baryo-chemical potential μ_B . Recent lattice QCD calculations predict a phase boundary between hadronic matter and quark-gluon matter with a critical endpoint [Fod04]: at zero baryo-chemical potential at a critical temperature T_c lattice QCD calculations predict a smooth crossover from the hadronic to the partonic phase (dotted line), whereas for values of μ_B larger than about 360 MeV a first-order deconfinement phase transition is expected. Up to now, the phase boundary is only predicted quantitatively at small values of μ_B (about up to 400 MeV). At higher baryon densities calculations are very difficult since the results strongly depend on the lattice size and quark mass, and the physical limit is not yet reached (lattice spacing $\rightarrow 0$, quark mass \rightarrow real quark mass). The predictions for the temperature of the critical endpoint cover a range from 150 to 190 MeV, Z. Fodor and S.D. Katz expect it at $T = 162 \pm 2$ MeV and $\mu = 360 \pm 40$ MeV [Fod04]. However, as mentioned above, even the existence of a critical endpoint is still debated. These results still need to be supported by more realistic calculations based on physical quark masses and a more accurate continuum extrapolation.

The data points in Fig. 1.2 are chemical freeze-out points characterizing the state at the time when the particle ratios are fixed, and they are obtained from a statistical model analysis of particle ratios measured in Pb+Pb and Au+Au collisions at SIS (Heavy Ion Synchrotron at GSI, Darmstadt), AGS (Alternating Gradient Synchrotron at BNL, New York), SPS (Super-Proton-Synchrotron at CERN, Geneva), and RHIC (Relativistic Heavy Ion Collider at BNL, New York) [BM01b, Bec04, BM01a].

The approach of the CBM experiment at the future FAIR Accelerator Facility in Darmstadt is the investigation of the QCD phase diagram at high baryon densities. The CBM experiment is described in Chapter 4 and details on FAIR can be found in Chapter 4.1. Very high baryon densities can be reached in heavy-ion collisions at moderate beam energies. The SIS 300 accelerator at FAIR will provide high-energy ion beams of maximum energies close to 35 GeV/A for fully stripped uranium beams, and the highest available proton energy is 89 GeV. The maximum intensities in this mode are 10^{13} particles/s for protons and close to 10^9 particles/s for gold ions.

The time evolution of the baryon density in the center of a head-on Au+Au collision can be calculated using transport codes, e.g. involving the quark-gluon string model (QGSM) [Ars07]. In Fig. 1.3 a), the net baryon density as a function of time is shown for beam energies between 5 and 40 AGeV. It can be seen that already for a beam energy

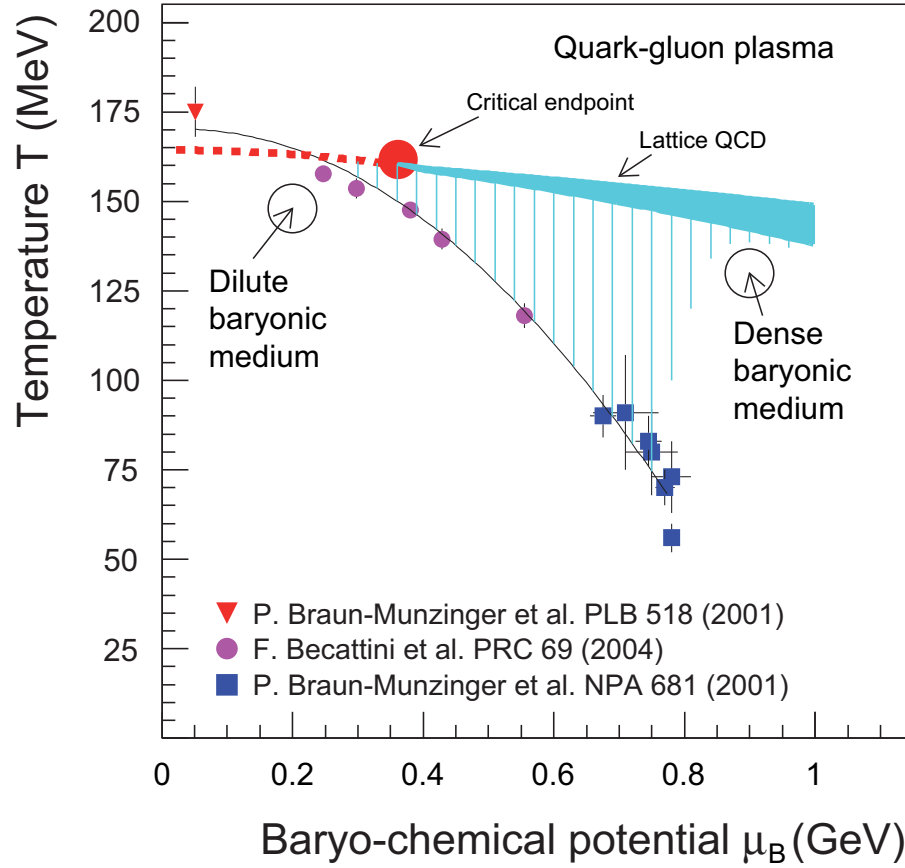


Figure 1.2: The phase diagram of strongly interacting matter as function of temperature and baryo-chemical potential. The full symbols represent chemical freeze-out points obtained with a statistical model analysis from particle ratios measured in heavy-ion collisions [BM01b, Bec04, BM01a]. The upper line represents lattice QCD calculations for a crossover phase transition (dotted region) [Fod04]; for values of μ_B larger than about 400 MeV the phase transition is expected to be of first order (band) but up to now it is not predicted quantitatively. The full point denotes the end-point of the crossover transition from Reference [Fod04].

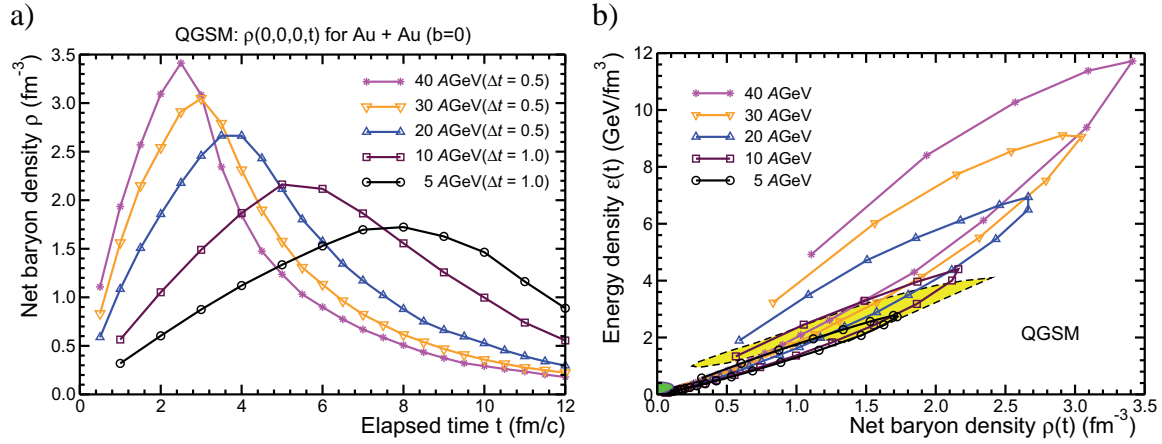


Figure 1.3: a) QGSM calculations of the evolution of the net baryon density $\rho(t)$ in the inner volume of central Au+Au collisions, and b) the dynamical phase trajectory in the plane of $\rho(t)$ and energy density $\epsilon(t)$ are shown for different beam energies between 5 and 40 AGeV, with the same increments Δt between the symbols [Ars07]. The yellow region, which depicts a schematic boundary with a critical point, serves as a reference for the phase trajectories.

of 5 AGeV for about 5 fm/c the baryon density exceeds a value of 1 fm^{-3} , which is more than 6 times the normal nuclear-matter density of about 0.15 fm^{-3} .

In these models, the energy density can be related to the baryon density at a given time. In Fig. 1.3 b), the dynamical phase trajectory $(\rho(t), \epsilon(t))$ is shown for different beam energies within the QGSM model. At each beam energy, the return path depicting the expansion lies below the early compression path, although the two paths generally differ only relatively little. Each path is fairly straight and its slope increases steadily with increasing beam energy. For the lowest energy, 5 AGeV, the trajectory is expected to just reach the predicted hadronic boundary of the schematic phase coexistence region. The energy density is predicted to reach a value of $2 \text{ GeV}/\text{fm}^3$ which is – according to lattice QCD calculations – already beyond the transition density to a partonic phase. The next energy, 10 AGeV, already shows a turning point on the plasma side beyond the schematic phase coexistence region. Thus, of all trajectories shown, this one spends the longest time traversing the phase coexistence region during the expansion phase, while the crossing time becomes shorter as the beam energy is increased.

Trajectories of nucleus-nucleus collisions in the $T-\mu_B$ plane have also been calculated within a 3-fluid hydrodynamics model [Iva06]. In Fig. 1.4, trajectories corresponding to different beam energies are shown. In this phase diagram, the critical endpoint as recently predicted by lattice QCD calculations is also shown (red star). According to these hydro-

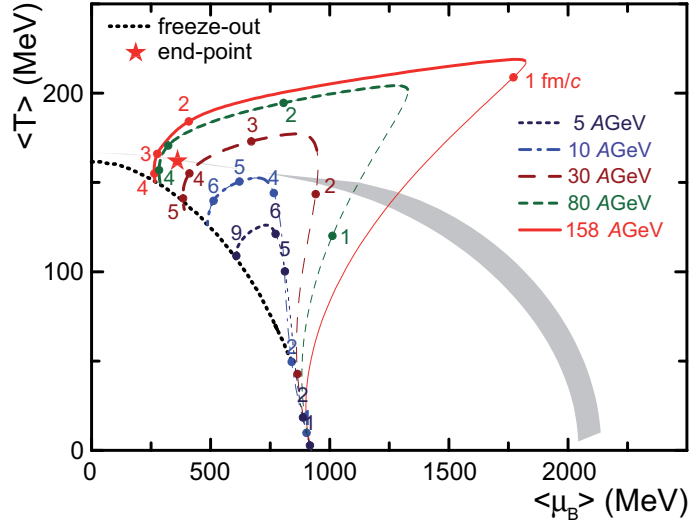


Figure 1.4: Dynamical trajectories in the $T-\mu_B$ plane, calculated by a 3-fluid hydrodynamics model, for central Pb+Pb collisions ($b = 2.5$ fm) at various incident energies [Iva06]. The numbers near the dynamical trajectories indicate the evolution time instants (in fm/c) in the c.m. frame of the colliding nuclei. The bold parts of trajectories are related to an approximately thermalized, baryon-rich subsystem, and the thin ones are related to the pre-equilibrium evolution. The gray-shaded region corresponds to an estimation of the boundary of the phase transition from the hadronic phase to the QGP. The dotted line is the “experimental” freeze-out curve fitted to observed multiplicities in the approximation of the ideal gas model under the condition that the energy per hadron is 1 GeV. The star-symbol denotes the predicted critical end-point from Reference [Fod04].

dynamic calculations, the critical endpoint may be found in the vicinity of the freeze-out point of central Pb+Pb collisions at a beam energy of about 30 AGeV. Therefore, the FAIR energy range is well suited to search for the first-order deconfinement phase transition and its critical endpoint.

1.3.2 Signatures for a Phase Transition

In high-energy nucleus-nucleus collisions hot and dense nuclear matter can be generated in a wide range of initial temperatures and densities, and its following spatio-temporal evolution can be investigated. In the collision zone, the matter is heated and compressed for a very short period of time. If the energy contained in the fireball is large enough the quark-gluon substructure of the nucleons comes into focus. Nucleons are excited to short-lived states (baryon resonances), which decay by the emission of mesons. At higher temperatures also baryon-antibaryon pairs can be created. This mixture of mesons, baryons

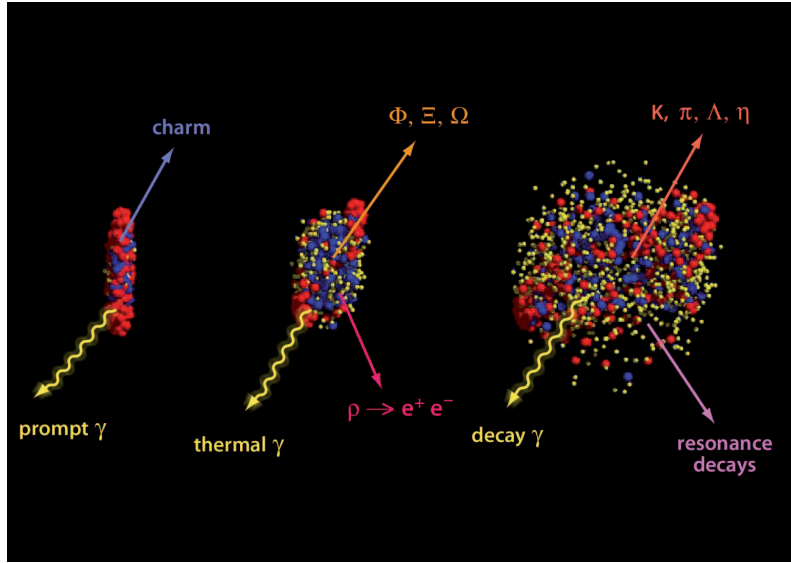


Figure 1.5: Snapshots of a simulation of the collision of two heavy nuclei at 23 GeV/nucleon beam energy performed by UrQMD [UrQ02].

and antibaryons is generally called hadronic matter, or baryonic matter if baryons preponderate. In accordance with QCD the strong force weakens with increasing energy and at sufficiently high temperatures and/or densities the hadrons overlap, and the partons may move freely forming the QGP. In the QGP the quarks and gluons are deconfined and can move throughout the volume of the expanding system (see Chapter 1.2).

The simulation of two colliding uranium nuclei at 23 GeV/nucleon beam energy has been carried out using the Ultra-relativistic Quantum Molecular Dynamics model (UrQMD) [UrQ02]. Snapshots of the reaction taken at different times are shown in Fig. 1.5. The figures show the collision in the center-of-mass system (CMS). The relativistic factor $\gamma = 1/\sqrt{1 - v^2/c^2}$ in a collision with 23 GeV/nucleon beam energy is about 7 in the CMS and thus, the nuclei are drawn Lorentz-contracted. The nuclei partially interpenetrate, and in the very early stage direct collisions between quarks and gluons with high momentum transfer (*hard processes*) appear. These hard processes can be described within pQCD. In the fireball volume between the non-interacting nuclear fragments, a system of large energy density is created. After a short time, a thermalized state, the QGP, can arise [Rey04]. By reason of the high pressure the QGP expands and cools. If a QGP had been created, the phase transition to the hadron gas will appear next in the evolution. The hadron gas then expands and cools. At thermal freeze-out the hadron gas has cooled such that the hadrons can disperse without further collisions.

Note the difference between chemical and thermal freeze-out. The chemical freeze-out point is the stage in the evolution of the hadronic system when inelastic collisions cease and the relative particle ratios become fixed. It is defined by the temperature, T , and also by the chemical potential, μ_B . These parameters, T and μ_B , determine the particle composition of the hadronic final state. After chemical freeze-out, the particle composition inside the fireball is fixed, but elastic collisions still allow to define the system until the final, thermal freeze-out. At this stage the momentum distributions of particles are no longer changed and are final. Therefore, the conditions at thermal freeze-out are reflected in the transverse-momentum spectra.

Indeed, it is challenging to find diagnostic probes which are associated with the chiral-symmetry restoration and the phase transition to deconfinement. The dynamics of the reaction is very important because after the plasma phase the system returns into a hadron gas and all observables can be affected. The signatures can be separated into sensitivities to physical processes:

- observables depending on the thermodynamics and hydrodynamics of the different phases and characterizing a phase transition,
- probes of deconfinement,
- observables which are influenced by chiral-symmetry restoration.

Probes for the Thermo- and Hydrodynamical Properties of a Phase Transition

The onset of a first-order phase transition is expected to cause a discontinuity in the excitation function of particular observables: thermodynamical properties such as the temperature, the pressure, the energy density, and the entropy of a system as well as their relation are influenced by a phase transition. Most of these thermodynamical properties show a distinct behavior only in the case of a first-order phase transition. This can be examined by a beam energy scan looking at different diagnostic probes. It includes the measurement of the phase-space distributions of strange particles, in particular multi-strange baryons and antibaryons, and particles containing charm quarks. Furthermore, event-by-event fluctuations are expected to arise when crossing the first-order phase transition, and in particular in the vicinity of the critical endpoint. For example, like in any other system, also in the QGP the average transverse momentum $\langle p_T \rangle$ is related to the temperature of the system. Fluctuations in T and thus $\langle p_T \rangle$ are expected at a phase transition of first or second order. Nevertheless, after the chemical freeze-out from the QGP the hadrons interact and thus the information might be distorted. Here, the time between the chemical

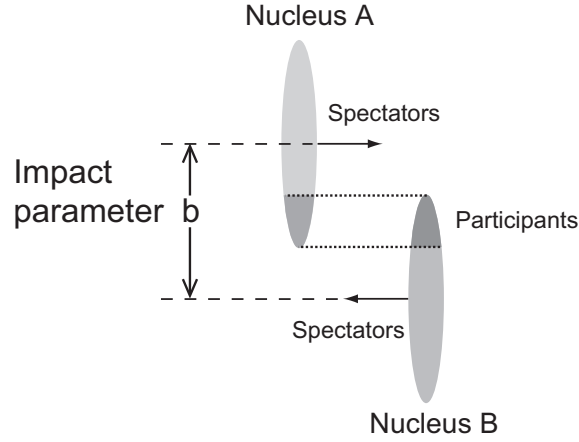


Figure 1.6: Schematic view of two colliding nuclei in the geometrical participant-spectator model. The distance between the centers of the two Lorentz contracted nuclei is the impact parameter b .

and the kinetic freeze-out is important. Electromagnetic probes like thermally produced dileptons and photons, which are not influenced by the strongly interacting medium, may allow to characterize the medium since they propagate largely unperturbed. These probes are discussed in detail in Chapter 2.

The entropy and energy density of the system is related to the measured particle multiplicity dN/dy and the transverse energy dE_T/dy at mid-rapidity. An important observable, being sensitive to the effective degrees of freedom, is the *collective flow*. Information about the equation of state (EOS) can be extracted from the collective flow of nuclear matter deflected sideways from the hot and dense region formed by the overlap of projectile and target nuclei. This flow reflects collective properties of the medium. In the hydrodynamical picture, the pressure gradient generates the collective flow. In the almond shaped region of a non-central collision (with impact parameter $b > 0$ as shown in Fig. 1.6), the pressure gradient is expected to be larger in the direction of the impact parameter. Thus, the particle production will have an elliptical azimuthal distribution characterized by the second Fourier coefficient (v_2) of a Fourier decomposition of these angular distributions. Since the pressure gradient is closely related to the EOS, it is important to measure the elliptic flow in order to detect the existence of the QGP pressure in the early stage. If the phase transition is of first order, the pressure remains constant during the phase transition. This results in a vanishing sound velocity, $c_s = \sqrt{\partial P / \partial \epsilon}$, which is referred to as “softening” of the EOS. The collective expansion velocity will be reduced significantly if softening occurs and the study of collective motion in the final state of the produced hadrons is expected to provide key information about the EOS [KY05].

Signatures from Deconfinement

A measurement of the yields and phase-space distributions of baryons containing strange quarks, in particular of multi-strange baryons, is expected to be sensitive to the early and dense stage of the collision. Initially, the production of strange (s)-quarks was expected to be enhanced in the deconfined QGP compared to a hadron gas [Raf82]. The temperature, which is expected to be necessary for the dissolving of nucleons and hadrons into quarks and gluons is similar to the energy, which is necessary to generate an $s\bar{s}$ -pair. Strange-quarks can be produced by gluon (g) fusion in the plasma $g + g \rightarrow s + \bar{s}$. A further reason for the expected enhanced production of s -quarks is the occupancy of energy states by lighter quarks, which may lead to a more probable generation of $s\bar{s}$ -pairs. Their subsequent hadronization can cause an enrichment of particles containing strange quarks (like the ϕ -meson) in comparison to a hadron reaction without creation of a QGP. However, the strange production depends on the temperature evolution of the system and the life-time of the two phases. Thus, significant changes in relative and absolute abundance of strange particles, such as Λ , and more exotic multistrange hadrons are expected.

Further interesting observables are hadrons containing charm quarks. The hadronic bound states (with a c or \bar{c} quark) have a much larger mass than the ordinary hadrons and it is expected that *charmonia*, in particular, can only be formed in the very early phase of the heavy-ion collision. In contrast to the condition for strange-particle production, the temperature is not high enough for significant thermal quarkonia production. The ground state of charmonium is the J/ψ , whose suppression has long been a proposed signature for deconfinement [Mat86]. In the QGP the attractive potential between a $c\bar{c}$ is screened by the large density of free color charges in the medium. Thus, at hadronization time the dissociated charm quarks couple with a larger probability to the abundant lighter quarks than recombining to a J/ψ .

At FAIR energies the charm production is of special interest, because charmonium and open charm such as D-mesons and charmed hyperons are created at beam energies close to the kinematic threshold: The highest FAIR energies $E_{\text{beam}} = 30 \text{ AGeV}$, corresponding to $\sqrt{s} = 7.74 \text{ GeV}$ for a nucleon pair, are slightly above threshold for the charm production process with the lowest threshold $NN \rightarrow D^- (\bar{D}^0) \Lambda_c N$, $\sqrt{s_{\text{thres}}} = 5.073(5.069) \text{ GeV}$ [TG08]. Since changes are likely to have a strong effect at near-threshold production, these particles are sensitive probes of the early stage of the collision. Due to the very high intensity heavy-ion beams provided at FAIR, the total abundances of charmonia and open-charm mesons become large. Fig 1.7 shows the multiplicities of π^+ , η , K^+ , K^- , ϕ , D , \bar{D} , and J/ψ -mesons for central collisions of Au+Au as function of beam energy from SIS to RHIC energies. These multiplicities are calculated in the Hadron-String Dynamics (HSD)

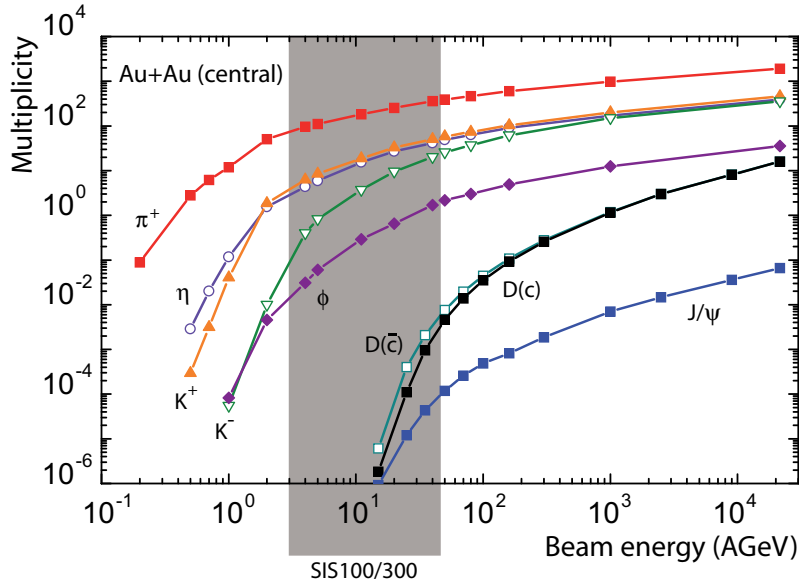


Figure 1.7: Multiplicities of π^+ , η , K^+ , K^- , ϕ , D , \bar{D} , and J/ψ -mesons for central collisions of Au+Au as function of beam energy in the HSD approach including elastic and inelastic reactions, but no in-medium modifications of their spectral functions [Cas01].

transport approach [Ehe96]. The high beam intensity at FAIR leads to sufficient statistics for more detailed measurements of charmed particles as their collective effects may be visible for the first time at these energies. Here, especially the transverse-momentum spectra are expected to provide valuable insight into the dynamics in the very early phase. Since the charm quarks are produced early in the reaction their rescattering – reflected in high- p_T suppression – and collectivity $v_2(p_T)$ are expected to reflect the dynamics in the early phase more sensitively [CBM09a].

Information on Chiral-Symmetry Restoration

The observation of in-medium modifications of hadron properties may be a signature for the onset of chiral-symmetry restoration (see Chapter 1.2.2). The in-medium spectral function of short-lived vector mesons can be measured directly via their decay into dilepton pairs as discussed in detail in Chapter 2.1. Since dileptons are essentially unaffected by the passage through the high-density matter, their study will provide information on the conditions in the interior of the collision zone.

2. Probing Heavy-Ion Collisions with Dileptons and Photons

Since photons and leptons are only affected by the electroweak interaction, electromagnetic probes from the fireball – direct photons on the one hand and virtual photons (detected as e^+e^- or $\mu^+\mu^-$) on the other hand – have been suggested long ago as promising carriers of information on the properties of superdense matter [Shu78, Shu80, McL85]. Photons and leptons have a large mean free path in comparison to the strongly interacting particles produced in heavy-ion collisions. Since they can pass through the matter almost undistorted by final-state interactions, these observables carry information on the entire collision history and thus provide an undistorted insight into the hot and dense phase in which they are produced.

Although photons and leptons can leave the produced medium unaffected, their measurement is subject to the complication that during the evolution of the heavy-ion collision different processes are leading to their production. Consequently, it is necessary to find an assignment to known processes to get information on the circumstances of their production. A rough ordering is given by their momentum; generally, the larger the momentum the earlier those photons and leptons have been produced.

2.1 Dileptons

Virtual photons, which are measured through their decay into lepton pairs, are a possible observable for the detection and characterization of a phase transition to the QGP, or for in-medium vector meson properties, and chiral symmetry restoration (see Chapter 1.2.2). The lepton pairs $l\bar{l}$ (e.g. e^+e^- , $\mu^+\mu^-$) created in the reaction $\gamma^* \rightarrow l\bar{l}$ are called *dileptons* and can be measured in the experiment. The dilepton is characterized by a four-momentum $P = P_{l^+} + P_{l^-}$. From this, the Lorentz-invariant quantities – the squared dilepton invariant mass $m_{\text{inv}}^2 = P^2$ and the dilepton transverse momentum $p_T = p_{T,l^+} + p_{T,l^-}$ – can be derived. After the lepton and its antiparticle partner are produced, they have to pass through the collision region to reach the detectors in order to be observed. Since the leptons interact with the particles in the collision only electromagnetically, they are not influenced strongly. Consequently, the mean free path of the leptons is expected to be

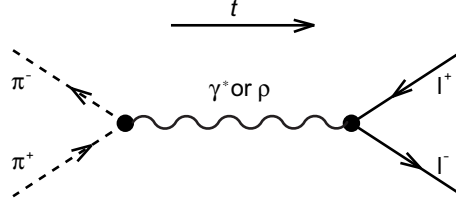


Figure 2.1: The diagram for the reaction $\pi^+ + \pi^- \rightarrow l^+ + l^-$.

quite large and the leptons are not likely to suffer further collisions after they have been produced.

Hadrons and resonances are produced in the initial nucleus-nucleus collision. Dilepton pairs can be produced in hadron-hadron interactions. As the dominant constituents of the hadronic matter are pions, many dileptons are produced by the interaction $\pi^+ + \pi^- \rightarrow l^+ + l^-$ which is illustrated by the Feynman diagram in Fig. 2.1. The wavy line represents a virtual photon γ^* in scalar electrodynamics and a ρ -meson intermediate state in the vector dominance model. The decay of the hadronic resonances will show up as sharp peaks in the invariant mass spectrum of l^+l^- pairs with a width reflecting the mean lifetime of the resonance and a magnitude depending on the abundance of the resonance. Hadron resonances such as the ρ , ω , and ϕ may arise from the initial nucleus-nucleus collision before thermalization, or they may also come from collisions of pions in the dense pion gas during the thermalization of the hadron gas. The decay of the J/ψ -resonance will be seen at a dilepton invariant mass of $3.1 \text{ GeV}/c^2$. Due to the large mass of the J/ψ -resonance it is unlikely that it can be produced via soft processes or during thermalization of the hadronic matter. Thus, J/ψ -production mainly results from hard-scattering processes. At FAIR energies, J/ψ -production at kinematic threshold and its assumed suppression play a particular role (see Chapter 1.3.2).

The potential of thermal dileptons as a signature for a phase transition to the QGP is described in detail in Reference [Won94]. In the quark-gluon plasma, a quark can interact with an antiquark to form a virtual photon γ^* , and the virtual photon can subsequently decay into a dilepton. The diagram describing the reaction $q + \bar{q} \rightarrow l^+ + l^-$ is shown in Fig. 2.2. The production rate and the momentum distribution of the produced l^+l^- pairs depend on the momentum distribution of quarks and antiquarks in the plasma, essentially given by the thermal (Boltzmann) distribution. Therefore, l^+l^- pairs can carry information on the thermodynamical state of the medium at the moment of their production. In order to be a good observable, the dilepton yield from the transient quark-gluon plasma must be larger than or comparable to the dilepton yields from non-QGP sources, at least in some momentum region.

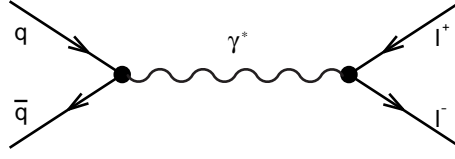


Figure 2.2: The diagram for the reaction $q + \bar{q} \rightarrow l^+ + l^-$.

When measuring dileptons, their major sources can be subdivided into:

- photon conversions within the target and in the material of the detector,
- Dalitz decays (mainly of π^0 and η),
- decay of the vector mesons ρ , ω , and ϕ ,
- hadron decays containing heavy quarks, i.e. semi-leptonic $D\bar{D}$ -decays, J/ψ etc.,
- thermal production of dileptons, either in the QGP or in the hot hadron gas,
- Drell-Yan production in early hard scatterings ($q\bar{q} \rightarrow l^+l^-$).

A schematic dilepton spectrum in the context of a heavy-ion collision as function of the invariant mass is shown in Fig. 2.3. In the region of high invariant masses (high mass region, HMR) the spectrum can be described by hard initial processes, for which perturbative QCD can be applied. This contribution to dileptons results from Drell-Yan processes in the nucleus-nucleus collision in which a quark of one of the nuclei interacts with a sea antiquark of the other nucleus. They annihilate to form a virtual photon which subsequently decays into an l^+l^- pair. In this process, the effects of the nucleons' binding within a nucleus are not important, and the nucleons can be considered to be independent. That is why the production of l^+l^- pairs from the Drell-Yan process in heavy-ion collisions can be considered as arising from a collection of independent nucleon-nucleon collisions. The yield should be equal to the one in p+p collisions after appropriate scaling.

At smaller invariant masses there are two peaks at $m_{\text{inv}} \approx 3.1 \text{ GeV}/c^2$ and $m_{\text{inv}} \approx 3.7 \text{ GeV}/c^2$ caused by decays of J/ψ - and ψ' -resonances. Further resonances are observed in the region of invariant masses smaller than $m_{\text{inv}} \approx 1 \text{ GeV}/c^2$ (low mass region, LMR) from the decay of ρ -, ω -, and ϕ -mesons. At even smaller masses the dileptons spectrum is dominated by Dalitz decays of π , η , and η' .

The mass region between the ϕ - and J/ψ -mesons (intermediate mass region, IMR) is a structureless produced by different sources. Among others, a contribution of dileptons from the correlated semi-leptonic decays of heavy quarks is expected.

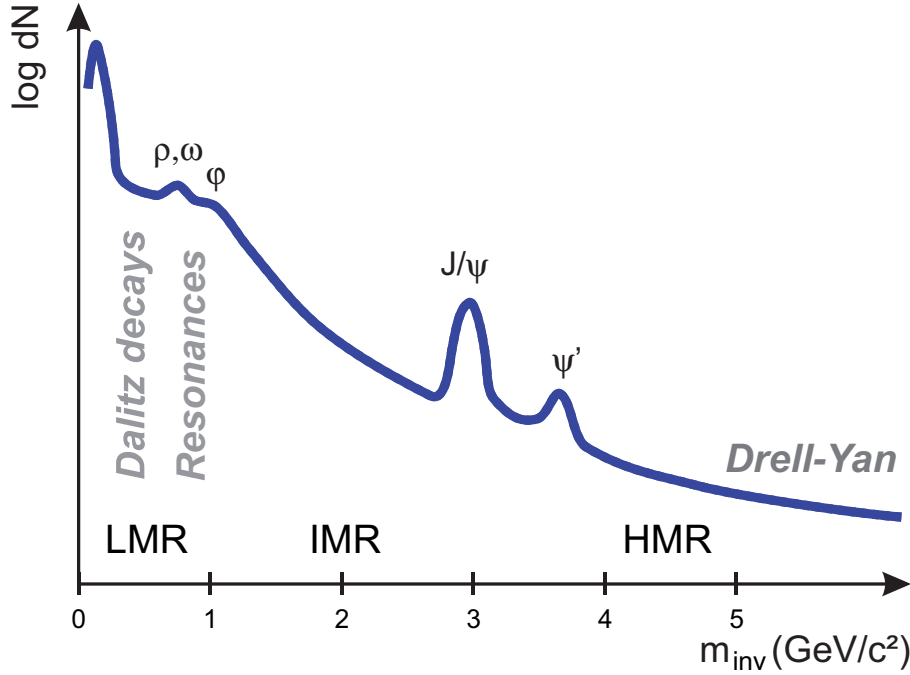


Figure 2.3: Schematic structure of a dilepton spectrum in heavy-ion collisions. In measurements with the CBM experiment, the kinematic reach will be limited by the available center-of-mass energy (see Chapter 4).

In the region of smallest invariant masses close to zero the spectrum is dominated by dileptons from conversions of real photons (not seen in Fig. 2.3 since they are subtracted in this spectrum) which are described in detail in Chapter 2.2.

2.1.1 Previous Experimental Results on Dileptons

For the investigation of dileptons from relativistic heavy-ion collisions the NA45 (CERES) experiment at CERN's Super Proton Synchrotron (SPS) accelerator did pioneering work. The CERES experiment was dedicated to the study of e^+e^- pairs at low invariant masses up to about $1.5 \text{ GeV}/c^2$. For the heavy-ion reaction S+Au at 200 AGeV , CERES found a considerable enhancement of the dielectron rates exceeding expectations from hadron decays (see Fig. 2.4), which was suggested to arise from two-pion annihilation [Aga95]. Also with the SPS experiments HELIOS-3 and NA38 a larger amount of dileptons (there: dimuons) than expected was observed in collisions of sulfur with heavy targets. The observations caused an intensive discussion on the production processes, and it was found that dileptons from pion annihilation and scattering processes are not suffi-

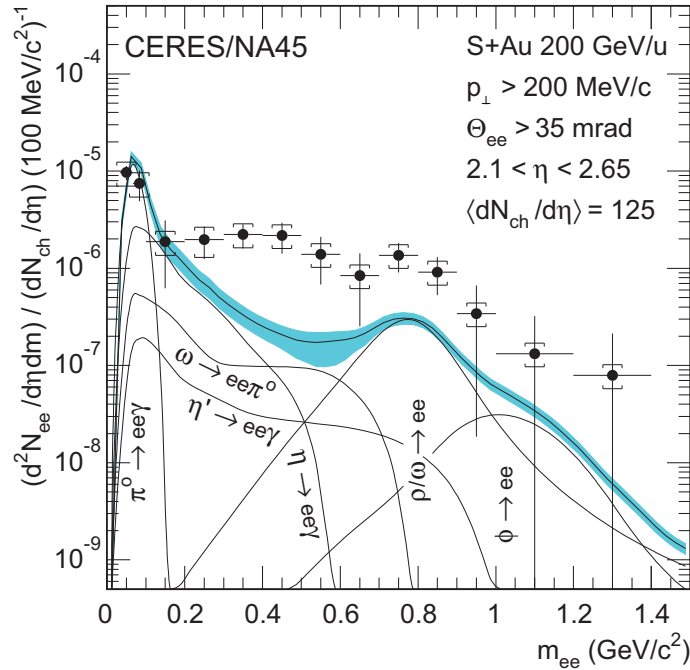


Figure 2.4: Inclusive invariant mass spectrum of e^+e^- pairs in 200 AGeV S+Au collisions measured by the CERES experiment [Aga95]. The full circles show the data and the lines represent the various contributions from hadron decays. The shaded region indicates the systematic error on the summed contributions.

cient to explain the observed enhancement. Thus, for the first time it was assumed that the enhancement may be due to a change in the properties of vector mesons in hot and dense matter.

Many open questions from the early SPS experiments were recently addressed by measuring dimuons with the NA60 experiment [NA606]. The NA60 experiment has been conceived as an upgrade of the NA50 experiment, in which muon production in p+A and nucleus-nucleus collisions have been studied. Behind a vertex spectrometer in a dipole magnet, this fixed-target experiment contains a muon spectrometer, consisting of hadron absorbers and multiwire tracking chambers as well as a zero-degree calorimeter for the centrality determination of the collisions.

In the NA50 experiment, it was possible to perform a high-statistics study of dimuon production by using an extremely selective trigger system. The mass resolution was of the order of $100 \text{ MeV}/c^2$ for the J/ψ and of $80 \text{ MeV}/c^2$ for the ϕ and ω [Ale05, CBM09a]. However, there were several limitations in the study of the muon-pair continuum. At low masses, the p_T acceptance was essentially zero below $1 \text{ GeV}/c$. Thus, the low p_T region,

where thermal dimuon yield may become sizable, could not be reached. Moreover, in the mass region beyond the ϕ , the vertex-determination capabilities did not allow to distinguish between prompt muon pairs and dimuons originating from open-charm decays.

Therefore, a silicon pixel telescope was added in the target region in the upgrade to the NA60 experiment. By using this telescope, performing a matching of the muon tracks before and behind the hadron absorber, in angular as well as in momentum space, became possible. Hereby, the dimuon-mass resolution could be improved in the region of the vector mesons ω and ϕ from ~ 80 to $20 \text{ MeV}/c^2$. Hence, the combinatorial background due to π - and K-decays could be significantly reduced and the muon offset, with respect to the interaction vertex, could be measured. Furthermore, the strength of the dipole field in the target region was increased, which enhanced the acceptance for opposite-sign dimuons at low mass and low transverse momentum with respect to all previous dimuon experiments.

In Fig. 2.5, a dimuon spectrum, measured in the NA60 experiment, is presented [Arn06]. It shows the opposite-sign, background, and signal dimuon mass spectra, integrated over all collision centralities. After subtracting the combinatorial background and the signal fake matches, the resulting net spectrum contains about 360,000 muon pairs in the mass range of the figure, roughly 50% of the total available statistics. For the first time in nuclear collisions, the vector mesons ω and ϕ were completely resolved in the dilepton channel; even the $\eta \rightarrow \mu\mu$ decay is seen. As mentioned before, the mass resolution of the ω is $20 \text{ MeV}/c^2$.

Within the NA60 experiment, also the first measurement of the ρ spectral function was obtained [Arn06]. Low-mass muon pairs were measured in 158 AGeV In+In collisions, and a significant excess of pairs was observed above the yield expected from neutral meson decays. The excess was isolated by subtraction of the decay sources, and the shape of the resulting mass spectrum is consistent with a dominant contribution from $\pi^+\pi^- \rightarrow \rho \rightarrow \mu^+\mu^-$ annihilation. The associated space-time averaged spectral function shows a strong broadening, but essentially no shift in mass. This precludes some models connecting hadron masses directly to the chiral condensate.

In the intermediate mass region, between the ρ and the J/ψ , the presence of an excess in the dimuon yield has been confirmed. NA60 was able to separate the prompt dimuons from the pairs resulting from open charm decays and showed that the excess dimuons are of prompt origin [Sha06]. The study of the transverse-momentum distributions of excess dimuons at low and intermediate mass implies that, beyond $m = 1 \text{ GeV}/c^2$, the yield is dominated by a thermal-like contribution, mainly of partonic origin.

Another evidence for the production of thermal-like muon pairs with masses above $1 \text{ GeV}/c^2$ was also observed in 158 AGeV In+In collisions [Arn09b]. The yield of muon pairs in the invariant mass region $1 \text{ GeV}/c^2 < m_{\text{inv}} < 2.5 \text{ GeV}/c^2$ significantly exceeds

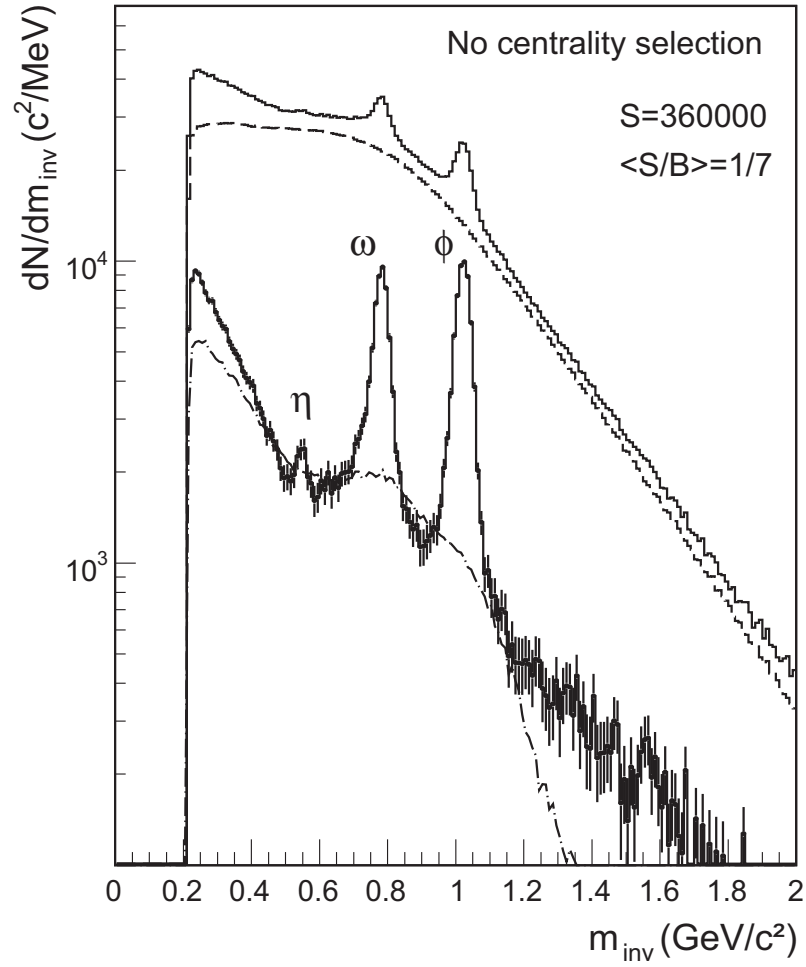


Figure 2.5: Mass spectra of the opposite-sign dimuons (upper histogram), combinatorial background (dashed), signal fake matches (dashed-dotted), and resulting signal (histogram with error bars) in 158 AGeV In+In collisions, measured in the NA60 experiment [Arn06].

the sum of the two expected contributions, Drell-Yan dimuons and muon pairs from the decays of D-meson pairs. By tagging dimuon vertices, it was found that this excess is not due to enhanced D-meson production, but originates from prompt muon pairs, as expected for a source of thermal dimuons specific to high-energy nucleus-nucleus collisions. The yield of this excess significantly increases from peripheral to central collisions, both with respect to the Drell-Yan yield as well as to the number of nucleons participating in the collisions. Furthermore, the transverse-mass (m_T) distributions of the excess dimuons are well described by an exponential function with inverse slope parameters T_{eff} around 190 MeV. The T_{eff} values are independent of dimuon mass for masses larger than $1 \text{ GeV}/c^2$ but significantly lower than those found at masses below $1 \text{ GeV}/c^2$. There, T_{eff} rises up to 250 MeV due to radial flow. This suggests the emission source of thermal dimuons above $1 \text{ GeV}/c^2$ to be largely of partonic origin, when radial flow has not yet built up.

Moreover, the J/ψ -suppression has been studied as a function of centrality in In+In collisions by the NA60 experiment [Arn07]. The J/ψ centrality distribution was compared to the one expected if absorption in cold nuclear matter would be the only mechanism responsible for the suppression of J/ψ -production. For collisions involving more than 80 participant nucleons, it was found that an extra suppression is present. This result is in qualitative agreement with previous Pb+Pb measurements by the NA50 experiment, but no theoretical explanation is presently able to coherently describe both results. However, recent results of the NA60 experiment with an improved cold-matter reference (p+A collisions) exhibit less suppression [Arn09a]. These results confirm the importance of understanding cold nuclear matter effects affecting the measured J/ψ cross section. The understanding is important for several physics reasons but is a very complicated task because of many competing effects. A signal of J/ψ elliptic flow has also been observed, largest in semi-peripheral collisions and at transverse-momentum values larger than $1 \text{ GeV}/c$ [Arn08].

The study of dielectron production in relativistic heavy-ion collisions and in elementary reactions at lowest energies has been studied by the HADES experiment with the available beam energies of 4.5 GeV for protons and $1 - 2 \text{ AGeV}$ for heavy ions at SIS/GSI. Thus, HADES focuses on pair invariant masses up to $1 \text{ GeV}/c^2$. The results of a C+C run at 2 AGeV beam energy provide evidence for a substantial contribution to the pair yield in the mass range between 0.15 and $0.5 \text{ GeV}/c^2$ from the early phase of the collision. Dielectrons from this phase are as abundant as pairs from the Dalitz decay of η -mesons [Aga07]. An even stronger excess above the cocktail of standard hadronic sources has been observed in the same invariant-mass region, spanning from the π^0 -Dalitz to the ρ/ω invariant mass, in the emission of dielectrons from C+C collisions at a beam energy of 1 AGeV [Aga08]. The beam-energy dependence of this excess is found to scale like the

pion production cross section, rather than like the η production cross section, corroborating earlier findings of the DLS collaboration. This finding supports the conjecture that the excess radiation stems predominantly from decays of baryonic resonances [CBM09a]. The C+C data agrees with an elementary cocktail within error bars. However, preliminary results from Ar+KCl collisions at 1.76 AGeV exhibit an excess above the elementary cocktail, and the yield grows faster than linearly with A_{part} [Kri09].

Dielectron measurements were also carried out with collider experiments. The dielectron continuum was measured by the PHENIX experiment at RHIC in $\sqrt{s_{NN}} = 200$ GeV Au+Au [Afa07] and p+p [Ada09] collisions. In minimum bias Au+Au collisions the dielectron yield in the mass range between 0.15 and 0.75 GeV/ c^2 is enhanced by a factor of 3.4 ± 0.2 (stat.) ± 1.3 (syst.) ± 0.7 (model) compared to the expectation from a model of hadron decays that well reproduces the mass spectrum in p+p collision. The integrated yield increases faster with the centrality of the collisions than the number of participating nucleons, suggesting emission from scattering processes in the dense medium. The observed yield between ϕ and J/ψ is consistent with the expectation from correlated $c\bar{c}$ production, but does not exclude other mechanisms [Toi07].

Studies on dielectrons at low energies have also been started by the PHENIX and the STAR collider experiments at RHIC, and upgrades of the detectors are planned in order to cope with the low luminosity at these energies. Both, STAR and PHENIX have expressed interest in low-energy running and have started to evaluate their physics capabilities. In parallel, the RHIC accelerator group is performing detailed studies in order to investigate possible luminosity upgrades of the machine at low energies.

In future, the upgraded HADES detector will be operated at FAIR. It will be located in front of CBM. There, HADES will perform systematic studies of dielectrons in the beam energy range from 2 – 10 AGeV. After its upgrade 20% double-hit probability, which is the maximum still allowing a decent reconstruction efficiency, will be reached for Au+Au collisions at 1.5 AGeV or Ni+Ni collisions at 8 AGeV beam energy. Higher energies will be studied only in the CBM experiment (see Chapter 4).

2.2 Direct Photons

For more than 20 years photons have been considered as one of the most valuable probes of the dynamics and properties of the matter formed in heavy-ion collisions. In contrast to hadronic particles photons only interact electromagnetically and have a long mean free path. This path is typically much larger than the transverse size of the hot dense medium created in nuclear collisions. Hence, photons do not interact after their production and

leave the fireball undisturbed. There are several production mechanisms for photons emitted in the course of a heavy-ion collision. The sources are initial-state hard scattering, interaction of hard partons with the medium, medium production in quark matter, and electromagnetic decay of hadrons. A pragmatic definition of direct photons is the difference between all inclusive photons and photons coming from electromagnetic hadron decays in the final state (decay photons). Direct photons can be subdivided into prompt photons produced in early hard scatterings and thermal photons emitted from a thermally equilibrated phase.

2.2.1 Thermal Photons

Thermal photons produced in nucleus-nucleus collisions can be further subdivided into thermal photons emitted from a QGP and those emitted from a hadron gas.

Thermal Photons from a QGP

Like every thermal source also a QGP emits photons due to the photon radiation from quarks having an electric charge. Due to the energy-momentum conservation these quarks have to interact with the thermal particles of the QGP in order to emit a photon. Hence, an ideal, non-interacting QGP cannot be seen. However, there will always be (strong and electromagnetic) interactions in the QGP, such as quark-antiquark annihilation. Due to energy-momentum conservation the direct annihilation of quarks and antiquarks into real photons is not possible. Instead, virtual photons are formed which can decay into lepton pairs (see Chapter 2.1). In lowest-order perturbation theory, real photons are produced in the annihilation of a quark-antiquark pair into a photon and a gluon ($q\bar{q} \rightarrow g\gamma$) and by absorption of a gluon by a quark emitting a photon ($qg \rightarrow q\gamma$), similar to Compton scattering in QED (see Fig. 2.6). A higher-order process for the photon production is, for example, bremsstrahlung, which means that a quark radiates a photon by scattering off a gluon or another quark in the QGP.

Thermal Photons from a Hadron Gas

Photons will also be emitted by a hot hadron gas. The microscopic description of the thermal photon emission from the hadron gas is based on the interactions between hadrons in the heat bath. The largest contribution to photon production originates from vector mesons, pions, and η s decaying into photons. The relevant hadronic processes are shown in Fig. 2.7. They are:

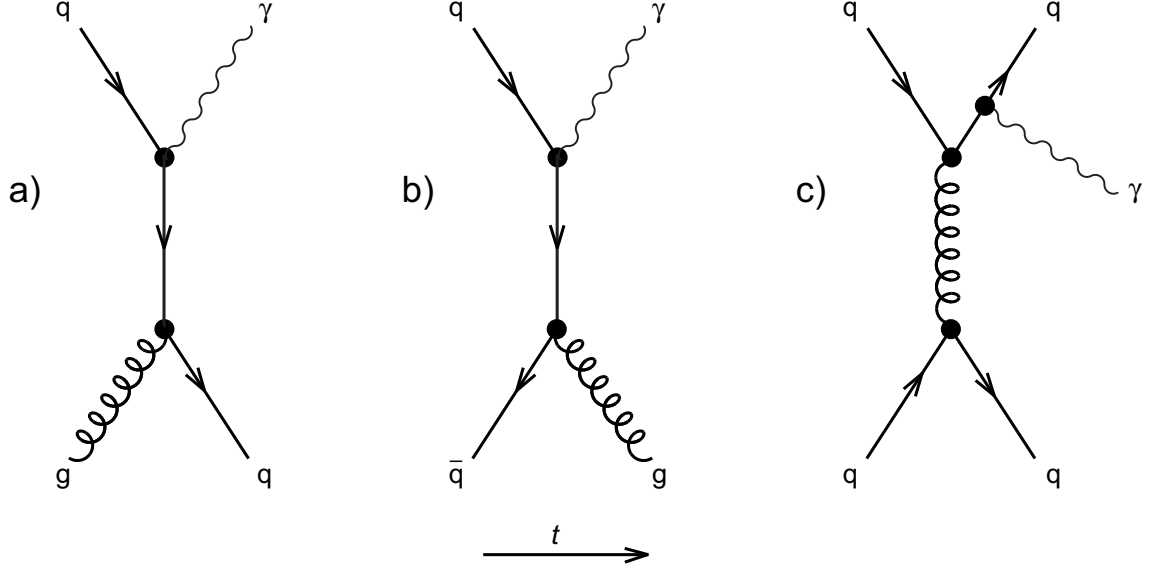


Figure 2.6: Feynman diagrams of the main production processes for direct photons: (a) quark-gluon Compton scattering of order $\alpha_s\alpha$, (b) quark-antiquark annihilation of order $\alpha_s\alpha$, (c) bremsstrahlung of order $\alpha_s^2\alpha$.

- $\pi^\pm \rho^0 \rightarrow \pi^\pm \gamma$, Compton scattering,
- $\pi^+ \pi^- \rightarrow \rho^0 \gamma$, annihilation process,
- $\rho^0 \rightarrow \pi^+ \pi^- \gamma$, ρ^0 -decay,
- $\omega \rightarrow \pi^0 \gamma$, ω -decay.

The rates of thermal photons in a nucleus-nucleus collision depend on the temperature via their production from qg or pions with a thermal distribution, and they have to be integrated over the whole temperature evolution in the collision. The temperature evolution can be calculated using hydro-dynamical models. For example, the yield of thermal direct photons for central Au+Au collisions at 25 AGeV, as expected at FAIR, has been evaluated with the BHD (Bjorken hydrodynamics) model in Reference [Kis08b]. It can be seen that the direct photon-spectrum is very sensitive to the initial temperature parameter T_0 in the model. A 10 MeV increase in T_0 leads to a twofold increase in photon yield (see Fig. 2.8).

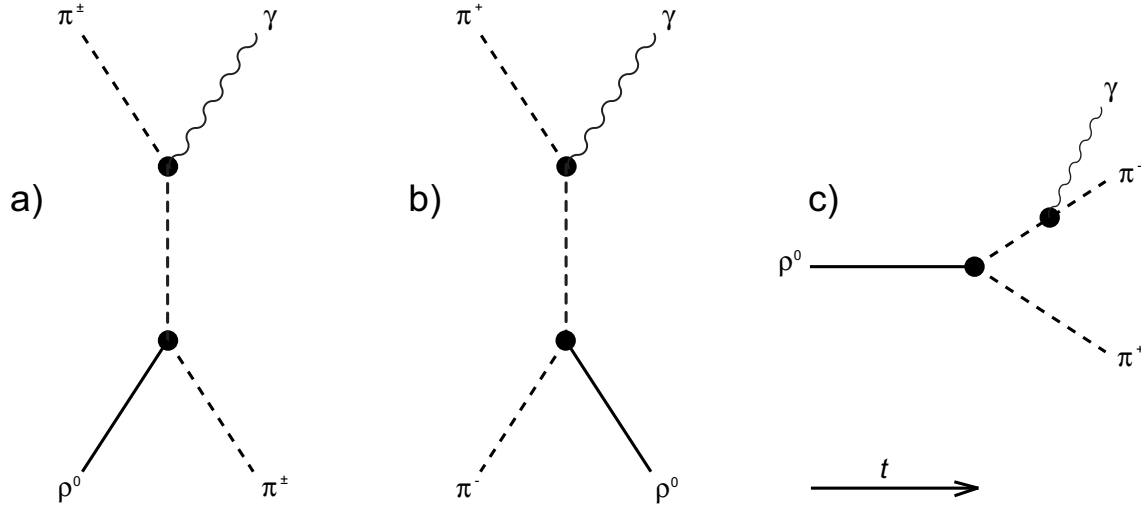


Figure 2.7: Feynman diagrams of the main production processes for direct photons in a hot hadron gas: (a) $\pi\rho$ Compton scattering, (b) $\pi^+\pi^-$ annihilation, (c) ρ -decay.

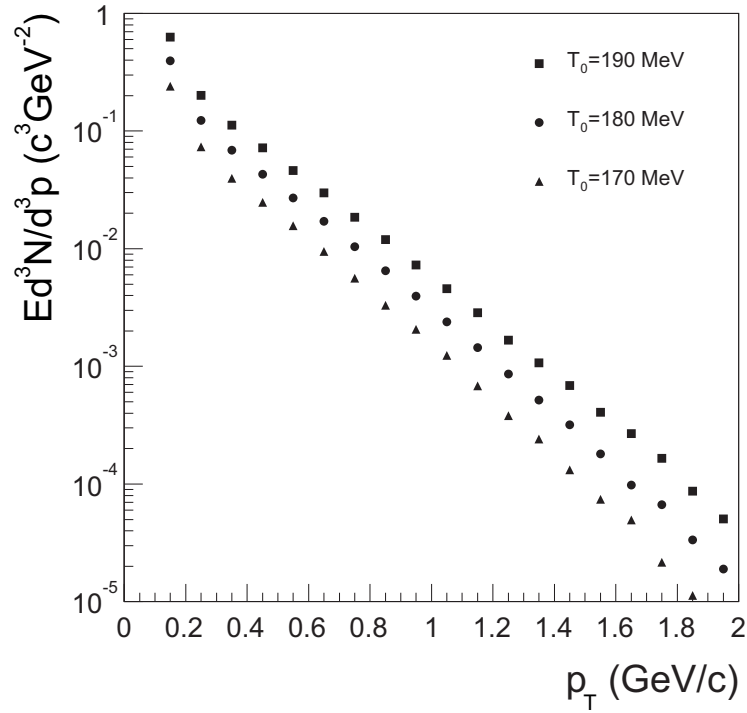


Figure 2.8: Direct-photon spectrum in the central rapidity region obtained in the BHD model for central Au+Au collisions at 25 AGeV for different values of the initial temperature T_0 [Kis08b].

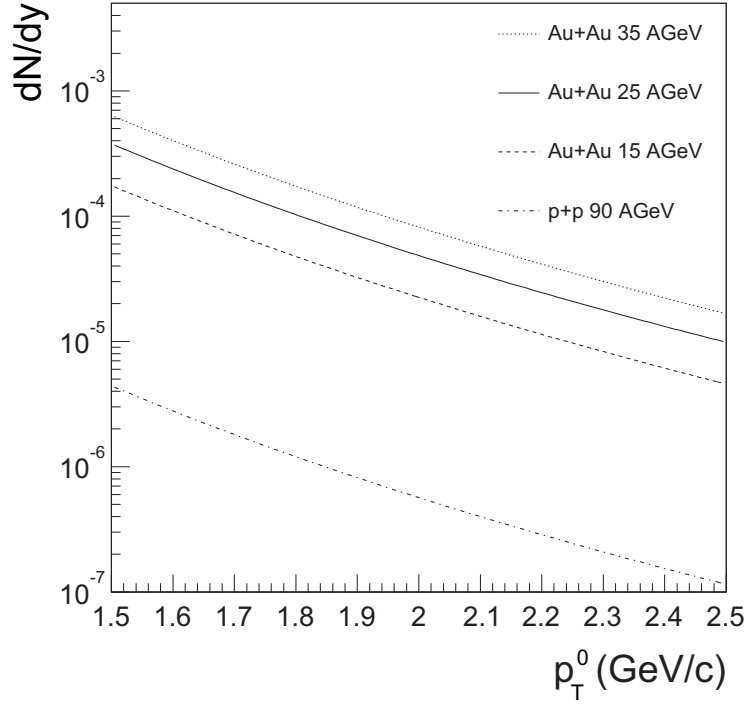


Figure 2.9: Rapidity density of prompt photons at $y = y_{\text{c.m.}}$ with $p_T > p_T^0$ at FAIR energies [Kis08b].

2.2.2 Non-Thermal Photons

Besides the thermal emission of photons from the QGP and the hadron gas there is another source for direct photons coming from hard parton collisions in the initial non-thermal stage of heavy-ion collisions. In Fig. 2.9, an extrapolated yield of prompt photons at FAIR energies is shown. For central Au+Au events ($N_{\text{coll}} = 650$) at 25 AGeV one can expect $\sim 10^{-4}$ prompt photons with $p_T > 1.5 \text{ GeV}/c$: for example, at a beam intensity of 10^9 ions per second, which is the expected maximum intensity at FAIR, a target with 1% interaction probability, and a selection of the 10% most central collisions about 10^2 prompt photons per second would be expected. Prompt photons are the main photon source at large p_T . Although the low- p_T region is the interesting part, in which the thermal photons are dominant, prompt photons provide information about hard scattering processes and are an important reference for jet-quenching measurements [Rey04].

2.2.3 Previous Experimental Results on Direct Photons

The first experiments for measuring photon yields in high-energy heavy-ion collisions have been carried out at CERN by the WA80/WA93 Collaboration and by the NA45

(CERES) Collaboration. The NA45 Collaboration measured photon yields by the *conversion* method. In this method, the target is used as a converter so that a produced photon is converted into an electron and a positron whose momenta are subsequently measured by a Ring Imaging Cherenkov (RICH) detector. In order to subtract the background, the π^0 -contribution is estimated from the measured π^- -distribution. The contributions of other mesons, including the relatively large contribution due to the decay of the η -mesons, were estimated by so-called m_T scaling. Within the systematic errors of 11%, no excess of the measured inclusive p_T spectrum over the expected yield from hadronic sources has been found [Irm94].

Evidence for direct-photon production in heavy-ion collisions was first found by the fixed target experiment WA98 at CERN SPS in central Pb+Pb collisions at $\sqrt{s_{NN}} = 17.3$ GeV (corresponding to 158 AGeV beam energy) [Agg00b] and later by the collider experiment PHENIX at RHIC in Au-Au collisions at $\sqrt{s_{NN}} = 200$ GeV [Adl05]. In both experiments, the direct-photon spectra are determined via the statistical subtraction of the calculated yield of photons from hadron decays from the total photon yield. Moreover, in PHENIX direct photons at low transverse momenta are observed in a measurement of internal photon conversions [Ada08].

One of the basic questions in both cases is whether thermal photons or photons from jet-plasma interactions are needed on top of the hard direct-photon component in order to explain the data [Rey07]. The measurement of direct-photon production in Pb+Pb collisions at 158 AGeV in the WA98 experiment was performed with a highly-segmented lead-glass calorimeter. The ratio of measured photons to calculated background photons, measured in Pb+Pb collisions with the WA98 experiment, is displayed in Fig. 2.10 as a function of transverse momentum [Agg00a]. The upper plot shows the ratio for peripheral collisions which is seen to be compatible with unity, i.e. no indication of a direct-photon excess is observed. The lower plot shows the same ratio for central collisions. The ratio increases from a value of 1 at low p_T to about 1.2 at high p_T . A significant direct-photon signal within statistical and systematic errors is seen at $1.5 \text{ GeV}/c < p_T < 3.5 \text{ GeV}/c$. The results constituted the first observation of direct photons in ultra-relativistic heavy-ion collisions which are significant for the diagnosis of quark-gluon plasma formation.

The final invariant direct-photon yield per central collision is presented in Fig. 2.11. The invariant yield of direct photons in central Pb+Pb collisions is extracted as a function of transverse momentum in the interval $0.5 \text{ GeV}/c < p_T < 4 \text{ GeV}/c$ [Agg00a]. As a comparison, prompt-photon yields for proton-induced reactions on fixed targets at 200 AGeV beam energy (E704, E629, and NA3) are also shown. In addition, a comparison to a pQCD calculation and to a scaled parametrization of p+p direct-photon data, which are assuming that direct photons in p+p and p+A are produced in hard scattering processes, are drawn.

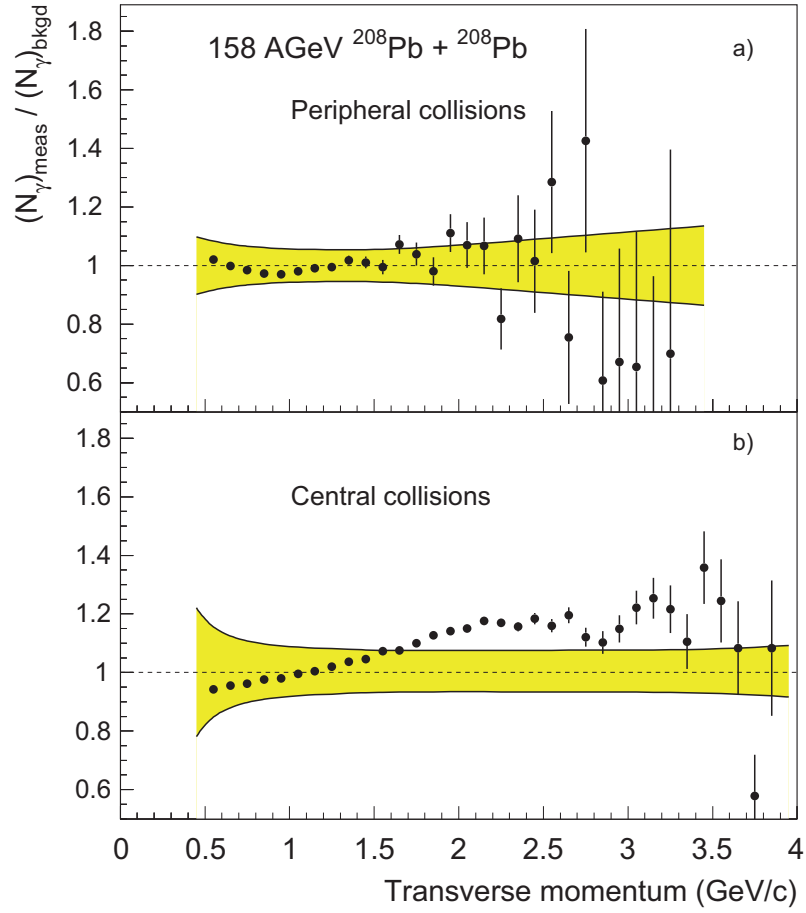


Figure 2.10: The Measured-to-Background ratio of photons in the detector as a function of transverse momentum for a) peripheral and b) central 158 AGeV Pb+Pb collisions. The errors on the data points indicate the statistical errors only. The p_T -dependent systematic errors are indicated by the shaded bands. A clear direct-photon signal is seen in central collisions between transverse momenta of 1.5 and 3.5 GeV/c [Agg00a].

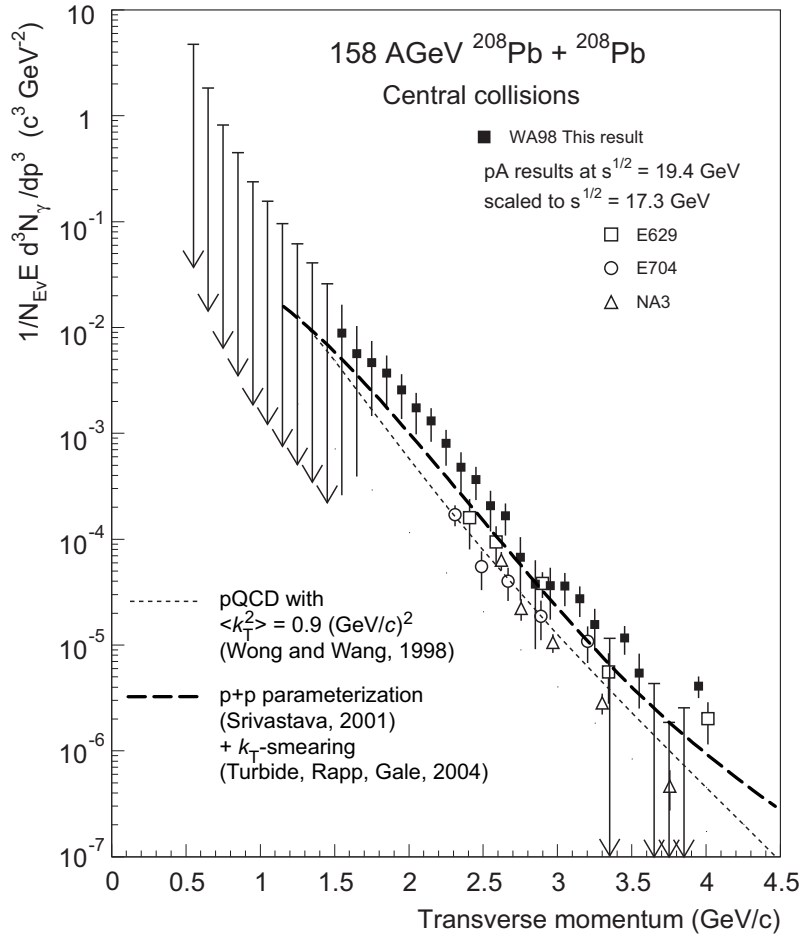


Figure 2.11: The invariant direct-photon multiplicity for central 158 AGeV Pb+Pb collisions [Agg00a]. The error bars indicate the combined statistical and systematic errors. Data points with downward arrows indicate unbounded 90% confidence level upper limits. Results of several direct-photon measurements (E704, E629, and NA3) for proton-induced reactions have been scaled to central Pb+Pb collisions at 158 AGeV for comparison. The short-dashed line shows a comparison to a pQCD calculation and the long-dashed line a scaled parametrization of p+p direct-photon data.

This comparison shows that for $p_T \gtrsim 2.5 \text{ GeV}/c$ the direct-photon yield is consistent with the expected yield from hard scattering. At lower transverse momenta ($p_T \lesssim 2.5 \text{ GeV}/c$), one possible explanation of the observed spectrum may be thermal photon production. However, from the comparison to a hard scattering contribution it is very difficult to draw firm conclusions since they are only based on a comparison to theoretical calculations and without an additional measurement of a p+A reference.

Direct photons were also measured by the PHENIX experiment at RHIC in central p+p and Au+Au collisions at $\sqrt{s_{NN}} = 200$ GeV [Ada08]. In Fig. 2.12, the direct-photon spectra are compared with the direct-photon data from Reference [Adl05, Adl07] and NLO pQCD calculations. The filled data points at $1 \text{ GeV}/c < p_T < 5 \text{ GeV}/c$ are obtained in a measurement of the production of e^+e^- pairs for $m_{e^+e^-} < 300 \text{ MeV}/c^2$. An enhanced e^+e^- yield above hadronic sources is observed. The excess can be related to virtual photons, and the invariant yield of direct photons is deduced. In central Au+Au collisions, an excess over p+p is observed, which is exponential in p_T , with an inverse slope parameter $T = 221 \pm 23(\text{stat}) \pm 18(\text{sys}) \text{ MeV}$, and can be related to a thermal origin of photons: hydrodynamical models with initial temperatures T_0 of $300 - 600 \text{ MeV}$ at formation times of $0.6 - 0.15 \text{ fm}/c$ after the collision are in qualitative agreement with the data. The high- p_T spectra (open points in Fig. 2.12) are obtained with electromagnetic calorimeters consisting of two subsystems: six sectors of lead-scintillator sandwich calorimeter (PbSc) and two sectors of lead-glass Cherenkov calorimeter (PbGl). The pQCD calculation is consistent with the p+p data within the theoretical uncertainties for $p_T > 2 \text{ GeV}/c$. The p+p data can be well described by a modified power-law function $(A_{pp}(1 + p_T^2/b)^{-n})$ as shown by the dashed curve in Fig. 2.12. The Au+Au data are above the p+p fit curve scaled by the nuclear overlap function T_{AA} for $p_T < 2.5 \text{ GeV}/c$. T_{AA} is related to the number of binary collisions via the inelastic cross section ($N_{\text{coll}} \approx T_{AA}\sigma_{pp}$) and is estimated on the basis of Glauber calculations for the different centralities. This so-called binary scaling is expected to hold if hard scattering is the only source of direct photons. It is seen that the direct-photon yield in the low- p_T range increases faster than the binary-scaled p+p cross section [Ada08].

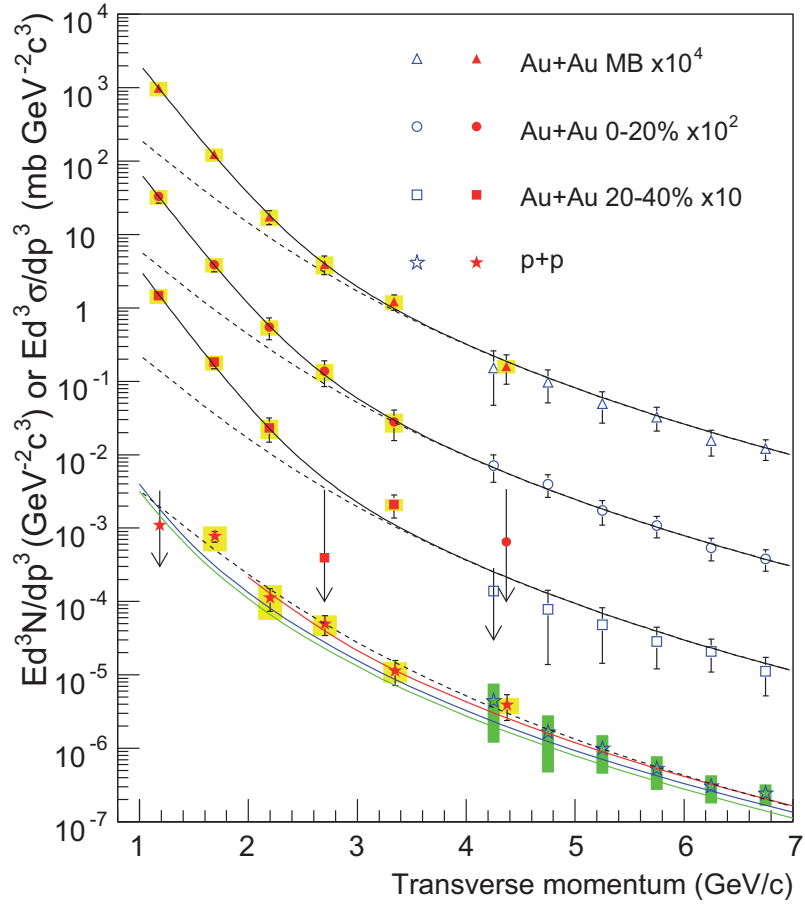


Figure 2.12: Invariant cross section (p+p) and invariant yield (Au+Au) of direct photons as a function of p_T . The filled points are from Reference [Ada08] and open points are from [Adl05, Adl07]. The three curves compared to the p+p data represent NLO pQCD calculations, and the dashed curve shows a modified power-law fit to the p+p data, scaled by T_{AA} . The black curves on top of the Au+Au data are exponentials plus the T_{AA} scaled p+p fit [Ada08].

3. Interaction of Charged Particles and Photons with Matter

In general, particles and electromagnetic radiation can only be detected through interaction with matter. Depending on the measurement technique (tracking, energy measurement, particle identification) different processes are relevant. Electrically charged particles can be detected as they leave characteristic trails because they lose energy when traveling through detector material, which can be gaseous, liquid, or solid. Charged particles lose energy in matter primarily by colliding with atomic electrons of the material (excitation and ionization) and by the emission of bremsstrahlung when they scatter off nuclei. Strongly interacting particles can in addition lose energy through hadronic interactions like inelastic nuclear collisions, or nuclear excitations. Photons interact via *Compton scattering* with atomic electrons, or they convert via the *photoelectric effect* and *pair-production*. The latter being dominant at high energies ($\gg 1$ MeV). Subsequently, the produced electrons and positrons can be detected, like other charged particles, through their energy loss mainly due to ionization and excitation of the medium. This energy loss is fundamental to most particle detectors, in particular to gaseous detectors.

3.1 Energy Loss of Charged Particles

Electrically charged particles can be detected via their electromagnetic interaction. Moderately relativistic charged particles other than electrons lose energy in matter primarily by ionization and atomic excitation, whereas high-energy electrons predominantly lose energy in matter via bremsstrahlung for momenta of interest in heavy-ion collisions. The mean specific energy loss for particles heavier than electrons is given by the Bethe-Bloch formula [Ams08]:

$$-\frac{dE}{dx} = Kz^2 \frac{Z}{A} \frac{1}{\beta^2} \left[\frac{1}{2} \ln \frac{2m_e c^2 \beta^2 \gamma^2 T_{\max}}{I^2} - \beta^2 - \frac{\delta_{\text{corr}}(\beta\gamma)}{2} \right], \quad (3.1)$$

with $K/A = 4\pi N_A r_e^2 m_e c^2 / A = 0.307075 \text{ MeV g}^{-1} \text{ cm}^2$ for $A = 1 \text{ g mol}^{-1}$, r_e and m_e are the classical electron radius and electron mass, ze is the charge of the incident particle, Z the atomic number of the absorber, A the atomic mass of the absorber, I the mean excitation energy, and $\delta_{\text{corr}}(\beta\gamma)$ is the density-effect correction to the ionization energy loss. T_{\max} is the maximum kinetic energy that can be imparted to a free electron in a single collision:

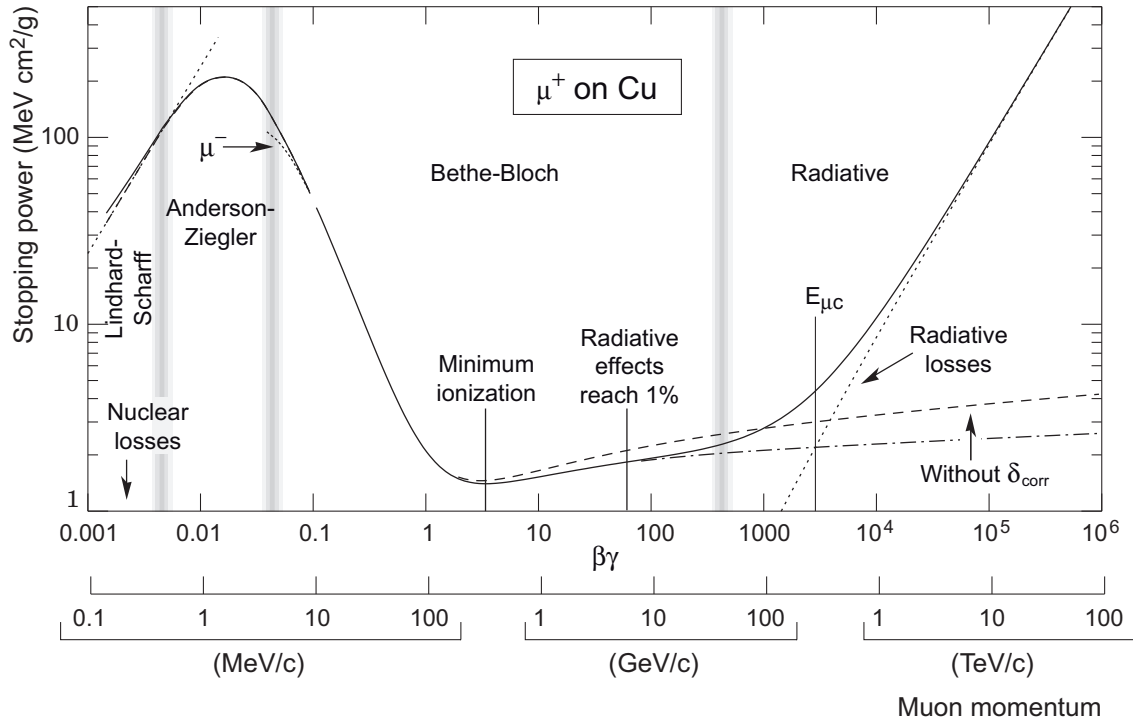


Figure 3.1: Stopping power ($=\langle -\frac{dE}{dx} \rangle$) for positive muons in copper as function of $\beta\gamma = p/Mc$ over nine orders of magnitude in momentum (12 orders of magnitude in kinetic energy) [Ams08]. For the energy loss due to ionization and excitation the curves with and without density-effect correction are shown. At the critical energy $E_{\mu c}$, the energy loss due to ionization equals the energy loss due to bremsstrahlung. The solid curve indicates the total energy loss which is the sum of the two.

$$T_{\text{max}} = \frac{2m_e p^2}{m^2 + 2\gamma m_e m + m_e^2}. \quad (3.2)$$

As the particle energy increases, its electric field flattens in the forward and backward directions and extends in the transverse direction, so that the distant-collision contribution to the total energy loss due to ionization and excitation increases as $\ln(\beta\gamma)$. Since materials become polarized, the electric field of the particle is partially screened. That is why the density-effect correction δ_{corr} was introduced.

Fig. 3.1 shows the stopping power due to ionization and excitation of muons in copper versus the muon momentum [Ams08]. It can be seen that here the density-effect correction becomes relevant for muon momenta $p_\mu \geq 200 \text{ MeV}/c$. A slight dependence on the incident particle mass at highest energies is introduced through T_{max} , but for all practical

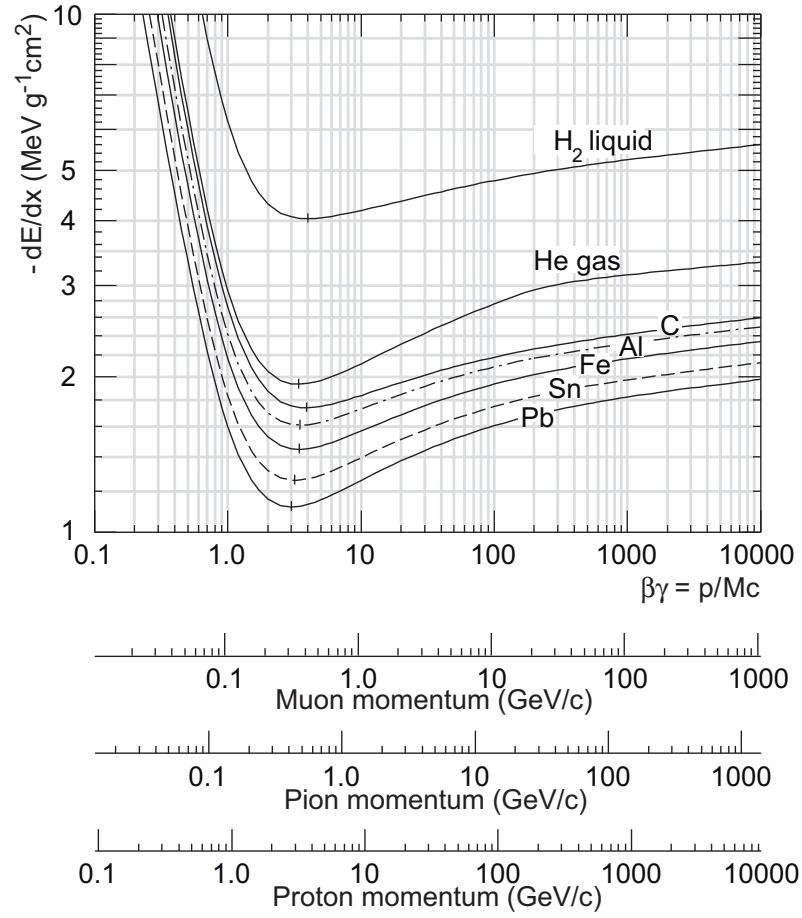


Figure 3.2: Mean specific energy loss in liquid hydrogen, gaseous helium, carbon, aluminum, iron, tin, and lead [Ams08]. Radiative effects, relevant for muons and pions, are not included. They become significant e.g. for muons in iron for $\beta\gamma \geq 1,000$, and at lower momenta for muons in higher- Z absorbers.

purposes in high-energy physics dE/dx in a given material can be regarded as a function only of $\beta\gamma$. The specific energy loss for particles of the same velocity are similar in different materials. A slow decrease in the energy loss with increasing Z can be seen in Fig. 3.2. Here, the Bethe-Bloch equation is shown for muons, pions, and protons.

The different shapes of the stopping power functions of a gas (He) compared to the other materials is due to the density-effect correction $\delta_{\text{corr}}(\beta\gamma)$. The stopping power functions are characterized by broad minima at about $\beta\gamma = 3$ to 3.5 for materials with Z from 7 to 100. For reactions considered here most of the produced hadrons have mean specific energy-loss close to the minimum and thus are called minimum ionizing particles, or MIPs.

The quantity $(-\frac{dE}{dx})\Delta x$ is the average energy loss due to ionization and excitation in a layer of the medium with thickness Δx . The exact energy loss fluctuates around this average value. For detectors of moderate thickness x , the energy-loss probability distribution is adequately described by a *Landau distribution* which is skewed towards larger values (the Landau tail). For thicker absorbers the distribution is less skewed and only for very thick absorbers, where the energy loss exceeds half of the original particle energy, the distribution is roughly Gaussian. However, it never approaches an exact Gaussian shape. It is expected that there is a long 'tail' at large energy losses due to delta ray ejection (secondary electrons with kinetic energies $T \gg I$) or other processes. This can be reduced by taking a large number of samples rejecting any large fluctuations from the mean. In addition, in a dilute medium, for example a gaseous detector, there can be a statistical fluctuation in the number of produced primary ion-electron pairs. When passing through a dilute material of the length L , the most probable energy loss is $\langle \Delta E \rangle \sim \langle dE/dx \rangle L$. The Landau distribution of deviations, $\Delta E - \langle \Delta E \rangle$, expressed in terms of fractional deviations of the mean loss about the most probable energy loss is [Gre00]:

$$P(\kappa) = \frac{1}{\sqrt{2\pi}} e^{-1/2(\kappa + e^{-\kappa})}, \quad (3.3)$$

$$\kappa \equiv \frac{(\Delta E - \langle \Delta E \rangle)}{\langle \Delta E \rangle}. \quad (3.4)$$

This distribution is asymmetric around the mean and skewed towards large values of κ as expected since it represents the effects of energetic delta rays. A plot of the charge deposited in a gas-filled proportional chamber is shown in Fig. 3.3 for MIP incident on the detector. The existence of a peak and a long Landau tail can be clearly seen.

Nevertheless, the Landau distribution fails to describe energy loss in thin absorbers such as gas TPC (Time Projection Chamber) cells and Si detectors. When going to thinner absorbers, the distributions become significantly wider. This is associated with another phenomenon known as *straggling*. For example, particles with the same initial energy do not all stop within the same distance, x . There are fluctuations in the energy loss, and also multiple scattering fluctuations in the path length.

For electrons and positrons the Bethe-Bloch equation (Eq. 3.1) has to be modified due to the small mass of the incident particle because in the case of electrons and positrons, the assumption that the incident particle remains undeflected during the collision process is invalid. In addition, for electrons the collisions are between identical particles and are thus indistinguishable, which also has to be taken into account. This means that the range of the kinetic energy extends only to half of the kinetic energy of the incident particle. At low energies electrons and positrons primarily lose energy by ionization, although other

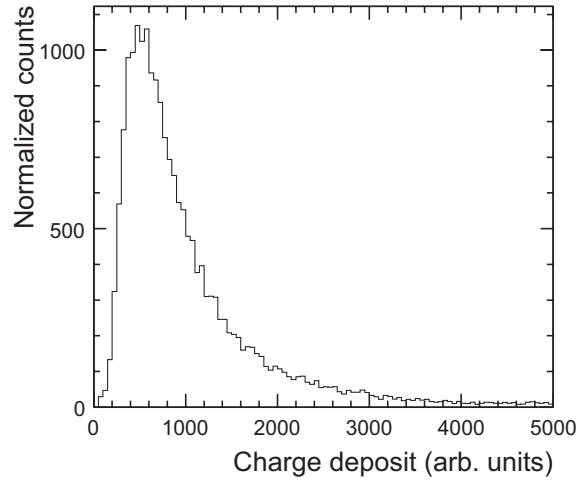


Figure 3.3: Typical Landau distribution of energy loss measured by the charge deposit on a wire-chamber cathode by the passage for MIPS. This wire chamber has a gas volume of 12 mm Xe(85%)CO₂(15%).

processes (Møller scattering, Bhabba scattering, e^+ annihilation) contribute. High-energy electrons predominantly lose energy by bremsstrahlung. In the bremsstrahlung process, the electron emits photons when being decelerated in the field of a nucleus. The process strongly depends on electron energy and the medium: it increases approximately linearly with the energy and quadratically with the atomic charge number Z of the medium. This effect dominates above the critical energy E_c , roughly parametrized as $E_c \approx 600 \text{ MeV}/Z$ [Pov99].

The characteristic amount of matter traversed these electromagnetic interactions is called *radiation length* X_0 . It is the mean distance over which a high-energy electron loses all but $1/e$ of its energy through bremsstrahlung. The radiation length is also the appropriate scale to describe high-energy electromagnetic cascades, and it is given in Chapter 3.3 (see page 62: Eq. 3.15). The fractional energy loss in units of radiation length as function of the electron or positron energy is shown for lead in Fig. 3.4. The radiation length in lead is $X_0(\text{Pb}) = 6.37 \text{ g/cm}^2$, and in Fig. 3.4, for this value the curves are shown [Ams08].

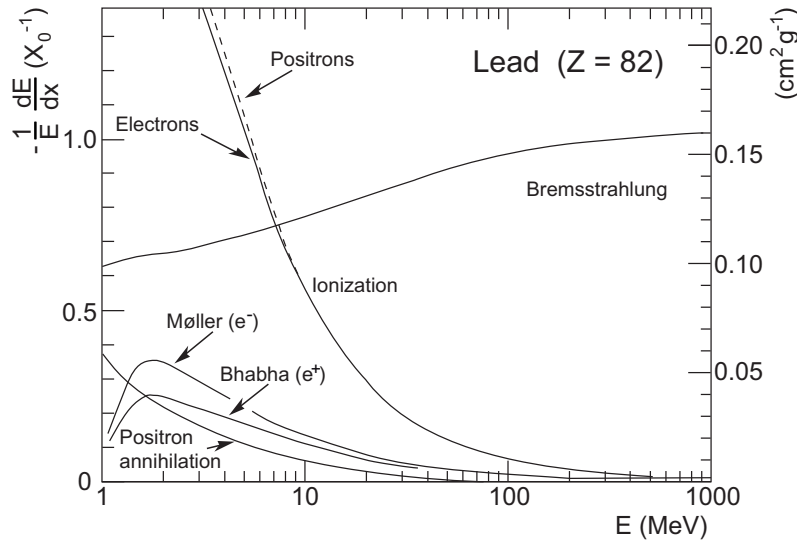


Figure 3.4: Fractional energy loss per radiation length in lead as function of electron or positron energy for a radiation length of $X_0(\text{Pb}) = 6.37 \text{ g/cm}^2$ [Ams08].

3.2 Additional Mechanisms for Radiative Energy Loss of Charged Particles

Besides the main sources of energy loss like ionization and excitation, as described in Chapter 3.1, charged particles can also lose energy by radiation like *Cherenkov radiation* and *transition radiation*.

3.2.1 Cherenkov Radiation

A charged particle in uniform unaccelerated motion in vacuum does not radiate. However, if a particle is moving with uniform constant velocity in a medium, its electric field will interact with the medium and in case of $v > c/n$, this interaction can result in the emission of real photons, the so-called Cherenkov radiation. Fig. 3.5 shows the geometry of the Cherenkov emission angle. Particles are moving with constant velocity in a medium with a refractive index n greater than 1. Thus, the speed of light in the medium is less than the vacuum speed of light. If the velocity of the particle is larger than the velocity of light in the medium, a wave front (in analogy to a *Mach cone*) is formed in the medium. It is shown that according to Huygens' principle wavelets are emitted from each point in time

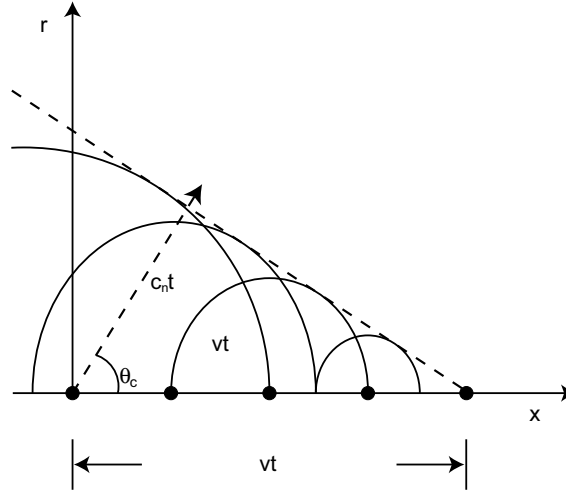


Figure 3.5: Construction of the Cherenkov emission angle via elementary waves [Gre00].

which add up constructively along a line defined by the Cherenkov angle θ_c . The angle relation can be derived with the geometry construction in Fig. 3.5:

$$\begin{aligned} c_n &= c/n, \\ \cos \theta_c &= c_n/v = c_n t / vt \\ &= c/nv = 1/\beta n \end{aligned}$$

for $v > c_n$ and $\cos \theta_c < 1$ if $\beta > 1/n$.

The mean number of photons produced by a particle with the charge ez at a given wavelength λ is [Ams08]:

$$\frac{d^2 N}{dx d\lambda} = \frac{2\pi\alpha_z^2}{\lambda^2} \left(1 - \frac{1}{\beta^2 n^2(\lambda)} \right). \quad (3.5)$$

The energy loss connected with this process is negligible compared to the particle's energy but the Cherenkov radiation can be used in the detection and identification of particles (e.g. electron/pion separation). Cherenkov counters utilize one or more of the properties of Cherenkov radiation: the existence of a threshold for Cherenkov radiation, the dependence of θ on the velocity $v = \beta c$ of the particle, and/or the dependence of the number of emitted photons on the velocity of the particle.

3.2.2 Transition Radiation

Transition radiation (TR) is produced when a relativistic particle traverses an inhomogeneous medium, specifically the boundary between materials with different dielectric constants ϵ . It is known from Cherenkov radiation that it is emitted when a charged particle, moving in a medium, has a velocity exceeding the velocity of light in that medium c_n (see Chapter 3.2.1). If the particle is moving with a uniform constant velocity, its electric field will interact with the medium and this interaction can cause the emission of real photons. Since the angle of emission and the intensity of radiation depend on the velocity of the particle, Cherenkov radiation can be used to determine the velocity of a charged particle.

The dielectric constant ϵ in a medium depends on the frequency ω of the electromagnetic radiation (dispersion). At frequencies far above the highest optical resonant frequency, ϵ takes on the simple form [Jac75]:

$$\epsilon(\omega) \simeq 1 - \frac{\omega_p^2}{\omega^2}, \quad (3.6)$$

where

$$\omega_p^2 = \frac{4\pi NZe^2}{m}. \quad (3.7)$$

The frequency ω_p , which depends only on the total number NZ of electrons per unit volume, is called the *plasma frequency* of the medium. The wave number is given by:

$$ck = \sqrt{\omega^2 - \omega_p^2}. \quad (3.8)$$

If Eq. 3.8 is solved for ω , it is often called *dispersion relation* or equation for $\omega = \omega(k)$. In dielectric media, Eq. 3.6 only applies for $\omega^2 \gg \omega_p^2$. The dielectric constant is then close to unity, although slightly less, and increases with frequency.

In a material with $\epsilon > 1$, the threshold velocity for Cherenkov emission is smaller than c . If $\epsilon < 1$, the threshold velocity is larger than c and no real photon emission is possible in an infinitely long radiator.

The optical behavior, characterized by the complex dielectric constant ϵ , is schematically illustrated in Fig. 3.6. In this picture, the real part ($\text{Re } \epsilon$) is the refractive index and the imaginary part ($\text{Im } \epsilon$) is a parameter for the absorption. Although ϵ is still smaller than unity for $\omega^2 \gg \omega_p^2$, under certain conditions a real photon is emitted instead of ionizing an atom or exciting the matter. These conditions are influenced by the radiator size and alignment.

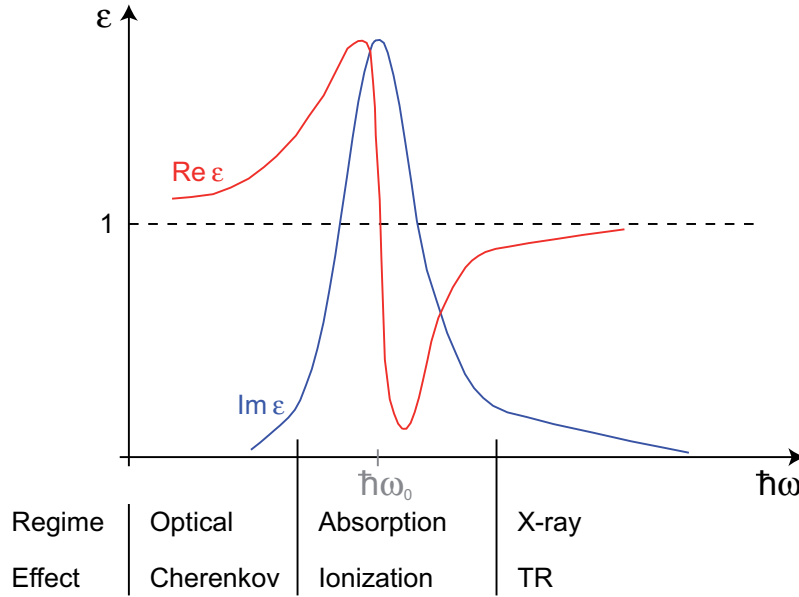


Figure 3.6: Schematic illustration of the dielectric constant as function of the photon energy [Jor05]. The real part ($\text{Re } \epsilon$) is the refractive index and the imaginary part ($\text{Im } \epsilon$) is a parameter for the absorption.

The conditions for real-photon emission can be fulfilled by finite length radiators where the emission angle is not unique (for a detailed description see Reference [Gre00]). Due to the diffraction broadening of the distribution of emission angles, a particle with velocity smaller than c can still emit photons with $\cos \theta < 1$. This phenomenon is called the *sub-threshold* emission of Cherenkov light. This sub-threshold emission of photons, when particles traverse a thin segment of material, is called transition radiation (TR) because it is caused by a transition in the index of refraction between the vacuum and the material (or two materials). TR already occurs when being below the β threshold for Cherenkov radiation but in a finite length medium.

If a charged particle traverses a thin film the radiation pattern can be described by the pattern due to a finite length Cherenkov radiator. The definition of quantities is shown in Fig. 3.7 a). In this illustration, the particle travels the distance L in the film. The wavelength in the medium is λ' , and the emission angle of the radiation in the medium is θ' . For a finite wave train there is a diffraction pattern because Cherenkov radiation is only emitted over a finite distance. When assuming a very long radiator the diffraction pattern can be approximated to a very sharp emission angle in the medium θ' . But for short radiators the problem can be treated as slit diffraction from the entrance and exit points (A and B).

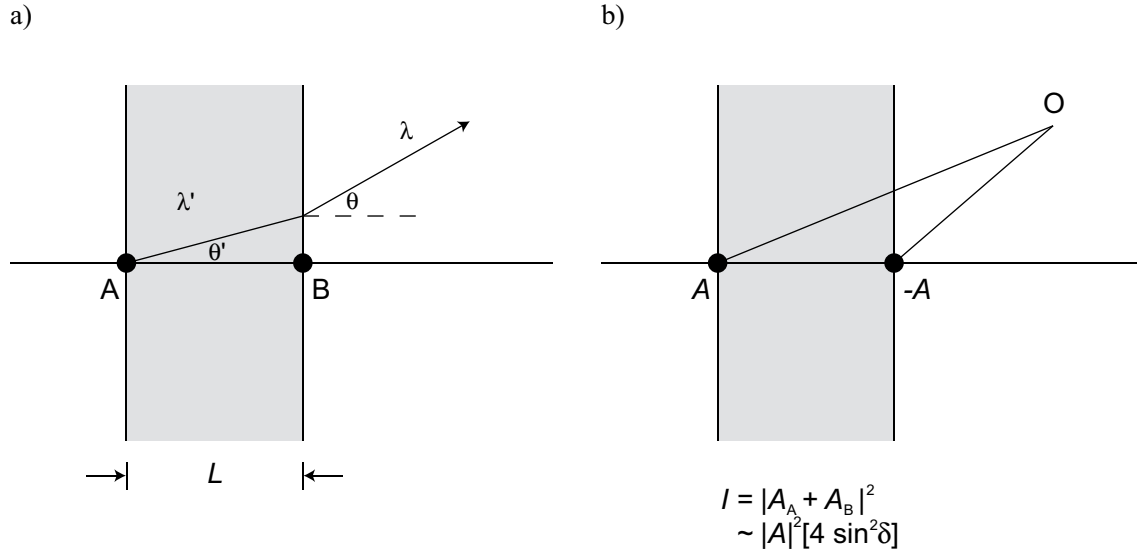


Figure 3.7: a) Definition of quantities used for the description of transition radiation effect. This effect can be thought of as a pattern due to a finite length Cherenkov radiator; b) an interference pattern is seen at the observation point O due to amplitudes A and $-A$ for emission from the front and back of the film, the optical path length difference is equivalent to the phase difference between the amplitudes.

The optical path difference to an observation point O (as seen in Fig. 3.7 b)) leads to a phase difference between waves produced from points A and B. The diffraction peak is centered at $\cos \theta' = 1/\beta\sqrt{\epsilon}$ (the *Cherenkov angle*), with an angular width of $\Delta\theta' \sim \lambda'/L$. For a very thin radiator, the chance for sub-threshold radiation is not necessarily negligible.

Considering the point O an interference pattern can be seen due to the amplitudes A and $-A$ from points A and B with an optical path length difference equivalent to the phase difference δ . The intensity I is $4|A|^2 \sin^2 \delta$. If $\delta \rightarrow \pi/2$, the intensity approaches $4|A|^2$, which is the maximum constructive interference value, while if $\delta \rightarrow 0$ the interference is destructive and the intensity approaches zero. For random phases the intensity is half of the maximum intensity.

Since there is a discontinuity in the phase at the entrance into the medium and none at the exit, the phase at the entrance and exit transition (for an infinitesimally small radiator) differs by 180° . Thus, a sufficient optical path length difference is needed to avoid destructive interference. This is an important consideration for the design and construction of radiators.

Frequency Spectrum

In contrast to Cherenkov emission the frequency spectrum of TR is not flat. It has high frequency components because its existence depends on the finite width diffraction pattern, $\delta \sim \omega L/c$, derived from the Cherenkov process for a finite length radiator. Typically, Cherenkov light is emitted in the optical region and near UV, while transition radiation is emitted in the X-ray region. This characteristic high frequency emission is a consequence of the diffraction broadening for sub-threshold Cherenkov emission occurring at a real angle.

The double differential cross section for transition radiation is proportional to the fine-structure constant α and is given below [Gre00]:

$$\frac{d^2 N_{\text{TR}}}{d\omega d\Omega} \sim \frac{\alpha}{\pi^2 \omega} \theta^2 \sin^2 \delta \left[\left(\frac{1}{\delta} \right)^2 - \left(\frac{1}{\delta_v} \right)^2 \right] \left(\frac{\omega L}{2c} \right)^2, \quad (3.9)$$

$$\delta_v = \frac{\omega L}{4c} \left(\theta^2 + \frac{1}{\gamma^2} \right),$$

where δ_v is the vacuum phase shift. Here, it ensures that there were no radiation if the thin film were a vacuum, i.e. without a transition in the index of refraction. The photon spectrum can be obtained by integrating Eq. 3.9:

$$\frac{dN_{\text{TR}}}{d\omega} = \frac{2\alpha}{\pi\omega} [-1 + [\ln(1 + 1/y^2)](y^2 + 1/2)], \quad (3.10)$$

$$\text{with } y = \omega/\gamma\omega_p.$$

The expression $dN_{\text{TR}}/d\omega$ falls off rapidly for $y > 1$ or when ω is larger than the characteristic frequency $\gamma\omega_p$ (with ω_p being the plasma frequency of the radiator material), respectively. For $y \ll 1$, a limiting case is $dN_{\text{TR}}/d\omega \rightarrow 2\alpha/\pi\omega[\ln(1/y)]$.

One can assume from Eq. 3.10 that the integral over transmitted frequencies $\Delta y \sim 1$, near $y \sim 1$ is $N_{\text{TR}} \sim \alpha$. This means that for transition radiation $\sim \alpha = 1/137$ photons per interface are emitted with energies of typically $\gamma(\hbar\omega_p)/3$.

As shown before, the angular distribution of transition radiation is peaked forward with a sharp maximum at $\theta = 1/\gamma$, hence strongly collimated along the direction for relativistic electrons [Gre00]. This typical emission angle of $1/\gamma$ is a consequence of special relativity:

$$N_{\text{TR}} \sim \Delta E/\varepsilon_\gamma \sim \alpha,$$

$$\varepsilon_\gamma \sim \hbar\omega \sim \frac{\gamma}{3}(\hbar\omega_p), \quad (3.11)$$

$$\langle\theta\rangle \sim \frac{1}{\gamma}.$$

In a simple picture, transition radiation can also be regarded as being due to the changing dipole moment formed by the charge and its *image* charge on the opposite of the interface. The image charge is equivalent in effect to the induced charge density at the interface needed to match the boundary conditions. The charge and image charge pair creates a dipole which changes with time and changes direction at the point of crossing the interface thus causing radiation. The interface is the point where the pointing of the dipole vector flips direction indicative of maximum acceleration.

Useful Properties

The previously discussed characteristics of transition radiation (TR) make it suitable for particle discrimination, particularly of electrons and hadrons in the momentum range that is reached by particles produced in heavy-ion collisions. Especially, the proportionality of the emitted energy by TR to the Lorentz factor allows the use in particle identification whereas e.g. the Cherenkov effect becomes useless when β approaches unity.

The effect of transition radiation can be exploited in a Transition Radiation Detector (TRD) for electron identification. A typical TRD consists of a radiator, in which TR is produced, and a multiwire proportional chamber (MWPC) for the measurement of energy loss of ionizing radiation [Dol93]. The electron identification in a TRD is based on the measurement of dE/dx by ionization plus TR for electrons and dE/dx by ionization for other charged particles. This detector principle is also envisaged for the CBM TRD, which is described in detail in Chapter 5.

The following properties of TR are of particular importance for the design of TRDs. The intensity of transition radiation is roughly proportional to the Lorentz factor:

$$I \sim \gamma = \frac{1}{\sqrt{1-\beta^2}}. \quad (3.12)$$

Hence, this radiation offers the possibility of particle identification at highly relativistic energies, where Cherenkov radiation or ionization measurements no longer provide useful particle discrimination. When also measuring transition radiation electron/hadron discrimination is possible for momenta from about 1 GeV/ c to 100 GeV/ c or higher, where this upper limit is determined by the radiation of highly relativistic particles.

The angular distribution of transition radiation is peaked forward with a sharp maximum at $\theta = 1/\gamma$, hence rather collimated along the direction of the radiating particle. The total energy radiated from passing a single foil is found to depend on the squared difference of the plasma frequencies ω_p of the two materials; if the difference is large (e.g. $\hbar\omega_{\text{air}} \approx 0.7 \text{ eV}$ and $\hbar\omega_{\text{polypropylene}} \approx 20 \text{ eV}$) the relation is [Boc98]:

$$E \approx \frac{2}{3} \alpha \gamma \hbar \omega_p, \quad (3.13)$$

where $\alpha = \frac{1}{137}$. The average number of radiated photons is of the order α :

$$\langle N \rangle \approx \frac{\alpha \gamma \hbar \omega_p}{\hbar \langle \omega \rangle}. \quad (3.14)$$

The emission spectrum typically peaks between 10 and 30 keV (see Reference [And06b]). In order to identify the photon flux, periodic arrangements of a large number of foils are in use, interleaved by X-ray detectors, e.g. MWPCs filled with xenon or a Xe/CO₂ mixture. Thin foils of lithium, polypropylene, polyethylene, or carbon are common radiator materials. Randomly spaced radiators are also in use, like foams, granules, or fiber mats (see Chapter 5.1).

3.3 Interaction of Photons with Matter

In order to be detected, photons have to produce charged particles or to scatter with them in interaction processes in the detector medium. These charged particles, mainly electrons, provide detector signals predominantly due to subsequent ionization. The interaction processes of photons with matter essentially differ from ionization processes of charged particles because in every photon interaction process the photon is either completely absorbed (*photoelectric effect, pair production*) or it is scattered at a large angle (*Compton effect*). On the one hand these processes provide the basis for the measurement of photons, on the other hand they are also the main source of background for the measurement of electrons and positrons.

Photoelectric Effect

The interaction of the photon with the atom as a whole leads to the photoelectric effect. This effect is due to the absorption of a photon by an atom and subsequent electron emission:

$$\gamma + \text{atom} \rightarrow \text{atom}^+ + e^-.$$

The maximum kinetic energy of the emitted electron is given by the maximum photon frequency ν_{\max} and the work function W_A :

$$E_{\text{kin,max}} = h\nu_{\max} - W_A,$$

where h is Planck's constant. Since a free electron cannot absorb a photon while conserving the total energy and momentum, the photoelectric effect always occurs on bound electrons with the nucleus absorbing the recoil momentum. The dependence of the cross section on the atomic charge number Z varies somewhat depending on the energy of the photon, however, at MeV energies, this dependence goes as Z to the 4th to 5th power. Thus, the higher Z materials are the most favored ones for photoelectric absorption. The photoelectric effect is dominant up to energies of around 100 keV for low- Z materials like carbon with $Z = 6$, whereas it is dominant even up to energies of around 10 MeV for lead with $Z = 82$ (see also Fig. 3.9). The photoelectric cross section is characterized by discontinuities (absorption edges) as thresholds for photo-ionization of various atomic levels are reached.

Compton Effect

The interaction of the photon with a free electron is called Compton scattering. The photon transfers a part of its energy/momentum to the electron initially at rest:

$$\gamma + e^- \rightarrow \gamma + e^-.$$

After the scattering with a free electron, the wavelength of the photon is increased by:

$$\Delta\lambda = \frac{h}{m_e c} (1 - \cos\phi),$$

where ϕ is the angle by which the photon direction has changed due to the scattering. The frequency and energy of the photon reduce according to the wave length, whereas the energy of the electron increases by this amount. The cross section for Compton scattering off atoms is proportional to Z since Z electrons are available as potential scattering partners. The Compton effect is most important for photon energies from about 100 eV to about 1 GeV (10 GeV) in carbon (lead) (see also Fig. 3.9).

Pair Production

The interaction of the photon with the Coulomb field of the nucleus leads to the phenomenon of pair production, whereby the photon disappears and an electron and a positron are created simultaneously:

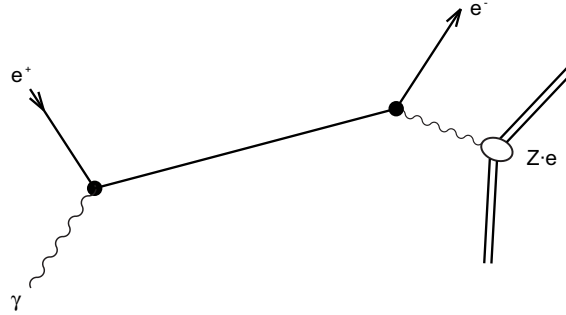


Figure 3.8: Feynman diagram of a photon conversion into an e^+e^- pair in the electromagnetic field of an electron or a nucleus with the charge $Z \cdot e$.

$$\gamma + \text{nucleus} \rightarrow e^+ + e^- + \text{nucleus}'.$$

The cross section for this process is proportional to Z^2 . At high energies it becomes independent of the photon energy, and screening of the electric field of the nucleus by the atomic electrons has to be taken into account.

Due to energy and momentum conservation, a photon cannot decay into an e^+e^- pair in the vacuum. A part of the momentum has to be transferred away from the electron or positron. This can happen by exchanging a photon with a charged particle as shown in Fig. 3.8. For a photon traversing detector material this charged particle can be an electron but most likely it is a nucleus.

Fig. 3.9 shows the contributions of different interaction processes to the photon cross section in a heavy element, here in lead. At low energies it is seen that the photoelectric effect dominates, although Compton scattering, Rayleigh scattering (elastic scattering), and photo-nuclear absorption also contribute. Starting at an energy of 1,022 keV, twice the electron mass, the conversion of the photon into an e^+e^- pair is possible in the electromagnetic field of a nucleus or an electron. Above a photon energy of 100 MeV pair production is the dominant process. The cross section for this process saturates at some higher photon energy.

Photon Radiation Length

As illustrated in Fig. 3.9, high-energy photons predominantly lose energy in matter by e^+e^- -pair production and the cross section is roughly constant at energies above 1 GeV.

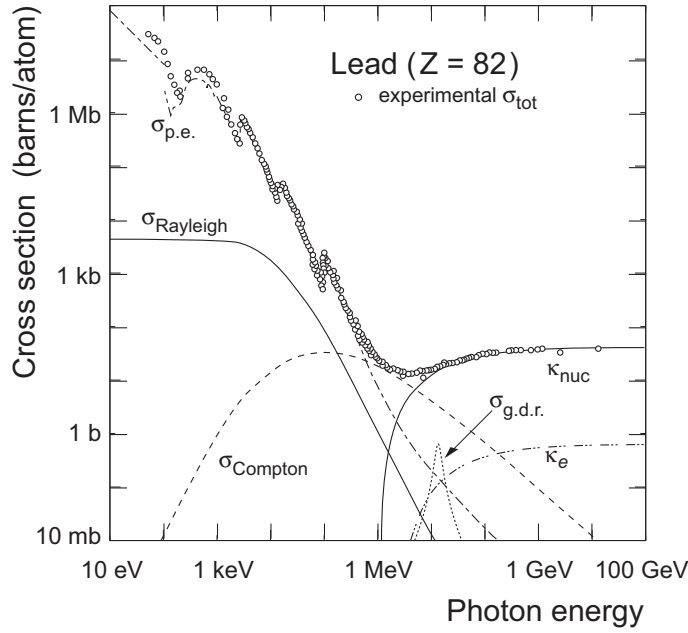


Figure 3.9: Photon total cross section as a function of energy in lead, showing the contributions of different processes [Ams08]: $\sigma_{p.e.}$ = atomic photoelectric effect (electron ejection, photon absorption), σ_{Rayleigh} = Rayleigh (coherent) scattering - atom neither ionized nor excited, σ_{Compton} = incoherent scattering (Compton scattering off an electron), κ_{nuc} = pair production, nuclear field, κ_e = pair production, electron field, $\sigma_{g.d.r.}$ = photo-nuclear interactions, most notably the Giant Dipole Resonance.

This allows to define a mean free path for photons which is directly related to the radiation length X_0 . The radiation length, as already introduced for electrons in Chapter 3.1, is usually measured in g cm^{-2} . As seen later, the mean free path for pair production by a high-energy photon is $\frac{9}{7}$ of the mean free path for bremsstrahlung by an electron [Ams08].

X_0 can be calculated with [Tsa74]:

$$\frac{1}{X_0} = 4\alpha r_e^2 \frac{N_A}{A} \{Z^2 [L_{\text{rad}} - f(Z)] + ZL'_{\text{rad}}\}, \quad (3.15)$$

where $\alpha \approx \frac{1}{137}$ is the fine structure constant, $r_e = 2.818 \text{ fm}$ the classical electron radius, $N_A = 6.022 \cdot 10^{23} \text{ mol}^{-1}$ the Avogadro number, A the atomic mass and Z the atomic number of the material. For $A = 1 \text{ g mol}^{-1}$, $4\alpha r_e^2 \frac{N_A}{A} = (716.408 \text{ g cm}^{-2})^{-1}$. The parameters L_{rad} and L'_{rad} are given in Table 3.1. The function $f(Z)$ is an infinite series, for elements up to uranium it can be represented by

$$f(Z) = a^2 [(1 + a^2)^{-1} + 0.20206 - 0.0369a^2 + 0.0083a^4 - 0.002a^6], \quad (3.16)$$

Element	Z	L_{rad}	L'_{rad}
H	1	5.31	6.144
He	2	4.79	6.144
Li	3	4.74	6.144
Be	4	4.71	6.144
Others	>4	$\ln(184.15Z^{-\frac{1}{3}})$	$\ln(1194Z^{-\frac{2}{3}})$

Table 3.1: Parameters L_{rad} and L'_{rad} , for calculating the radiation length of an element using Eq. 3.15 [Ams08].

where $a = \alpha Z$. The radiation length X_0 as seen in Eq. 3.15 depends on the square of the atomic number Z . This functional dependence of X_0 on Z is more obvious when regarding a fit to the data by Dahl [Ams08]:

$$X_0 = \frac{716.4 \text{ gcm}^{-2} A}{Z(Z+1) \ln(287/\sqrt{Z})}. \quad (3.17)$$

The results obtained by using this formula agree with the values of Eq. 3.15 better than 2.5% for all elements except helium, where the result is about 2.5% low.

With some approximations the differential cross section is determined for electrons and photons as follows. The differential cross section for photons can be described by

$$\frac{d\sigma}{dx} = \frac{A}{X_0 N_A} \left[1 - \frac{4}{3} x(1-x) \right] \quad (3.18)$$

in the complete-screening limit at high energies. Here, $x = E/k$ is the fractional energy transfer to the pair-produced electron (or positron), and k is the incident photon energy. Eq. 3.18 can be integrated to find the high-energy limit for the total e^+e^- -pair production cross section:

$$\sigma = \frac{7}{9} \frac{A}{X_0 N_A}. \quad (3.19)$$

Eq. 3.19 is accurate to within a few percent down to energies as low as 1 GeV, particularly for high- Z materials. This formula can be used to calculate the expected conversion probability for photons in selected converter material and is important for the reconstruction of photons via conversions into e^+e^- pairs (see Chapter 7.4.2).

Analogously to Eq. 3.18, at high energies, the differential cross section for electrons radiating bremsstrahlung can be described by

$$\frac{d\sigma}{dk} = \frac{A}{X_0 N_A k} \left[\frac{4}{3} - \frac{4}{3} y + y^2 \right], \quad (3.20)$$

where $y = k/E$ is the fraction of the electron's energy transferred to the radiated photon. The formulas for the differential cross sections for pair-production (Eq. 3.18) and for bremsstrahlung (Eq. 3.20) are essential for the description of electromagnetic showers e.g. produced in electromagnetic calorimeters.

4. The CBM Experiment

The CBM (Compressed Baryonic Matter) experiment at the future Facility for Antiproton and Ion Research (FAIR) is designed for the investigation of highly compressed nuclear matter. This super-dense nuclear matter can be created in the reaction volume of relativistic heavy-ion collisions (see Chapter 1.3). By varying the beam energy and the reaction systems, different states and phases of strongly interacting matter are expected to be produced. The CBM research program includes the search for the deconfinement phase transition at high baryon densities, the study of chiral symmetry restoration in superdense baryonic matter, the search for the critical endpoint, and the study of the nuclear equation of state at high baryon densities (see Chapter 1).

4.1 The Future Facility for Antiproton and Ion Research (FAIR)

The FAIR accelerator facility comprises a multifaceted science program, with beams of stable and unstable nuclei as well as antiprotons in a wide range of intensities and energies and excellent beam qualities [FAI06]. A sketch of the future FAIR together with the existing GSI facilities is presented in Fig. 4.1.

FAIR comprises two synchrotrons (SIS 100/300) with a circumference of about 1,000 m and with magnetic rigidities of 100 Tm and 300 Tm, respectively. In conjunction with an upgrade for high intensities, the existing GSI accelerators UNILAC and SIS 18 serve as injectors for the new synchrotrons. Adjacent to the double-synchrotron is a complex system of storage-cooler rings and experiment stations, including a superconducting nuclear fragment separator (Super-FRS) and an antiproton production target. Beyond, there is the storage ring for antiprotons (high-energy storage ring (HESR)), the collector ring (CR), and the new experimental storage ring (NESR).

On the one hand, FAIR provides beams of rare isotopes and antiprotons with an unparalleled intensity and quality and on the other hand, the facility is designed to provide particle energies twenty times higher than those achieved at GSI so far. Up to now, this energy regime has only been explored at the AGS up to about 14 AGeV.

Due to the intrinsic cycle times of the accelerator and storage-cooler rings, up to four research programs can be run in parallel. The experimental facilities include the CBM experiment investigating nucleus-nucleus collisions at highest baryon densities, the PANDA

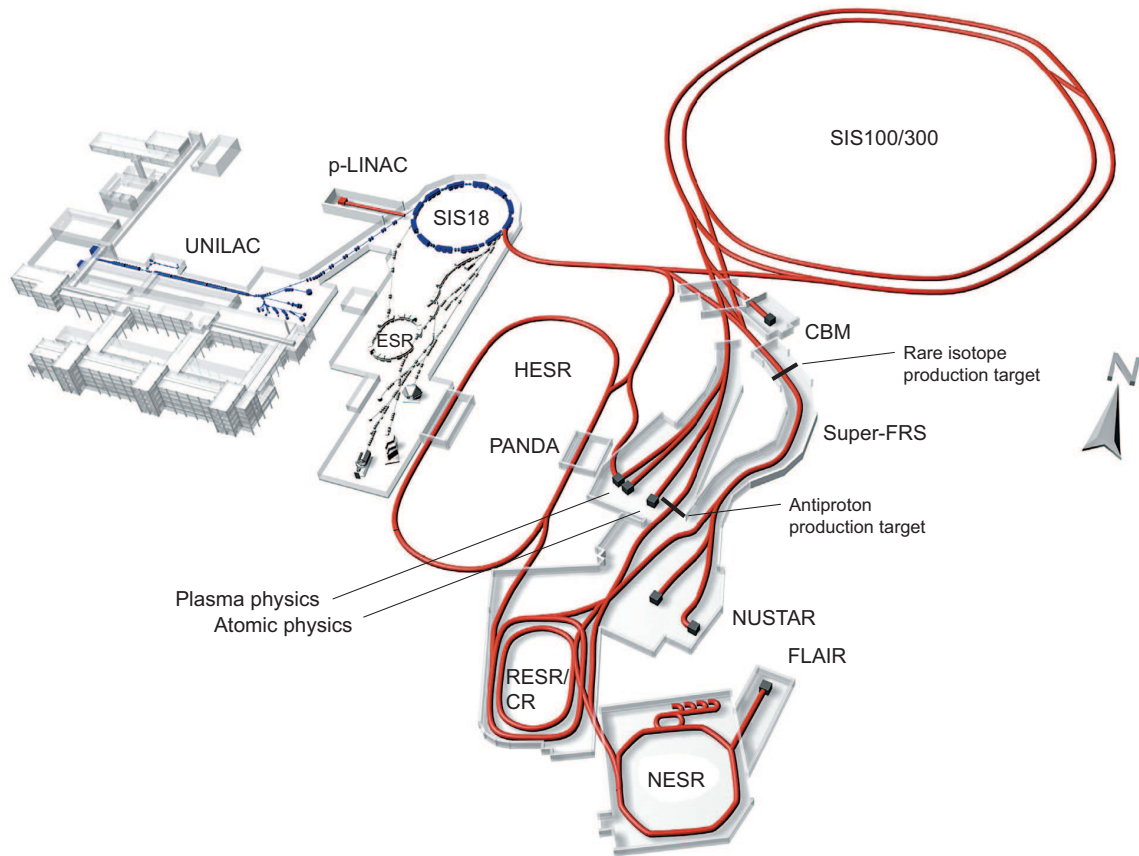


Figure 4.1: Present layout of the the existing GSI facility (blue and black) (UNILAC, SIS 18, ESR) and the intended FAIR facility (red): the superconducting synchrotrons SIS 100 and SIS 300, the collector ring CR, the accumulator ring RESR, the new experimental storage ring NESR, the superconducting fragment separator Super-FRS, the proton linac, and the high energy antiproton ring HESR. The experimental stations for plasma physics, relativistic nuclear collisions (CBM), radioactive ion beams (Super-FRS), atomic physics, and low-energy antiproton and ion physics (FLAIR) are also shown.

detector for hadron physics experiments using cooled high-energy antiproton beams, the NUSTAR detectors used for experiments on the structure of unstable nuclei and on nuclear astrophysics as well as experimental setups for plasma physics and atomic physics.

In order to meet the demands of all experiments, the FAIR accelerator facility has to fulfill a set of very different requirements. FAIR is expected to provide beams of all ion species, from hydrogen to uranium, as well as antiprotons covering a large energy regime (from particles at rest up to several tens of AGeV energy in the laboratory frame). In order to achieve highest baryon densities and enable charm production in high-energy nucleus-nucleus collisions, the SIS 300-synchrotron is designed for beam energies of up to 35 AGeV for U^{92+} (see Chapter 1.3.1).

A unique feature of the FAIR facility, which is the major advantage for heavy-ion physics, compared to RHIC and CERN at the same energy, is the possibility of providing extremely high beam intensities. For primary beams, the intensity increase aimed for is a factor of several hundred for the heaviest ion species compared to present installations at GSI.

SIS 300 Synchrotron

The beams for CBM will finally be provided by the SIS 300 synchrotron. The two synchrotrons SIS 100 and SIS 300 will be built on top of each other in an underground tunnel. They are equipped with rapidly cycling superconducting magnets. Both heavy-ion and proton beams can be compressed to very short bunch lengths required for the production and subsequent storage and efficient cooling of exotic nuclei and antiprotons. These short ion bunches are also needed for plasma-physics experiments.

The available kinetic beam energy per nucleon depends on the bending power $B \cdot r$ provided by the dipole magnets:

$$E/A = \sqrt{(0.3 \cdot B \cdot r \cdot Z/A)^2 + m^2} - m, \quad (4.1)$$

with $B \cdot r = 300 \text{ Tm}$ for the maximum beam rigidity of SIS 300. A is the atomic mass, Z is the atomic number, and m is the average mass of a nucleon. According to Eq. 4.1, the SIS 300 provides high-energy ion beams of maximum energies around 45 AGeV for Ne^{10+} beams and close to 35 AGeV for fully stripped U^{92+} beams. The highest available proton energy for a beam rigidity of 300 Tm is 89 GeV. The maximum intensities in this mode are 10^{13} s^{-1} for protons and close to 10^9 s^{-1} for Au ions. These high-energy beams are extracted over periods of 10 – 100 s in quasi-continuous mode.

According to the current FAIR schedule, beams in the SIS 100 might become available as of 2014, and the SIS 300 synchrotron will be completed at the earliest in 2016.

4.2 Physics Goals and Observables of the CBM Experiment

The main challenge of the CBM research program is to find diagnostic probes which are associated with the equation-of-state of dense baryonic matter, the chiral symmetry restoration, and the phase transition to deconfinement, including the QCD critical endpoint. CBM is a heavy-ion fixed target experiment in the energy range of 10 – 45 AGeV, and its goal is to look for rare probes, in particular, by taking advantage of FAIR in terms of high intensity heavy-ion beams.

The observation of in-medium modifications of hadron properties might be a signature for the onset of chiral symmetry restoration. The in-medium spectral function of short-lived vector mesons (ρ , ω , and ϕ) can be measured directly via their decay into dilepton pairs (see Chapter 2.1). Since dileptons are essentially unaffected by the passage through the high-density matter, their study will provide information on the conditions in the interior of the collision zone.

In-medium production processes and the properties of highly compressed strongly-interacting matter can be probed by measuring particles containing charm, since they are created in the early phase of the collision (see Chapter 1.3.2). At FAIR energies, the charm production plays a particular role since charmonium (a bound state of $c\bar{c}$), D-mesons (a bound state of a heavy charm quark and a light quark), and charmed hyperons are created at beam energies close to the kinematic threshold. Thus, the production cross sections are very sensitive to the surrounding medium at the time of their creation, which is the early, high-density phase of the collision.

The anomalous suppression of charmonium due to screening effects in the QGP was predicted to be an experimental signal of the QGP [Mat86]. In 2000, J/ψ data from heavy-ion collisions were measured with the NA50 experiment at CERN-SPS [Abr00, Abr01], but the interpretation of the results is still under discussion as the data can be explained as well within hadronic scenarios. However, the yield and phase-space distributions of open and hidden charm is regarded as a very promising probe for the QGP. Up to now, no data on J/ψ production have been measured in nucleus-nucleus collisions at beam energies below 158 AGeV. Quarkonium states like the J/ψ decay electromagnetically into lepton pairs of definite mass: the pair has the mass of the decaying bound state. The peak in the dilepton continuum at the J/ψ mass can be identified after background subtraction, determined e.g. by combinations of like-sign lepton pairs. With the CBM experiment, it may even be possible to measure collective effects modifying the phase-space distribution of the charm production.

The production of D-mesons is also predicted to be sensitive to in-medium effects: the effective masses of D-mesons are expected to be modified in dense matter. Such a change would be reflected in the relative abundance of charmonium and D-mesons. D-mesons can be identified by their decay into kaons and pions ($D^0 \rightarrow \pi K$, $D^\pm \rightarrow \pi \pi K$). The measurement of D-mesons in heavy-ion collisions is very difficult because of the large combinatorial background of pions and kaons. Nevertheless, with the CBM experiment the D-meson measurement is expected to be possible for the first time with sufficient statistical accuracy at low energies. This is also important for the comparison to measurements by STAR and PHENIX with heavy-flavor tracker upgrades, which will probably be ready at the CBM start, and by ALICE with its Inner Tracking System. The goal of the design and thus experimental challenge for CBM is to measure the displaced vertex of kaon-pion pairs with an accuracy of better than $100 \mu\text{m}$.

Another signature for the QGP, the enhanced production of strangeness was predicted [Raf82] and later found by the NA57 experiment at 40 AGeV and 158 AGeV beam energy [Bru04]: it was seen that the multiplicity of Ξ and Ω -hyperons per participant is larger in Pb+Pb collisions than in p+Be collisions. The hyperon yields can be reproduced by statistical models showing an equilibrium of strangeness, which is non-trivial to be achieved by rescattering in a hadron gas. The data at SPS and RHIC energy comprise multi-strange hadrons including the Ω and $\bar{\Omega}$. Their yields agree with the chemical-equilibrium calculation and are strongly enhanced as compared to approximately scaled cross sections measured in p+p collisions. The time needed to achieve this equilibrium for baryons via two-body collisions was estimated to be much longer than reasonable lifetimes of the fireball [BM04]. The observations were thus interpreted as a sign that the system had reached a partonic phase prior to hadron production. According to Reference [BM04] it is likely that also there the phase transition drives the particle densities and causes chemical equilibration. Whether the phase transition also plays a role at lower beam energies is currently an open question. Since data is only available at energies of 158 AGeV and 40 AGeV the Ω -measurement in CBM will be very important.

Another interesting observation was made by the NA49 experiment at CERN SPS [Blu05]. A peak was found in the K^+/π^+ ratio as a function of \sqrt{s} in Pb+Pb collisions at around 30 AGeV and a flattening of the slope of the K^+ -spectra. This cannot easily be explained by transport codes or statistical models. Thus, using strangeness as a probe for the QGP is still lively discussed and further information on the subject is needed. Comprehensive studies in CBM with reduced statistical and systematic errors, especially for (multi-strange) hyperons could produce the missing information in the strangeness sector. Up to now, there is only little information on the production of multistrange hyperons below SPS energies. Indeed, only the yield of Ξ^- -hyperons has been measured at top AGS

energies in 6 AGeV Au+Au collisions via reconstruction of their decay into π^- and Λ . The latter reconstructed via their decay into π^- and p. In central collisions the Ξ^- -yield is found to be in excellent agreement with statistical and transport model predictions, suggesting that multistrange-hadron production approaches chemical equilibrium in high baryon density nuclear matter [Chu03].

Hydrodynamics model calculation indicates that a critical endpoint of the deconfined phase transition, which is seen on page 23: Fig. 1.4 at the end of the first-order transition line, might be found in the vicinity of the freeze-out of a Pb+Pb collision at a beam energy of about 30 AGeV [Iva06] (see Chapter 1.3.1). In the vicinity of this critical endpoint, dynamical density fluctuations have been predicted to cause non-statistical fluctuations of experimental observables. In order to investigate the phase transition, anomalies in the energy dependence of event-by-event fluctuations can be explored for different variables like the mean transverse momentum $\langle p_T \rangle$ (see also Chapter 1.3.2). The critical endpoint, for example, is expected to cause a sudden change in the dynamical fluctuation as function of the beam energy. Such dynamical event-by-event fluctuations were already observed in the $(K^+ + K^-)/(\pi^+ + \pi^-)$ ratio at different beam energies. Up to now, beam energies from 20 AGeV to 158 AGeV have been investigated [Alt08]. The highest fluctuations were seen in central Pb+Pb collisions around 20 AGeV by the NA49 experiment and up to now there is no information available at lower energies.

Another interesting observable are direct photons which leave the hot and dense medium unscathed (see Chapter 2.2). Thermal photons from the partonic phase are predicted to be the dominant source of direct photons at low transverse momenta in Au+Au collisions. Due to the very high luminosity, the CBM experiment offers the possibility of measuring the yield of thermal photons with unrivaled high statistical accuracy. The experimental challenge is to extract a direct-photon signal above the large decay-photon background and to identify other sources of direct photons which are not of thermal origin. This is described in detail in Chapter 7.4.

4.3 Detector Concept

The experimental task of the CBM experiment is to identify hadrons and leptons in collisions with up to 1,000 produced charged particles at event rates of up to 10 MHz [Fri08]. The measurements require fast self-triggered read-out electronics, a high-speed data acquisition (DAQ) architecture, and an appropriate high-level event-selection concept. The currently planned setup for the CBM detector is illustrated in Fig. 4.2. The core of CBM is a Silicon Tracking System (STS) located in a dipole magnet. It consists of several layers

of silicon microstrip detectors and has to provide the track reconstruction and momentum determination. In addition, a Micro-Vertex Detector (MVD) will be implemented for the determination of primary and secondary vertices with a very high precision. A typical target is a gold target of $250\text{ }\mu\text{m}$ thickness (1% hadron interaction length Λ_{int}).

For the lepton measurement in CBM, two options are envisaged: the identification and reconstruction of electrons (upper sketch in Fig. 4.2) and the measurement of muons (lower sketch in Fig. 4.2).

The electron identification is provided in conjunction with a Ring Imaging Cherenkov (RICH) detector and a system of Transition Radiation Detectors (TRD). The TRD also serves as tracking detector for charged particles with a large lever arm at its position of about 5 m, 7.25 m, and 9.5 m from the target which is especially important for the TOF matching. The RICH will be constructed such that it can be removed and replaced by a muon detection system consisting of hadron absorber layers (made of iron) sandwiched by large area tracking detector layers.

The hadron identification is facilitated by a Time-of-Flight (TOF) measurement with a wall of timing Resistive Plate Chambers (RPC). In addition, the TOF helps for the electron identification at low momenta. An electromagnetic calorimeter (ECAL) is used for the identification of photons.

4.3.1 The Silicon Tracking and Vertex Detection System

The STS provides the track measurement, momentum determination, and the determination of primary and secondary vertices. Currently, eight stations are planned. They cover polar angles from 2.5° to 25° , which are arranged in the 1 m long gap of a superconducting dipole magnet providing the bending power required for momentum determination with a resolution of $\Delta p/p = 1\%$. A higher magnetic field decreases the efficiency towards low momentum particles while a lower magnetic field worsens the momentum resolution obtained with the STS. In order to achieve the required momentum resolution, the superconducting dipole magnet has a bending power of 1 Tm. The tracking layers are located in the gap of the magnet between 30 and 100 cm downstream of the target. As aimed for in the current setup (see Fig. 4.3), the first two STS stations behind a vacuum volume might be hybrid pixel detectors providing space points of the particle trajectories [Heu07]. The other six stations (with an active area of 1.5 m^2 the largest part) will be built from thin, double-sided micro-strip detectors, which are planned to be read out in individual sections of single or several chained sensors.

One of the most challenging tasks for the tracking system is the reconstruction of the D-meson decay vertices ($D^0 \rightarrow K^- \pi^+$ and $D^\pm \rightarrow K^\pm \pi^\pm \pi^\mp$) in a typical distance of

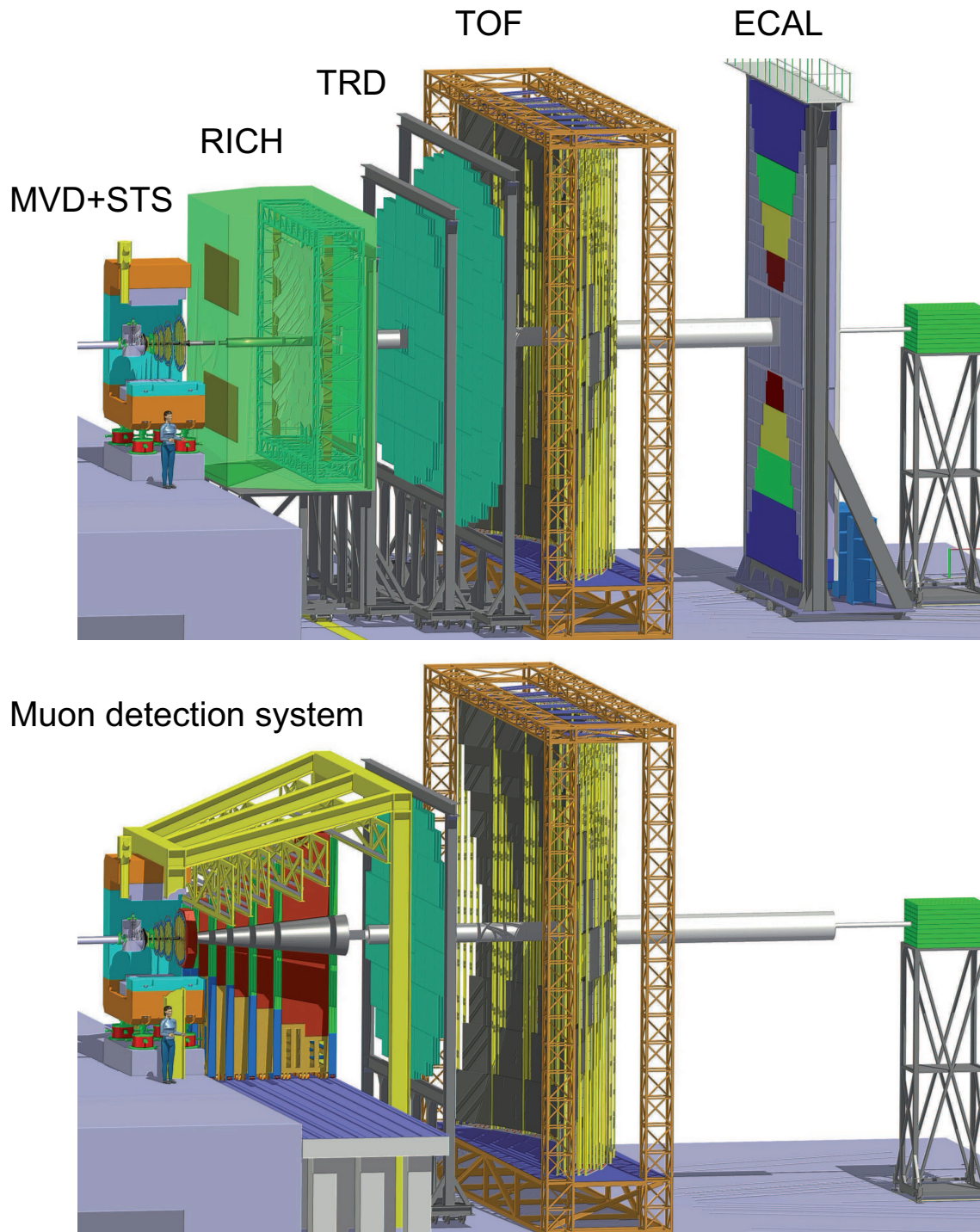


Figure 4.2: Current setup for the CBM experiment planned at FAIR [Sen09]. It consists of a high-resolution STS, a TOF made from RPCs, and an ECAL based on lead/scintillator layers. The upper part shows the option which allows an electron measurement with a RICH and three stations TRD with 3-4 layers each. In the lower part a muon detection system consisting of hadron absorber layers and tracking detector layers is shown.

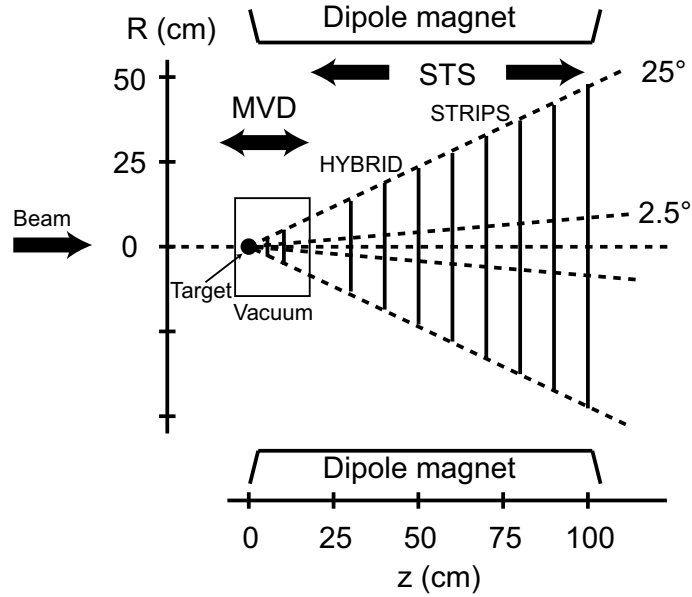


Figure 4.3: Schematic cross section of the Silicon Tracking and Vertex Detection Systems in the dipole magnet. The illustration has been modified from Reference [Heu07] in order to reflect the currently envisaged setup.

the order of $100\text{ }\mu\text{m}$ from the collision vertex ($D^0 : c\tau = 122.9\text{ }\mu\text{m}$, $D^\pm : c\tau = 311.8\text{ }\mu\text{m}$ [Ams08]). Thus, in front of the hybrid pixel detectors, an MVD (Micro-Vertex Detector) is planned, which provides a particularly good position resolution while keeping the material budget low and the radiation tolerance high (see Fig. 4.3). In order to provide the best possible position resolution for the vertex measurement, these first two stations (located upstream close to the target) are composed of very thin pixel detector stations. The current setup foresees Monolithic Active Pixel Sensors (MAPS), for the stations located 5 and 10 cm downstream from the target. They cover an active area of about 150 cm^2 . These stations will be installed in vacuum to prevent beam-gas interactions in-between the MVD stations. The envisaged pixel size is between $25 \times 25\text{ }\mu\text{m}^2$ and $40 \times 40\text{ }\mu\text{m}^2$. For the latter pixel size, a position resolution of $\sigma = 3\text{ }\mu\text{m}$ can be achieved [CBM09a].

4.3.2 The Ring Imaging Cherenkov Detector

In conjunction with the TRD, the RICH will provide electron identification. The requirement for the RICH is an electron identification with an efficiency of 90% for $p \lesssim 10\text{ GeV}/c$ in a wide acceptance with a pion suppression of the order of 10^3 [Höh08b]. A cone of

Cherenkov light is produced when a high speed particle traverses a radiator, with a velocity greater than the speed of light in that medium (see Chapter 3.2.1). In the RICH detector, this light cone is reflected by a mirror to a position sensitive photon detector, which allows to reconstruct the produced rings. The currently planned setup considers a gaseous RICH detector with a radiator with low refractive index and two photo-detector planes, each with an active area of $1.7 \times 0.7 \text{ m}^2$. A nitrogen volume of 2.5 m is envisaged as radiator: at ambient pressure, with $\gamma_{\text{th}} \geq 41$, the pion threshold for Cherenkov radiation is $p_{\pi, \text{th}} = 5.6 \text{ GeV}/c$. A 3 mm glass mirror with a radius of curvature of 4.5 m is envisaged with an Al+MgF₂ coating. The photo detector planes may consist of multi-anode photomultipliers with UV-transparent windows.

In central Au+Au collisions at 25 GeV beam energy, about 600 charged particles are emitted within the acceptance and about 90 rings are produced in the RICH detector. The estimated number of measured photons per ring is about 20. Within this layout a pion suppression of about 500 – 1,000 is achieved in simulations for $p \lesssim 10 \text{ GeV}/c$. The layout can still be optimized in terms of cost and radiation length in particular by minimizing its dimensions. A first compact RICH design has been developed. In simulations it was shown that using CO₂ as radiator and mirrors of 3 m radius, the required performance can be kept while the RICH volume can be reduced by a factor of 2 – 3 [Höh08b].

4.3.3 The Transition Radiation Detector

The TRD contributes to the electron identification and tracking of charged particles. Transition radiation (TR) is produced when a relativistic particle traverses an inhomogeneous medium, in particular the boundary between materials with different dielectric constants ϵ (see Chapter 3.2.2). For the expected particle momenta, TR is produced only by electrons and positrons ($\gamma > 1,000$), and this offers the possibility of separating them e.g. from pions. Currently, the TRD is envisaged to be a system composed of three stations with three to four layers each. These stations will be located at distances of 5 m, 7.25 m, and 9.5 m from the target. They cover a total active area of about 600 m^2 . Each layer consists of a radiator, in which the TR is produced by electrons, and of a gaseous detector, in which the deposited energy of charged particles and the TR can be measured. The gas mixture of the readout detector is based on Xe in order to maximize the absorption of TR (see Chapter 5.2.2). A very fast readout detector is required to cope with the high interaction rates of up to 10^9 Hz . Also the large multiplicities pose a challenge. For a fixed-target experiment such as CBM, in particular in the inner part of the detector, covering forward emission angles, high counting rates are expected. The central part of the TRD will be exposed to counting rates of up to $100 \text{ kHz}/\text{cm}^2$. Thus, in order to minimize possible space

charge effects, the gas volume must be sufficiently thin. At the same time, the aim is to achieve a high pion suppression factor of the order of 100 at an electron efficiency of 90% for the entire TRD. In addition, the TRD will be used for tracking of all charged particles with a position resolution of $300 - 500 \mu\text{m}$ in both directions, x and y , perpendicular to the beam direction. By way of example, this can also be realized with a position resolution of $300 - 500 \mu\text{m}$ in one direction and $3 - 30 \text{ mm}$ in the other direction when rotating every second layer by 90° [CBM09a].

Up to now, two design options have been under consideration for such a detector: either a detector built from straw tubes or a multiwire proportional chamber (MWPC) with pad readout. Such a design based on straw tubes has already been developed for the Transition Radiation Tracker (TRT) in the ATLAS experiment at LHC. It provides very good spatial resolution of about $200 \mu\text{m}$ even at rates of 4.5 MHz/cm^2 [Pes06]. The other layout based on MWPCs with pad readout is comparable to the TRD based on drift chambers developed for the ALICE experiment at LHC [ALI01]. This design has the advantage of providing an unrivaled electron/pion separation. It also provides sufficient tracking capability. Due to the much higher rates in CBM, this layout has to be modified in order to reduce the drift distance, i.e. going towards thinner gas volumes. Both TRD versions have been investigated as alternative designs. At present, the straw tubes are not considered as an option for the TRD anymore. Nevertheless, they are still possible as pure tracking chambers for the last three stations of the muon detection [Zin09]. The straw tube option looks quite promising for this application because of the good coordinate resolution of such detectors ($200 \mu\text{m}$ in the drift direction) and the fact that this detector technology is rather simple and has shown to be reliable. This thesis will focus on the aspects of the MWPC-based TRD.

4.3.4 The Time-of-Flight Detector

A time-of-flight (TOF) measurement can be used to identify charged particles: the determination of the particle mass is based on the measurement of the time of flight, the particle momentum and the particle track length. The TOF wall, which is presented in Fig. 4.2, consists of approximately 60,000 independent cells providing a resolution of $\sigma_{\text{TOF}} \leq 80 \text{ ps}$ [GD08]. The TOF stop detector of CBM has an active area of about 150 m^2 located at a distance of 10 m from the target. A diamond pixel (or micro-strip) detector provides the start signal for the TOF measurement. It directly counts the beam particles at intensities of up to 10^9 ions/s . The requirements for the TOF detector can be satisfied by a tRPC (timing Resistive Plate Chamber) with $25 - 30^\circ$ coverage in θ ($\sim 150 \text{ m}^2$). In order to cope with the high beam luminosity, the tRPC must handle rates of up to 20 kHz/cm^2 ,

while the FEE must process the GHz signals from the tRPC at an interaction rate of up to 10 MHz. The current development of tRPCs shows very good performance in terms of high rate capability, low resistivity material, long term stability, and the possibility to build large arrays with sufficient timing performance. First prototypes with glass electrodes have already been built and tested. With an efficiency of 95% they showed a time resolution of 120 ps at rates of 18 kHz/cm² [Aki07]. With an overall efficiency of 80% to 90%, a separation of kaons and pions can be achieved up to laboratory momenta of about 3.5 GeV/c, while protons can be identified up to 7 GeV/c (see Fig. 4.4).

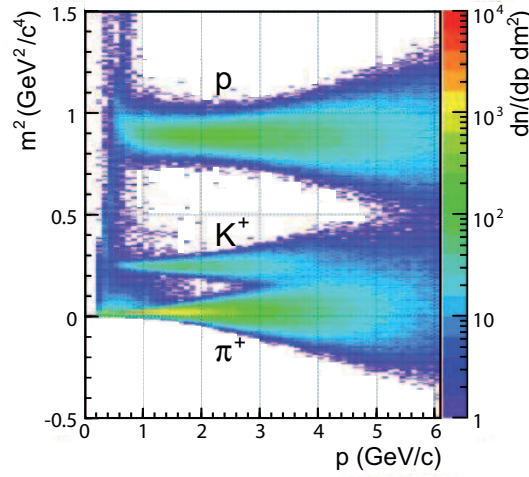


Figure 4.4: Squared mass vs. momentum of hadrons reconstructed by TOF in central Au+Au collisions at 25 AGeV beam energy [Kre09].

4.3.5 The Electromagnetic Calorimeter

In order to reconstruct photons, a “shashlik” type calorimeter shall be installed which consists of modules with granularities of $3 \times 3 \text{ cm}^2$, $6 \times 6 \text{ cm}^2$, and $12 \times 12 \text{ cm}^2$. Each module will be composed of 140 layers of 1 mm lead and 1 mm scintillator. Such techniques are commonly used, e.g. in the HERA-B experiment at DESY, in the PHENIX experiment at RHIC, and in LHCb at LHC.

4.3.6 The Projectile Spectator Detector

The Projectile Spectator Detector (PSD) is a compensating, modular lead-scintillator calorimeter, which is used to determine the collision centrality. Good knowledge of the impact parameter is particularly important for analyzing event-by-event fluctuations, and in order to study collective effects like flow for which a well defined reaction plane is important. The PSD will measure nucleons from the projectile nucleus which did not interact. It is composed of 12×9 modules, each consisting of 60 lead/scintillator layers with a surface of $10 \times 10 \text{ cm}^2$. The photons produced in the scintillator are measured via wavelength shifting by Multi-Avalanche Photo-Diodes (MAPD) of the size of $3 \times 3 \text{ mm}^2$ and with a pixel density of $10^4/\text{mm}^2$.

By using this layout, within a simulation of Au+Au collisions at 10 AGeV, an impact parameter resolution of $\Delta b/b = 0.1$ was determined for peripheral collisions and worsens to $\Delta b/b = 0.5$ for most central collisions [Iva09]. Note that the resolution is dominated by the physical fluctuations of the number spectators.

4.3.7 Data Acquisition

In order to access very rare probes and to measure all particles with the required statistical accuracy, measurements at very high event rates are envisaged for CBM. At a beam intensity of 10^9 ions/s and an interaction probability of 1% in the target, event rates of 10 MHz will be reached. Assuming a bandwidth of 1 GByte/s and an average event volume of about 40 kByte for minimum bias Au+Au collisions, an event rate of 25 kHz will be accepted by the data acquisition. For this storage rate, online event selection systems are required which reject less interesting events. With event rates of 10 MHz, only one in 400 events can be archived, and online software and hardware selections have to be applied to ensure that none of the interesting rare events are lost and cross sections can be reliably extracted.

4.3.8 The Muon Chamber System

As an alternative approach to the dielectron measurement the possibility of detecting vector mesons, like ρ , ω , ϕ , and J/ψ , via their decay into dimuons is currently under investigation. For this measurement, hadrons would be suppressed with several absorber layers located behind the STS. A possible setup for the Muon Chamber System (MuCh) is presented in Fig. 4.5. Like in the “electron setup” (as seen in the upper part in Fig. 4.2), the momentum of these tracks is determined with the STS. Subsequently, all charged particles

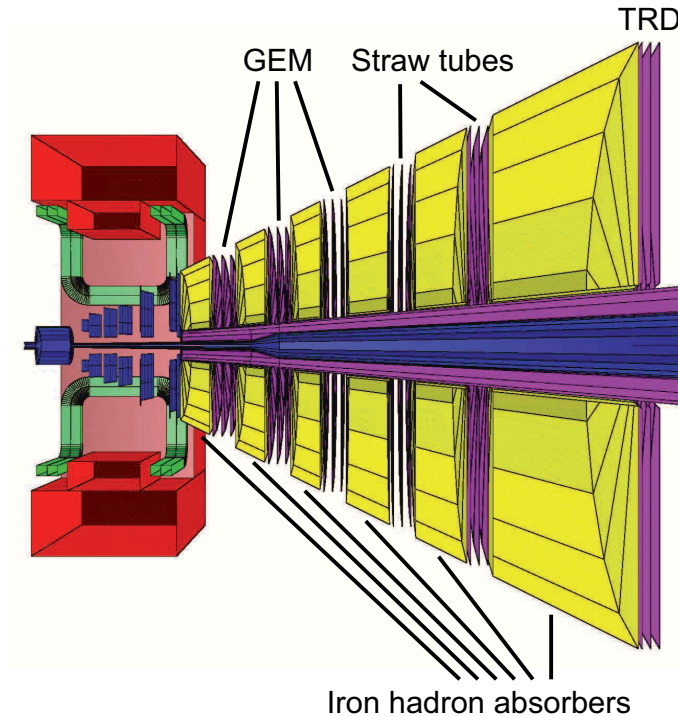


Figure 4.5: The CBM muon detection system consisting of alternating layers of iron hadron absorbers and detectors [Fri08].

are tracked through the absorber in order to match the muons, which pass the absorber, to the STS tracks. This can be achieved by highly granulated and fast detectors which are located in each gap between the absorber layers. The current design of the muon detection system foresees 18 detector stations and 6 segmented iron absorbers. In this case, the total material budget would correspond to 13.5 times the nuclear interaction length. Promising candidates for the fast and highly granulated detectors, located in the five gaps between the absorber layers, are gaseous detectors based on GEM technology [Dub08], straw tubes, and one of the TRD stations. The total area of the muon chambers would cover an area of about 70 m^2 .

Currently, it is not yet decided if the “electron” or the alternative “muon setup” will be built. The solution offering the most comprehensive research program would be to build both setups which can be used alternately. In that case, the RICH has to be temporary removed and the last 3 detectors of the MuCh can correspond to tracking detectors which will anyway be in place in order to cover the gap between STS and TOF. The TRD, for

example, could be used for this purpose, too. Of course, the ECAL cannot be used in conjunction with the muon detection system.

4.4 Dilepton Spectroscopy in CBM

For the dilepton measurement with the CBM experiment both options, the dielectron as well as the dimuon measurement, are currently investigated in simulations with the CBM simulation framework CbmRoot [Cbm09b] (see also Chapter 7). The simulations were performed with an implementation of the standard CBM detector layout as described in Chapter 4.3. The low and high mass vector meson (namely ρ , ω , ϕ , J/ψ , ψ') decays were simulated with the PLUTO generator [Frö07], and the multiplicities for central Au+Au collisions at 25 AGeV beam energy were taken from the HSD transport code [Ehe96]. The background was estimated using the UrQMD event generator [Bas98]. Both, signal and background, are propagated through the detector setup using the transport code GEANT3 [Com93] within CbmRoot. For background simulations of the J/ψ , an event-mixing technique was used but for the reconstruction of the low-mass vector mesons the background-to-event ratio is too much correlated for using the same method. Thus, the background was simulated with a so-called *superevent* technique as discussed in Reference [CBM05].

There are different advantages and disadvantages of the two options which play an important role in simulations and detector R&D. When measuring dielectrons, the main challenge is the large background of electrons from physical sources like π^0 -Dalitz decays and from γ -conversions in the target. In order to minimize this background, for the dielectron measurement a thinner target than the standard one (0.1% interaction length instead of 1%) is used. On the other hand, γ -conversions provide an additional observable since direct photons can be analyzed by reconstructing them via the produced e^+e^- -pairs. This will be shown in detail in Chapter 7.4.

A handicap in analyzing dimuons is the background from misidentified muons due to pion decay in flight or track mismatches [Höh08a]. In order to keep track mismatches on a low level, the tracking is performed by additional tracking stations between single absorber parts.

In both measurements the events are reconstructed starting from track reconstruction in the STS. Electron identification is done in conjunction with the information provided by the TRD, RICH, and TOF detectors. One important cut in the dielectron analysis is a track cut in order to reject electrons from γ -conversions in the target and π^0 -Dalitz decays. For muon identification, the full tracking through the muon absorber is performed. In addition,

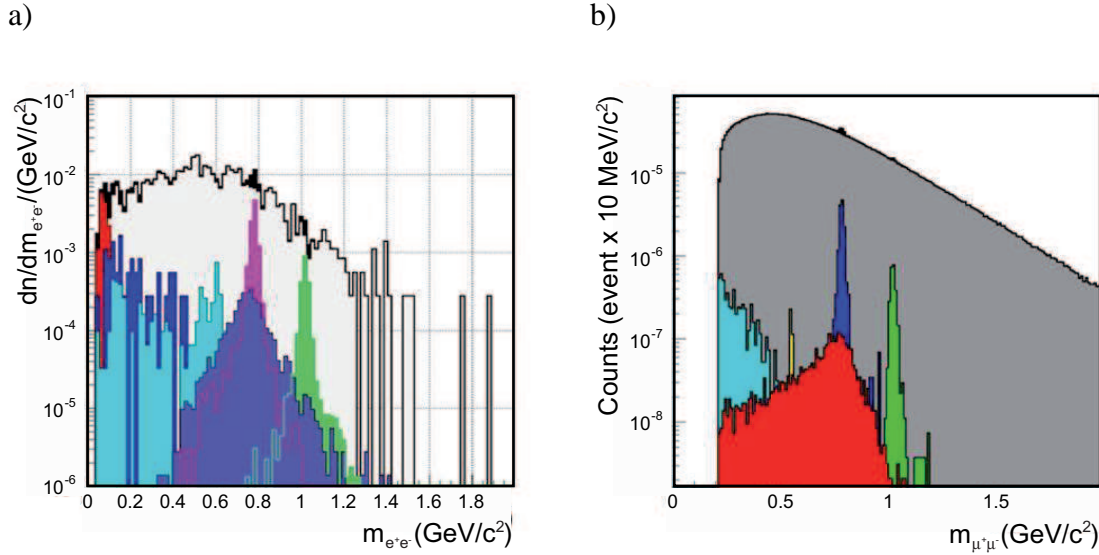


Figure 4.6: Invariant-mass spectra of low-mass vector mesons: a) reconstructed via dielectrons (200k events, $p_T > 0.2 \text{ GeV}/c$) and b) reconstructed via dimuons (4×10^8 events) in central Au+Au collisions at 25 AGeV beam energy [Höh08a]. The different sources shown are (with increasing invariant masses): π^0 -, η -, ω -Dalitz, ρ -, ω -, ϕ -meson decays.

the TOF information is used to reject protons still reaching this detector, which is located behind the muon detection system. In this J/ψ -analysis via dimuons only a p_T cut is used.

In Fig. 4.6, the reconstructed invariant-mass spectra are presented for a full analysis of low-mass vector mesons. Fig. 4.6a) shows the electron decay channel, and Fig. 4.6b) shows the corresponding spectrum obtained via the muon decay channel, both in central Au+Au collisions at 25 AGeV beam energy. The different sources, shown in both spectra, are (from left to right) π^0 -, η -, and ω -Dalitz, ρ -, ω -, and ϕ -meson decays. The simulated data sample (200k events) corresponds to approximately 10 seconds of beam time [Gal08]. At larger invariant masses, the J/ψ and ψ' signals can be found which is shown in Fig. 4.7. This measurement is also feasible via the electron decay channel (Fig. 4.7a)) and via the muon decay channel Fig. 4.7b)). Besides the different shapes of the background from different sources, the radiative broadening in the dielectron measurement can be seen in the J/ψ peak in Fig. 4.7a). With both decay channels, a very comparable performance is obtained despite their completely different background origin, which is dominated by π^0 -Dalitz decays in the dielectron case and by misidentified muons mainly

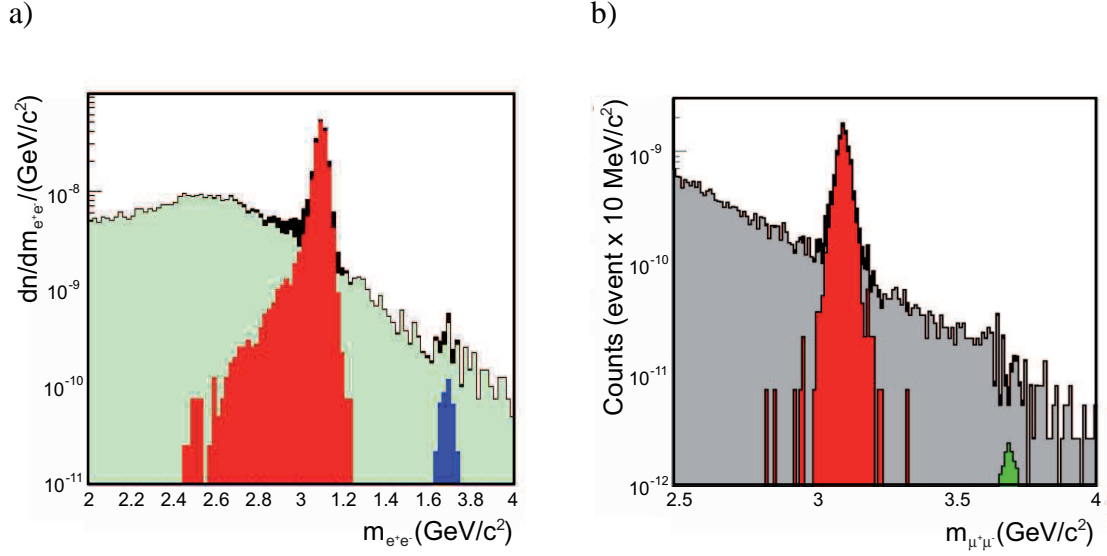


Figure 4.7: Invariant-mass spectra of J/ψ and ψ' : a) reconstructed via dielectrons (4×10^{10} events, $p_T > 0.2 \text{ GeV}/c$) and b) reconstructed via dimuons (3.8×10^{10} events) in central Au+Au collisions at 25 AGeV beam energy [Höh08a].

from pion decay in the dimuon case. In both measurements, the efficiencies for low-mass vector mesons are of the order of 3% – 10% and for charmonium of about 20% [Höh08a]. In all signals shown, a wide phase space is covered reaching down to the lowest p_T . This constitutes an important prerequisite for the near-threshold production studies. Only the low-mass vector mesons close to mid-rapidity in the dimuon channel are more difficult to detect as they are most affected by the absorption. For the dimuon channel masses below the 2-muon threshold are cut off whereas the dielectron channel offers the possibility of performing measurements at lowest masses. The aim of the CBM experiment is measuring both, dielectrons and dimuons, in order to obtain the best systematic check possible within one experiment.

5. The Transition Radiation Detector

The identification of electrons (and positrons) as well as the tracking of charged particles are important tasks of the CBM detector (see Chapter 4). Since electrons give access to very rare particle decays, such as those containing heavy quarks, a high electron efficiency is required. At the same time, a high hadron-rejection capability is needed because they are the most frequently produced charged particles from a nucleus-nucleus collision. Especially the suppression of pions is important as pions are the most abundant hadrons produced. They are the lightest hadrons and therefore most difficult to separate experimentally from electrons. In conjunction with other detectors, the charged-particle tracking and the electron/pion separation is to be provided by a Transition Radiation Detector (TRD). A survey of principles of TRDs can be found in Reference [DoI93].

The production of transition radiation (TR) is very interesting for particle identification – especially for electron/hadron separation – in high-energy physics because the energy and number of the emitted TR photons depend on the Lorentz factor γ of the particle. The total energy radiated e.g. by an electron traversing a single radiator foil in air depends on the squared difference of the plasma frequencies ω_p of the two radiator materials. For a large difference, the relation is

$$E \approx \frac{2}{3} \alpha \gamma \hbar \omega_p, \quad (5.1)$$

where $\alpha = \frac{1}{137}$. The average number of radiated photons is of the order α . A detailed description can be found in Chapter 3.2.2.

Most of the exploited physical effects like energy loss via ionization, time of flight, or Cherenkov radiation depend on the particle's velocity. Thus, changes become marginal when approaching the speed of light, and they do not offer good identification possibilities for relativistic particles. Hence, an additional detection method depending on γ is very useful for particle identification at high energies.

Apart from the physics requirements, the detector needs to fulfill specific criteria to be suitable for the CBM experiment. The large multiplicities and high interaction rates in this heavy-ion experiment demand very fast detectors with high granularity that go in hand with high detection efficiencies and low material budget in terms of radiation length. A TRD system probably consisting of three stations with several layers has been conceived in order to fulfill all these tasks. A single TRD layer consists of two different parts: a radiator, in which an electron creates the transition radiation, and a detection

part consisting of a multiwire proportional chamber (MWPC) filled with a mixture of Xe and CO₂. The electron identification is based on the measurement of dE/dx by ionization plus TR for electrons and dE/dx by ionization for other charged particles. The MWPC technology also offers charged-particle tracking with a good position resolution due to a readout of the cathode which is subdivided into pads providing a high granularity. Detailed design considerations can be found in Chapter 5.3.

5.1 Radiator Material

Transition radiation (TR) is produced when a highly relativistic charged particle ($\gamma \gtrsim 1,000$) traverses the boundary between two media of different dielectric constants (see Chapter 3.2.2). Since the probability for TR production at a single boundary is very small (the average number of photons per particle is of the order of $\alpha = 1/137$) it is advantageous to use a multilayer dielectric radiator in order to increase the radiation yield cumulatively.

Regular foil radiators are the most efficient radiators available but they have the disadvantage to be very heavy and expensive because of a complex production. Another option is the usage of irregular radiators made of foams or fibers like they have been developed for the TRD of the ALICE experiment at LHC (see a detailed description in Reference [ALI01]). Since ALICE is a collider experiment with a radial geometry, the radiator of this TRD has to fulfill strong geometrical and mechanical constraints. Sandwich radiators consisting of foam and fibers are used in order to provide the optimal combination of TR efficiency, minimum weight and mechanical stability. The fiber mats, consisting of polypropylene fibers of $17\ \mu\text{m}$ (*fiber17*), which are predominately layered in two dimensions, are comparable in performance to regular foil radiators since the fiber thickness provides a well defined spatial separation between two consecutive boundaries, and a large fraction of the boundaries are approximately perpendicular to the particle flight direction. In that case the particles traverse a circular cross-sectional area of the fibers, and they prevalently see the same distance between the boundaries, twice the fiber radius, which is important to match the condition for constructive interference. The poly-methacrylimide foam (*ROHACELL HF71*) is a slightly less efficient radiator because of the random orientation of the boundaries and variably sized spatial gaps between them. However, the mechanical properties of foams are very advantageous. The sandwich radiators consisting of fibers, foams, and a glass fiber laminate provide a good compromise in terms of TR efficiency, radiator thickness, mechanical support and radiation length, and they are also an interesting option which should be considered for the CBM experiment.

Nevertheless, more efficient radiators can be built using stacks of a few hundred polypropylene foils having a regular periodic structure. In order to obtain the highest possible TR photon intensity, the design of radiators in terms of foil thickness, gaps etc. is dominated by the consideration of interference effects (see Chapter 3.2.2). The energy spectra of TR using two different regular foil radiators and irregular radiators (fiber, foam, sandwich) have been measured in a beam of electrons of momentum 1 to 10 GeV/ c with drift chambers operated with a mixture of Xe and CO₂ [And06b]. The first regular foil radiator (Reg1) consists of 120 foils of the thickness 20 μm and the spacing of the foils is 500 μm . The second regular foil radiator (Reg2) has 220 foils of the same thickness with a spacing of 250 μm . The results obtained in these measurements show that the total TR yield for the regular foil radiator is, depending on the momentum, about a factor of 1.5 (for Reg1) and 1.7 (for Reg2) larger than for the sandwich radiator.

Although regular foil radiators are the most efficient radiators available, the production is complex and has not yet been done for large areas. Using foil radiators would require to mount hundreds of foils with uniform separation in strong metal frames. Nevertheless, due to the fixed-target geometry of CBM and the TRD setup with nine to twelve vertical layers, the construction of regular foil radiators provides a realizable and attractive design option which needs to be investigated in detail. One possibility is to fix small foil radiators e.g. in front of every single TRD cell where the challenge would be the minimization of the material shadowing the following detectors. An alternative is the construction of a large foil radiator of the size of a TRD station. In this case, guaranteeing the uniform separation of the foils is very demanding.

For the in-beam test of the MB-TRD (Münster-Bucharest TRD) prototypes of the CBM TRD, small sandwich radiators very similar to the ALICE TRD radiators as well as two different regular foil radiators were used. The sandwich radiators were constructed using *ROHACELL* foam of 2.0 cm thickness without any reinforcement and *fiber17* sheets of about 4.0 cm thickness. The regular foil radiators are the same as described above (Reg1 and Reg2). The results of the in-beam test of the MB-TRD prototypes are discussed in Chapter 6.

5.2 Multiwire Proportional Chambers

Proportional counters are widely used for the measurement of energy loss of ionizing radiation. The first effective multiwire proportional chambers (MWPC) were operated in 1967 – 68 by Charpak and collaborators [Cha68]. They comprised a set of anode wires closely spaced, all at the same potential, and each wire acting as independent counter.

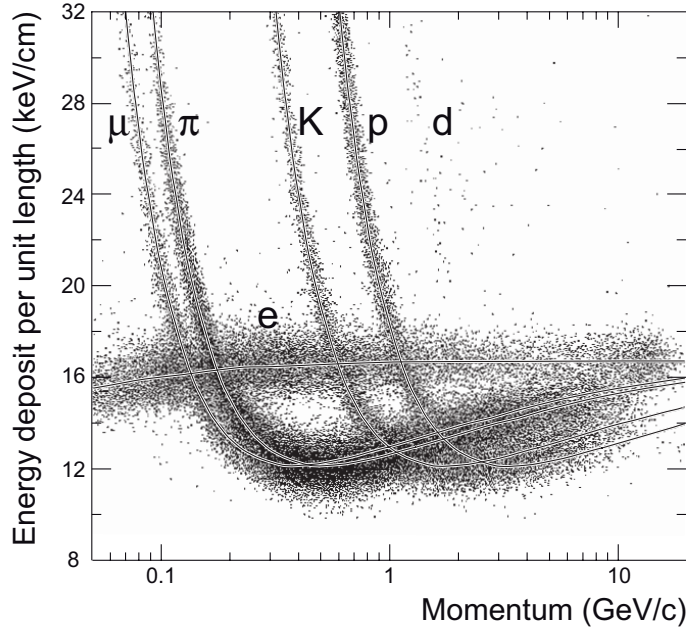


Figure 5.1: Energy deposit for different particles in Ar(80%)CH₄(20%) measured with the PEP4/9-TPC in multi-hadron events [Yao06]. The curves are corresponding to the energy loss given by the Bethe-Bloch formula as described in Chapter 3.1.

The TRD, proposed for the CBM experiment, consists of layers made of a dielectric radiator and a subsequent MWPC with pad readout. MWPCs are high-granularity fast detectors which allow track reconstruction of charged particles with good position resolution and the determination of their energy loss in the sensitive chamber volume. Furthermore, depending on the choice of gas, these chambers are very convenient X-ray detectors which is important to measure the TR at the same time. Thus, a combination of a high-efficiency TR radiator and an MWPC for the detection of both X-rays and dE/dx may provide a good electron/pion separation and tracking capability.

In Fig. 5.1, the energy deposit of different particles in Ar(80%)CH₄(20%), measured with a Time Projection Chamber (TPC), is shown [Yao06]. It can be seen that the electron/hadron separation via the measurement of energy loss is possible and depends on the particle momentum (see a detailed description of the energy loss of charged particles in Chapter 3.1). In the momentum region of several GeV/ c , which is interesting for the electron/pion separation in a heavy-ion experiment, the energy loss of electrons is almost constant and much higher than the energy loss of hadrons, which have not reached the Fermi plateau at these momenta. Significantly higher values for the energy loss by elec-

trons than by pions are expected in the momentum region of $0.3 - 10 \text{ GeV}/c$. In principle, it is also possible to separate them at low momenta smaller than $0.1 \text{ GeV}/c$, where the energy loss of pions is much higher than the one of electrons. But within the fixed-target experiment CBM, charged particles with these momenta do not reach the acceptance of the particle identification detectors since they are bent strongly in the magnetic field before.

Charged particles can be detected in ionization detectors since they produce electron-ion pairs along their path traversing a gas. The energy loss of the charged particles by ionization is very small, typically a few keV per centimeter of gas under normal conditions. Electric signals that contain information about the original location and ionization density of the segment are recorded. The gaseous ionization detectors can be separated into three devices working at different voltages: the ionization chamber, the proportional counter, and the Geiger-Müller counter. At zero voltage, no charge is collected as the electron-ion pairs recombine under their own electrical attraction. As the voltage is raised, the recombination forces are overcome and the current begins to increase as more and more of the electron-ion pairs are collected before they can recombine. In the operating region of the ionization chamber, all created pairs are collected and a further increase of the voltage has no effect. Ionization chambers are commonly used for measuring gamma ray exposure and as monitoring instruments for large fluxes of radiation [Leo87]. When further increasing the voltage the current increases again. This so-called proportional-counter region is described later in detail since it is the operating condition for MWPCs. When applying a very high voltage beyond the proportional region the energy of the electrons freed in primary ionizations becomes so large that a discharge occurs in the gas. Instead of a single, localized avalanche at some point along the anode wire, a chain reaction of many avalanches is triggered. The output current becomes completely saturated, always giving the same amplitude regardless of the energy of the initial event. Detectors working in this voltage region are called Geiger-Müller counters.

With an applied voltage in the so-called proportional-counter region the number of electron-ion pairs in the avalanche is proportional to the number of primary electrons. The electric field is strong enough to accelerate freed electrons to an energy where they are also capable of ionizing further gas atoms or molecules in the chamber. The electrons, liberated in these secondary ionization processes, are also accelerated to produce still more ionization etc. This results in an ionization avalanche. Since the electric field is strongest close to the anode, this avalanche occurs very quickly and almost entirely within a few radii of the wire. The number of electron-ion pairs in the gas avalanche is directly proportional to the number of primary electrons. This gives a proportional amplification of the current with a multiplication factor depending on the working voltage, the choice

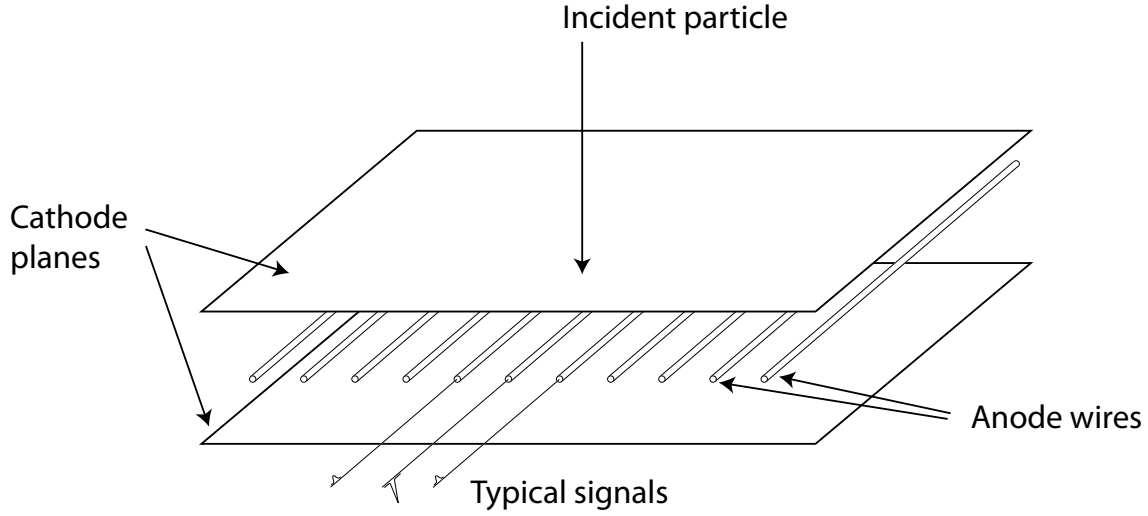


Figure 5.2: Basic configuration of a multiwire proportional chamber [Leo87].

of gas, and the chamber geometry. This factor can be as high as 10^6 [Leo87]. If the chamber is used in proportional mode, the pulse height is a measure of the energy loss of the particle in the gas. Multiple measurements of the energy deposit along the trajectory combined with the measurement of momentum in a magnetic field allow for excellent particle identification.

A basic MWPC consists of a plane of equally-spaced anode wires centered between two cathode planes (see Fig. 5.2). In principle, each wire acts as an independent proportional counter. If a negative potential is applied to the cathode planes, the anodes being grounded, an electric field arises. In the region far away from the anode wires (~ 20 times the wire-diameter), the field lines are essentially parallel and the field density is almost constant. Close to the anode wires, the field shows an $1/r$ dependence similar to a single wire cylindrical proportional chamber (see Fig. 5.3): The wire radii, typically $10 - 30 \mu\text{m}$, are much smaller than the distance between the wires. Typically, a few millimeters distance are chosen between the wire and the cathode. This fact causes the electric field radial to the wire as seen in Fig. 5.3. If the wires are assumed to be infinitely long, the electric field at a distance r close to the wire is given by:

$$\mathbf{E}(r) = \frac{q}{2\pi\epsilon_0 r} \hat{\mathbf{r}}. \quad (5.2)$$

Far away from the anode wires, when electrons and ions are liberated in the constant field region, they drift along the field lines toward the nearest anode wire and opposing cathode, respectively. Upon reaching the high field region, the electrons are quickly accelerated to produce an avalanche. The electron avalanche is rapidly (in a few ns) collected

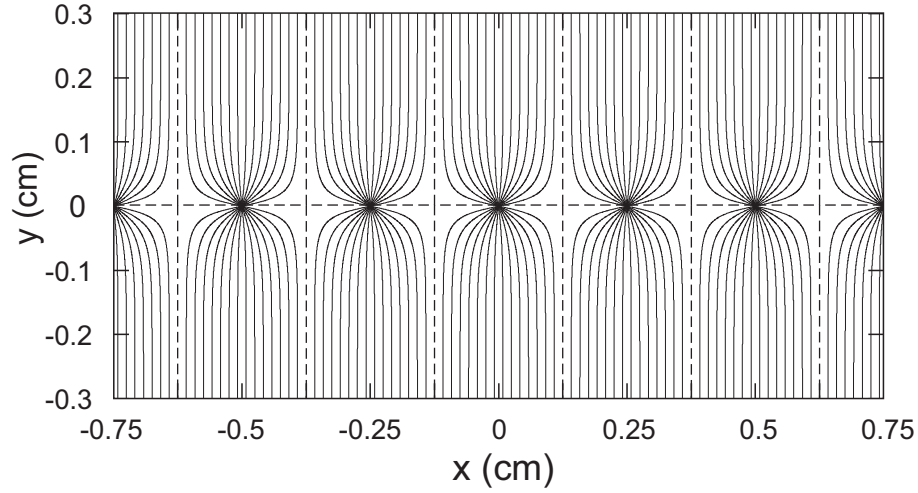


Figure 5.3: Schematic view of the electric field in an MWPC.

by the wires, the positive ions left over in the trail of multiplying electrons move in opposite direction toward the cathode. In their motion, they induce image charges in all surrounding electrodes and these result in a negative signal on the wire where the avalanche originated (as drawn in Fig. 5.2). The neighboring wires are also affected, however, the signals induced here are opposite (i.e. positive) and of small amplitude. In a similar manner, a positive signal is induced on the cathode. Thus, there is no ambiguity which wire is closest to the ionizing event. The signal from one anode plane does only give information on one coordinate of the ionizing event. The second coordinate can be obtained by using a second detector whose anode wires are oriented perpendicularly to the first. To measure the trajectory of a particle, two or more aligned MWPCs can be used to reconstruct the track.

5.2.1 Signals Induced on Cathode Pads

Besides the circuit described above, another possibility is to ground the cathode planes and to apply a positive voltage on the wires, respectively. Then, the cathode signal is read out, and the coordinate of the induced charge can be obtained by a subdivision of the cathode into readout pads perpendicular to the anode wires as indicated in Fig. 5.4. The avalanche can be localized in the direction parallel to the sense wire as seen in the typical induced signals also drawn in Fig. 5.4.

If the wires are enclosed between two cathode planes, the sum of all chamber signals is zero at any time and the cathode signal $I_c(t)$ is equal to the negative summed wire

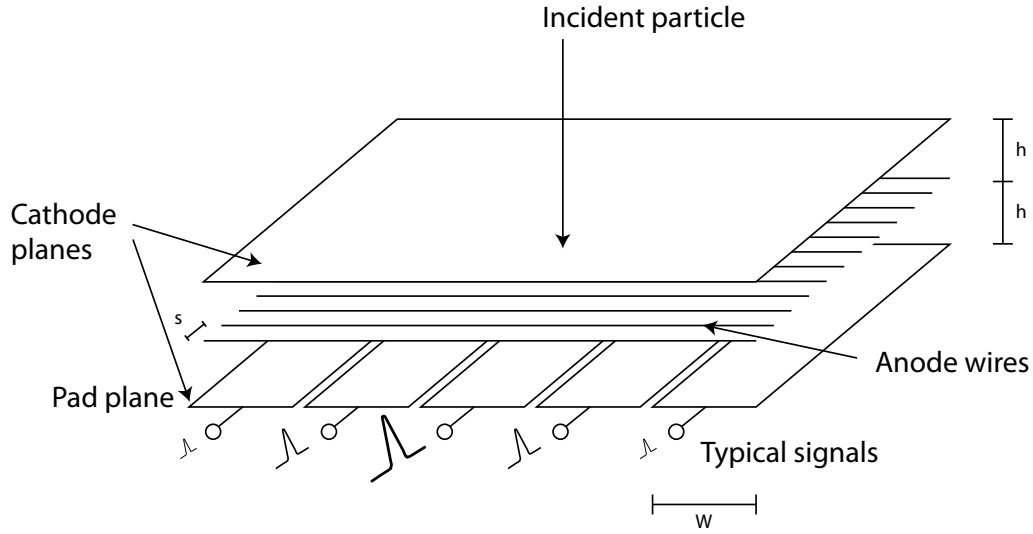


Figure 5.4: Basic configuration of a multiwire proportional chamber with segmenting the cathode into pads [Gat79].

signal $-I_w(t)$. In the example shown in Fig. 5.4, the cathodes are symmetrically placed with respect to the wire plane, so the signal I_{c1} on a single cathode plane (e.g. the pad plane) in the coaxial approximation is [Blu08]:

$$I_{c1}(t) = \frac{1}{2}I_c(t) = -\frac{1}{2}I_w(t) = \frac{1}{2} \frac{N_{tot}e_0}{4\pi\epsilon_0} \frac{C_{wg}}{t + t_0}. \quad (5.3)$$

This is the current induced by N_{tot} ions of charge e_0 , and C_{wg} is the wire capacitance with respect to ground. If the charge is induced on a cluster of adjacent pads, the accuracy of the cluster localization in an MWPC is determined by the anode-wire spacing. However, there is a limit of about 2 mm minimum spacing, since smaller spacings are increasingly difficult to operate [Sau77].

In order to achieve the best possible position resolution in azimuthal direction, the induced charge distribution should be shared between typically two or three adjacent pads. If more than three pads give a signal, the resolution suffers from a poorer signal-to noise ratio, and this leads to an overall increase of the data volume and a limitation of the two-track separation as well as a loss in the electron/pion discrimination. In the case of a one-pad cluster (when the cluster is recognized by only one pad), the position can be reconstructed only with the resolution of $1/\sqrt{12}$ times the pad width. That is why a one-pad cluster is to be avoided. Therefore, a proper matching of the pad width W to the width of the induced charge distribution is required.

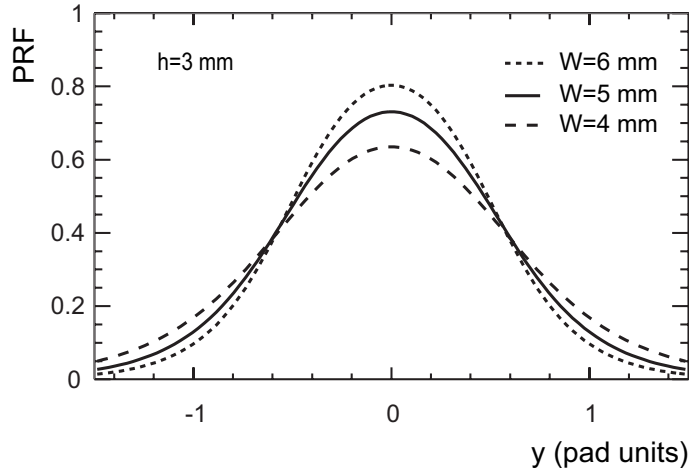


Figure 5.5: Pad response functions for a distance of $h = 3$ mm, $s = 2.5$ mm, an anode radius of $25 \mu\text{m}$, and different pad widths calculated according to Reference [Mat88].

An important characteristic of the MWPC is the pad response function (PRF), which determines the fraction of the total cathode signal that is induced on the pad as function of the distance between the center of the pad and the avalanche position (measured in the cathode plane). It can be calculated by integrating the induced charge distribution over the pad width in y -direction:

$$\text{PRF}(y) = \int_{y-W/2}^{y+W/2} \rho(y') dy'. \quad (5.4)$$

The induced charge distribution $\rho(y')$ depends on the wire geometry and can be calculated following Reference [Mat88]. The essential quantity, affecting the shape of the PRF, is the ratio of the pad width W to the anode-cathode distance h . In Fig. 5.5, the calculated PRFs are shown for three different pad widths ($W = 4, 5$, and 6 mm) and for a distance of $h = 3$ mm between the pad plane and the anode wire plane. As W decreases, the PRF amplitude becomes smaller, and the fraction of the induced charge signal on the center pad decreases. The pad width W and the anode-cathode distance h determine the typical pulse height induced on two or three adjacent pads. Together with the readout electronics, all parameters have to be adjusted in a way that this pulse height falls into the dynamic range of the readout electronics. The resolution for position determination along the wire is limited by the pulse-height measurement. A pad width close to the anode-cathode distance ($W \approx h$) yields the best position resolution [Gat79].

5.2.2 Gas Mixture

Due to the large mobility of electrons and ions, gas is the obvious medium to use for the collection of ionization. The filling gas for proportional counters has to meet different requirements: low working voltage, high gain, proportional behavior, and – in particular for the CBM TRD – high rate capability. For meeting all conditions at the same time, in general, gas mixtures are rather used than pure gases. For a minimum working voltage, noble gases are usually chosen due to the lowest electric field intensities necessary for avalanche formation. In contrast to molecules they do not have vibrational and rotational states which can be excited and thus the ionization dominates.

Using a pure noble gas, the chamber cannot be operated with a very high gas gain without continuous discharge occurring. Excited noble gas atoms formed in the avalanche deexcite giving rise to high-energy photons capable of ionizing the cathode and causing further avalanches. This problem can be minimized by the addition of a *quencher* e.g. a polyatomic gas, such as methane or alcohol, or an inorganic gas, such as CO₂. The quencher molecules absorb the radiated photons and dissipate this energy through dissociation or elastic collisions. With a small amount of polyatomic gas one can safely obtain gains of up to 10⁶.

The cheapest applicable noble gas is Ar because it is the largest noble gas contribution to the atmosphere. Nevertheless, the gas mixture in the TRD should be based on Xe because of its higher atomic number ($Z = 54$ in comparison to $Z = 18$ for Ar). The yield of ionization encounters for a MIP (minimum ionizing particle) traversing a gas layer is 25/cm for Ar and 46/cm for Xe. Thus, the thickness of the gas layer for 99% efficiency amounts to 18 mm for Ar and 10 mm for Xe. The number of released electrons produced by a MIP averages 103 for Ar and 340 for Xe [Yao06]. The absorption coefficient for X-rays in the relevant energy region of the TRD is only large enough when using Xe. In particular, for thin gas volumes like in the MB-TRD prototype, the absorption of TR produced in the radiator has to be maximized. In the MB-TRD prototype, the gas mixture used is 85% Xe and 15% CO₂.

5.2.3 Signal Generation

The moving charges between the electrodes of a chamber give rise to electric signals that can be picked up by amplifiers connected to the electrodes. Every avalanche creates a signal in the wire and in the cathodes. For the purpose of position measurement, the cathode is subdivided into several pads. In principle, apart from cross-talk effects, the signals in each pad of the cathode plane have the same time dependence that only depends

on the distance to the avalanche. For the purpose of localizing the avalanche the cathode pads have independent signal readouts. The total energy deposit can be determined by integrating the signals on adjacent readout pads belonging to the same cluster. The signals are amplified by a charge sensitive amplifier and are pulse-analyzed by ADCs. In this way, the energy deposited by the ionizing particle and by the transition radiation is measured. Since the energy released by a particle radiating TR (with large γ , e.g. an electron) is on average larger than the energy released by a particle that does not radiate TR (e.g. a pion), the discrimination can be based on an energy cut (the discrimination method is described in detail in Chapter 6.4). The main factor limiting the rejection of particles that do not radiate (small γ) is the Landau tail of ionization loss, which can mimic a large energy deposition comparable to that of a particle which radiates.

The spatial resolution of an MWPC depends on many details like the anode-wire spacing, anode-cathode gap, and the readout-pad layout (see the detailed description in Chapter 5.3). An additional capability of the MWPC is the multiple-track resolution. Since each wire is a separate detector, two or more tracks can in principle be detected at the same time. However, this depends on their relative separation which must be at least as large as the wire spacing. Even at higher spacings, ambiguities in the reconstruction of the tracks may arise because of their proximity.

5.3 Design of the MB-TRD Prototype

The physics requirements of the CBM TRD, as described in Chapter 4, impose different design considerations. The desired pion rejection is mostly driven by the measurement of rare probes like low-mass vector mesons or charmed hadrons. As outlined in Reference [And06a], for efficient electron identification a factor of 100 in pion rejection for electron transverse momenta above 1.5 GeV/c has to be achieved by the TRD.

The tracking performance of the TRD is important in two aspects: (i) matching of the identified electrons to the track segment in the STS (silicon tracking system), where the momentum measurement is performed; (ii) matching of the hits in the TOF (time of flight) detector to the STS track segment in order to identify hadrons up to several GeV/c. Hence, for the TRD, a good position resolution in both directions perpendicular to the beam axis is needed. In order to extrapolate the STS tracks through the TRD stations and to match them to hits in the TOF detector, for the TRD the required position resolution is of the order of 300 – 500 μm in one direction in the plane defined by the readout pads [CBM09a]. In the other direction of this plane, a value of 3 – 30 mm suffices if every second layer is rotated by 90°. The designated position resolution of the TRD, which is

e.g. influenced by the cathode pads in the readout chambers, is driven by the required capability to identify and track electrons efficiently. Certainly, the electron identification achieved in conjunction with all detectors directly depends on the global tracking. The granularity of the TRD is determined by the maximum occupancy, which gives the readout cell size. Furthermore, the number of feasible readout channels is limited. Cell size and geometry have to be optimized as a function of these criteria.

The radiation thickness of the TRD has to be kept to a minimum. Any unnecessary material causes additional background, basically because of photon conversion, and increases the pixel occupancy due to additional tracks. Furthermore, electron loss due to bremsstrahlung removes electrons from the sample leading to a loss of efficiency. In order to limit small-angle scattering and conversions the envisaged material budget is $X/X_0 \approx 15 - 20\%$ [And06a].

The most important and challenging aspect of the TRD design is that all tasks have to be fulfilled in the context of high interaction rates up to 10^7 Hz and high particle multiplicities in CBM. The multiplicity of charged particles is up to 600 per event within the detector acceptance [CBM09a]. These conditions lead to counting rates of up to 100 kHz/cm^2 in the central part of the TRD.

Simple multiwire proportional chambers (MWPC) based TRDs are good candidates for high-granularity fast detectors, if the gas thickness is reduced in order to reach the required speed and to reduce space-charge effects in a high counting-rate environment. Space-charge effects are caused by the positive ions. During their drift they reduce the electric field and thus the gas gain, particularly at high counting rates. However, reducing the detector volume causes a smaller absorption probability for the transition radiation in a single layer of the detector. In order to circumvent this aspect, while keeping the number of readout channels, TRD prototypes based on a symmetric arrangement of two MWPCs with a double-sided central pad readout electrode were designed in collaboration with the group of Prof. M. Petrovici in Bucharest. This is illustrated in Fig. 5.6, where a conceptual drawing of the prototype is presented.

The detector is composed of two anode and two cathode frames, which are made of a 3 mm printed circuit board (PCB) each. The two anode planes, placed at either side of the central pad readout electrode (pad plane), are made of gold plated tungsten wires with a diameter of $20 \mu\text{m}$ and a wire pitch of $s = 2.5 \text{ mm}$. The anode-cathode gap h is 3 mm; it has been optimized to provide appropriate charge sharing between adjacent pads (see Chapter 5.2.1). The inner pad plane is described in detail in Chapter 5.3.2. The entrance windows of $25 \mu\text{m}$ aluminized polyimide foil serve simultaneously as gas barrier and cathodes. All engineering detail drawings can be found in App. B.

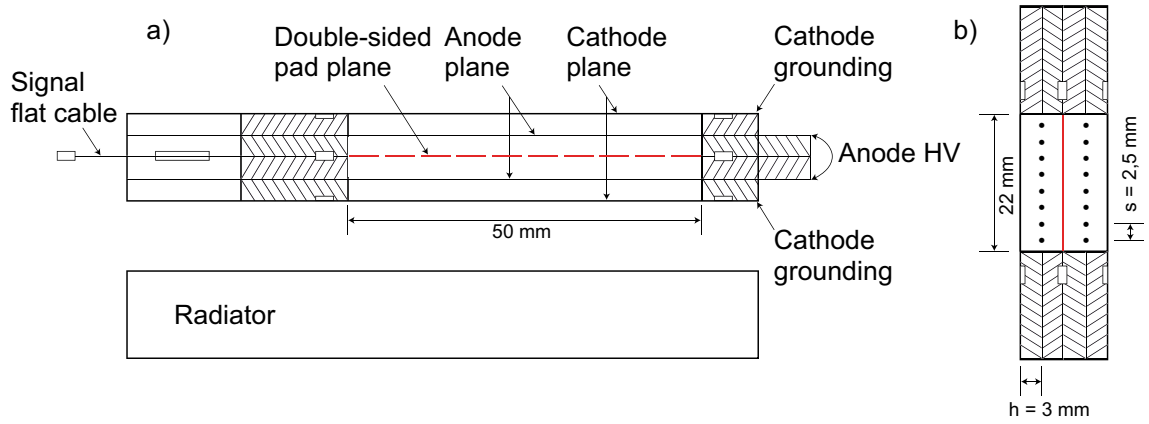


Figure 5.6: Schematic configuration of the so-called MB-TRD prototype: a) projection on a plane perpendicular to the detector surface and parallel to the wire direction and b) projection on a plane perpendicular to the detector surface and anode wire plane.

5.3.1 Absorption Efficiency of TR in the Gas Volume

The first generation of CBM TRD prototypes, tested in 2004, had a very thin (6 mm), single gas volume to reach the required speed and to minimize space-charge effects [CBM05]. In the new generation of prototypes (MB-TRD), which are investigated in this thesis, the gas volume is twice as thick (12 mm) and has the same anode-cathode gap of 3 mm.

In Fig. 5.7, the influence of the new geometry on the transmission probability for TR photons is displayed. In the radiator transition radiation is produced with an average energy depending on the radiator type and on the electron momentum [And06b]. For the following comparison an average TR photon energy of 10 keV is assumed. The absorption probability for photons with 10 keV in a Xe(85%)CO₂(15%) gas mixture of 6 mm length is 39% [Hen93] (Fig 5.7 a)). In a gas mixture of 12 mm length it is 63% [Hen93] (Fig 5.7 b)). In addition, the pad plane in the center of the 12 mm gas volume, which is described in Chapter 5.3.2, has to be considered. In this pad plane, about 15% of the TR is lost, as obtained in a measurement of the absorption in the central part of the pad plane described in Chapter 6.1. The pad plane consists of a Kapton foil with double-sided pad structures made of copper. The theoretical absorption in a layer of 25 μm Kapton (polyimide) and $2 \times 0.3 \mu\text{m}$ copper is 11.5% [Hen93]. The difference between the measured and the theoretical absorption values is due to the Gaussian shape of the copper coating profile. An absorption of 15% corresponds to a Kapton foil with a double-sided copper layer of 0.45 μm which is a reasonable thickness in the central part of the pad plane. In

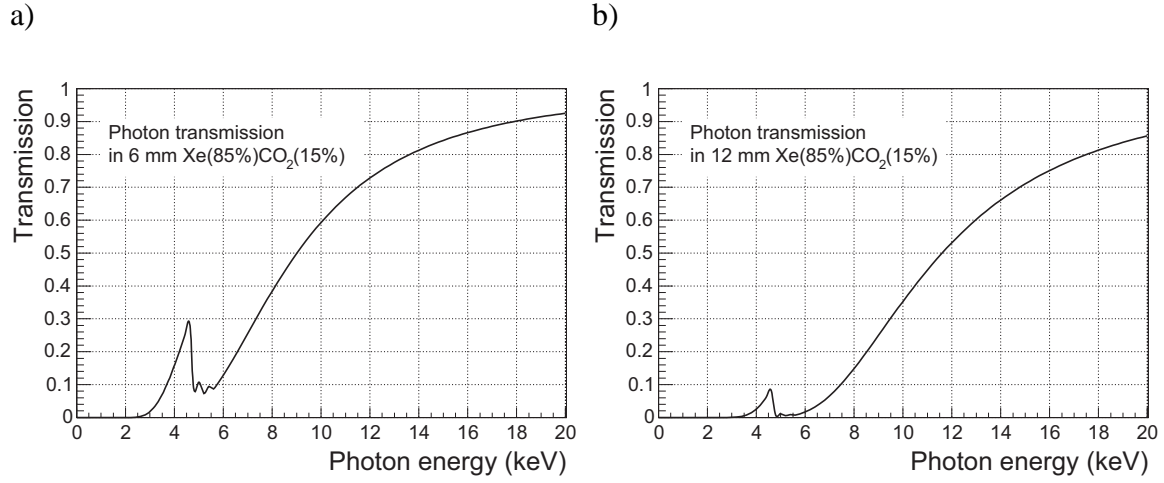


Figure 5.7: Transmission of photons in different gas volumes [Hen93]: a) in 6 mm Xe(85%)CO₂(15%) and b) in 12 mm Xe(85%)CO₂(15%).

the following, the absorption of 15% shall be considered in order to set an upper limit of the absorption in the pad plane.

In total, one obtains an absorption probability for TR photons (of 10 keV) in the detector gas of

- 39% in 6 mm Xe(85%)CO₂(15%),
- 63% in 12 mm Xe(85%)CO₂(15%),
- and $39\% + 61\% \cdot 85\% \cdot 39\% = 59\%$ in the MB-TRD prototype (12 mm Xe(85%)CO₂(15%) + central pad plane).

The value for the total TR absorption probability in the MB-TRD prototype is composed of the total absorption in the two gas volumes each of 6 mm thickness. In the first gas volume a fraction of 39% of the TR is absorbed. By reason of the TR loss in the pad plane, only 85% of the 61%, which remain behind the first gas volume, reach the second gas volume. Subsequently, 39% of the entering TR ($61\% \cdot 85\%$) is absorbed in the second gas volume having also a thickness of 6 mm. Thus, the new geometry increases the absorption probability for TR from 39% to 59% in comparison to the previous TRD design with a single gas volume.

The tail of the Landau distribution of the deposited energy by electrons and pions does not allow to reach sufficient rejection power with a single TRD layer. Furthermore,

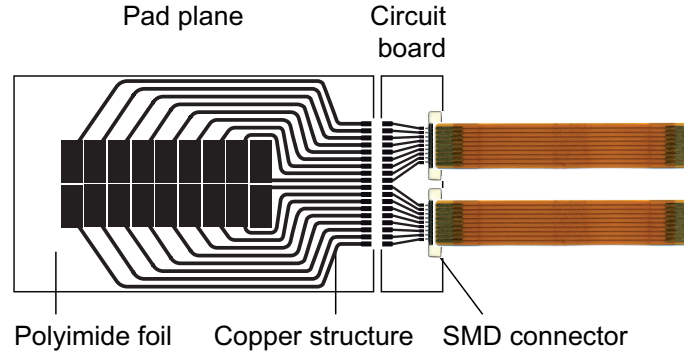


Figure 5.8: Layout of the double-sided pad plane consisting of a 25 μm Kapton foil and a copper pad structure.

the absorption probability will not reach 100% in a single TRD layer designed for these high beam intensities. Hence, it is envisaged that the TRD within the CBM experiment will be organized in a larger number of layers in order to reach the required electron/pion separation. The layers are separated into three stations placed at 4, 6, and 8 meters from the target, where each station is envisaged to contain three or four separate layers, altogether 9 or 12. The final number of TRD layers depends on the beam-test results, which are shown in Chapter 6.

5.3.2 Double-sided Pad Readout Electrode

A maximization of the absorption of the TR in one single gas layer with the described architecture can only be reached by using a readout electrode (pad plane) with low X-ray absorption between two detector sections. At the same time, small and accurate pad sizes are needed for the tracking of charged particles with a good position resolution. The central double-sided pad plane separates the detector into two identical sections, each of them forming entire MWPCs. The pad plane is made of a 25 μm Kapton foil, on both sides coated with a low absorption copper pad structure (see the drawing in Fig. 5.8). The active detection part has two rows, each with 9 pads of the size of $5 \times 10 \text{ mm}^2$. The corresponding pads on both surfaces are connected on the edge of a circuit board to which also two flat ribbon cables for the signal transfer are fixed.

For the construction of the pad plane several options were considered and tested, which are partly presented in the following. The final construction was done by vacuum copper evaporation and subsequent etching of the metalized foil. The photo-lithographic

Photo-lithographic pad plane production

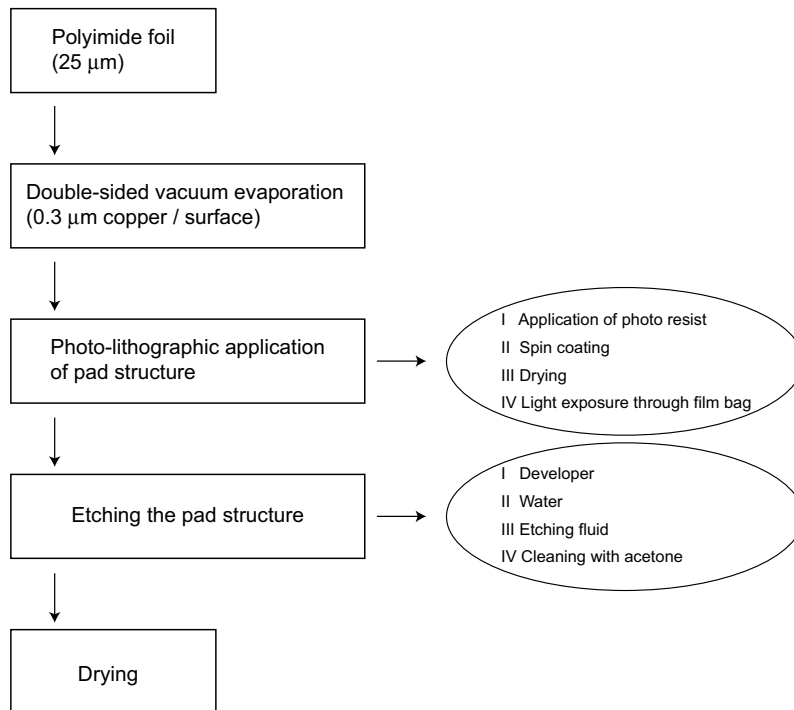


Figure 5.9: Flow chart of the production process of the double-sided pad plane.

method of production turned out to be the most accurate and the single steps of pad plane production are summarized in Fig. 5.9.

In order to get a stable, very thin, and accurate conductor structure with a strong adherence to the Kapton foil the best solution for metalization is vacuum evaporation. Copper was chosen as conducting metal since it offers a good compromise between conductivity, solder-ability and low X-ray absorption. Due to a new prototype design without solder contacts, for the next generation of prototypes an aluminum pad structure, providing even better transmission, can be realized (see Chapter 6.6.5).

An alternative method to the photo-lithographic application of the pad structure is the evaporation through a mask, but the temporary application of the mask at a constant distance is very challenging. Some trials with a simple mask having holes with the size of the pads showed that this procedure causes inaccuracies at the pad borders and especially at the very thin data lines which is not acceptable. Gluing a flexible mask on the Kapton foil was also tested. Besides the danger of residual glue on the film the worse accuracy of fixing the mask with such small structures is a disadvantage.

Hence, both surfaces of the Kapton foil are completely vaporized with an average copper layer of $(0.23 \pm 0.05) \mu\text{m}$. The thickness of the layer has been determined by weighing a small reference foil which has been evaporated simultaneously. This reference foil was positioned next to the Kapton foil where the copper density was smaller than in the central part. Thus, the coating is slightly thinner than the average thickness of the Kapton foil (see also the results of measuring the absorption in Chapter 6.1).

In order to determine the etching possibilities in terms of conducting path thickness and distance, a film with different traces was prepared for testing the application. Based on the results of this measurement the final pad plane structure (as seen in Fig. 5.8) was developed, which is a compromise between etching possibilities and space exploitation.

The first step in the etching process is the application of a photoresist, which is a light-sensitive material. When using a positive photoresist, the portion that is exposed to light becomes soluble to a photoresist developer whereas the portion of the photoresist that is unexposed remains insoluble.

For the etching process the photoresist (Positiv 20, *Kontakt-Chemie*) is first applied to one side of the copper-covered Kapton foil, and the foil is fixed on a spin rotator to uniformly distribute the photoresist. After 15 minutes in the spin rotator the foil is dried at 70°C for 30 minutes. After drying, the other side of the foil is prepared in the same way. In order to obtain a double-sided pad plane with a perfect alignment of pad structures on both surfaces, a film bag in which the foil can be put during light exposure was built (see Fig. 5.10 a)).

The pad structure is printed on both inner sides of this film bag, and in addition the sides show negative and positive crop marks, respectively. The metalized foil is put into the film bag and has to be exposed from both sides for 5 minutes. Subsequently, the pad plane is developed in the resist developer (*Bungard*), rinsed with water, and etched in sodium per-sulfate. The developer has to be changed after a few foils. The foil has to be rapidly pulled through the warm etching fluid very fast because if staying some seconds in the bath the copper structure forms small cracks. As soon as the structure can be seen the etching process is finished and the foil can be cleaned with acetone. The photoresist has to be removed very carefully without using any cloth to avoid scratches. Finally, it is air-dried..

The corresponding pads on both surfaces have to be interconnected and two SMD-connectors have to be stably mounted for data transfer. Since the mechanical load would be too high when mounting the connectors on the foil, an additional small circuit board is needed (see Fig. 5.10 b)). The board consists of a standard circuit-board material which was etched with the same procedure as the foils. The circuit board of 1.5 mm is 60 times thicker than the Kapton foil. Therefore a small slit is milled into the side where the foil is

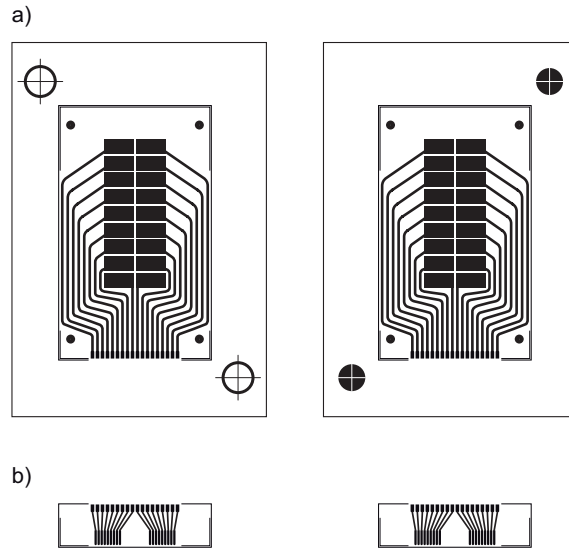


Figure 5.10: a) Both sides of the film bag for the light exposure of the Kapton foil, b) film for the light exposure of the adjacent circuit board.

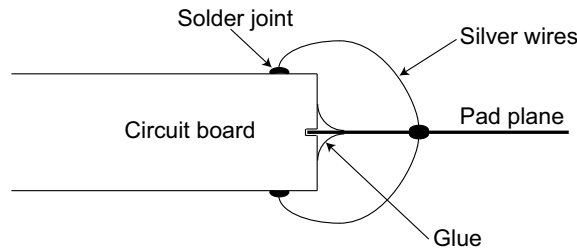


Figure 5.11: Lateral view of the pad-plane fixing to the circuit board.

to be attached. After fixing the foil, the connections can be done by using thin silver wires which are soldered to the pad plane and the circuit board (see Fig. 5.11).

Photographs of the finished pad plane and the attached circuit are shown in Fig. 5.12 and Fig. 5.13. Instead of standard vias, the connection of the corresponding pads on both surfaces is also done via silver wires at the brink of the circuit board.

5.3.3 Prototype Assembly

After production of the pad planes the prototypes were assembled. The two detector halves are glued together and hold the inner pad plane (see Fig. 5.14). The left picture presents one detector half with the fixed pad plane and the right picture presents the two

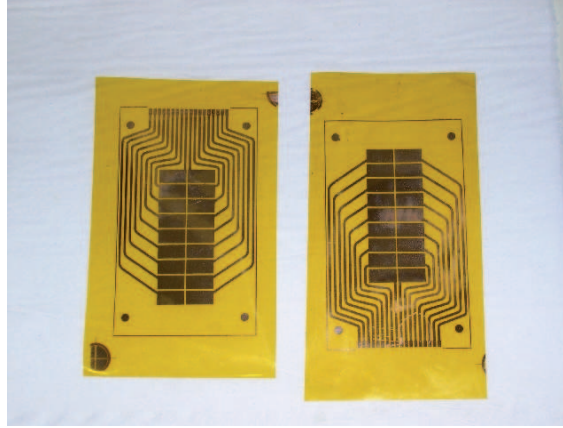


Figure 5.12: Picture of the pad plane consisting of a Kapton foil with a $0.3\ \mu\text{m}$ copper pad-structure on both sides.

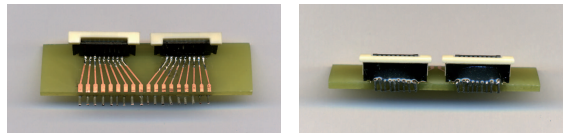
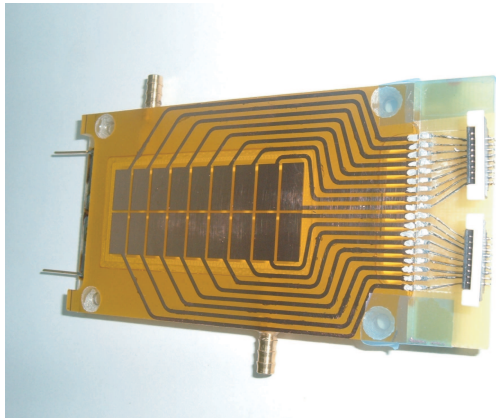


Figure 5.13: Picture of the circuit board on which the connection of the corresponding pads on both surfaces is realized. Moreover, the connectors for the flat ribbon cables are mounted here.

identical MB-TRD prototypes which were used for the in-beam test. Here, the outer gas windows and a plastic cover are removed to show the inside of the chamber structure. Fig. 5.14 also shows the gas in- and outlets for each detector half.

a)



b)

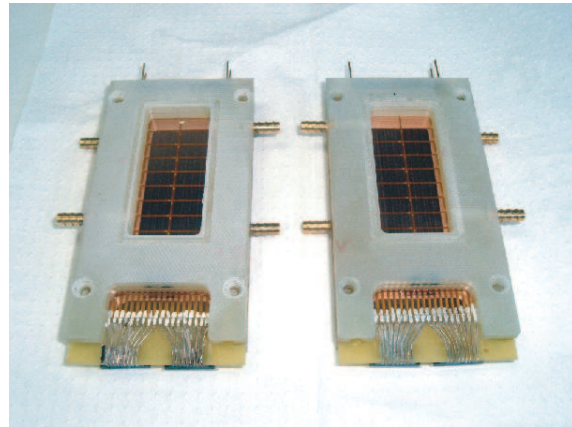


Figure 5.14: A photograph a) of the central electrode fixed to one half of the chamber and b) of the total chamber structure before mounting the gas foils (two MB-TRD prototypes).

6. Performance of the MB-TRD Prototypes

The performance of two identical MB-TRD prototypes (which are described in detail in Chapter 5.3) has been investigated using a ^{55}Fe X-ray source of 5.9 keV and mixed electron, pion, and proton beams with momenta of up to 2 GeV/ c provided by the SIS 18 accelerator at GSI.

6.1 ^{55}Fe Source Measurements

The energy resolution of different versions of the prototypes was measured using a ^{55}Fe X-ray source of 5.9 keV [Pet07]. In the following, only the two prototypes with a double-sided copper-coated Kapton pad plane are labeled MB-TRD. Besides them, two similar prototypes, which are identical chambers with different readout electrode materials, were built for comparison.

One of these chambers was built with a central readout electrode made from a printed circuit board (PCB) of 250 μm thickness, which has the same pad structure as the MB-TRD prototypes on both sides. It was made in order to test the basic functionality of such a structure with the materials available before starting to design and build the MB-TRD configuration. The other chamber contained a 3 μm aluminized Mylar foil (1.8 $\mu\text{g}/\text{cm}^2$ aluminum layer) without a pad structure as central readout electrode. This one was built in order to be able to use the configuration according to the main purpose of this design, to have a double thickness of the gas layer of a previous prototype (based on a single MWPC) for the detection of TR, preserving the rate performance. Furthermore, this kind of electrode provided a negligible absorption. The third one (MB-TRD) is analyzed in detail in this thesis and was the technically most advanced solution at that time for a readout electrode with low absorption of TR and a pad structure.

The measurements were performed at 1,700 V anode voltage using an Ar(70%)CO₂(30%) gas mixture. Custom built charge-sensitive preamplifier/shapers (gain: 2 mV/fC; noise: 1,800 electrons RMS) were used to process the detector signals which were digitized by a peak sensing ADC (ORTEC AD811). The preamplifier is the same as the one used for ALICE TRD prototype testing [Cio01]. The source was

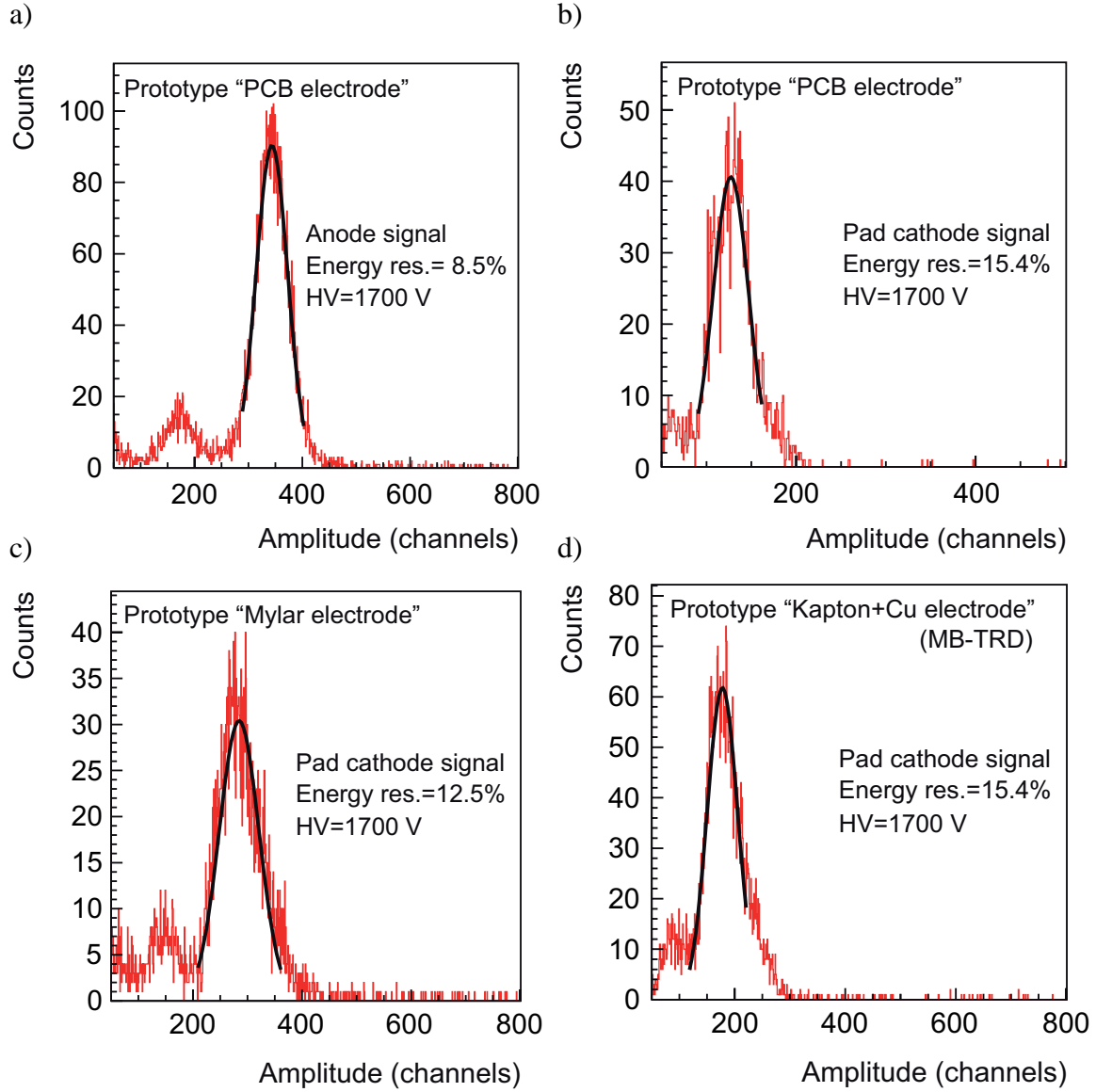


Figure 6.1: Amplitude spectra of a ^{55}Fe source for prototypes with different readout electrodes: anode signals for a) a PCB readout electrode and pad cathode signals for b) PCB, c) Mylar and d) copper-covered Kapton (MB-TRD).

collimated onto the central pad to prevent the influence of electric field distortions at the edge of the chamber.

In Fig. 6.1, the measured energy spectrum of the ^{55}Fe source is shown for the three different prototypes. The amplitude spectra for the prototype with the PCB readout elec-

trode are presented in Fig. 6.1 a) for signals taken by the anode and in Fig. 6.1 b) for signals taken from the pads. To obtain the total deposited charge, the charge sum over one pad row, as shared between the adjacent pads, is performed. Beside the main peak corresponding to the full energy deposit of 5.9 keV, an escape peak corresponding to the partial energy deposit of about 2.9 keV is visible in the amplitude spectra (e.g. in Fig. 6.1 a)). The escape peak is due to the following process: when a primary X-ray photon knocks out an electron from the K -shell of an argon atom, the hole can be filled with electrons from higher shells. The energy difference ΔE is released either by a radiation-less transition (Auger effect), or in form of another X-ray photon. If this photon leaves the detector volume, the full energy detection of the primary X-ray photon is impossible. Instead, the energy difference $E_\gamma - \Delta E$ is deposited. The K_α line of argon has an energy of 2.96 keV and K_β of 3.19 keV [Tho01]. Thus, the escape peak positions are expected at 2.94 keV and 2.71 keV with an intensity ratio of 10:1, respectively, which is in agreement to the observed escape peak position in Fig. 6.1 a).

The curves in Fig. 6.1 are obtained by fitting a Gaussian to the main peak, and the observed energy resolution of 8.5% in Fig. 6.1 a) corresponds to the anode signal. The observed energy resolution in Fig. 6.1 b) of 15.4% was obtained by using the pad information. It is worse than the measured resolution corresponding to the anode signal since only one row of pads was read out. Consequently, the part of the signal shared between the two pad rows (approximately 63%) was missed.

Fig. 6.1 c) presents the cathode signal of the prototype with the Mylar foil. The energy resolution of 12.5% is mainly due to the larger capacitance of the Mylar readout electrode. In Fig. 6.1 d), the spectrum of an MB-TRD prototype (containing the Kapton foil with copper pad structure) was measured also by taking the signals from one pad row. The energy resolution of 15.4% is equal to the one obtained for the PCB version.

The X-ray transmission for the intermediate electrode was measured by comparing the counting rate in a measurement with the standard setup to a measurement to that one obtained with the same conditions and an additional electrode positioned between the source and the prototype. The measured X-ray transmission has a value of 85%. The theoretical absorption of 5.9 keV photons in a layer of 25 μm Kapton and $2 \times 0.3 \mu\text{m}$ copper is calculated to 11.5% [Hen93]. It is a little bit smaller than the measured one because it is calculated for a homogeneous copper coating. The real copper coating has a slightly Gaussian profile due to the vacuum-evaporation method of production. Since the ^{55}Fe source was collimated onto the central part of the pad plane, where the copper coating has the largest thickness, the measured absorption of 15% can be interpreted as upper limit. The absorption efficiency for TR photons in the gas volume is calculated considering this measured absorption in the pad plane. Hence, the double-sided configuration is equivalent

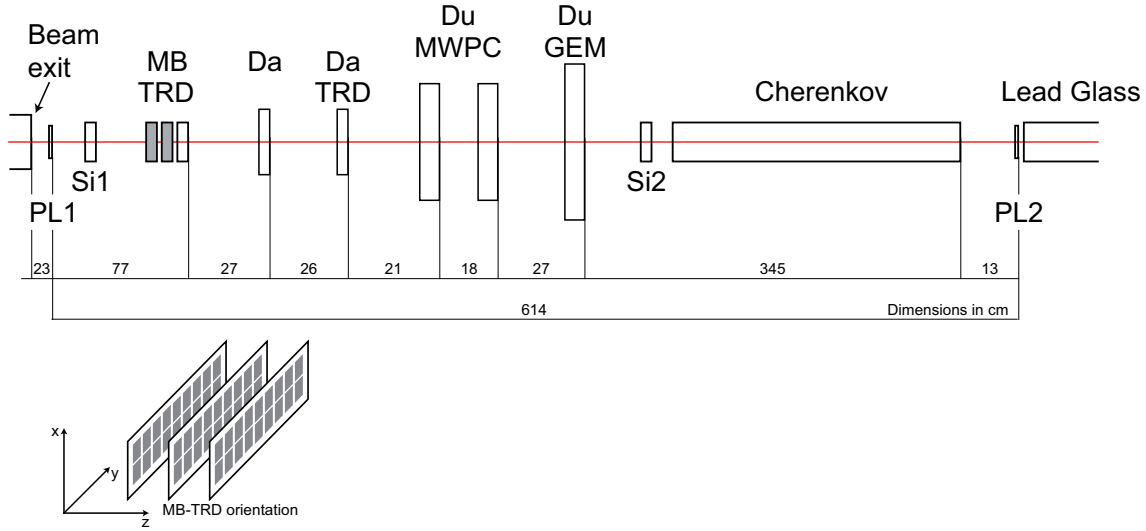


Figure 6.2: Experimental configuration used for the in-beam tests in 2006 at GSI.

to a detector of 12 mm gas thickness in which about 15% absorption in the center of the volume has to be subtracted. The total absorption efficiency for TR photons in the detection gas of the MB-TRD prototype is determined to a value of 59% which is consequently a lower limit (the detailed calculation can be found in Chapter 5.3.1).

6.2 In-Beam Test at GSI

An in-beam test of the TRD prototypes was performed in February 2006 in a joint measurement campaign of the JRA4-I3HP collaboration. The measurements were carried out at beam momenta of up to 2 GeV/c. Mixed electron-pion (negative particles) and positron-pion-proton (positive particles) beams were used, which were provided by the secondary beam facility at GSI Darmstadt. The experimental setup is shown in Fig. 6.2, and a photograph of the setup is presented in Fig. 6.3.

The detectors discussed in this thesis are the first two detectors labeled MB-TRD (gray boxes in Fig. 6.2). The third one has the same chamber structure with a PCB readout electrode. The other prototypes (Da TRD, Du MWPC, and Du GEM) are discussed in References [And07b, And07a, And07c]. Sandwich radiators made of *fiber17* sheets of about 4.0 cm thickness and *ROHACELL* foam of 2.0 cm thickness without any reinforcement (as described in detail in Chapter 5.1) were positioned in front of each MB-TRD prototype. In addition, one run was performed in which a regular foil radiator (120 foils, 20 μm thickness, 500 μm gap) was positioned in front of one chamber. The prototypes were tested

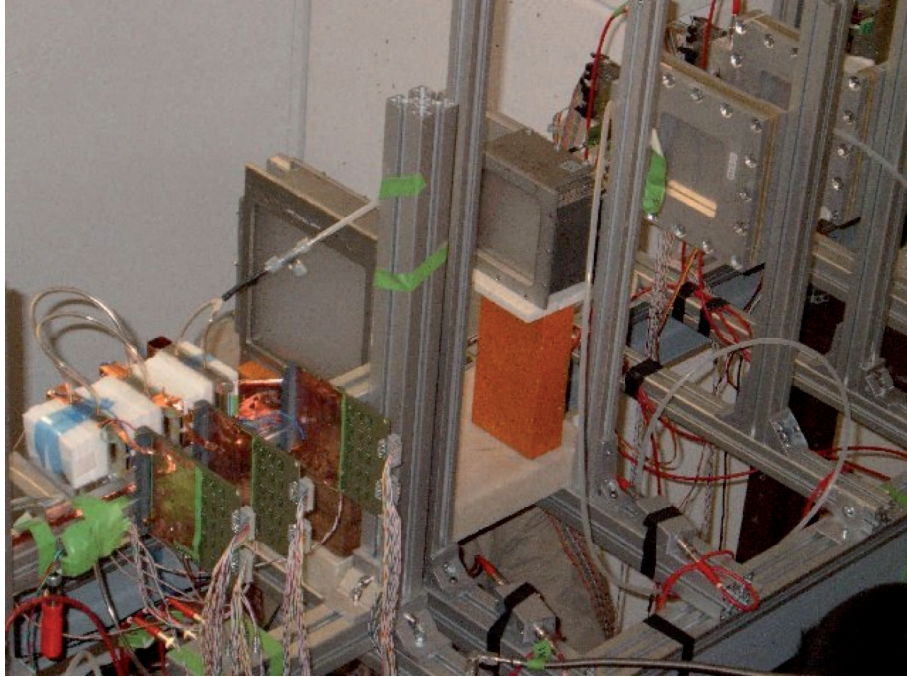


Figure 6.3: Photograph of the setup of the in-beam test in February 2006 at GSI. In the left part one can see the MB-TRD prototypes with the attached radiators.

at different gas gains and beam intensities, different Xe-based gas mixtures (with 10%, 15%, and 20% CO₂ as quencher) and momenta of up to 2 GeV/c for pions, electrons and protons. The online run summary can be found in the appendix (see Tab. A.3). The beam intensity was varied by changing the extraction time from the SIS 18 accelerator, and it was determined by two arrays, each one consisting of four plastic scintillators (PL1 and PL2). Two silicon strip detectors (Si1 and Si2) were used to monitor the beam profile as presented in Fig. 6.4. The signals for one run are separately shown for the directions x and y in Fig. 6.5. With the full width at half maximum (FWHM) of the distributions in x and y , a cross-sectional area of 4.2 cm² is determined, for which the average beam intensity will be specified.

The beam trigger was defined by the scintillator counters, to which the Pb-glass calorimeter signal was added as electron trigger. Electrons were identified with respect to hadrons using a Pb-glass calorimeter and an air-filled Cherenkov detector. The TRD signals delivered by all pads were processed using a new generation of preamplifier/shaper (PASA) front-end electronics [Sol07]. The pad signals are amplified with a 16-channel ASIC (application specific integrated circuit) preamplifier/shaper with a peaking time of

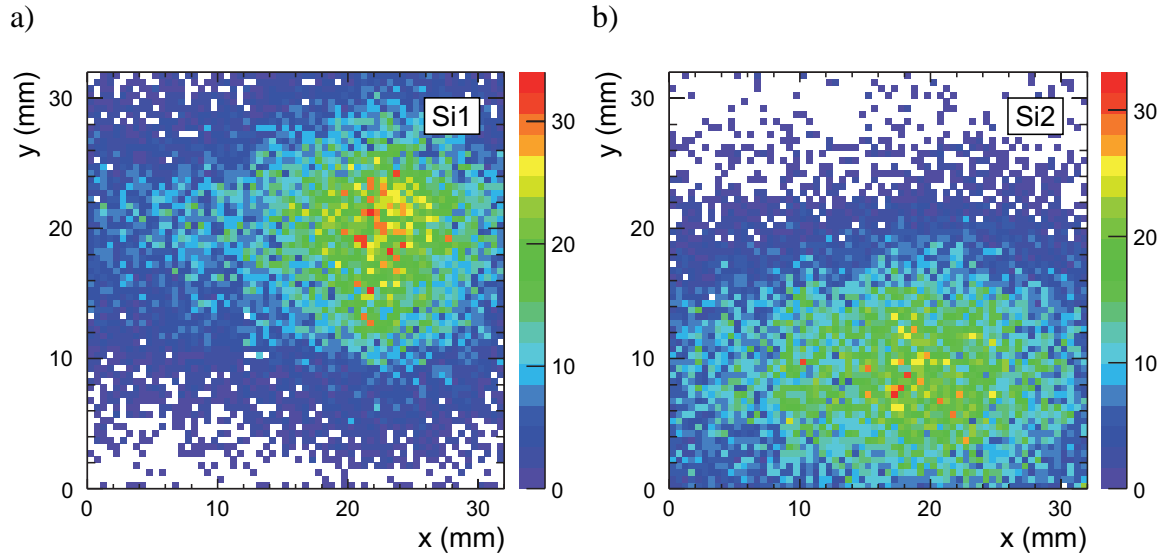


Figure 6.4: The beam profile measured with the two silicon strip detectors a) Si1 and b) Si2.

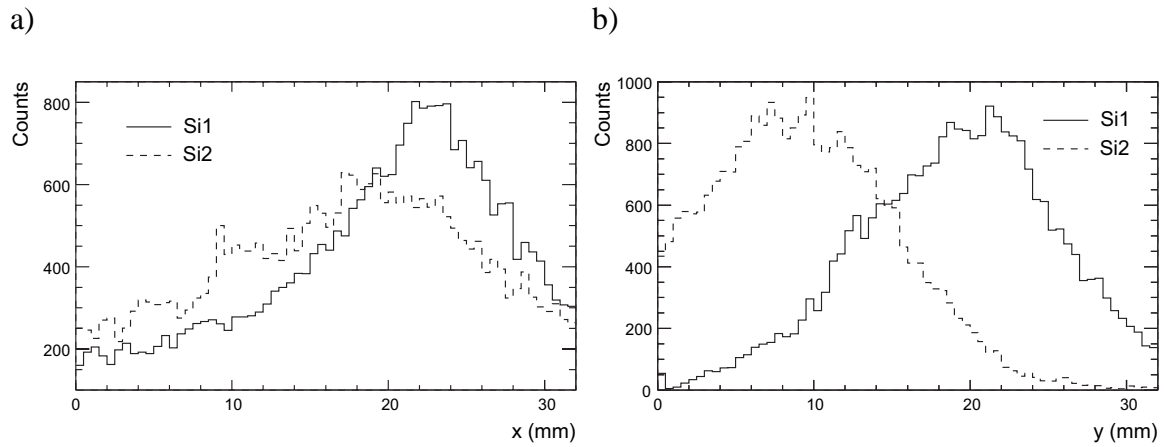


Figure 6.5: The beam profile measured with the two silicon strip detectors (Si1 and Si2) a) in x - and b) in y -direction. The displacement, in particular in y -direction, is due to the positions of the Si detectors, which were not aligned precisely to the beam direction. In this measurement, the FWHM is 2.8 cm in x and 1.5 cm in y which gives a cross-sectional area of 4.2 cm^2 , for which the average beam intensity is determined.

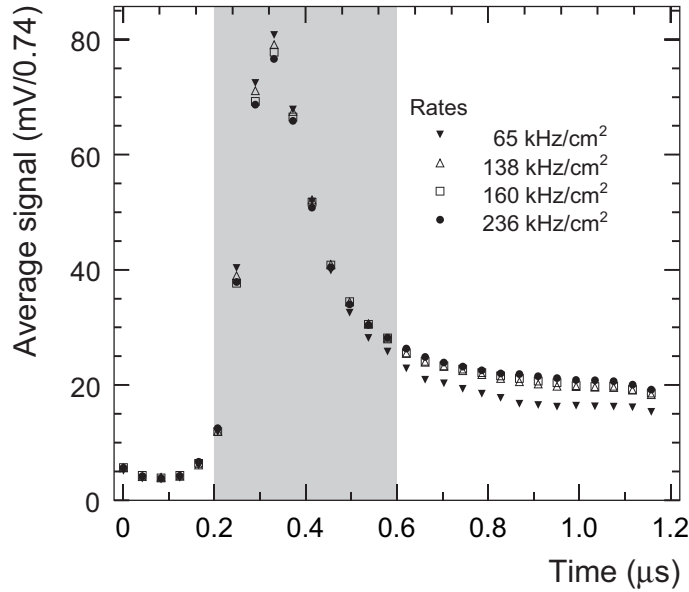


Figure 6.6: Average pulse height (charge sum over three pads) in the MB-TRD as function of time for different particle rates at $p = 1.5$ GeV/ c . The total time of $1.2 \mu\text{s}$ is sampled in 30 time bins.

about 70 ns and with the FWHM of about 70 ns. They were digitized by an 8-bit non-linear Flash ADC (FADC) system with 25 MHz sampling frequency (0.6 V swing and an adjustable baseline) in conjunction with an acquisition system which was developed for the in-beam tests of the ALICE TRD [And01].

6.3 Pulse Height Distribution

An example of the time dependence of the average signals in the MB-TRD prototypes is presented in Fig. 6.6 for particle momenta of 1.5 GeV/ c . The signals correspond to the sum of the signals from three readout pads: the pad with the maximum value and the two adjacent pads. Subsequently, the obtained values are averaged over a large number of events. Due to the slowly-moving Xe ions created in the gas avalanche the spectra have long ion tails visible at later times. The average pulse height is measured at different particle rates. The rate is determined by dividing the number of particles in a spill by the spill length and by a surface determined by using the FWHM of the beam profile. Only a slight degradation of the amplitude and extension of the ion tails is observed for very high rates of up to 240 kHz/cm^2 . For the pad-charge integration in the following analysis, the signals in the time interval $0.2 - 0.6 \mu\text{s}$ (corresponding to time bins 5 – 15 out of 30)

are used since the avalanche signal is located in this time region (see the gray band in Fig. 6.6). The integrated charge in this region shows only a weak dependence on the rate of $< 2\%$.

6.4 Electron/Pion Separation

The main task of the CBM TRD is the identification of electrons (and positrons) and the rejection of pions, respectively. As described in detail in Chapter 5, the electron identification in the TRD is based on the measurement of the energy loss by ionization plus TR for electrons and the energy loss by ionization for other charged particles like pions. In the test-beam data the electron and pion events are selected off-line by using the correlation between the signals delivered by the Cherenkov and the Pb-glass detectors as shown in Fig. 6.7 for a momentum of a) 1.5 GeV/ c and b) 1.0 GeV/ c . The readout of the Cherenkov detector is triggered by the scintillator counters and the Pb-glass detector. In the test beam electrons and pions have the same momentum but different velocities due to their different masses. At these momenta (up to 2 GeV/ c) only electrons emit Cherenkov light and thus produce larger detector signals. In the Pb-glass calorimeter electrons generate electromagnetic showers and deposit most of their energy. Since the hadronic interaction length is larger than the electromagnetic radiation length, pions deposit only a small fraction of their energy. Thus, electrons can be separated by their larger energy deposit in both detectors. As demonstrated by the lines in Fig. 6.7, defining threshold signals in both detectors, two samples of pions and electrons can be isolated. Naturally, the separation is better at 1.5 GeV/ c than at 1.0 GeV/ c .

In Fig. 6.8, the distributions of the integrated charge deposit are shown for electrons and pions with momenta of a) 1 GeV/ c and b) 1.5 GeV/ c , a gas mixture of Xe(85%)CO₂(15%), an anode voltage of 1,800 V and with the small sandwich radiators in front of the detectors. Again, the signals correspond to the sum on three adjacent readout pads. The average electron signal is larger than the pion signal because in this momentum region (of some GeV/ c) pions are minimum ionizing particles and thus they deposit less energy than electrons, which are already in the Fermi plateau (see Chapter 3.1). In addition, the pure Landau distribution of the energy loss is modified in the case of electrons: it is shifted towards higher values due to the contribution of TR produced in the radiators in front of the chambers. The integrated charge-deposit spectra show slightly higher values for electrons with momenta of 1.5 GeV/ c than for those with 1 GeV/ c since the TR yield increases with the electron momentum [And06b].

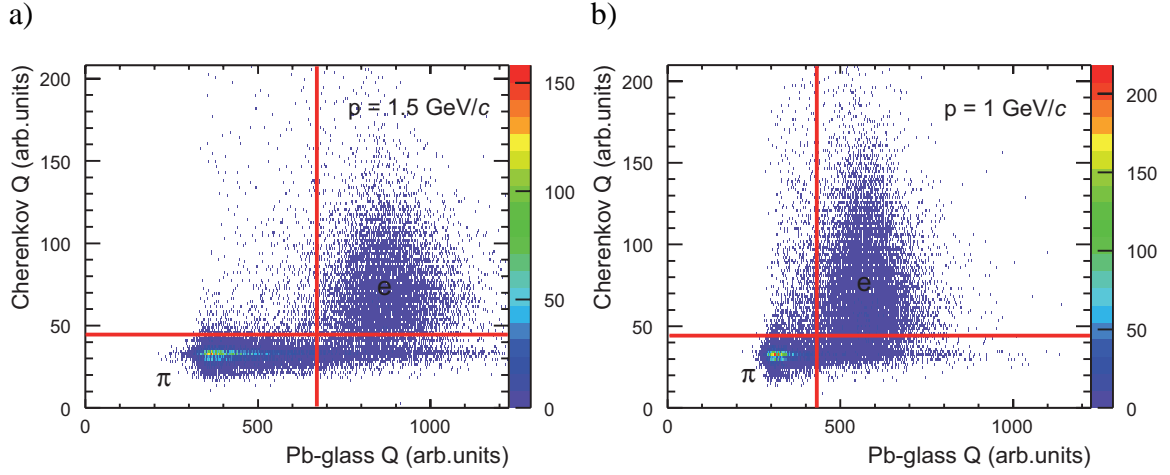


Figure 6.7: The correlation of the signals from the Cherenkov detector and the Pb-glass calorimeter. The thresholds used to identify pions and electrons are plotted for momenta of a) 1.5 GeV/c and b) 1.0 GeV/c.

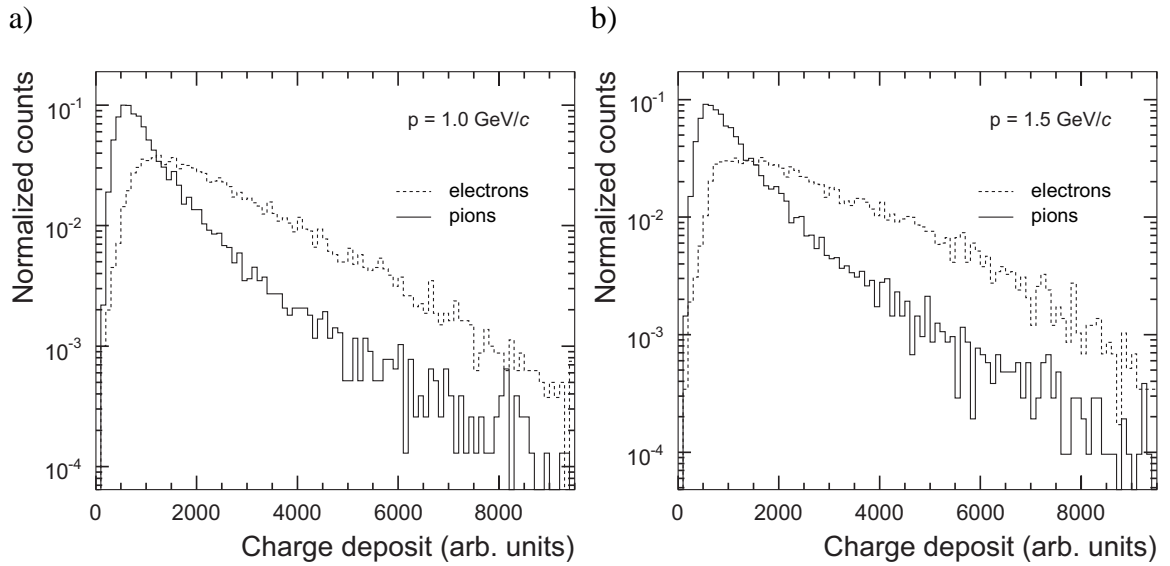


Figure 6.8: Integrated charge distributions of electrons (dashed line) and pions (solid line) for a) 1.5 GeV/c and b) 1.0 GeV/c, using a Xe(85%)CO₂(15%) gas mixture and an anode voltage of 1,800 V in the MB-TRD. The electron distributions contain the contribution of TR produced in a sandwich radiator.

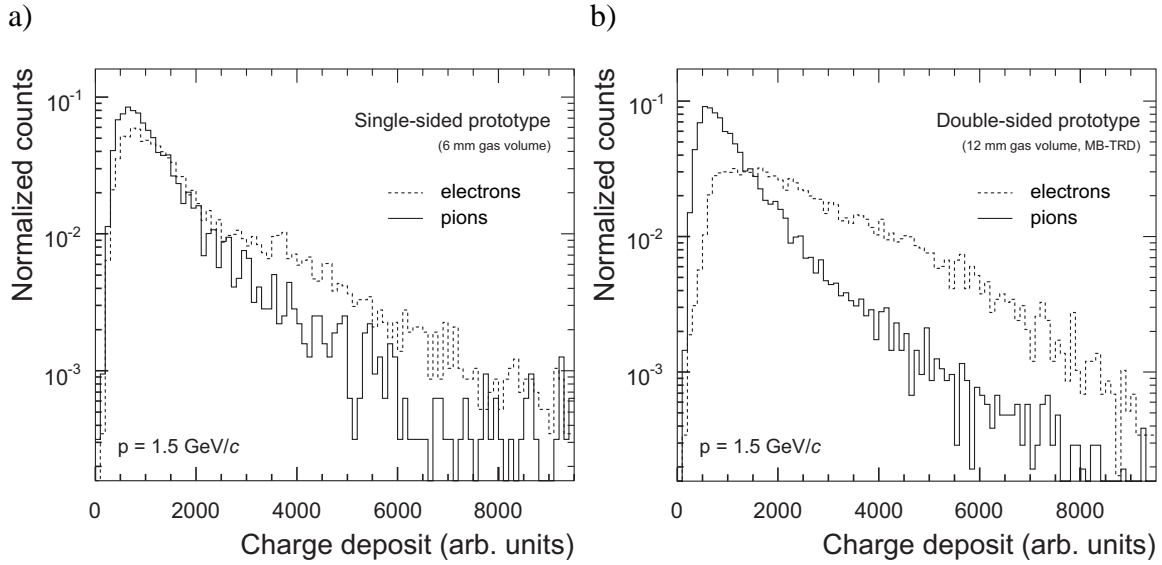


Figure 6.9: Integrated charge distributions of electrons (dashed line) and pions (full line) for a) a previous (single sided) TRD prototype and b) the new (double-sided) TRD prototype (MB-TRD). The electron distributions contain the contribution of TR produced in a sandwich radiator.

The MB-TRD provides the advantage of higher detection probability of TR photons due to the double-sided geometry. This can be seen in a comparison of the charge-deposit spectrum to the one of a previous prototype with a single gas volume, which was tested at GSI in 2004 (see Fig. 6.9). The single-sided prototype, which is shown in Fig. 6.9 a), was the first version of prototypes with only one gas volume of 6 mm thickness [CBM05], and the other spectrum is obtained with the MB-TRD (see Fig. 6.9 b)). In the previous prototype the ratio of the mean deposited charge is 1.5 times higher for electrons than for pions and thus barely higher than the expected ratio due to the higher energy loss of electrons. This means that the efficiency of detected TR is very small. In the new detector geometry the ratio of the mean charge deposits is 2.2 and the considerably higher absorption probability of TR photons in the detector gas, which increased from 39% (6 mm gas volume) to 59% (see Chapter 5.3.1), can also be seen in the different shapes of the distributions. The peak in the electron distribution due to direct ionization is washed out, and the mean value moves towards larger values because of the extra contribution of TR converted with a higher probability in the larger gas volume. The larger deposited charge by electrons in comparison to pions enables a better pion-rejection performance which is discussed in the following.

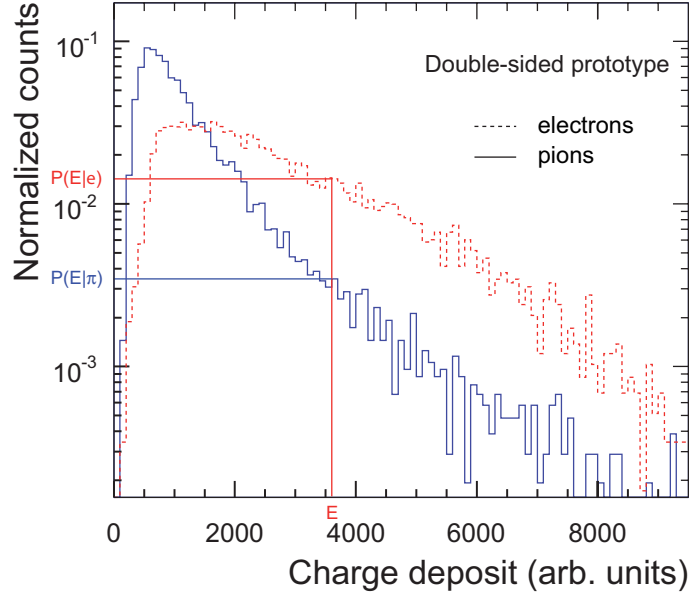


Figure 6.10: Determination of the probability to deposit an energy E for an electron ($P(E|e)$) or a pion ($P(E|\pi)$).

6.4.1 Pion Efficiency

The charge-deposit distributions of electrons and pions, as shown in Fig. 6.8, can be used as probability distributions in order to determine the pion-rejection factor for the TRD prototypes. Electrons and pions have a probability $P(E)$ to deposit an energy E in the detector. Assuming that the measurements are independent, every single chamber is simulated individually and then the pion-rejection factor can be extrapolated to n detector layers (here it is determined for $n = 9$ layers). For electrons and pions random energy deposits E_n^e and E_n^π ($n = 1, \dots, 9$) are sampled according to the measured charge-deposit spectra and then the probability that this energy is deposited by an electron or a pion can be determined (as demonstrated in Fig. 6.10).

$P^n(E_n|e)$ is the probability for an electron to produce an energy signal E_n in chamber n . The total probability for an electron to produce a tuple of energy deposits $E = \{E_1, \dots, E_n\}$ is:

$$P_e(E) = \prod_{n=1}^9 P^n(E_n|e) = \prod_{n=1}^9 P(E_n|e), \quad (6.1)$$

with $P = P^n$ because the n layers are inferred from one as they are assumed to be identical and independent. This is permitted since the geometry of all TRD layers will be identical.

The total probability for pions can be determined correspondingly:

$$P_\pi(E) = \prod_{n=1}^9 P^n(E_n|\pi) = \prod_{n=1}^9 P(E_n|\pi). \quad (6.2)$$

With the values for the total probabilities the identification probability of electrons can be calculated. Corresponding to the random numbers E_n^e for electrons the relative probability L_e (likelihood) to be an electron is:

$$L_e = \frac{P_e(E^e)}{P_e(E^e) + P_\pi(E^e)}, \text{ with } 0 \leq L_e \leq 1. \quad (6.3)$$

Using the values E_n^π the relative probability that a pion is wrongly identified as an electron is:

$$L_\pi = 1 - L_e = \frac{P_e(E^\pi)}{P_e(E^\pi) + P_\pi(E^\pi)}, \text{ with } 0 \leq L_\pi \leq 1. \quad (6.4)$$

For the determination of the pion suppression factor a large number of electron and pion events is obtained from the charge-deposit distributions, and the likelihood values are filled into a spectrum as shown in Fig. 6.11.

Two efficiencies play a role for the electron/pion separation. The electron efficiency ϵ_e gives the fraction of electrons which are identified correctly. The pion suppression is the inverse value of the pion efficiency ϵ_π , where the pion efficiency is defined as the number of misidentified pions at a given ϵ_e . Typically, an ϵ_e of 90% is used. This process is illustrated in Fig. 6.11. The likelihood distribution of electrons is integrated and the lower integration limit is chosen to include 90% of the electrons with the highest likelihood values:

$$0.9 = \frac{\int_{L_{\epsilon_e=90\%}}^1 f^e(L_e) dL_e}{\int_0^1 f^e(L_e) dL_e}, \quad (6.5)$$

where f^e is the likelihood distribution of electrons. The pion efficiency is the fraction of pions lying in the integration limits for electrons:

$$\epsilon_\pi = \frac{\int_{L_{\epsilon_e=90\%}}^1 f^\pi(L_e) dL_e}{\int_0^1 f^\pi(L_e) dL_e}. \quad (6.6)$$

As described above, in the test-beam data electrons and pions are separated using the information of the Cherenkov and the Pb-glass calorimeter. Since the electron and pion

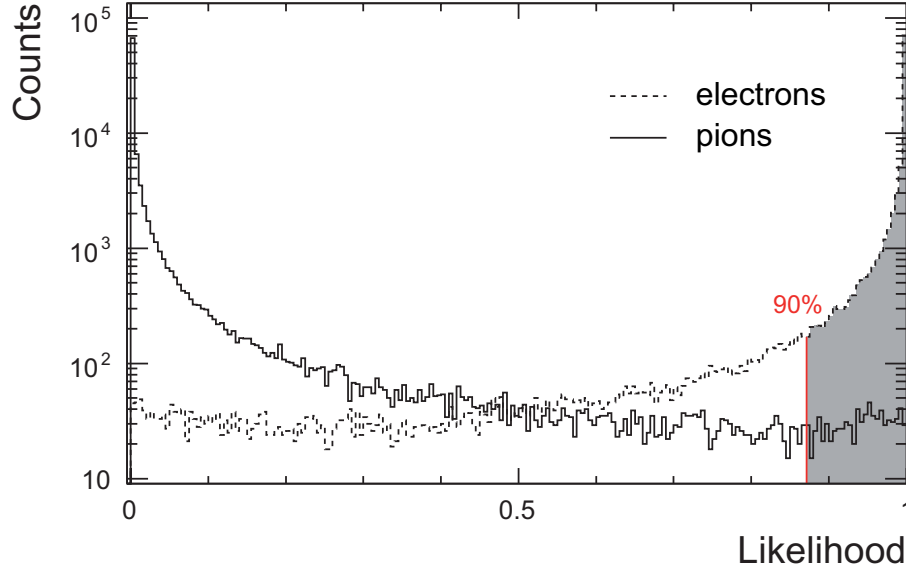


Figure 6.11: Likelihood distribution of electrons (dashed line) and pions (solid line). The electron entries are integrated from the right until 90% of all electrons are included (gray region).

signal regions in the Pb-glass calorimeter overlap it is advantageous to use two thresholds in this detector to obtain cleaner samples of both particle species. Here, for particle momenta of $1.5 \text{ GeV}/c$, the upper limit for the track to be classified as pion is a Pb-glass signal of 440 and the lower limit to be classified as electron is a Pb-glass signal of 640 (both in arbitrary units) (compare to Fig. 6.12). Tracks with signals in the gap are not taken into account for the pion-efficiency determination. After applying these thresholds, 72% of all events are used for the analysis. The elliptic average cross-sectional area of the beam can be determined by using the full width at half maximum (FWHM) of the beam in x and y as half-axes. This area has a size of 3.3 cm^2 .

In order to separate clusters from noise, different cuts are applied before calculating the pion efficiency. After baseline subtraction, the charge integral on the pad with maximum charge (pad_{max}) has to exceed a threshold of 50 (in arbitrary units) (see Fig. 6.13 a)) and the charge integral of the two adjacent pads (pad_{left} and $\text{pad}_{\text{right}}$) has to be positive (see Fig. 6.13 b) and c)). The latter cut has to be applied as the signal, which is integrated in the time bins 6 – 10 (corresponding to a time of $0.2 - 0.4 \mu\text{s}$), can also be negative after baseline subtraction. This is caused by overshoots from previous hits and happens very rarely. As expected, the spectra for pad_{left} and $\text{pad}_{\text{right}}$ are very similar. In order to illustrate the effect of noise, in Fig. 6.13 b)) the spectrum is normalized, and the pure noise signal is additionally plotted. The MPV of the signal distribution is only a little bit

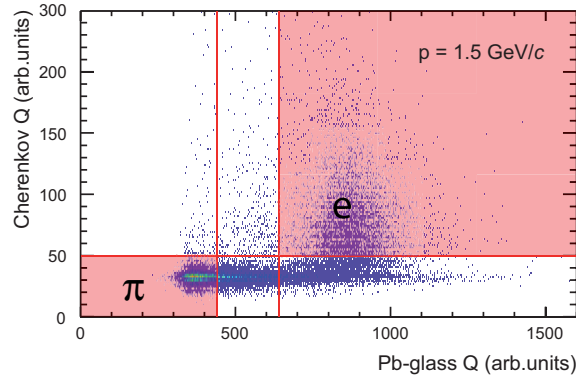


Figure 6.12: The correlation of the signals from the Cherenkov detector and the Pb-glass calorimeter. These thresholds are used to identify pions and electrons with momenta of 1.5 GeV/c.

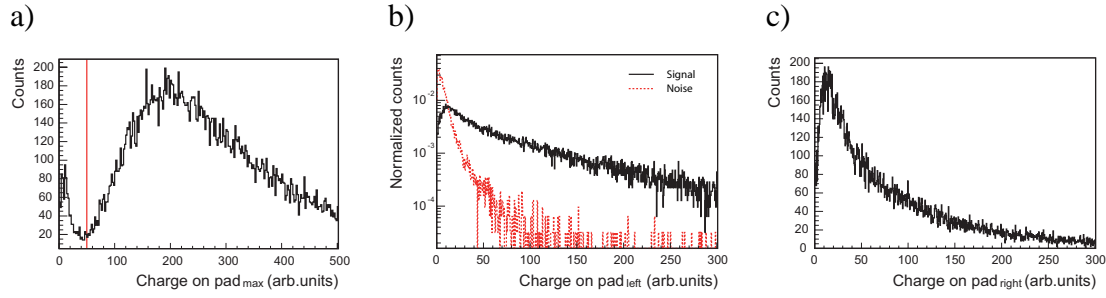


Figure 6.13: Charge distribution a) on the pad with maximum charge (pad_{max}) and the two adjacent pads b) (pad_{left}) and c) ($\text{pad}_{\text{right}}$). For pad_{left} the pure noise signal is additionally plotted. The noise is defined as the signal integrated in the time bins where no signal is expected. The number of time bins used for the integration is the same in the noise and the signal case.

higher since in every one- and two-pad cluster only noise is recorded on at least one of the neighboring pads. Since the information on an adjacent pad is missing in events with maximum induced charge on a border pad, they are also not considered in this analysis.

During the tests with the ^{55}Fe X-ray sources it was observed that the chamber, which has a small size, has a larger amplification at the edges than in the central region. Hence, a condition is put to the pulse height sharing between the pad with the maximum charge in one pad row and the corresponding pad in the second pad row. Thus, only clusters close to the center of the detector (in x -direction) are considered for the determination of the electron/pion separation.

All applied cuts and the corresponding efficiencies are listed in Tab. 6.1. In total 58% of all events are used for the determination of the pion efficiency.

Cut for the determination of the pion efficiency	Used events of all events	Used e^- of all e^-	Used π^- of all π^-	Pion efficiency for 6 layers
No cut	100%	100%	100%	9.6%
Cut 1: Minimum charge on pad_{max} , pad_{left} , and $\text{pad}_{\text{right}}$	85%	88%	84%	7.5%
Cut 1 + Cut 2: Exclusion of border pads as pad_{max}	78%	81%	76%	7.1%
Cut 1 + Cut 2 + Cut 3: Exclusion of cluster positions at the edge of the chamber (in x)	58%	59%	57%	4.9%

Table 6.1: Applied cuts for the determination of the pion efficiency, the ratio of used events, and the corresponding pion efficiencies simulated for 6 detector layers.

In Fig. 6.14, the resulting pion efficiency is shown as a function of the number of layers for measurements with different anode voltages and radiators. As described before, the pion efficiency is extrapolated with the charge-distribution measurement in one detector layer. For a 9-layer configuration the pion efficiency at 90% electron efficiency for 1.5 GeV/ c momentum is better than 1% using the sandwich radiator. For an anode voltage of 1,700 V the pion efficiency is 0.9% and for 1,800 V even 0.6%. In Fig. 6.14, a direct comparison of the results obtained with a sandwich and a regular foil radiator is also shown for an anode voltage of 1,700 V. For such a regularly spaced radiator an efficiency of 0.4% can be reached with 9 layers, the separation performance is increased by more than a factor of two.

For the electron identification in CBM, a factor of 100 in pion rejection for electron transverse momenta above 1.5 GeV/ c is the performance goal (see Chapter 5.3). The measured performance shows that this goal can be reached with the MB-TRD geometry for 9 detector layers and these results encourage the further development of this design. In the CBM experiment, the PID will certainly be decreased e.g. by the tracking efficiency, the hit-reconstruction efficiency, fake tracks, and the production of secondary particles. Hence, a full event simulation including all CBM sub-systems is necessary as described in Chapter 7.

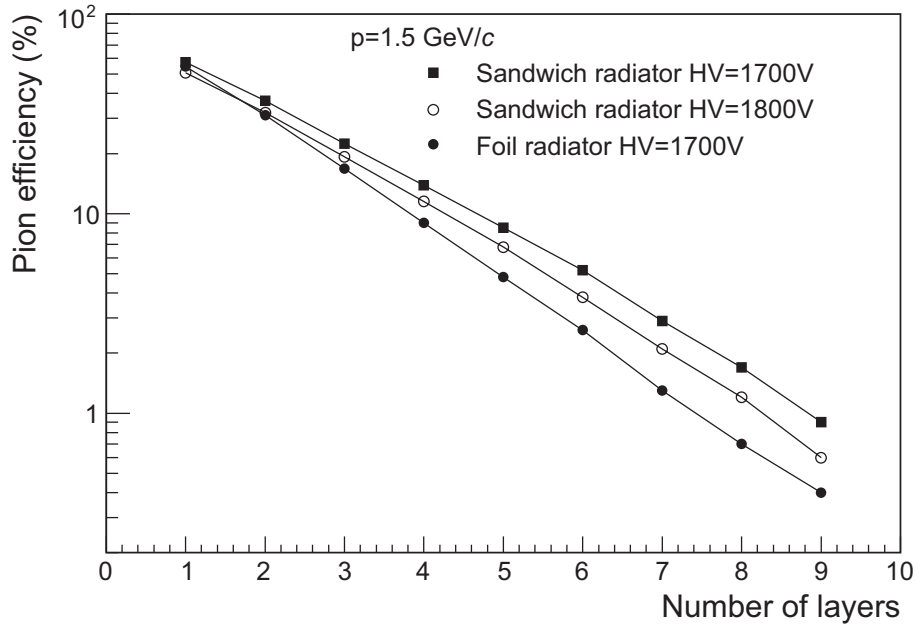


Figure 6.14: Pion efficiency at 90% electron efficiency at 1.5 GeV/c momentum as a function of the number of layers. The pion efficiency is extrapolated with the charge-distribution measurement in one detector layer.

The method used for the pion-efficiency determination is convenient to compare different chamber configurations and to obtain an estimate of the number of layers which are needed to obtain a desired pion suppression. Nevertheless, correlations between the chambers are not considered using this method. More realistic results can be obtained using a larger number of prototypes. This is planned for the next beam time with real-size prototypes of the TRD (see Chapter 6.6.5).

Correlations Between Different Detector Layers

Up to now, no correlations between different detector layers were investigated. This will be possible by a measurement with a larger number of prototypes. But first experience has been gained with the ALICE TRD. The ALICE experiment at LHC, which is planned to go on line in the end of 2009, also uses a TRD for the electron/pion separation and for the tracking of charged particles [ALI01]. It will be comprised of 540 detector modules arranged in 18 supermodules. Each supermodule will contain six layers of detectors (MWPC + radiator), subdivided into five sections. A fully integrated TRD supermodule was tested in 2007 in a mixed electron-pion beam with momenta of 1, 2, 4, and 6 GeV/c, provided by the PS accelerator at CERN. Each gas volume is filled with

Xe(85%)CO₂(15%) and has a thickness of 3.7 cm. Hence, the absorption probability for TR is about 95% in each TRD layer. In this test-beam data, weak correlations in the electron signals and thus also in the electron/pion separation in the single layers have been observed [Kli09]. It can be ascertained that higher charge deposits by electrons (and not by pions) are obtained in five of the six TRD layers, which slightly improve the electron/pion separation. This correlation is short-ranged: it has a length of 1 – 2 layers and no higher charge is observed in the first layer. This indicates that the extra deposited charge might be due to bremsstrahlung or TR photons from the previous layer. The reason for this observation is not yet fully clarified, measurements in the ALICE setup within a magnetic field can help to investigate the cause. This point has to be considered when planning the CBM TRD layout. For example, if this extra deposited charge for electrons is due to TR from a previous TRD layer, this effect could be even stronger in the CBM case since the TR and consequently the bremsstrahlung transmission probability in one layer is much larger than in the ALICE-TRD case. It has to be properly understood, and it does not necessarily imply a disadvantage. Since the CBM TRD will not be located in a magnetic field, and the TR is peaked in forward direction, this effect might improve the electron/pion separation.

6.5 Simulation of Electron/Pion Separation

In addition to the analysis of the test-beam data, the measured spectra of deposited charge have been described by a GEANT3 [Com93] simulation in order to provide a realistic input for the TRD in the simulation framework (CbmRoot) of the CBM experiment (see Chapter 7). The GEANT3 transport code describes the passage of particles through matter. It is used to propagate particles through an experimental setup, to simulate the detector response, and to represent graphically the setup and the particle trajectories.

6.5.1 Simulation of Energy Loss by Ionization and Transition Radiation

For a realistic determination of the electron-identification capabilities provided by the TRD, it is essential to correctly describe the energy loss of charged particles in the detector gas. Since transport models do not provide a reliable description of TR, it is modeled separately according to the experimental data. For the TR production and absorption a routine with foil-stack parameters as input is used. The parameters of the simulated radiator are the number and the thickness of the foils as well as the gap thickness. Since a realistic simulation of a radiator consisting of fibers and ROHACELL is impossible due

to its irregular structure, each radiator is represented by a foil stack. The set of parameters is chosen such that the measurements are best reproduced. For the ionizing energy loss, a correct description of measured data can be achieved within GEANT3 [Uhl08].

6.5.2 Implementation of the New Detector Design

In a geometry file an idealized configuration of the TRD is created which is sensitive in the entire detector plane: The TRD consists of 3 stations with 4 layers each. In front of each layer of the TRD a radiator is located. In addition, it contains an active gas volume of 12 mm with a Kapton pad plane, a Mylar foil, and a layer of gold and copper representing the electronics (see Fig. 6.15).

In this simple geometry the pad plane is located in front of the gas volume instead of a complex geometry with two gas volumes in each layer. This geometry describes the material distribution and is used to calculate the energy loss. The pad-plane position does not strongly affect the energy loss by ionization and causes a negligible error. For the TR calculation the pad plane is located at the correct position in the center of the gas volume. For an estimate of the error in the energy loss due to the position of the pad plane the energy-loss distribution with a pad plane in front of the gas volume is compared to a measurement with a pad plane behind the gas volume. The difference in the energy loss is so insignificant that no noticeable changes in the spectra have been observed.

6.5.3 Particle Simulation

The particles are simulated by using a so-called box generator. Electrons and pions are produced with fixed momenta distributed uniformly in a ϕ and $\cos(\theta)$ window, 1 cm in front of the first layer TRD. In order to simulate a single prototype the readout of the energy loss and TR is done in the first layer.

6.5.4 Comparison of Simulated and Measured Energy-Loss Spectra

The simulated energy-deposit spectra for electrons and pions have to be compared to the measured charge spectra of the MB-TRD prototypes. Since the measured charge originates from ADC signals in arbitrary units, which are proportional to the deposited energy, a scaling is necessary to calibrate the measured data. For the scaling a Landau function is fitted to the pion distributions obtained from test-beam data and from simulations. The pion distributions are used for the scaling because they do not contain a contribution from

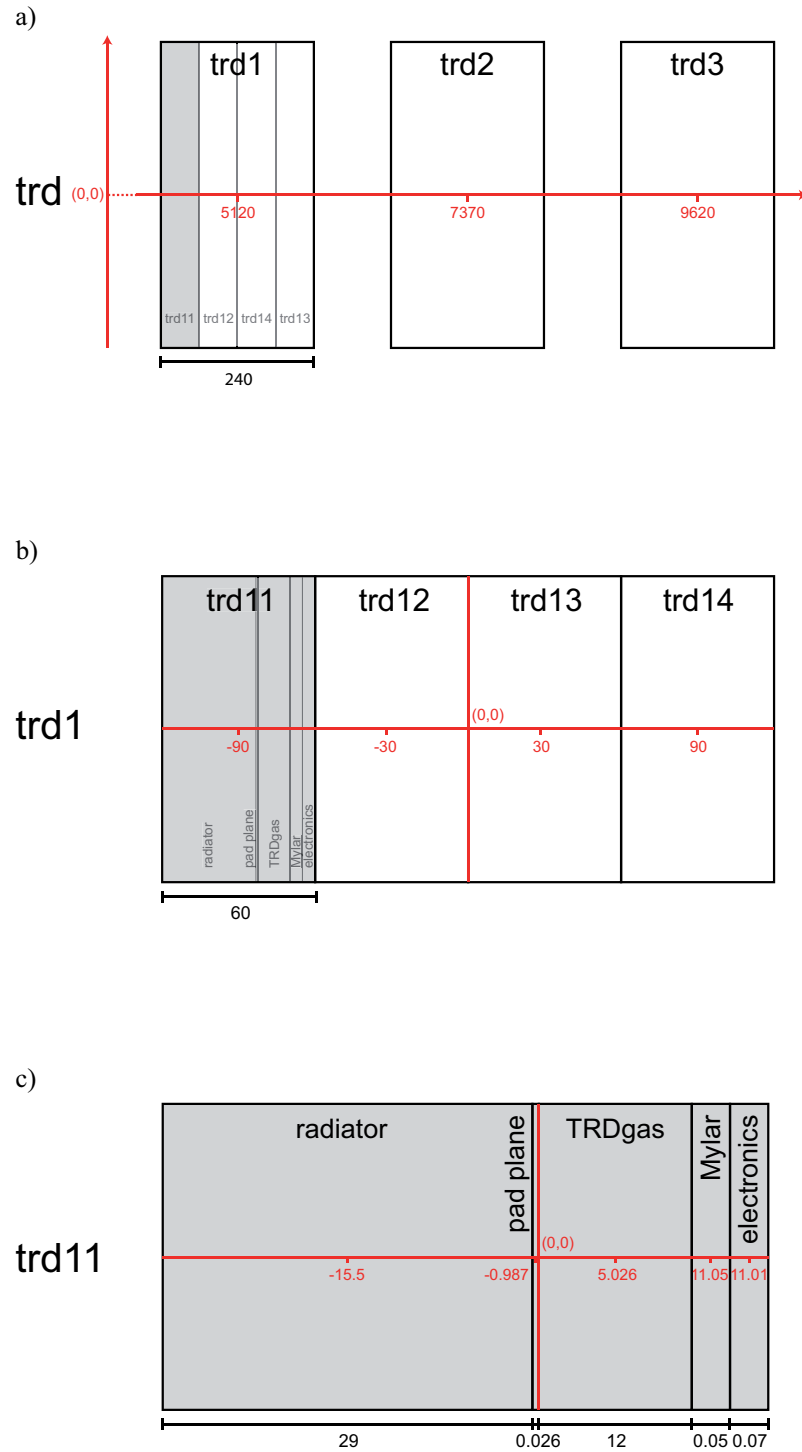


Figure 6.15: TRD geometry based on the MB-TRD layout in CbmRoot [trd-standard-MB.geo]. The TRD is composed of three stations (a) each consisting of four layers (b). One of these layers is shown in c). Each level represents a new mother volume with new origin (0,0). The sizes and positions are given in mm.

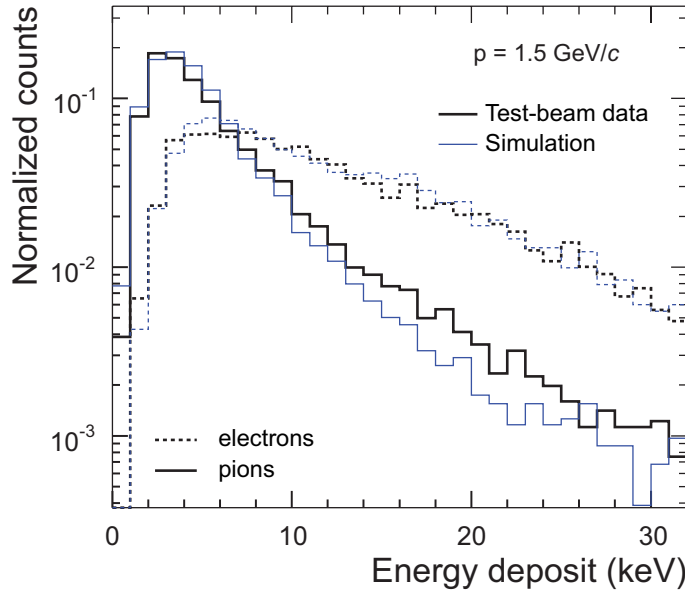


Figure 6.16: dE/dx in simulation (thin lines) and test beam (thick line) for electrons (dashed lines) and pions (solid lines).

TR. The ratio of the most probable values is the scaling factor which is used for calibration. After calibrating the energy loss by pions and electrons the radiator parameters are chosen in order to get the best description of the TR contribution in the electron energy loss.

The thin lines in Fig. 6.16 show the simulated energy-deposit spectra for electrons and pions. In addition, the measured charge-deposit distributions of the prototypes are presented for comparison (thick lines).

The particle momentum is $1.5 \text{ GeV}/c$. In both measurements the same number of events is used in order to get the same statistical accuracy. The chosen set of radiator parameters leads to a good agreement of the electron distributions obtained in the simulation and the test-beam data, but for pions the parameter set does not reproduce the data. At higher values of the energy loss the simulated energy-loss distribution produced by pions is below the measured distribution as seen in Fig. 6.16. It has been excluded that higher values of the pion distribution obtained from measured data are due to multiple hits as the observed effect does not depend on the particle rate.

Since the electron/pion separation is not ideal in the experiment (as seen in Fig. 6.12), the simulated pion sample has been contaminated artificially with electrons in order to best describe the data. This seems to be a good approach because the best consistency of

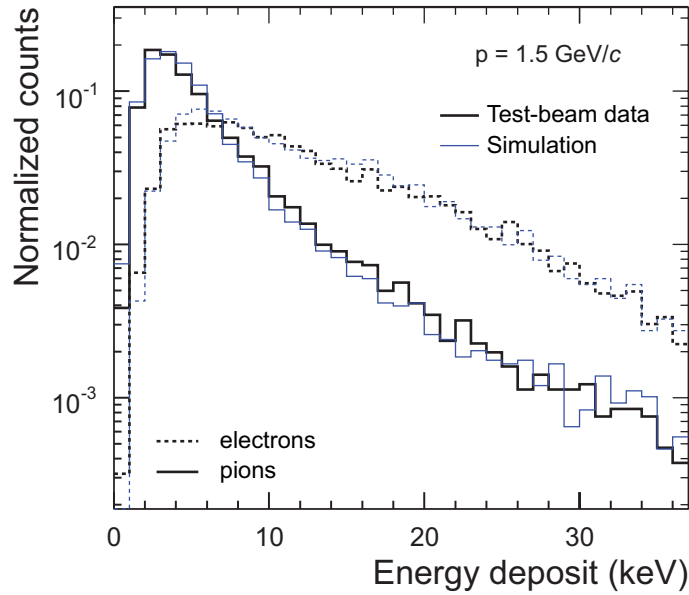


Figure 6.17: dE/dx in simulation (thin lines) and test beam (thick line) for electrons (dashed lines) and pions (solid lines) with a 5% electron contamination of the simulated pion sample.

the simulated and measured pion curves is obtained with a contamination level of 5% (see Fig. 6.17). In contrast to the pion case the electron curve is described very well without contaminating the electron sample. Any conclusion about a possible contamination of the electron sample is difficult as the parameters in the TR-production routine were selected in order to reproduce the measurements. Furthermore, such a contamination is unlikely. This can be understood from page 116: Fig. 6.12. The electron distribution appears broader in the Pb-glass/Cherenkov plane whereas the pions are sharply limited by the Cherenkov detector. This causes a higher probability for the pion sample to be contaminated by electrons than the inverse case leading only to an unilateral contamination. The contamination of the simulated pion sample, which is necessary to describe the test-beam data, indicates that the separation of pions and electrons via lead glass and Cherenkov detectors at momenta of 1.5 GeV/c is not 100%. Unfortunately it is not possible to tighten the PID cuts in the test-beam data in order to get a cleaner sample because in that case the statistical accuracy would not suffice to draw conclusions from the obtained charge-deposit spectra and even more to use the spectra for the determination of the pion efficiency. However, the contamination of the pion sample in the test-beam data provides a plausible explanation for the deviation between the measured and the simulated pion distribution as it can be confirmed when investigating higher contamination levels. Higher contamination

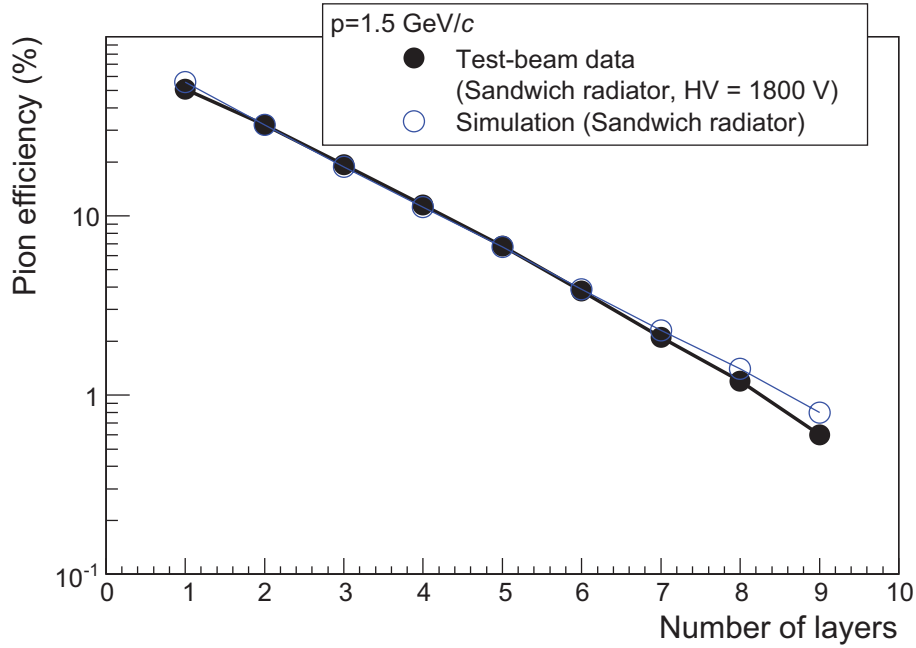


Figure 6.18: dE/dx in simulation and test beam with a 5% electron contamination of the pion sample.

levels can be obtained in the test-beam data by choosing weaker cuts in the electron/pion separation with the Pb-glass calorimeter and Cherenkov detector signals. The resulting charge-deposit spectra for electrons and pions can be well described by simulations in which the contamination levels are increased by the same factor.

6.5.5 Pion Efficiency in Simulation

In the simulation the pion efficiency is determined using the simulated energy-loss spectra with the same method as for the test-beam data (as described in Chapter 6.4). The pion efficiency at an electron efficiency of 90% versus the number of simulated detector layers shows a quantitative agreement of simulated and test-beam data (see Fig. 6.18).

This agreement is only reached by contaminating the pion sample with 5% electrons (as described in the previous section). For an investigation of this effect a comparison of the pion efficiencies with different fractions of electrons is shown in Fig. 6.19. The pion efficiency decreases to lower contamination levels. Nevertheless, the level of 5% cannot be improved in the test-beam data because then the statistical accuracy would not suffice to draw conclusions from the obtained charge-deposit spectra and even more to use the spectra for using the likelihood method (as described in Chapter 6.5.4). With

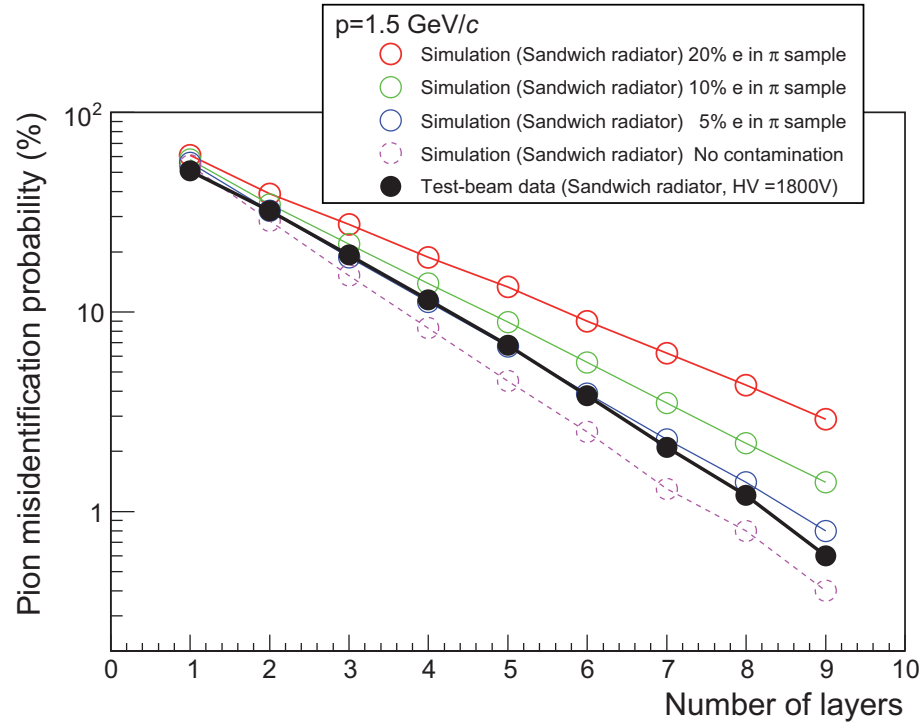


Figure 6.19: Pion efficiency as function of the number of simulated detector layers in test-beam data (black points) and in simulation (circles) for different contamination levels of the simulated pion sample.

this assumption, the dashed curve (0% contamination level) in Fig. 6.19 represents the performance of the detector in a pure electron and pion beam.

The energy loss of charged particles in the detector gas and the contribution from TR produced by electrons is described using simulations. As described before, the radiator parameters are chosen to reproduce the measurements of the deposited charge. These parameters are implemented together with the MB-TRD geometry in CbmRoot and are used for physics analyses like the study discussed in Chapter 7.

6.6 Position Resolution

In conjunction with the STS, the TRD has to facilitate the tracking of charged particles with good position resolution in the CBM experiment. In order to reconstruct charmonium and low-mass vector mesons, for the TRD, the required position resolution in bending direction of the magnetic field is of the order of $300 - 500 \mu\text{m}$ at count rates of up to 100 kHz/cm^2 [CBM09a] (all TRD requirements are described in Chapter 5.3). The posi-

tion reconstruction capability of the MB-TRD prototypes was investigated with the same test-beam data as used for electron/pion separation provided by the SIS 18 accelerator at GSI in 2006. The following results are already partly published in Reference [KB08].

A charged particle traversing the detector creates a signal via gas ionization as described in Chapter 5. The charge cluster can be reconstructed from the signal distribution on adjacent readout pads at the cathode pad plane. With this information, the position of the cluster can be determined with better resolution than that obtained for a single pad. Assuming a uniform distribution, the cluster position can be reconstructed with a resolution of $1/\sqrt{12}$ times the pad width. However, with the additional knowledge of the pad response function (PRF), a considerably better position resolution can be obtained as discussed in the following.

6.6.1 The Pad Response Function

The inner double-sided cathode plane of the TRD is subdivided into two rows, each consisting of nine separate pads with independent charge sensitive readout (see Fig. 6.20). In the upper plot of Fig. 6.20, the pulse height versus time on the readout pads is shown for a typical event. The readout pad structure with the labeled hit position of the same event is shown in the lower picture. Due to the number of available readout channels, only 16 of the 18 pads were read out during the test beam.

The measurement of the coordinate of the avalanche along the wire direction is done by interpolating the pulse height recorded on adjacent readout pads of the width W . The degree of charge sharing is measured by the PRF, defined as the ratio of the charge deposited on a pad i (Q_i) to the total charge on three adjacent pads ($Q_{\text{tot}} = Q_{i-1} + Q_{i+1} + Q_i$) as a function of the position of the hit relative to the pad center y (see a detailed description in Reference [Blu94]). The nomenclature for the position on the pad row is illustrated in Fig. 6.21. If pad i is the pad with maximum charge, the PRF is called PRF_0 .

The PRF is obtained by integrating the charge density $\rho(y)$ over one pad width:

$$\text{PRF}_0(y) = \frac{1}{Q_{\text{tot}}} \int_{y-W/2}^{y+W/2} \rho(y') dy'. \quad (6.7)$$

It represents the amount of induced charge that has to be collected on the pad, and y denotes the distance between the track and the center of the pad; y is the coordinate to be determined for a track by comparing the pulses on neighboring pads. It is experimentally found that the PRF can be approximated by a Gaussian curve within a few percent of its

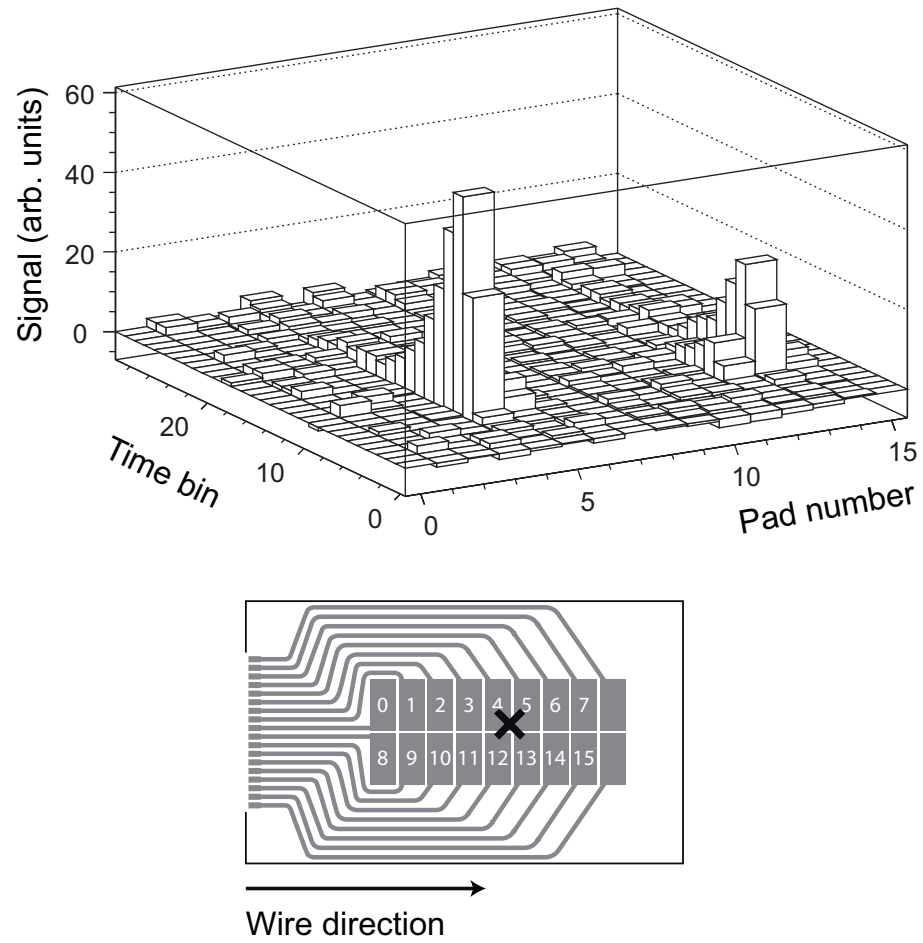


Figure 6.20: The upper plot shows the pulse height versus time on 16 readout pads for a typical event (16 pads were operated: 0 – 7 and 8 – 15). In the lower picture a schematic view of the readout pad structure with the labeled hit position of the same event is shown.

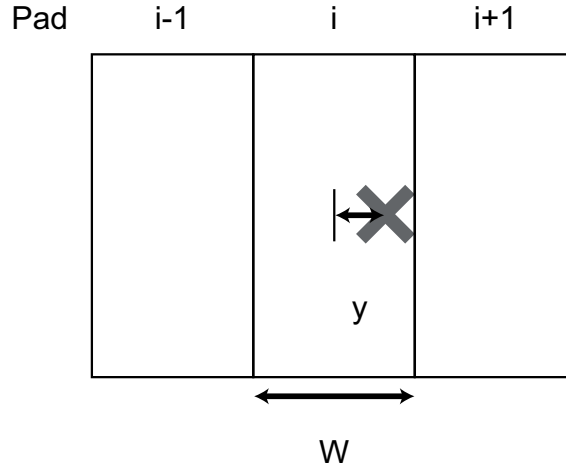


Figure 6.21: Nomenclature of the positions: the cross designates the center of the cluster and i is the pad with maximum charge.

maximum value [Fan79]. Thus, the position of the hit can be reconstructed by assuming a Gaussian shape of the PRF. With this assumption the PRF can be parametrized to:

$$\frac{Q_i}{Q_{i-1} + Q_i + Q_{i+1}} = A e^{-\frac{y^2}{2\sigma^2}} = \text{PRF}_0(y),$$

where Q_i, Q_{i-1} , and Q_{i+1} are the charges on the center pad i as well as on the neighboring pads on the left and on the right side, respectively. The total charge can be well approximated by the sum of the three pads.

By using the coordinates of the centers of three adjacent pads $y_i - W$, y_i and $y_i + W$, the pulse heights recorded on them can be determined. For a hit given at $y = y_i = 0$, the fraction of charge deposited on pad $i - 1$, i , and $i + 1$ can be determined by the function values $\text{PRF}_0(y + W)$, $\text{PRF}_0(y)$, and $\text{PRF}_0(y - W)$, respectively:

$$\begin{aligned} \frac{Q_{i-1}}{Q_{i-1} + Q_i + Q_{i+1}} &= A e^{-\frac{(y+W)^2}{2\sigma^2}}, \\ \frac{Q_i}{Q_{i-1} + Q_i + Q_{i+1}} &= A e^{-\frac{y^2}{2\sigma^2}}, \\ \frac{Q_{i+1}}{Q_{i-1} + Q_i + Q_{i+1}} &= A e^{-\frac{(y-W)^2}{2\sigma^2}}, \end{aligned}$$

where A is proportional to the total charge of the avalanche. In this set of equations, A , y and σ are unknown. In order to determine the PRF, the displacement y has to be deter-

mined without knowledge of the parameter σ . With this goal the ratios of two equations at a time may be determined to:

$$\frac{Q_i}{Q_{i-1}} = e^{\frac{2yW+W^2}{2\sigma^2}} \text{ and} \quad (6.8)$$

$$\frac{Q_{i+1}}{Q_i} = e^{\frac{2yW-W^2}{2\sigma^2}}. \quad (6.9)$$

Two further ratios can be calculated by building the product and the ratio of Eqs. 6.8 and 6.9:

$$\frac{Q_{i+1}}{Q_{i-1}} = e^{\frac{2yW}{\sigma^2}} \text{ and} \quad (6.10)$$

$$\frac{Q_i^2}{Q_{i-1}Q_{i+1}} = e^{\frac{W^2}{\sigma^2}}. \quad (6.11)$$

Subsequently, the Eqs. 6.10 and 6.11 can be solved for y :

$$y = \frac{W}{2} \frac{\ln(Q_{i+1}/Q_{i-1})}{\ln(Q_i^2/Q_{i-1}Q_{i+1})}. \quad (6.12)$$

The hit-position information for a large number of tracks can be used to plot the PRF as in Fig. 6.22. The picture shows the relative pad charge ($Q_i/(Q_{i-1} + Q_i + Q_{i+1})$) as function of the reconstructed cluster position in pad units. The measured PRF is approximated by a Gaussian curve which is illustrated in Fig. 6.22 a). It is seen that the Gaussian approximation is not perfect; in particular, it is steeper for large values of $|y|$.

An empirical formula by Mathieson [Mat88] for the induced charge distribution $\rho(y)$ describes the average behavior in symmetric MWPCs along the anode wires well, where the y -coordinate is given by the wire direction (see Fig. 6.20). With the Mathieson formula the charge distribution can be described in terms of a single parameter only. This single-parameter formula for the cathode induced charge distribution $\rho(\lambda)$ in a symmetric chamber may be written as:

$$\frac{\rho(\lambda)}{q_a} = K_1 \frac{1 - \tanh^2(K_2\lambda)}{1 + K_3 \tanh^2(K_2\lambda)}, \quad (6.13)$$

where

$$K_1 = \frac{K_2\sqrt{K_3}}{4\tan^{-1}\sqrt{K_3}} \text{ and} \quad (6.14)$$

$$K_2 = \frac{\pi}{2} \left(1 - \frac{\sqrt{K_3}}{2} \right). \quad (6.15)$$

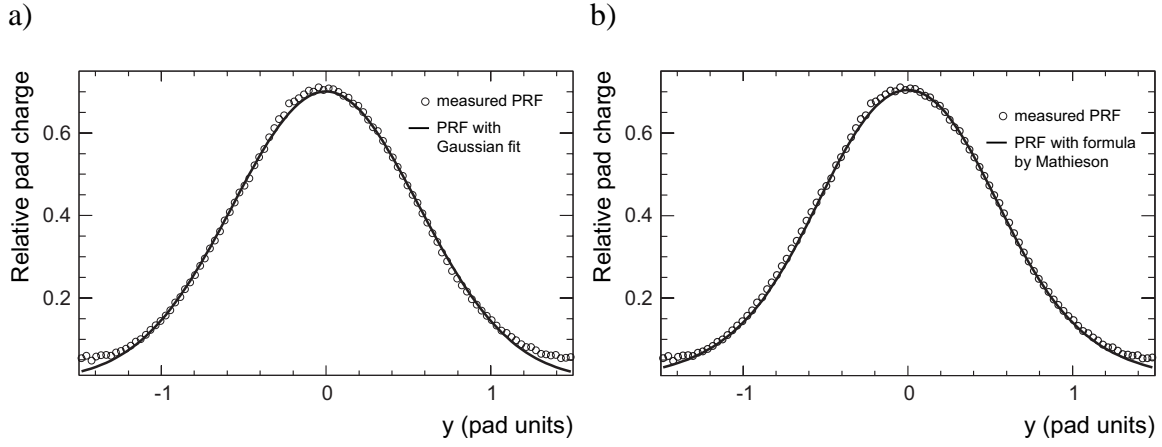


Figure 6.22: Pad response functions for $W = 0.5$ cm of the MB-TRD prototype. The avalanche is in the center of the pad. The circles show the measured PRF. In a) the line shows a Gaussian fit to the measured PRF and in b) the line shows results of a calculation using the Mathieson formula [Mat88].

Here, λ is defined as $\lambda = x/h$, the x -axis being either parallel or perpendicular to the anode wire direction, the value q_a is the net anode charge, and h is the anode-cathode separation. The parameter K_3 is a function of the radius of the anode wires, the gap between the anode wires, and the distance from the anode wires to one cathode plane. K_3 is given for different chamber geometries in Reference [Mat88]. For the determination of the PRF, the charge distribution has to be integrated over a pad width:

$$\int_{\lambda - \frac{W}{2}}^{\lambda + \frac{W}{2}} d\lambda \frac{\rho(\lambda)}{q_a} = -\frac{1}{2 \arctan \sqrt{K_3}} \left[\arctan \left(\sqrt{K_3} \tanh \left(\pi(-2 + \sqrt{K_3}) \frac{W + 2x}{8h} \right) \right) + \arctan \left(\sqrt{K_3} \tanh \left(\pi(-2 + \sqrt{K_3}) \frac{W - 2x}{8h} \right) \right) \right] \quad (6.16)$$

In Fig. 6.22 b), the measured PRF and a comparison to the calculated Mathieson formula is shown. The Mathieson formula describes the measured PRF even better than the Gaussian fit, especially at the edges of the neighboring pads. Over the complete fit region, the value χ^2/ndf improves by a factor of two. The agreement shows that the PRF of the chamber is understood within the context of the Mathieson formula. Nevertheless, the position of the cluster can be adequately reconstructed using the Gaussian assumption and the widths of the $\text{PRF}(y)$ are taken from the Gaussian fit. The obtained values are $\sigma_1 = 0.541 \pm 0.004$ and $\sigma_2 = 0.541 \pm 0.003$ pad units for the measured PRFs of the two identical MB-TRD prototypes.

6.6.2 Cluster Reconstruction

Measuring the PRF's width, the displacement y of the hit from the center of pad i (pad with maximum charge) can be determined with a better resolution, either by using the pads $i - 1$ and i (see Eq. 6.8)

$$y = \frac{\sigma^2}{W} \ln \frac{Q_i}{Q_{i-1}} - \frac{W}{2}, \quad (6.17)$$

or, alternatively, by using the pads i and $i + 1$ (see Eq. 6.9)

$$y = \frac{\sigma^2}{W} \ln \frac{Q_{i+1}}{Q_i} + \frac{W}{2}. \quad (6.18)$$

In the case of 2-pad clusters (when the cluster can only be recognized on two adjacent pads) the displacement and thus the position can be determined by using Eq. 6.17 (in the case of signals on pad i and $i - 1$) and Eq. 6.18 (in the case of signals on pad i and $i + 1$). If the track gives a signal on three adjacent pads, which is the most common case, the best results are obtained by combining these two measurements of y to a weighted average with weights w_1 and w_2 [Blu94]:

$$y = \frac{1}{w_1 + w_2} \left[w_1 \left(-\frac{W}{2} + \frac{\sigma^2}{W} \cdot \ln \frac{Q_i}{Q_{i-1}} \right) + w_2 \left(\frac{W}{2} + \frac{\sigma^2}{W} \cdot \ln \frac{Q_{i+1}}{Q_i} \right) \right]. \quad (6.19)$$

Here, σ is the width of the Gaussian fitted to the PRF, and W is the pad width. Since the statistical error is roughly inversely proportional to the collected charges on the side pads, one can use a standard weighted least-squares procedure with $w_1 = Q_{i-1}^2$ and $w_2 = Q_{i+1}^2$, where Q_i is the charge on pad i . Being aware of the displacement the cluster position can be reconstructed.

6.6.3 Position Resolution Along Wire Direction

For the determination of the position resolution the alignment of two identical prototypes can be calculated with the reconstructed cluster positions in both chambers $y_{cl,1}$ and $y_{cl,2}$. This is shown in Fig. 6.23, where the average difference of the reconstructed positions in the two chambers is presented as a function of the position in the first chamber. In this plot, the two pad rows are drawn consecutively. Subsequently, this distribution can be fitted with two linear fits. For $5 \text{ mm} \leq y_{cl,1} \leq 35 \text{ mm}$, the obtained fit is $f_1(y_{cl,1}) = (0.008 \pm 0.001)y_{cl,1} + (0.303 \pm 0.008) \text{ mm}$ and for $45 \text{ mm} \leq y_{cl,1} \leq 75 \text{ mm}$, it is $f_2(y_{cl,1}) = (0.010 \pm$

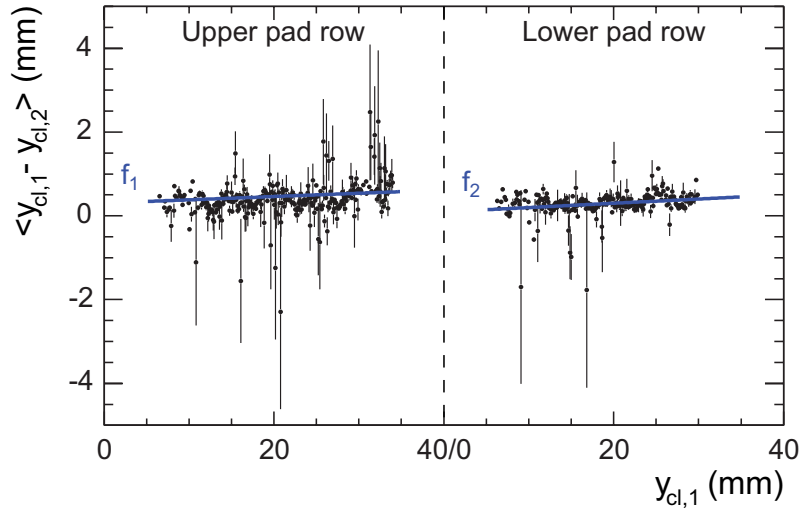


Figure 6.23: Alignment of two MB-TRD chambers with linear fits. On the y-axis the difference of the reconstructed cluster positions in two chambers is shown. The x-axis shows the position in the first chamber where the two pad rows are plotted consecutively.

$0.001)y_{cl,1} - (0.31 \pm 0.03)$ mm. The positive slope of the fits is due to an misalignment between the two chambers in the form of a rotation in the x - z plane. Within the errors the slopes of both fits agree as expected for the pad rows as they are arranged at the same cathode. The beam divergence does not play any role as it is negligible due to the small distance between the prototypes.

The wavelike structure in the distribution of the alignment, which can be seen in Fig. 6.23, is caused by the deviation of the Gaussian parametrization from the PRF at the edges of the neighboring pads. For the small prototypes, which are investigated here, it is sufficient to apply a linear fit to the alignment as described above. However, when choosing another chamber geometry in terms of anode-cathode distance and pad size, as e.g. planned for the real-size prototypes (see Chapter 6.6.5), the PRF might have an even less Gaussian shape which would amplify this effect. In that case it should be considered to use a more complex PRF parametrization for the determination of the position resolution.

For given tracks one can define residuals as the distance between the reconstructed $[y_{cl,1} - y_{cl,2}](y_{cl,1})$ and the fitted value $f_{1,2}(y_{cl,1})$ of the displacement between the cluster positions in the two chambers (see Fig. 6.23):

$$\Delta_y = [y_{cl,1} - y_{cl,2}] - f_{1,2}. \quad (6.20)$$

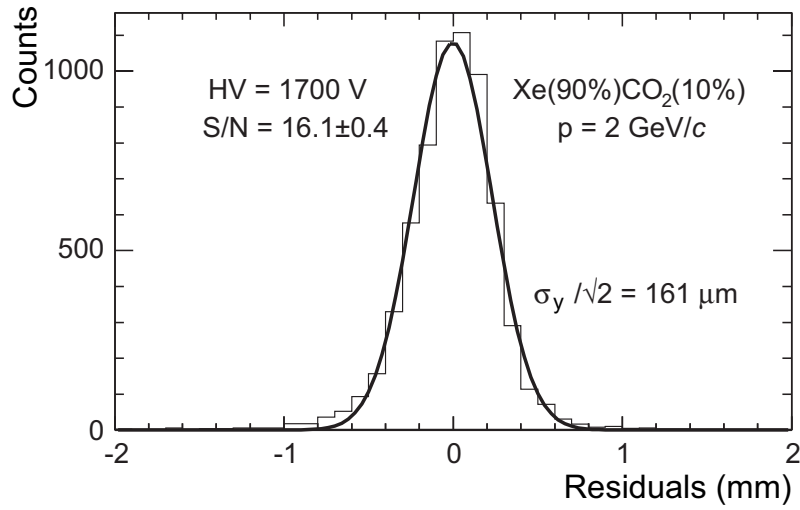


Figure 6.24: Distribution of residuals with a Gaussian fit for a single run with HV=1,700 V and $p = 2$ GeV/c, using a Xe(90%)CO₂(10%) gas mixture. The signal-to-noise ratio S/N as defined later, is 16.1 ± 0.4 .

The position resolution σ_y of two detectors is given by the standard deviation of a Gaussian fitted to the distribution of residuals Δ_y for a large number of tracks. With this method no external tracking devices are needed for the position-resolution determination. Since the two prototypes are identical in construction, the position resolution of a single prototype is given by $\sigma_y/\sqrt{2}$. A typical distribution of residuals for moderate particle rates is shown in Fig. 6.24. This resolution of two prototypes does not strongly depend on external effects like multiple scattering in front of the gas volume of the wire chamber and/or beam divergence because of the small distance between the prototypes. It thus represents the intrinsic position resolution of two identical prototypes.

For the determination of the pure tracking performance of the MB-TRD different cuts are applied to minimize disturbing factors. Since the information on both adjacent pads is needed, events with maximum induced charge on a border pad are not considered for the determination of the position resolution.

Multiple hits, which occur particularly at very high particle rates, worsen the measured position resolution, and they can be reduced by a cut on the charge ratio of the adjacent pads. Due to the additional deposited charge, multiple hits may cause a deviation from the mean charge ratio of the adjacent pads. Fig. 6.25 shows the distribution of the ratio $Q_{i-1}Q_{i+1}/Q_{i+1}^2$, which has a MPV of 0.23 ± 0.06 and a long tail to higher values. An event

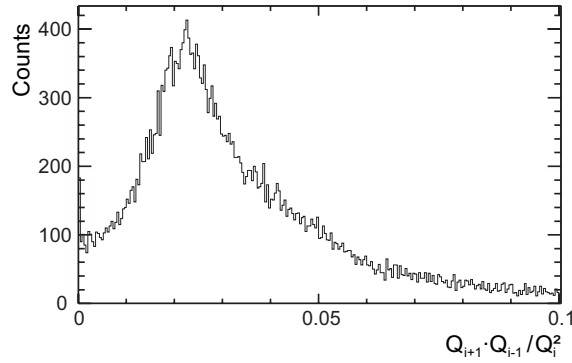


Figure 6.25: Distribution of the measured amplitude ratio.

with a large deviation of this average value produces a detector response very different from the PRF which is probably caused by multiple hits.

It is important to find reasonable cuts in order not to prefer certain cluster positions for the determination of the position resolution. With the measured PRF a cluster-quality measure (CQM) can be calculated to separate isolated clusters from shared clusters:

$$\text{CQM} = \frac{\text{PRF}(y-1) \cdot \text{PRF}(y+1)}{\text{PRF}^2(y)}. \quad (6.21)$$

In the case of a Gaussian parametrization, the value CQM would be constant for all cluster positions. For example, for the Gaussian curve fitted to the measured data, which is presented by the line in Fig. 6.22 a) a calculation of CQM gives the same result of $\text{CQM} = 0.035 \pm 0.002$ for each y between 0 and 0.5. Since the measured PRF differs from a Gaussian curve, especially for hits at the border of a pad, the CQM values depend on the hit position. In Fig. 6.26, the measured CQM (obtained from the data which are e.g. seen in the open symbols in Fig. 6.22) as a function of the cluster position is shown.

As expected from the Gaussian shape of the measured PRF at cluster positions near the center of the pad with maximum charge, the distribution is rather constant in this region. It can also be seen that positions that are closer to the center of the pad lead to lower values of the CQM, while the maximum values are reached at the border between two pads. In order not to suppress valid clusters, the thresholds for shared cluster discrimination should be chosen in a way that they include these CQM values.

A cut can be set to the amplitude ratio $Q_{i-1}Q_{i+1}/Q_i^2$ since this ratio can be determined for every single event. As explained in the following, the amplitude-ratio distribution in Fig. 6.25 does not show the same MPV as the CQM calculation. In Fig. 6.27, the amplitude ratio is shown as a function of the reconstructed cluster position. It can be seen

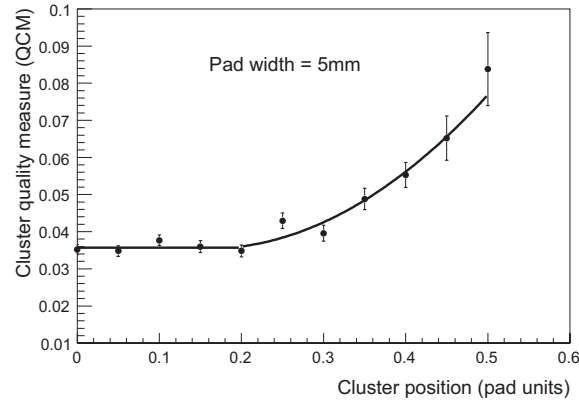


Figure 6.26: Quality measure for ideal clusters as a function of cluster position, extracted from the measured PRF. The line shows a composition of a constant fit for $0 \leq y \leq 0.2$ and a second order polynomial for $0.2 \leq y \leq 0.5$.

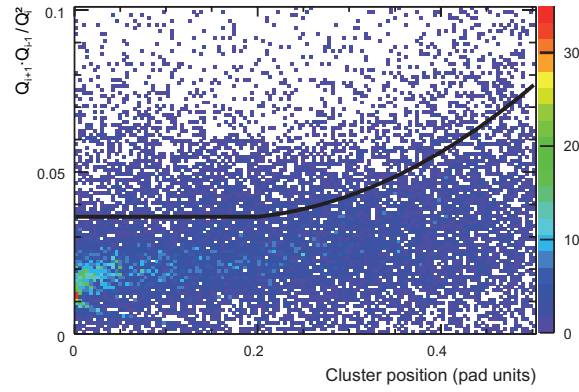


Figure 6.27: Amplitude ratio as function of the reconstructed cluster position. The black curve shows the CQM calculation.

that the mean amplitude ratio values are smaller than the expected CQM values (illustrated as black curve). This can be understood when comparing these two measurements: for the CQM using the PRF the ratio

$$\frac{\langle Q_{i-1} \rangle \langle Q_{i+1} \rangle}{\langle Q_i \rangle^2} \quad (6.22)$$

is determined. Since the normalization to the cluster size appears in the numerator as well as in the denominator, it is canceled. In the contrary, the measured amplitude ratio, averaged over the events, is:

$$\langle \frac{Q_{i-1}Q_{i+1}}{Q_i^2} \rangle. \quad (6.23)$$

Since the variables Q_{i-1} , Q_{i+1} , and Q_i are highly correlated, the covariances have to be considered. It can be shown that the difference between the mean values is caused by the covariances of the variables when calculating the ratio given in Eq. 6.22 directly with the measured data. This gives the same mean value as the CQM illustrated in Fig. 6.26.

The difference of the mean values is illustrated in Fig. 6.27 and it can be observed that the measured distribution of the amplitude ratio follows the same trend as the CQM. Thus, a reasonable cut can be set at a lower value without removing valid clusters. For the determination of the position resolution a threshold of 0.04 for measurements with moderate particle rates is used.

The cuts described above are adapted to get a constant efficiency in all runs when investigating different beam intensities. As events with multiple hits are removed from the analysis, not only the accuracy increases, but the detector efficiency decreases. Thus, the resolution versus rates is determined at the same efficiency as the cluster-quality cut is slightly softened for runs with higher beam intensities.

Fig. 6.28 shows the rate dependence of the position resolution with a constant efficiency: in these measurements, the fraction of the used hits for calculating the position resolution is 25.2% after application of all cuts mentioned above. This efficiency was obtained in the measurement with the lowest rate and the cluster-quality cut was subsequently loosened in measurements with higher rates in order to get the same efficiency.

The signal to noise ratio S/N and thus the gain has been varied by changing the anode voltages. Here, S/N is defined as the ratio of the signal integrated in the time bins 6 – 10 (corresponding to a time of 0.2 – 0.4 μ s) to the signal integrated in the time bins 1 – 5 (corresponding to a time of 0 – 0.2 μ s), where no signal is expected (see the average pulse height distribution as a function of time in Fig. 6.6). All signals are integrated after baseline subtraction. Increasing S/N leads to a better position resolution. The position resolution for different voltages is shown in Fig. 6.29.

Due to technical difficulties, it was not possible to perform these measurements using the same gas mixture. In addition, with a gas mixture of Xe(90%)CO₂(10%) the chambers were not operated with voltages higher than 1,700 V in order to prevent the chambers from sparking. Nevertheless, from the comparison in Fig. 6.29 the strong dependence of

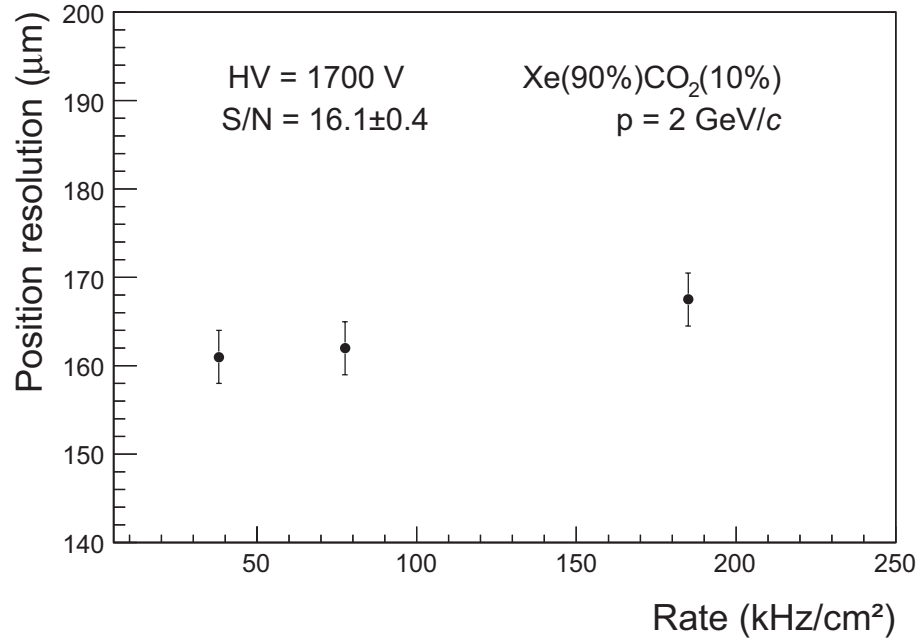


Figure 6.28: Position resolution as a function of particle rates with $HV = 1,700$ V and $p = 2$ GeV/c, using a Xe(90%)CO₂(10%) gas mixture.

the position resolution on the applied voltage can be seen. The best resolution of (141 ± 4) μm was measured at the highest anode voltage of 1850 V, with $p = 2$ GeV/c, and a Xe(80%)CO₂(20%) gas mixture.

However, for measuring the rate dependence shown in Fig. 6.28, a moderate voltage of 1,700 V was chosen in order to prevent the chambers from instabilities at high rates. In these measurements, for the lowest rate, the most probable value of the S/N , obtained from a Landau fit to the S/N -spectrum, is 16.1 ± 0.4 and decreases to 14.0 ± 0.6 for the highest rate.

By using a gas mixture of Xe(90%)CO₂(10%), the value of the position resolution at moderate intensity is (161 ± 3) μm or 3.2% of the pad width. No significant deterioration of the position resolution is observed up to average particle rates of 200 kHz/cm². The design goal for the TRD is a position resolution of 300-500 μm (see Chapter 5.3) for particle rates of up to 100 kHz/cm². It can be seen from the results of the test-beam data that the measured position resolution of the MB-TRD prototypes is clearly better even for the highest rates, which are considerably higher than the expected rates in CBM.

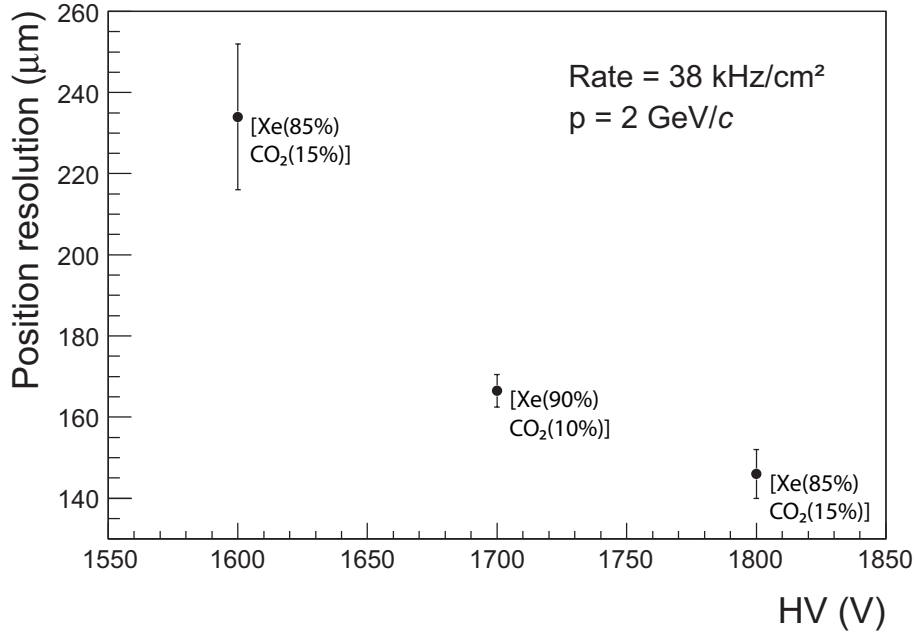


Figure 6.29: Position resolution as a function of the anode voltage with a constant rate of 38 kHz/cm² and $p = 2$ GeV/c.

6.6.4 Position Resolution Perpendicular to the Wire Direction

Due to the subdivision of the readout pads in two rows, it is also possible to obtain a position measurement in x -direction (perpendicular to the wire direction) with a resolution better than the pad height. As a first approach, this is done analogously to the position determination along the wire direction by measuring the charge sharing between the two pad rows (see the pad layout in Fig. 6.30). Therefore, the charge sum on five adjacent pads around the pad with maximum charge pad_{max} ($\sum_{i=-2}^{i+2} Q_i$) is divided by the charge sum of ten pads: the five pads mentioned before and the adjacent five pads belonging to the opposite pad row ($\sum_{j=-2}^{j+2} Q_j$), respectively. The index i can take the values 2 – 5 and 10 – 13; for $2 \leq i \leq 5$: $j = i + 8$ and for $10 \leq i \leq 13$: $j = i - 8$. Five adjacent pads are taken in order to be able to fit the cluster distribution with a Gaussian as described in the following. The inverse value of this ratio is plotted separately for the case that pad_{max} belongs to the upper row and for the case that pad_{max} belongs to the lower pad row, respectively (see the red and the green lines in Fig. 6.31). The peaks in the ratio distribution are caused by high field gradients near to the anode wires. The displacement between the peaks is caused by the position of the wires which are not accurately symmetric to the pad rows. It can also

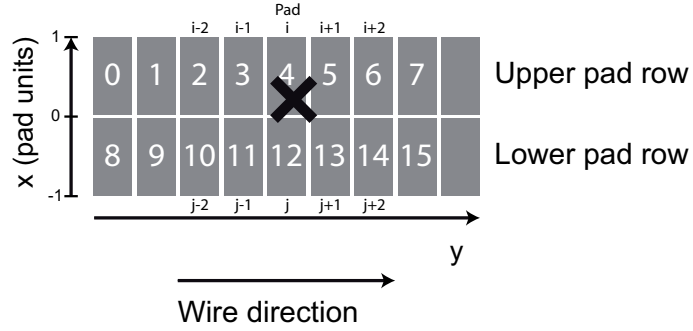


Figure 6.30: Layout of the readout pads in x - and y -direction. The appellation of the pads is given for an example in which the cluster position is designated by the cross. In this example, pad number 4 is $\text{pad}_{\text{max}} = \text{pad}_i$.

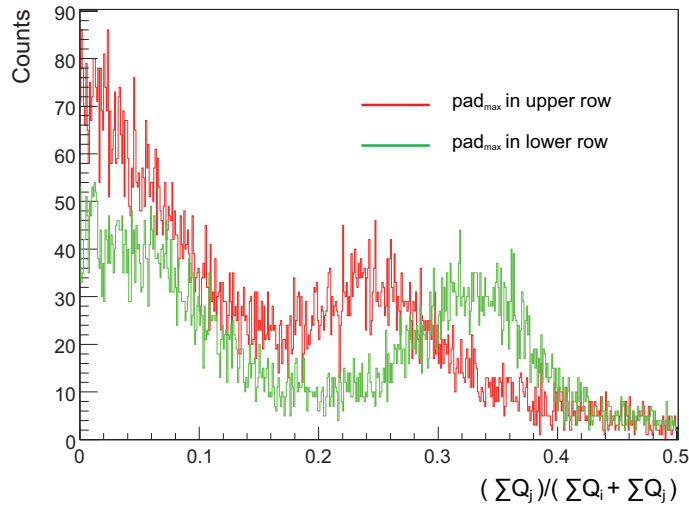


Figure 6.31: Charge ratio $[\sum_{j-2}^{j+2} Q_j / (\sum_{j-2}^{j+2} Q_j + \sum_{i-2}^{i+2} Q_i)]$ for the case that pad_{max} belongs to the upper row (red) and for the case that pad_{max} belongs to the lower pad row (green).

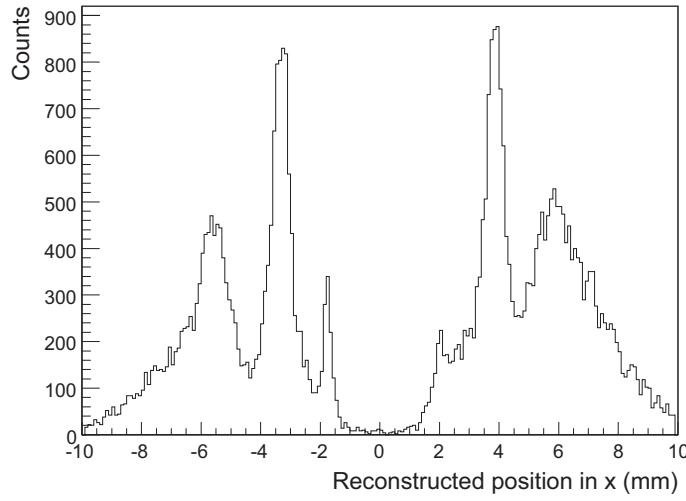


Figure 6.32: Reconstructed cluster position in x -direction. The peaks correspond to the wire positions which are shifted towards the borders due to the field geometry.

be seen from the number of entries that more tracks lead to a pad_{max} in the upper pad row since the center of the beam was located above the center of the chamber.

To simplify matters, the same width in x and y -direction and a Gaussian shape is assumed for the charge cluster. In order to determine the cluster position in x -direction, a Gaussian curve with the same cluster width and amplitude, which was determined for every single event, was shifted along the x -direction until the measured charge sharing is reproduced. This is justified by the rather quadratic shape of the area covered by the pads, on which the charge is integrated. In addition, the integrated charge is equal along x - and y -direction by using the same pads for the charge integration. Further details on this analysis will be available in Reference [Ber10]. A spectrum of the reconstructed cluster positions is shown in Fig. 6.32. In this distribution, the influence of the anode wires can be seen very clearly as peaks. An alignment between the two MB-TRD prototypes and a determination of the residuals (the procedure is identical as for the y -position described in Chapter 6.6.3) gives an average value for the position resolution of $(1230 \pm 11) \mu\text{m}$ for a measurement at moderate rates (38 kHz/cm^2 , $\text{HV} = 1,800 \text{ V}$, $p = 2 \text{ GeV}/c$, $\text{Xe}(90\%)\text{CO}_2(10\%)$). Unlike in y -direction, this resolution strongly depends on the position itself.

This can also be seen from the widths of the peaks induced by the field close to the wires in Fig. 6.32. The resolution of the wire image gets worse at larger distances to the center of the chamber. Here, the resolution deteriorates from $(330 \pm 90) \mu\text{m}$ (for the innermost wire) to $(560 \pm 10) \mu\text{m}$ (for the second wire) and to $(1055 \pm 210) \mu\text{m}$ (for the

third wire). The field of the outermost wire is not even visible anymore. From a simulation it can also be seen that the determination of x -positions, which are located at a large distance from the center ($|x| \geq 8$ mm), the resolution gets very bad within this chamber geometry. In that case the opposed pad row would not give a signal and the position can be anywhere between $x = 8$ mm and $x = 10$ mm or between $x = -8$ mm and $x = -10$ mm, respectively. The aforementioned position resolution in x -direction has been determined for the whole detection area ($|x| \leq 10$ mm).

Although the position of the charge cluster can be determined with a good resolution, the position itself is shifted towards the anode wires and does not reproduce the beam profile as clearly seen in Fig. 6.32. By using this method, the position of the particle track can be related to the position of the closest wire. Thus, it can be determined with a resolution of the order of the wire distance 2.5 mm divided by $\sqrt{12}$.

The pad design of the MB-TRD, which is limited to two rows because of the readout path, may be convenient for a comprehensive position measurement perpendicular to the wire direction. Of course, excellent resolution in both directions is obtained when rotating every second TRD layer by 90° . In order to test the possibility of a two-dimensional position measurement with the required position resolution in both directions already with one layer and a realistic cell size, the design of the prototypes has been optimized as described in the following section.

6.6.5 The Next Generation of CBM TRD Prototypes

The MB-TRD prototypes investigated in this thesis show very good performance in terms of electron/pion separation and in terms of position resolution, which both meet the requirements of CBM even for the highest measured particle rates. With the results of the performance measurement of the small-size prototypes, the next generation of TRD prototypes has been developed and is currently under construction in collaboration with the group in Bucharest. These new devices are real-size prototypes for a TRD in the CBM experiment, and are briefly described in the following.

Due to the good electron/pion separation the inter-wire distance (2.5 mm) and anode-cathode gap (3 mm) of the chamber will be retained: the new chambers also have a double-sized gas volume of 12 mm thickness with a central pad-readout cathode. Only the detection area will be increased from 20 mm to 80 mm in x - and from 50 mm to 377.5 mm in y -direction.

A challenge for the TRD is to offer a two-dimensional measurement of the cluster position across the entire area. The design goal for the real-size prototypes is a structure fulfilling all the requirements and being as simple as possible at the same time. Thus,

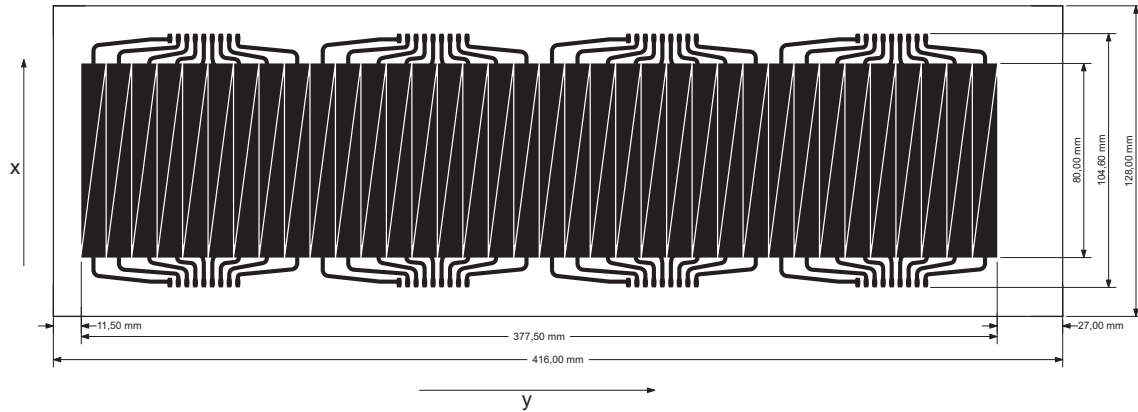


Figure 6.33: Drawing of the pad plane of real-size prototypes.

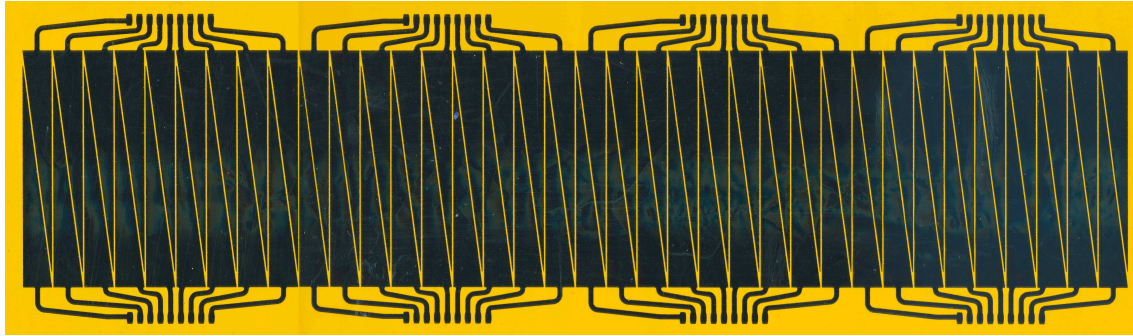


Figure 6.34: Photograph of the first constructed pad plane of real-size prototypes made from a Kapton foil with a double-sided pad structure from 20 nm chromium and 200 nm aluminum.

the single TRD cells are rectangular detectors. A rotation of rectangular planes relative to each other in order to access a two-dimensional position information is difficult. In addition, within a rotated geometry, the frame and electronics material shadows active detection areas of the following layers. If it is possible to choose the same geometry and orientation in subsequent layers, only the same non-sensitive regions in each layer would be shadowed. Hence, the idea of the real-size prototypes is a structure which allows a two-dimensional position measurement with the required position resolution within a single layer. For this reason, the rectangular readout pads are subdivided into two triangles each. Moreover, the new TRD geometry with one pad row per counter allows for a large active area without electronics in the central region or on the back side of the active detection area, which would shadow subsequent active areas. A principle drawing of the pad plane is shown in Fig. 6.33.

As shown with the small prototypes, the position resolution along the wire direction is of the order of the design goal. This can be assumed without large losses also for the new geometry by considering the rectangular pads consisting of two triangles each. With this new structure it is also possible to get a position resolution perpendicular to the wire direction better than the pad size divided by $\sqrt{12}$ by considering the charge sharing between two adjacent triangles. For the measurement of the track position in y -direction, the rectangles (consisting of two triangles) are considered with a pad width of 1 cm and for the position measurement in x -direction the charge sharing between the rectangles of a length of 8 cm can be used. Since the active detection part in one TRD cell consists of 2×36 readout pads, it has a total size of $80 \text{ mm} \times 377.5 \text{ mm}$ (see Fig. 6.33). In these prototypes, the rectangles have twice the width of the pads in the small prototypes, which were optimized for the chamber geometry in terms of anode-cathode gap and anode wire spacing. For this new pad size a larger anode-cathode gap is conceivable. The final pad size and geometry has to be chosen also in dependence on the possible number of readout channels.

Even though the electron/pion separation was already sufficient for the MB-TRD, it can still be improved by a pad plane providing higher transmission between the two detector halves. Thus, a pad plane consisting of a Kapton foil, on both sides coated with a pad structure from chromium and aluminum, was developed. It is vaporized in two steps: initially with 20 nm chromium to obtain a strong adherence and afterwards with 200 nm aluminum which is the smallest thickness that still allows to etch the structure. The contacts can be realized with small screws with two nuts on both sides acting at the same time as through-connections, or by gluing with silver epoxy through a small hole. The expected absorption in the pad plane is reduced from 15% to 2% [Hen93] in comparison to the previous electrode with the copper pad structure. A photograph of the first pad plane constructed in this way is shown in Fig. 6.34.

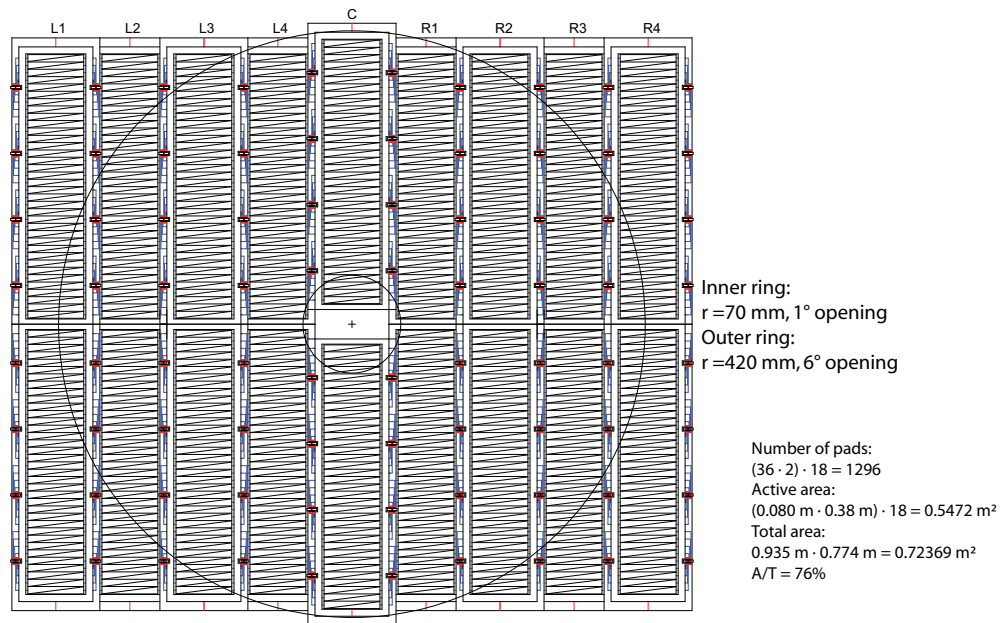
The performance of single cell prototypes shall be investigated in a test-beam time in 2009. A main goal of this in-beam test is to measure the position resolution in x - and y -direction and the rate dependence of the position resolution for these larger pads, which might be influenced by more multiple hits. Results of simulations and of the test-beam data shall be investigated in Reference [Ber10].

Currently, this TRD technology is a promising option for the CBM TRD applicable at the highest particle rates which are expected in the center of the detector. Since the construction of TRD layers with this technology is very challenging and expensive, one solution is a hybrid TRD with the MB-TRD in the inner and a more simple MWPC-based TRD (e.g. a single gas volume and a standard PCB pad readout) in the outer part of the CBM acceptance.

[illegible]

In the case of a successful performance of these prototypes the design of the inner part of the TRD ($1^\circ - 6^\circ$ polar angle) can be constructed as seen in Fig. 6.35 and in Fig. 6.36 [Sim08]. Fig. 6.35 shows the top view of one TRD station consisting of three detector layers. The single cells are staggered in order to minimize the shadowing of the following layers. In Fig. 6.36 the first TRD layer is shown in beam direction. This design is a proposal for the inner part of the first station of the TRD using the new detector layout and considering the simplest and most efficient construction. The layer is composed of the real-size prototypes described above, and the ratio of the active to the total area is 76%.

CBM TRD design - view in beam direction

**Figure 6.36:** View in z -direction of the inner part of the first TRD layer. Proposal from Reference [Sim08].

7. Dielectron Reconstruction in CBM by Using the MB-TRD Geometry

In this chapter studies on dielectron reconstruction in CBM using the MB-TRD geometry as described in Chapter 6.5.2 are shown. A brief survey of simulations on dilepton spectroscopy in CBM has been given in Chapter 4.4. In order to reconstruct photons via conversions into e^+e^- pairs, in the following analysis the lowest invariant-mass region ($< 100 \text{ MeV}/c^2$) of dielectrons has been investigated, where the main contribution is due to γ -conversions and π^0 -Dalitz decays. For this purpose the CBM simulation framework CbmRoot [Cbm09b] has been used. It provides the possibility to perform feasibility studies for physics measurements and further optimization of the detector layout.

7.1 The CbmRoot Simulation Framework

The CbmRoot framework is based on the ROOT system developed at CERN and commonly used for analyses in high-energy physics [Bru97]. In CbmRoot particle generation and detector simulation can be carried out within the same framework. A Virtual Monte Carlo concept allows to perform simulations using different transport codes such as GEANT3, GEANT4, or Fluka without changing the user code. In this concept, the same framework is used for simulation and data analysis. It delivers base classes which enable the user to set up the detector layout, magnetic field maps, and analysis tasks in a simple way.

As standard event generator the UrQMD (Ultra-relativistic Quantum Molecular Dynamics, version 1.3) [Bas98] code is used in CbmRoot. The UrQMD model is a microscopic model that is utilized to simulate ultra-relativistic heavy-ion collisions in the energy range from Bevalac and SIS ($\sim 1 \text{ AGeV}$) up to AGS ($2 - 15 \text{ AGeV}$), SPS ($40 - 200 \text{ AGeV}$), and RHIC ($\sqrt{s_{\text{NN}}} = 200 \text{ AGeV}$). It is designed as a multi-purpose tool for studying a wide variety of heavy-ion reaction mechanisms. These vary from *multi-fragmentation* (when the nuclei break up into many intermediate-mass fragments) and collective flow, to particle production and correlations. Since this code does not include rare probes such as vector mesons and charmed hadrons, the results of different models are embedded into UrQMD events: for the dilepton simulation the PLUTO [Frö07] model is used as thermal source and multiplicities are taken from HSD (Hadron-String Dynamics) [Ehe96].

Type	Key parameter	Configuration file
Target	250 μm gold, non-segmented target	target.geo
STS	8 stations	sts-standard.geo
MVD	2 stations	mvd-standard.geo
Magnetic field	Field center position: 0 cm, 0 cm, 50 cm, field at origin: $B_x = 0.007735$ kG, $B_y = -5.573$ kG, $B_z = 0.1368$ kG	FieldActive, Map sym3
RICH	Radiator: N_2 , mirror: 3 mm glass, 450 cm radial curvature	rich-standard.geo
TRD	12 layers, 12 mm gas volume each	trd-standard-MB.geo
TOF	RPC arrays, 10 m downstream of the target	tof-standard.geo

Table 7.1: CBM setup used for the analysis described in this thesis.

HSD multiplicities are also used for charm production plus a Pythia [Sjo06] decayer. Unless otherwise specified a data set of 20,000 pure UrQMD events (central Au+Au collisions at 25 AGeV beam energy) is being used in the analyses presented here. In the following studies the particles are propagated through the CBM detector model using the transport code GEANT3. Simulated events are reconstructed using different track and ring-reconstruction routines as well as vertex-finding algorithms.

The charged-particle identification is carried out by using RICH, TRD, and TOF information which is combined for the single tracks. The detector responses are implemented as realistically as possible, e.g. obtained from measurements with prototypes in test beams. The resolution and granularity of the detectors are still implemented very roughly since the detailed structures and the supporting material are not yet defined. In Table 7.1 the CBM detector configuration is presented that is employed as from now.

7.2 Track and Vertex Reconstruction

The CBM detector is able to track charged particles which are emitted at polar angles θ between 2.5 and 25 degrees with respect to the beam axis. This geometrical acceptance corresponds to a pseudorapidity window of $\Delta\eta = 2.31$ (η between 3.82 and 1.51). The particle tracks are reconstructed in the Silicon Tracking System (STS), which consists of 8 silicon-strip stations in the standard STS geometry implemented in CbmRoot.

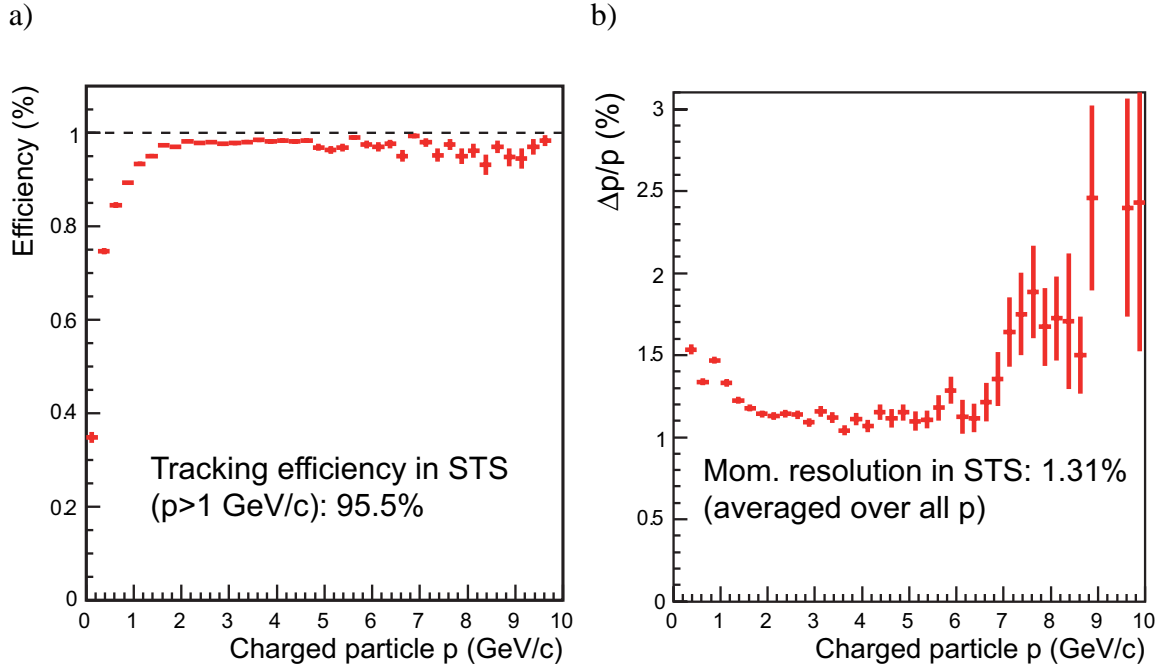


Figure 7.1: a) Track-reconstruction efficiency for tracks originating from the primary vertex and b) momentum resolution in the STS.

The efficiency of the track reconstruction and the momentum resolution are shown in Fig. 7.1 a) and b), respectively. The tracking efficiency of the STS increases with the momentum of the charged particle and is almost constant for momenta larger than 1.5 GeV/c; for $p > 1$ GeV/c on average 95.5%. The momentum resolution is very good with values clearly better than 1.5% for particle momenta between 1 and 7 GeV/c. Owing to the condition that a track has to contain at least four hits in the eight STS stations, the momentum resolution worsens below 1 GeV/c as particles with very low momenta see less stations before leaving the acceptance. In addition, a deterioration towards lower momenta is caused by small-angle scattering. After reconstruction of the primary vertex STS tracks are extrapolated through the TRD stations and matched to hits in the TOF detector. These so-called global tracks are reconstructed with an efficiency of 86%.

7.3 Electron Identification

The identification of electrons and positrons is based on reconstructed tracks in the STS and the TRD, ring recognition in the RICH, ring-track matching, and a statistical analysis

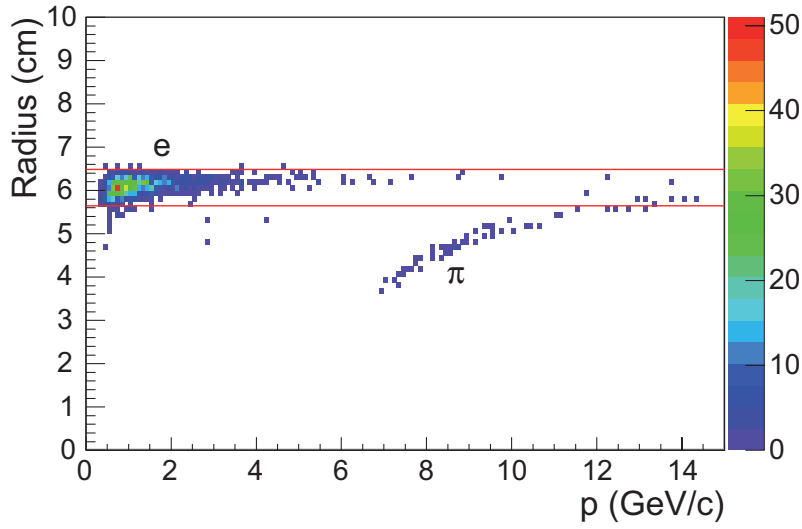


Figure 7.2: Reconstructed ring radius as function of momentum for 500 UrQMD events from central Au+Au collisions at 25 AGeV beam energy.

of the energy loss signal in the TRD. In addition, the TOF measurement supports the pion rejection at low momenta and completely suppresses protons and kaons.

7.3.1 Electron Identification in the RICH

The RICH ring-recognition algorithm is based on a Hough Transform [Bal82] ring finder, and the information obtained by propagating tracks from the STS is added afterwards. Since the rings in the photo-detector plane have a slightly elliptic shape, an ellipse fitting method is used in order to achieve a precise determination of the ring parameters and thus a good ring-track matching [Leb07, Leb08]. These rings are reconstructed with a radius resolution better than 3%. They can be assigned to global tracks with an efficiency of 95%.

Fig. 7.2 shows the distribution of the reconstructed ring radii as a function of the particle momentum. By applying a cut on the ring radius, electrons and pions can be well separated up to momenta of 10 GeV/c. The red line shows a $\pm 3\sigma$ range around the mean radius of electrons. Tracks with ring radii exceeding this range are not considered as electrons.

As will be shown later the ring finder works with a good efficiency of about 90%. However, a considerable number of *fake* rings occurs during the ring-finding process. Fake rings are reconstructed rings consisting of accidentally combined hits that are not caused

by the same particle, e.g. by utilizing hits from neighboring rings. It is also possible to obtain *false* electrons from true electron rings, which are subsequently matched to a wrong hadron track.

Due to the material in front of the RICH, approximately 100 rings are produced in a central (impact parameter $b = 0$) Au+Au collision at 25 AGeV beam energy, but only a small fraction of those electrons (about 10 – 20%) originates from the collision (primary electrons). The other rings belong to secondary electrons. In addition, the track density is very high (about 600 charged-particle tracks in the RICH acceptance). This increases the probability of matching hadron tracks to secondary electron rings.

In order to reject fake and false rings a method based on an artificial neural network (ANN) algorithm and several cuts, which are presented in the following, on a set of ring parameters are used without strongly affecting the ring-finding efficiency. In one event, the number of primary electrons (with more than 6 STS hits) averages 22. The integrated ring-finding efficiency for primary electrons is 93.6% with an average number of fake rings of 4.0 per event. After applying the fake-rejection routine, the number of fake rings was reduced to 0.29 per event at an efficiency of 90.9% [Leb08]. For these efficiencies the matching of rings to global tracks is not yet included.

Since the highest track densities and thus fake-ring rates are located in the central region of the photo-detector plane, a radial cut at a distance of 130 cm from the beam axis is applied. The electron acceptance of the RICH is not strongly affected by this cut for electron momenta of up to 10 GeV/c. The cut causes a reduction of the acceptance only by 5% at 1 GeV/c and by 10% at 10 GeV/c. A cut on the distance between the ring center and the closest track projection is also used because these values are higher for fake combinations. Since the radius resolution decreases towards lower momenta, this cut position depends on the momentum. A further cut is applied to the number of hits in a ring since the distribution for true rings has a Gaussian shape and fake rings normally consist of fewer hits. The cut allows for any number of hits within a 3σ range around the mean. In addition, high-momentum pions producing rings can be rejected by this cut since the number of hits on a ring is small for them as well. A summary of the cuts which were chosen for the studies described in this thesis is shown in Table 7.2. The resulting efficiency and pion suppression factor of the RICH as function of the momentum are displayed as circles on page 155: Fig. 7.4 a) and b).

7.3.2 Electron Identification in the TRD

There are several options that need to be taken into account for electron identification by the TRD. If the momentum of the track is smaller than a specified value (in this analysis

Cut for electron identification in the RICH	Cut position
Ring-track distance	$< 2 \text{ cm}$ for $p < 0.5 \text{ GeV}/c$ $< (\frac{7}{3} - \frac{2}{3} \cdot p) \text{ cm}$ for $0.5 \text{ GeV}/c \leq p < 2.0 \text{ GeV}/c$ $< 1 \text{ cm}$ for $p \geq 2.0 \text{ GeV}/c$
Radial distance in photo-detector plane	$> 130 \text{ cm}$
Number of hits on a ring	23.8 ± 5.1
Ring radius	$(5.96 \pm 3 \cdot 0.2) \text{ cm}$
Ring selection (ANN)	> 0.4

Table 7.2: Applied electron identification cuts in the RICH which are used in this analysis.

1.5 GeV/c), the identification by the TRD is ignored and the identification is carried out by using only the RICH and TOF information. If the track does not have an assigned TRD track, it is not identified by the TRD. Nevertheless, in this analysis it is checked whether this track has been identified by RICH as an electron and if true the track is used for further analysis. After making these decisions the actual identification by the TRD is performed. The tracks from TRD are assigned with values from several identification algorithms as described in the following section. Depending on the selection of the method used and the cut values for that method, a track is identified as an electron or not. For defining reasonable cuts it is necessary to calculate the electron efficiency. The electron efficiency and the corresponding pion efficiency are also defined and discussed in the following section.

PID Methods for TRD

Three different algorithms for electron/pion separation have been developed and implemented in CbmRoot. The first one is based on a *likelihood* method using the normalized energy-loss spectra of electrons and pions as obtained from simulations which describe the test-beam data from TRD prototypes (see Chapter 6.5).

The second method, called ω_h^k , is also a probabilistic approach (as described in Reference [Aki08]). It requires only the parameters of the dominant distribution (in our case, the distribution of pion energy loss), and it provides results comparable to the method described in the following.

The third method uses an artificial neural network (ANN) which was trained with pure electron and pion signals from a simulation with a so-called box generator: the par-

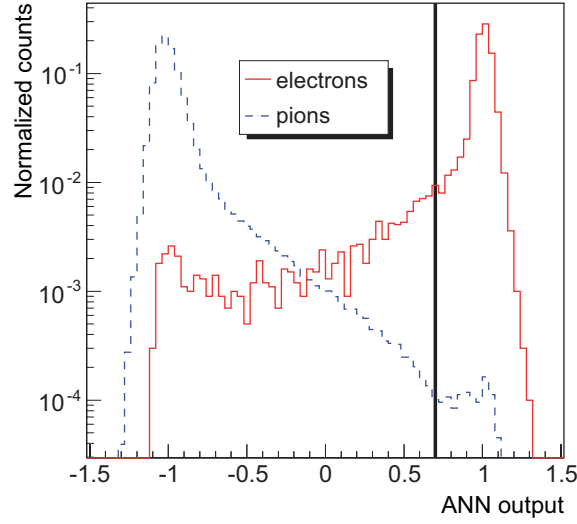


Figure 7.3: ANN output values for electrons (solid) and pions (dashed) for 12 layers of TRD.

ticles are created at the target with a uniform distribution in momentum ($0 \text{ GeV}/c < p < 10 \text{ GeV}/c$). In this analysis, a momentum above $0.5 \text{ GeV}/c$ is required in the first TRD layer. Fig. 7.3 shows the ANN output values for electrons and pions and 12 layers of TRD integrated over all momenta. The output signals of the neurons are a measure of the probability for electrons and pions to be identified as electron. At the stage of network training, the output for a pion event was set to -1 , and for an electron event to $+1$. Since linear output neurons were used, this may also lead to results larger than $+1$ or smaller than -1 when the probability to be one species is very high. The vertical line in Fig. 7.3 indicates the applied cut to obtain an electron efficiency of 90%.

In the following analyses the ANN method is chosen and the cuts are tuned to provide an electron efficiency of 90%. Fig. 7.4 shows the electron efficiency and the corresponding pion efficiency in an analysis of 10,000 UrQMD events from central Au+Au collisions at 25 AGeV beam energy. The pion efficiency is the fraction of pions that is misidentified as electrons at a given electron efficiency. Since in this analysis the TRD electron PID is used only for momenta above $1.5 \text{ GeV}/c$, the efficiency and thus the pion suppression factor are identical up to $1.5 \text{ GeV}/c$ for the options ‘RICH’ and ‘RICH \oplus TRD’. In these momentum regions the efficiency and the pion suppression factor are determined by the conditions in the RICH and the TOF.

7.3.3 Electron Identification in the TOF

The TOF measurement in this analysis is used for a momentum-dependent cut on the reconstructed mass square (m^2):

$$\begin{aligned} \text{for } p < 1 \text{ GeV}/c : \quad & m^2 < 0.01 (\text{GeV}/c^2)^2, \\ \text{for } p \geq 1 \text{ GeV}/c : \quad & m^2 < 0.01 (\text{GeV}/c^2)^2 + 0.09 \cdot [p - 1 \text{ GeV}/c] (\text{GeV}/c^3). \end{aligned}$$

It is seen in Fig. 7.4 that the TOF enhances electron/pion separation for momenta of up to 1 GeV/c. In addition, it provides rejection of all kaons and protons which can falsely be matched to electron rings. Nevertheless, the pion suppression performance gets worse towards higher momenta; at momenta above 1.5 GeV/c TOF has no noticeable influence on the pion suppression anymore. Here, it is entirely determined by the cuts in the RICH and TRD.

7.4 Feasibility Study of Measuring Direct Photons via Conversion into e^+e^- Pairs

At FAIR energies direct photons are expected to originate mainly from thermal production in the medium and therefore probe the temperature of the medium (see Chapter 2.2). Since pair conversion is the dominant process of photon interactions in the detector material at energies much larger than 1 MeV (see also page 62: Fig. 3.9), this mechanism can be used to detect direct photons from heavy-ion collisions. The feasibility of measuring direct photons via conversions has been studied in the following using full event simulation and reconstruction within CbmRoot.

7.4.1 Photon Measurement in CBM

In CBM, an electromagnetic calorimeter (ECAL) is designated to provide photon identification. The ECAL consists of materials with high nuclear charge to maximize the conversion probability. In the material, the photons convert into electrons and positrons, which produce new photons in subsequent interactions mainly via bremsstrahlung. Thus, an electromagnetic shower is produced in the detector. The ECAL intended for CBM consists of alternating layers of lead and scintillator plates [Bri07]. In the scintillator material the shower particles can be detected by excitation and subsequent emission of photons with larger wavelengths close to or within the visible spectrum. The resulting low-energy photons are detected using photo-multipliers, and the measured energy allows a determination

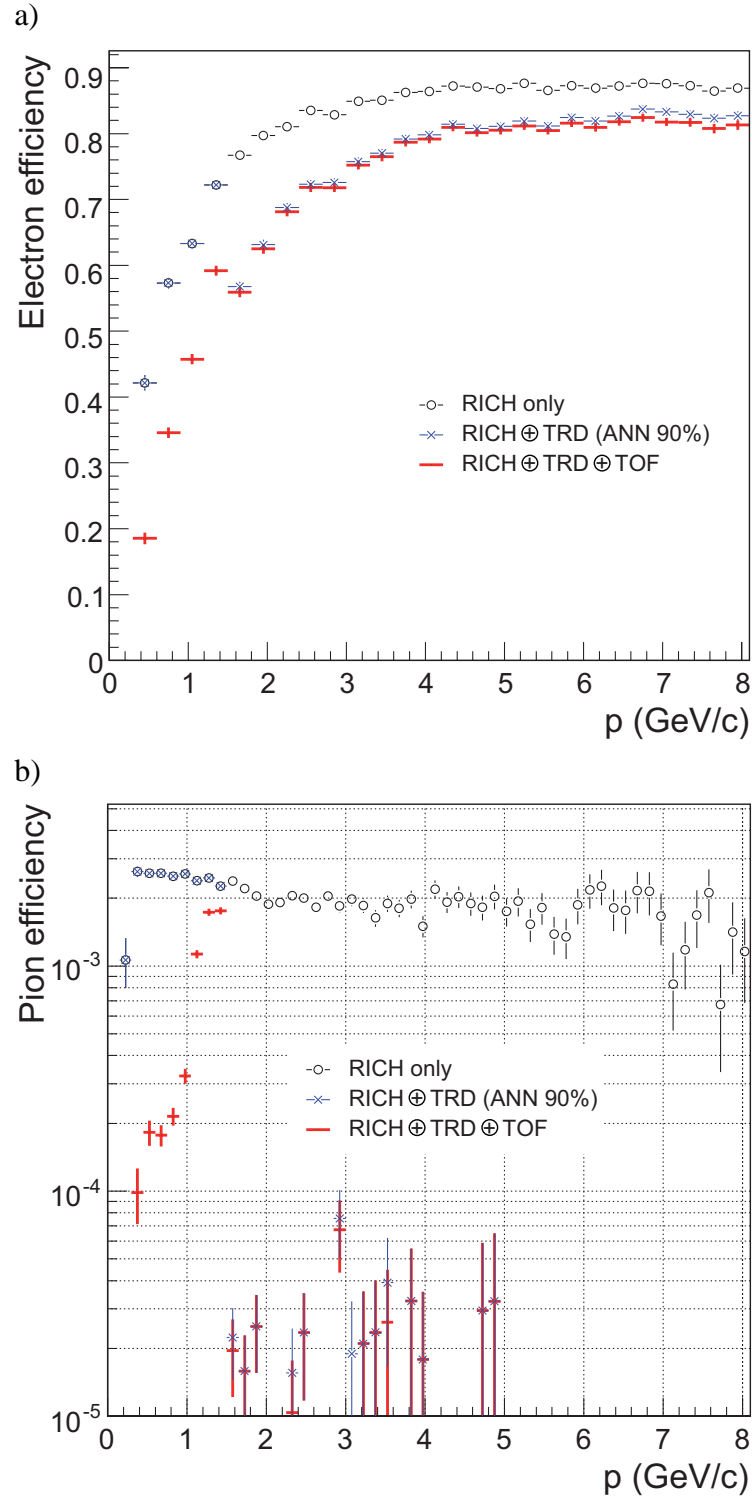


Figure 7.4: a) Electron efficiency and b) pion efficiency versus momentum either using only RICH (black circles), or RICH and TRD (blue crosses), or the combined RICH, TRD, and TOF information (only red error bars). Here, 10,000 UrQMD events from central Au+Au collisions at 25 AGeV beam energy are analyzed.

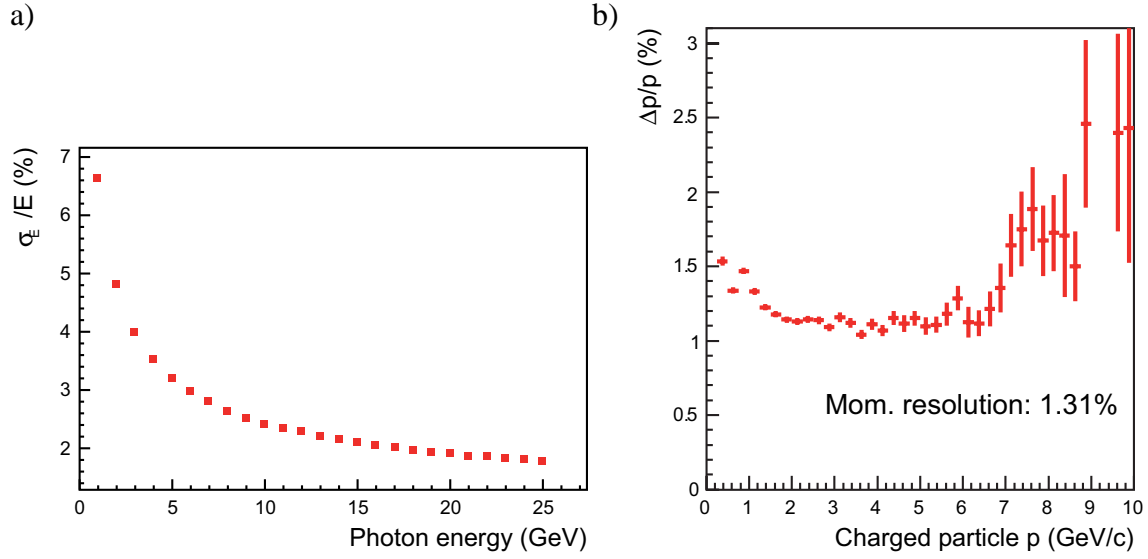


Figure 7.5: a) Energy resolution of photon reconstructed with the ECAL [Kha08], b) momentum resolution of the charged-particle tracking with standard STS layout.

of the full energy of the shower and thus the original photon. The energy resolution of an ECAL module consisting of 160 layers (Pb 0.7 mm + Sci 1.0 mm) has been determined by a simulation of single primary photons. The results are shown in Reference [Kha08], and the energy resolution of the photon reconstruction is shown in Fig. 7.5 a).

Photon measurement with an electromagnetic calorimeter is subject to systematic uncertainties, which are large compared to the direct-photon contribution to the inclusive photon spectra, in particular for CBM where all other detectors are placed in front of the ECAL, and their material budget causes an additional background. Thus, an additional measurement with a different method provides a useful check of systematic uncertainties.

In order to increase the precision, a complementary measurement of dielectrons from photon conversions can be used to determine the ratio of direct photons to decay photons. This method is very auspicious especially at low momenta because of the good momentum resolution of the electron tracking with the STS in CBM (see Fig. 7.5 b). Using momentum conservation, the photon properties can be reconstructed from the momenta of the electron and positron because the momentum transfer to the nucleus is negligible. With the assumption of an identical momentum resolution of the electron and the positron, the momentum resolution of the photon can be estimated to $\sqrt{2}$ times the momentum resolution for electrons in Fig. 7.5 b). This resolution is still much better than the expected resolution of the photon measurement with the ECAL as shown in Fig. 7.5 a).

In comparison to the ECAL measurement this method has further advantages: besides the good momentum resolution with the dielectron tracking it does not suffer much from misidentified charged and neutral hadron background. The low efficiency of the photon-conversion method caused by the low conversion probability is partially compensated by the high event rate in CBM.

7.4.2 Reconstruction of Photon Conversions

When traversing material, photons can convert in the electromagnetic field of a nucleus or the atomic shell into pairs of electrons and positrons. These two daughter particles can be measured using the charged-particle tracking (STS and TRD) and electron identification detectors (RICH, TRD, and TOF). They can subsequently be used to reconstruct the photon from which they originated.

The photon measurement via conversion poses a special challenge because the CBM experimental setup will be designed to create as little conversions as possible in order to optimize e.g. the measurement of low-mass vector mesons via dileptons, where the dominant background sources are random combinations of e^- and e^+ from photon conversions (see Chapter 4.4). Thus, the current dielectron studies are using a thin target of $250\text{ }\mu\text{m}$ (1% hadronic interaction length), which can be further segmented into individual $50\text{ }\mu\text{m}$ disks, and as little material as possible between the target and the first tracking stations of the STS.

The photon conversions in the target are the measured observable of this analysis and at the same time a background in measurements of observables like ρ , ω , ϕ , and J/ψ . Later conversions in the detector material are objectionable in all measurements and have to be reduced in order to avoid a large background of electrons and positrons. Concerning conversions in the target, the photon measurement is parasitic to the other dielectron measurements. Thus, for the photon measurement either the thin target has to be accepted which decreases the statistical accuracy, or one has to consider an extra run with a thicker target or with a dedicated converter especially for the photon measurement via conversions.

In the CBM setup, a fraction of the produced photons is converting inside the target. For the feasibility study of measuring photons via conversions a non-segmented gold target of $250\text{ }\mu\text{m}$ thickness is used in the simulation. Using page 62: Eq. 3.15 the radiation length of gold ($Z = 79$, $f(79) = 0.3129$, $A = 197\text{ g mol}^{-1}$) is

$$\frac{1}{X_0} = 0.1547\text{ cm}^2\text{g}^{-1}. \quad (7.1)$$

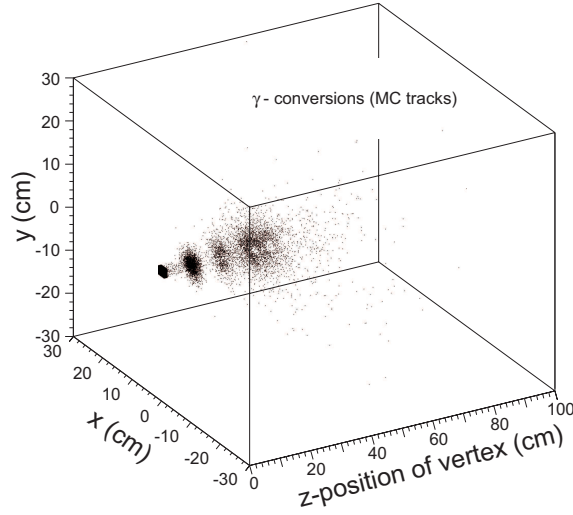


Figure 7.6: Distribution of conversion MC vertices associated with reconstructed tracks in the xyz -space from 20,000 UrQMD events from central Au+Au collisions at 25 AGeV beam energy.

With a density of $\rho=19.32 \text{ g/cm}^3$ the resulting radiation length of gold in cm has a value of

$$X_0(\text{gold}) = 0.334 \text{ cm}. \quad (7.2)$$

A good approximation for the mean conversion probability of photons in the gold target can be calculated using Eq. 3.19, the intensity relative to I_0 after traversing in the average $\frac{1}{2} \cdot 250 \mu\text{m}$ gold is:

$$I/I_0 = e^{-\frac{7}{9} \frac{x}{x_0}} = 97.13\%. \quad (7.3)$$

Thus, the expected conversion probability for photons in the gold target is about 2.9%.

As seen in Fig. 7.6 the distribution of photon-conversion points in space reflects the distribution of material within the experimental setup where the locations of the target and the tracking stations are clearly visible. Most of the conversions occur within the target (86%). Further conversions occur in the material of the STS stations. Conversions which occur behind the STS are not reconstructed.

In order to measure photons converting into e^+e^- pairs, charged-particle tracking detectors can measure the momenta of the two conversion daughters, from which the momentum of the photon can be reconstructed. In CBM the STS, located in a dipole magnet, provides the track reconstruction and momentum determination. As described in detail in

Chapter 7.3, electrons are identified in conjunction with a RICH, TRD, and TOF measurement. In the event reconstruction particles are first tracked, and PID information from RICH, TRD, and TOF is then associated with these tracks to form a global track. In order to investigate the influence of different cuts on the photon reconstruction, the analysis was initially performed using perfect electron PID. This means that the identification of electrons and positrons was done using the MC information about the particle type. The influence of the real detectors' electron PID on the photon reconstruction is subsequently investigated.

Vertex Reconstruction

For the reconstruction of the simulated tracks, different track-finding algorithms are currently implemented in CbmRoot. In this analysis, the STS tracks are reconstructed with the so-called L1 track finder (CbmL1StsTrackFinder) [Cbm09b], and then the particle trajectories (including momentum and charge of the particle) are fitted based on the STS hits. At this stage of reconstruction the primary vertex is not yet known but the target position provides an estimate of the event vertex. The track fit and final momentum calculation is performed using an algorithm based on a Kalman filter (CbmStsTrackFitter) [Kis08a]. The algorithm uses the information from tracks found in the STS. The TRD tracks are also found and fitted in a track-following approach using STS tracks as seeds and a Kalman-filter method (CbmL1TrdTrackFinderSts, CbmTrdTrackFitterKF) [Cbm09b].

A package for the reconstruction of decayed particles based on the Kalman-filter method has been developed for CBM [Gor07]. For the reconstruction of the parameters and associated covariance matrices of the mother particles a set of daughter-track estimates and their covariance matrices are used. Since the reconstructed mother particle contains all necessary information – at the point of its generation as well as at the point of its decay – this method is suitable for the complete reconstruction of decayed particles as well as for the reconstruction of their vertices with a high accuracy and reliability.

The x -, y - and z -position of the reconstructed dielectron vertices are displayed in Fig. 7.7. Here, only reconstructed e^+e^- pairs with the same mothers are plotted. The green line shows all e^+e^- pairs, the red line shows the fraction with photon mothers and the blue line those originating from π^0 -Dalitz decays. It can be seen that most of the photon conversions (86%) occur inside the target. There the main contamination is caused by e^+e^- pairs from π^0 -Dalitz decays. There are also photon conversions in the material of the STS stations far away from the target which are more difficult to track because of the STS geometry and acceptance. These e^+ and e^- tracks are not seen by all stations and

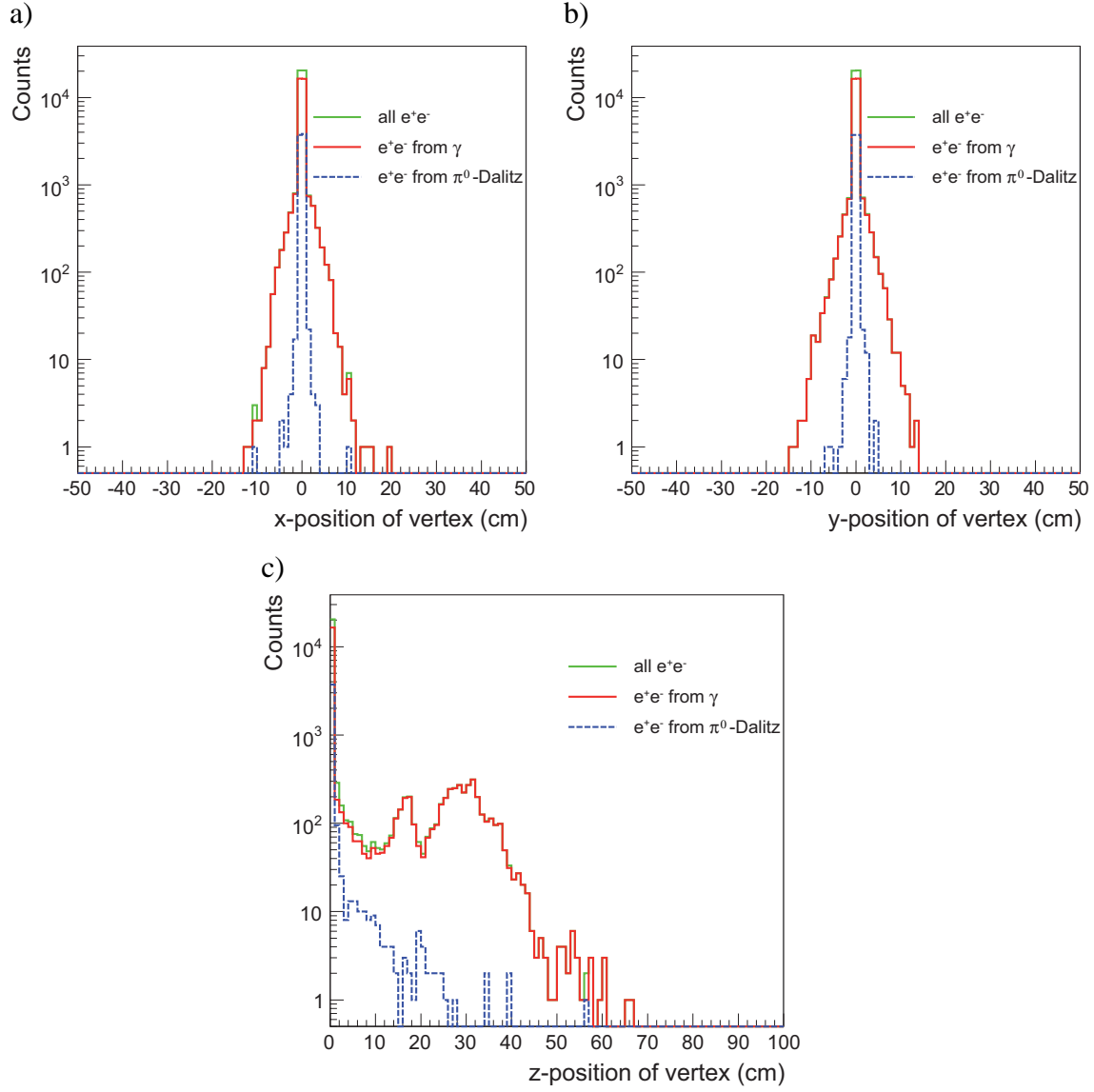


Figure 7.7: x -, y -, and z -position of reconstructed vertices of all e^+e^- pairs (green) and the contribution originating from photon conversions (red, solid line) and π^0 -Dalitz decays (blue, dashed line). Here, 20,000 UrQMD events from central Au+Au collisions at 25 AGeV beam energy are analyzed.

thus the momentum and vertex determination has a large uncertainty. In addition, the STS track finder uses a vertex constraint to the target which even increases the uncertainty. On the other hand, there are hardly any π^0 -Dalitz decays at these positions farther from the target. This leads to a high purity of the photon signal. The reconstruction of these photon conversions may be investigated in a different analysis. In the study described here, solely photon conversions in the target are used by applying a cut on the reconstructed vertex position.

Invariant Mass of e^+e^- Pairs

In general, mother particles can be reconstructed with the invariant-mass method by measuring the momenta \vec{p}_i and the energies E_i of the daughter particles. The invariant mass of the mother particle X is given by:

$$M_X^2 c^4 = p_X^2 c^2 = \left(\sum_i \vec{p}_i c \right)^2 = \left(\sum_i E_i \right)^2 - \left(\sum_i \vec{p}_i c \right)^2. \quad (7.4)$$

The invariant mass of the e^+e^- pairs from a photon conversion is close to zero due to the rest mass of a photon being zero and the small momentum transfer to the nucleus. The other contribution to the invariant-mass spectrum of e^+e^- pairs originates mainly from π^0 -Dalitz decays ($\pi^0 \rightarrow e^+e^-\gamma$) with values up to the rest mass of the π^0 . Even larger invariant masses like e.g. those from η -Dalitz decays ($\eta \rightarrow e^+e^-\gamma$) are negligible in this photon analysis. In Fig. 7.8, the invariant mass is shown for true reconstructed e^+e^- pairs having the same mother, in the following called true pairs. As seen, the measurement of the invariant mass helps to separate between e^+e^- pairs from photon conversions and other dielectrons from hadron decays.

Opening Angle of e^+e^- Pairs

The opening angle ϑ of e^+e^- pairs is another interesting variable which is related to the invariant mass by:

$$M_X^2 c^4 = 2(m_e^2 + E_1 E_2 - p_1 p_2 \cos \vartheta). \quad (7.5)$$

Since photons do not have a mass which can contribute to the opening of the pair (and the contribution from the nucleus is small), the electron and positron from a photon conversion propagate almost in the same direction as the parent photon did. Hence, the opening angle ϑ is expected to be close to zero for e^+e^- pairs from photon conversions

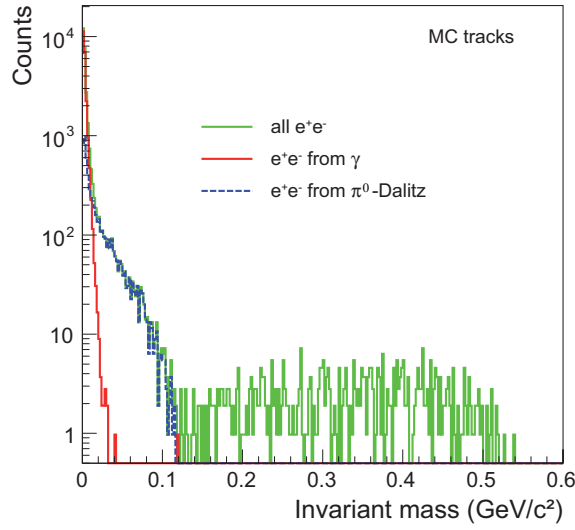


Figure 7.8: Invariant mass of all e^+e^- pairs (green) and the contribution originating from photon conversions (red) and π^0 -Dalitz decays (blue), using the MC information on PID and momentum from the reconstructed tracks. Here, 20,000 UrQMD events from central Au+Au collisions at 25 AGeV beam energy are analyzed.

whereas a broader distribution is expected for e^+e^- pairs from π^0 -Dalitz decays. This is illustrated in Fig. 7.9. Here, the distribution of the reconstructed opening angles is compared to the contribution from photon conversions and π^0 -Dalitz decays.

The measurement of the opening angle can be used to increase the S/B (signal-to-background) ratio of the photon measurement. The ratio of e^+e^- pairs originating from photons to those from π^0 -Dalitz decays increases towards smaller opening angles, which can be seen in the γ - and π^0 -mother contributions in Fig. 7.10 a). The goal is to find an optimal cut for obtaining the largest γ/π^0 -Dalitz ratio and keeping as many photons as possible at the same time. In Fig. 7.10 b), the integrated contributions are displayed as a function of the opening angle cut. When calculating the difference between photon and π^0 -mother contributions a local maximum exists at an opening angle cut of about 1.5° , which corresponds to the intersection in Fig. 7.10 a). In the analysis a somewhat tighter opening angle cut of 1° is applied to remove a larger fraction of fake e^+e^- pairs as described later.

For increasing the γ/π^0 -Dalitz ratio, it can also be useful to apply an even tighter opening-angle cut at higher transverse momenta. In Fig. 7.11, the opening angle is shown as a function of p_T for the reconstructed e^+e^- pairs originating from photon conversions and from π^0 -Dalitz decays. The solid lines in Fig. 7.11 a) and b) show the applied cut on

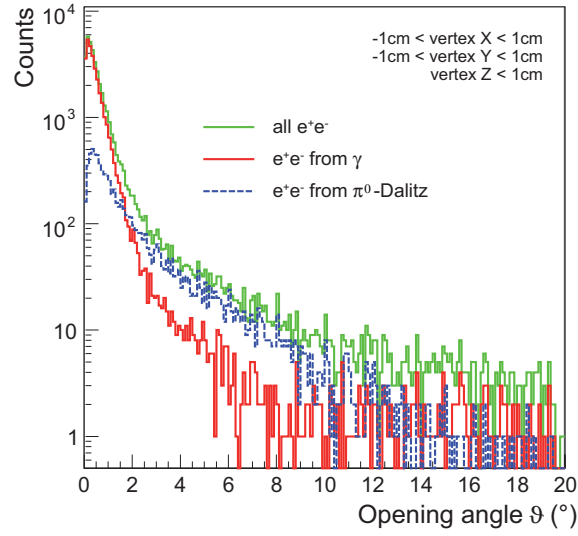


Figure 7.9: Opening angle of all reconstructed e^+e^- pairs (green) and the contribution originating from photon conversions (red) and π^0 -Dalitz decays (blue). Here, 20,000 UrQMD events from central Au+Au collisions at 25 AGeV beam energy are analyzed.

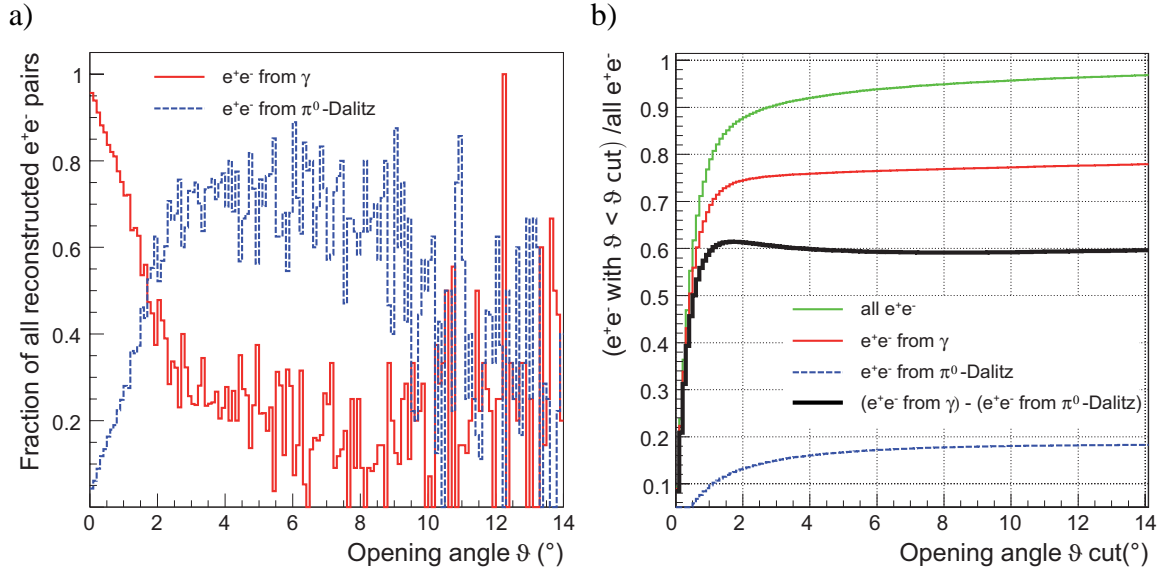


Figure 7.10: a) Fraction of γ and π^0 mothers in all reconstructed e^+e^- pairs as function of opening angle and b) integrated fraction of γ and π^0 mothers in all reconstructed e^+e^- pairs as function of the maximum opening angle cut.

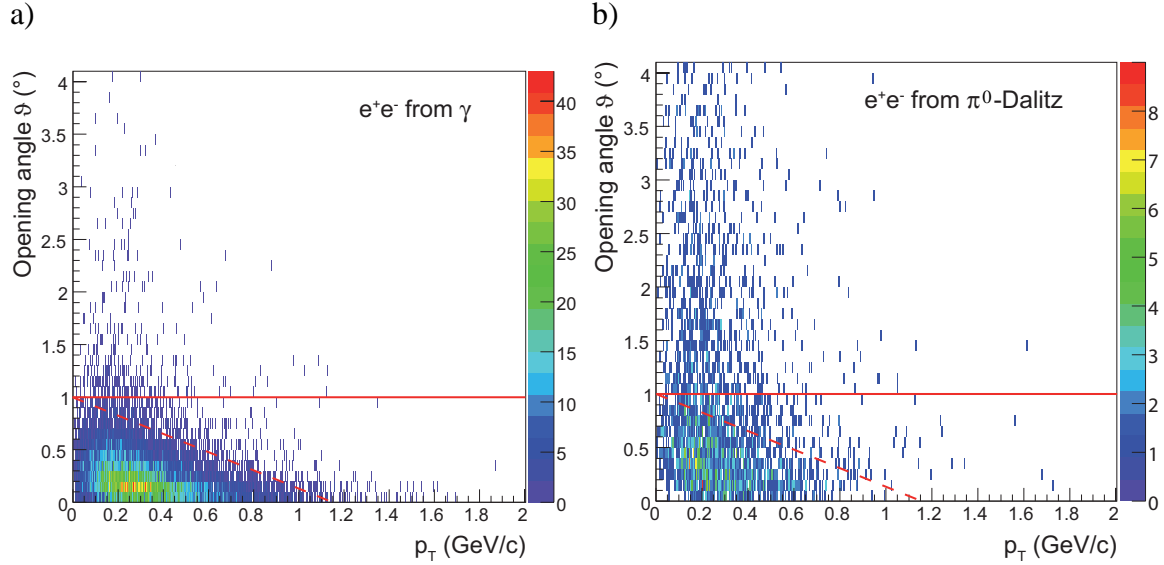


Figure 7.11: Opening angle of reconstructed e^+e^- pairs as function of p_T for the contribution originating a) from photon conversions and b) from π^0 -Dalitz decays. Here, 20,000 UrQMD events from central Au+Au collisions at 25 AGeV beam energy are analyzed.

the opening angle at 1° , and the dashed lines are drawn to indicate the region where the photons are concentrated. In order to investigate a reasonable p_T -dependent cut, especially at higher p_T , much more statistics would be required. In the analysis of 20,000 UrQMD events, which is shown here, a cut like this is expected to have a larger effect at $p_T > 1$ GeV/c, but the statistics is not sufficient to derive a cut and study the effect even below 1 GeV/c. Nevertheless, this cut has to be considered in the analysis of real data from the experiment.

In order to find the optimal analysis cuts in the previous figures, true e^+e^- pairs from the same mother are exclusively shown while ignoring the combinatorial background. In the analysis of real data also fake e^+e^- pairs are reconstructed. These are e^+e^- pairs originating from different mothers misidentified as an associated dielectron pair. The green line in Fig. 7.12 a) shows the opening angle of all reconstructed e^+e^- pairs. Besides the peak at small opening angles of true e^+e^- pairs a large combinatorial background of fake e^+e^- pairs can be seen. A large fraction of this combinatorial background can be removed by limiting the opening angle to $\vartheta = 1^\circ$ (see the close-up view in Fig. 7.12 b)).

The application of the cut on the opening angle already removes the majority of fake e^+e^- pairs. The additional cut on the invariant mass further enhances the γ/π^0 -Dalitz ratio and the fake- e^+e^- -pair rejection (see Fig. 7.13).

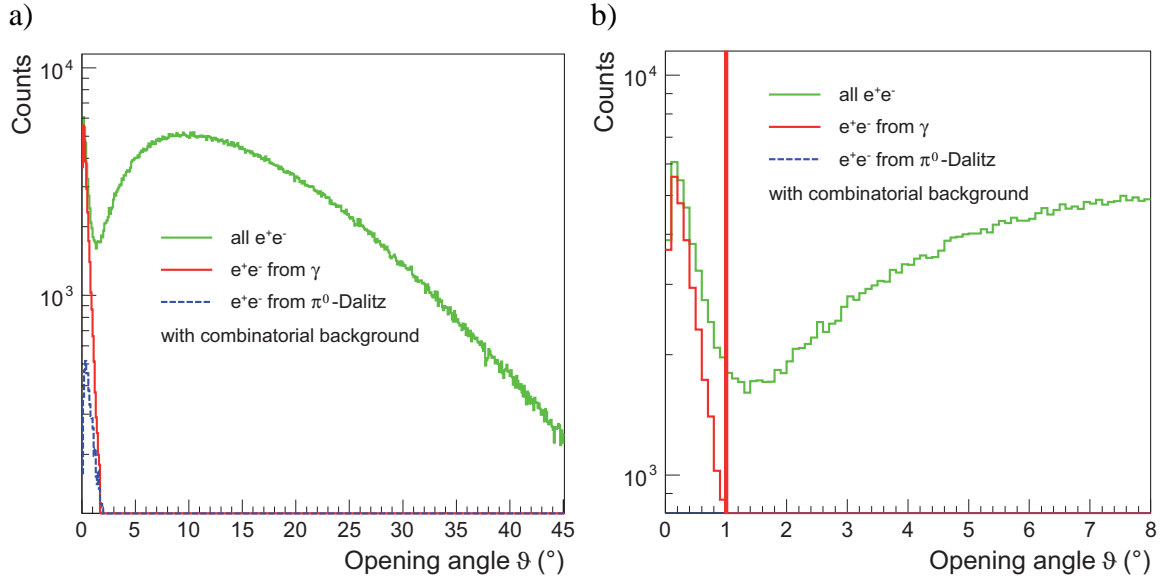


Figure 7.12: a) Opening angle of all reconstructed e^+e^- pairs with full combinatorics (green line) and for the contribution from photon conversions (red) and π^0 -Dalitz decays (blue). In b), a close-up view with the opening angle cut is shown. Here, 20,000 UrQMD events from central Au+Au collisions at 25 AGeV beam energy are analyzed.

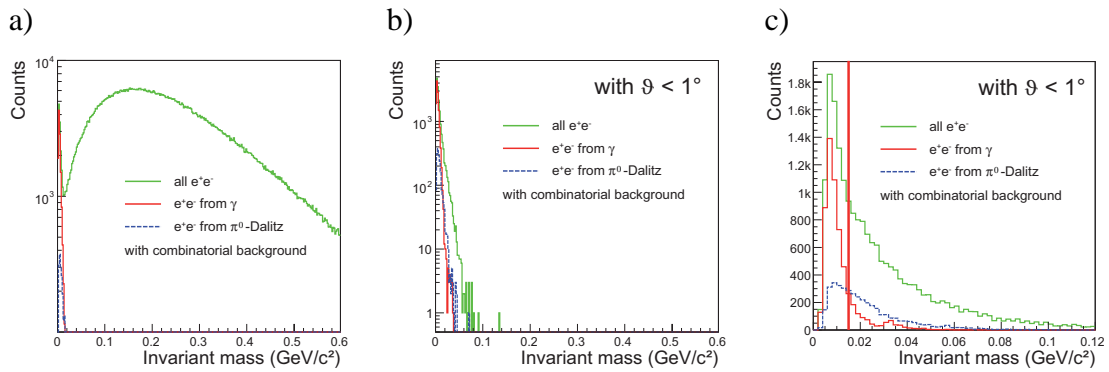


Figure 7.13: Invariant-mass distribution for all reconstructed e^+e^- pairs (green) with full combinatorics and for the contribution from photon conversions (red) and π^0 -Dalitz decays (blue) a) without and b) with the application of the cut on the opening angle. In c), a close-up view with the invariant-mass cut is shown. Here, 20,000 UrQMD events from central Au+Au collisions at 25 AGeV beam energy are analyzed.

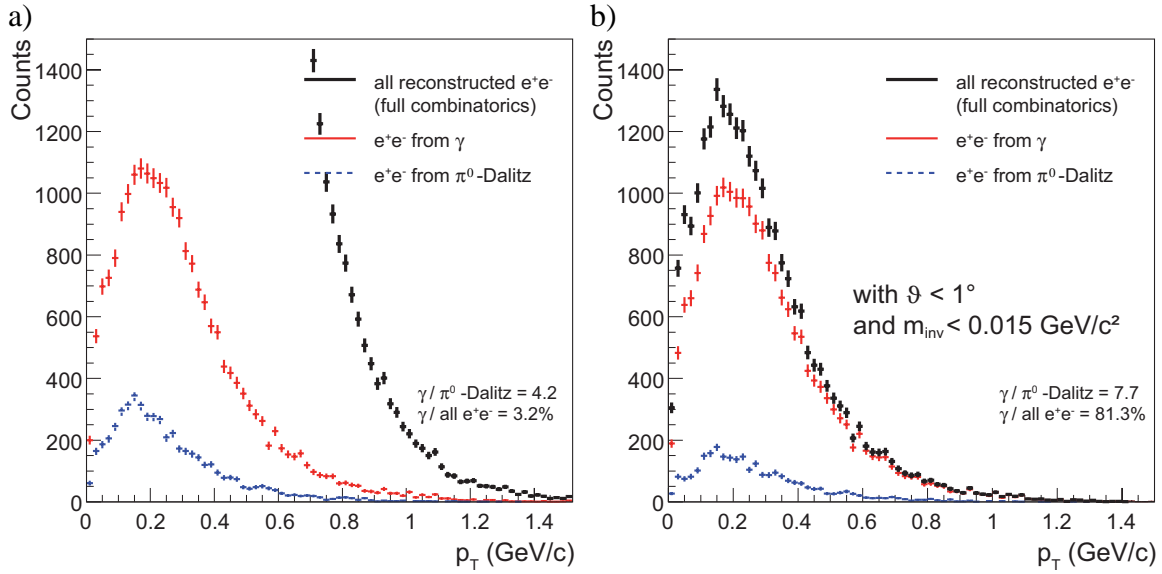


Figure 7.14: p_T distribution of all reconstructed e^+e^- pairs (black) and for the contribution from photon conversions (red) and π^0 -Dalitz decays (blue) a) before and b) after application of a cut on the opening angle and the invariant mass. Here, 20,000 UrQMD events from central Au+Au collisions at 25 AGeV beam energy are analyzed.

In Fig. 7.14, the transverse-momentum (p_T) distribution of the reconstructed e^+e^- pairs is shown before and after application of the cuts on the opening angle and the invariant mass. In total, the γ/π^0 -Dalitz ratio increases from 4.2 to 7.7. The fraction of photons to all (true and fake) reconstructed e^+e^- pairs increases from 3.2% to 81.3%. This is the purity of the reconstructed photon signal.

Inclusive Photon Spectrum

Using the p_T distribution of the reconstructed e^+e^- pairs after application of the quality cuts for the contribution from photons, a raw inclusive photon spectrum can be determined. It shows the p_T distribution of all photons reconstructed via conversions in the target. In Fig. 7.15, the inclusive photon spectrum is shown. The black points represent all direct photons and photons from decays reconstructed from central Au+Au collisions at 25 AGeV beam energy normalized to the number of events and to the p_T bin width.

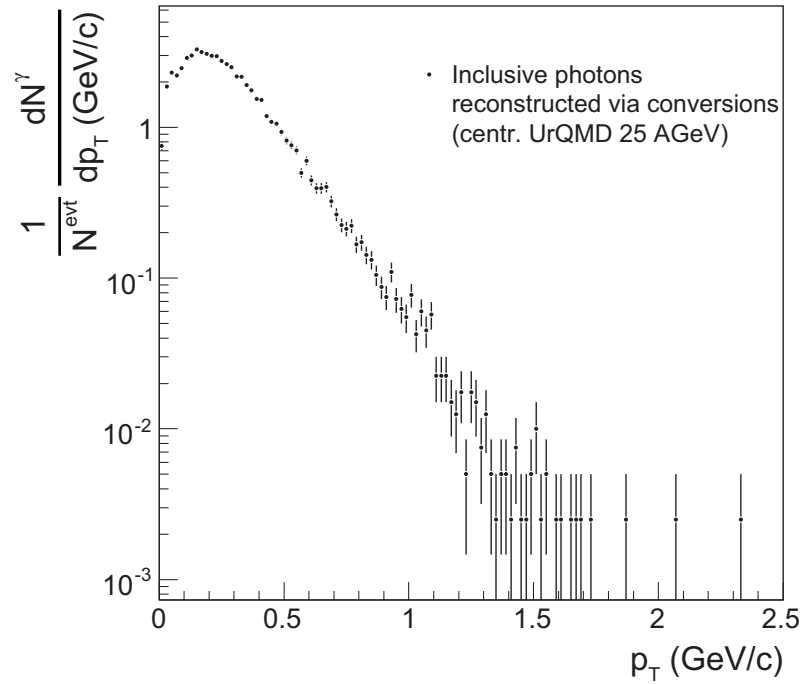


Figure 7.15: Inclusive photons reconstructed via conversions from 20,000 UrQMD events from central Au+Au collisions at 25 AGeV beam energy.

Momentum Resolution of Reconstructed Photons

The momentum resolution of the reconstructed photons is shown in Fig. 7.16. For the determination of the momentum resolution, a pure data set of 10^6 photons, which are uniformly distributed in p_T ($0 \text{ GeV}/c < p_T < 3 \text{ GeV}/c$), Φ ($0^\circ < \Phi < 360^\circ$), and θ ($2.5^\circ < \theta < 25^\circ$), is used. It can be seen that, especially at low momenta (up to $8 \text{ GeV}/c$), a very good resolution of $< 2.5\%$ is obtained, which is considerably better than the expected momentum resolution in a photon measurement with the ECAL (as shown in Chapter 7.4.1). This is mainly due to the good momentum resolution of the charged-particle tracking.

The uniform distribution of the simulated photons in θ is justified since there is no strong theta dependence of the momentum resolution as seen in Fig. 7.17. Here, the resolution is shown for three data sets of $5 \cdot 10^5$ photons each, which are uniformly distributed in different θ regions. A slight improvement of the momentum resolution can be observed for the highest polar angles, which are reached only by photons with momenta below $8 \text{ GeV}/c$.

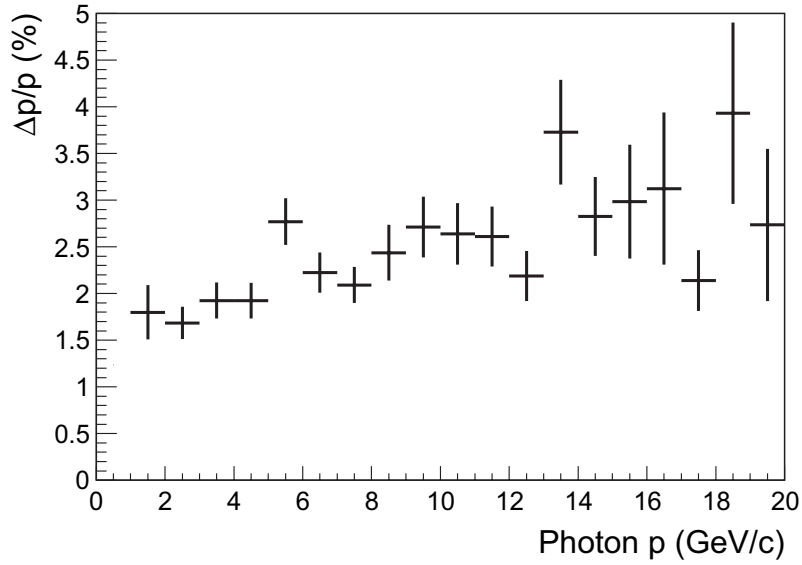


Figure 7.16: Momentum resolution of photons reconstructed via conversions. A flat distribution with a resolution of $< 2.5\%$ for $p < 8 \text{ GeV}/c$ is obtained.

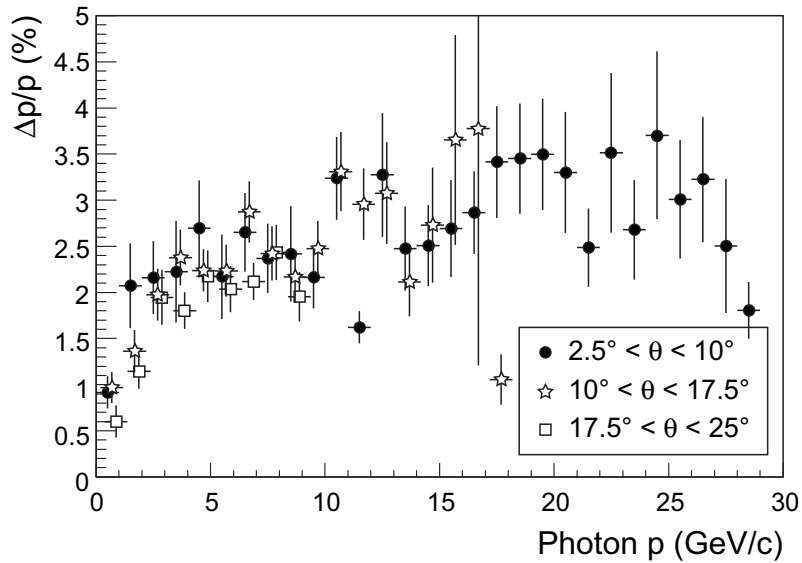


Figure 7.17: Momentum resolution of photons reconstructed via conversions for photons, which are uniformly distributed in different θ regions. The dots label a data set of photons with $2.5^\circ < \theta < 10^\circ$. In order to improve the visibility, the stars ($10^\circ < \theta < 17.5^\circ$) are shifted in momentum by $0.2 \text{ GeV}/c$, and the squares ($17.5^\circ < \theta < 25^\circ$) are shifted by $0.4 \text{ GeV}/c$ in comparison to the first data set.

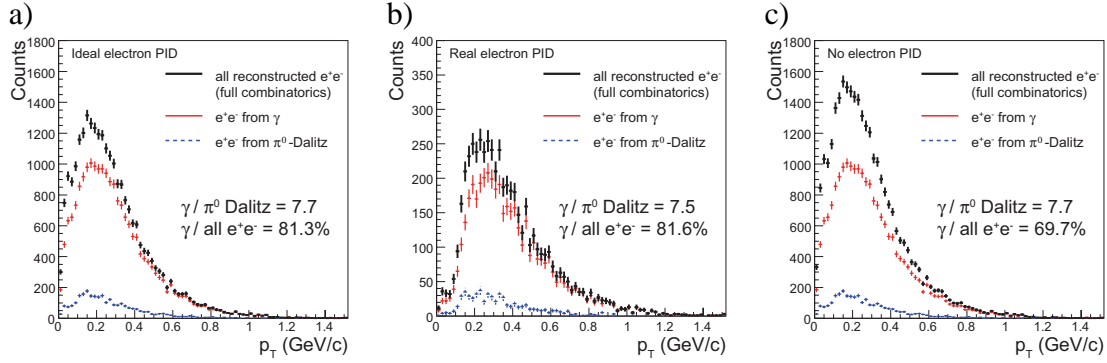


Figure 7.18: Reconstructed photons and purity of the signal from 20,000 UrQMD events (central Au+Au collisions at 25 AGeV beam energy) as function of p_T using a) *ideal electron PID*, b) *real electron PID*, and c) *no electron PID*.

Applied electron PID	Definition
<i>Ideal electron PID</i>	Electron identification using the MC information
<i>Real electron PID</i>	Two out of three detectors (RICH, TRD, and TOF) send positive electron decision
<i>No electron PID</i>	All charged-particle tracks

Table 7.3: Definition of different options for the electron PID conditions.

Reconstruction Efficiency of Photons via Conversions

The efficiency of the photon reconstruction as well as the purity of the reconstructed photon spectrum using the conversion method depend on the conditions applied in the electron identification. Fig. 7.18 shows a comparison of the reconstructed p_T -spectra using a) *ideal electron PID*, b) *real electron PID* and c) *no electron PID*. Here, *ideal electron PID* means that the electrons and positrons are identified using the MC information and *real electron PID* means that two out of three detectors (RICH, TRD, and TOF) have to send a positive electron decision. In the case of *no electron PID* all charged-particle tracks are used. These definitions can also be found in Table 7.3.

The reconstruction efficiency of photon conversions can be determined by dividing the number of reconstructed photons by the number of photons in the MC input spectrum which are in the θ acceptance of the CBM detector. For the determination of this efficiency a pure data set of 10^8 photons is used. The simulated photons are uniformly distributed

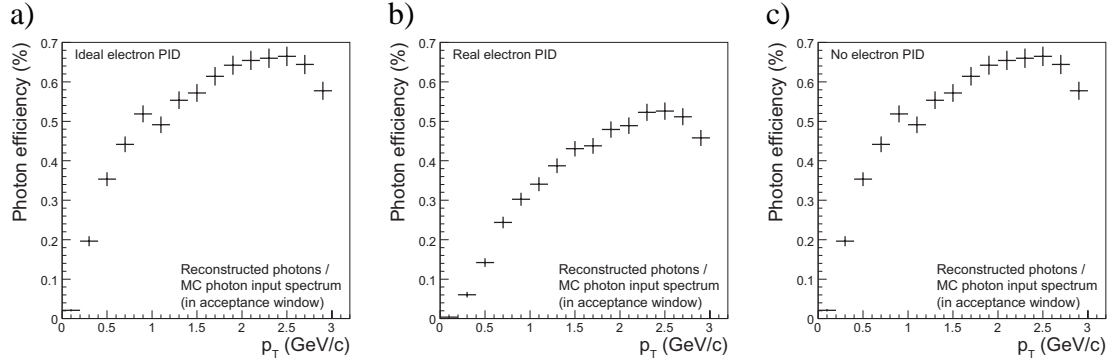


Figure 7.19: Identification probability for photon conversions as function of p_T using a) *ideal electron PID*, b) *real electron PID*, and c) *no electron PID*. The acceptance window for the photon input spectrum is ($2.5^\circ < \theta < 25^\circ$).

in $p_T(0 \text{ GeV}/c < p_T < 3 \text{ GeV}/c)$, $\Phi(0^\circ < \Phi < 360^\circ)$, and $\theta(2.5^\circ < \theta < 25^\circ)$. Due to the constant p_T -spectrum the efficiency can be determined in all p_T regions with sufficient statistical accuracy. In Fig. 7.19, the corresponding photon-reconstruction efficiency is shown for the different conditions with a) *ideal electron PID*, b) *real electron PID*, and c) *no electron PID*.

The photon efficiency decreases towards lower p_T because of the larger curvature for low p_T electrons and positrons in the magnetic field and thus the smaller electron and positron acceptance (note that the acceptance window is only a condition for the photons and not for the daughter particles). The kink in the p_T -dependent efficiency at $p_T = 1 \text{ GeV}/c$ is an artifact due to the chosen track-finding conditions related to the vertex positions of the tracks. In the case of *real electron PID* this effect is smeared because of the lower acceptance and efficiency. The difference to the theoretical conversion probability of photons in the gold target of 2.9% (see Chapter 3.3) is reflected in the sum of losses caused by the electron and positron acceptance and efficiency for the analyses with the different PID conditions.

In the case of *real electron PID* (Fig. 7.18 b)) the purity of the photon signal is about as good as for *ideal electron PID* (Fig. 7.18 a)) whereas the efficiency decreases strongly (as seen in the comparison of Fig. 7.19 b) and a)) because of the electron efficiency of the RICH, TRD, and TOF detectors (see Chapter 7.3). In the strict sense, the photon-signal purity with *real electron PID* conditions is even a little bit better than in an analysis using *ideal electron PID*. This is a consequence of the electron efficiency of the RICH, which

decreases strongly towards lower momenta (see Fig. 7.4a)), where the γ -to- π^0 -Dalitz ratio is low. Thus, a larger number of e^+e^- pairs in a bad-purity p_T region is removed when using *real electron PID*. Since photon-signal purity with *real electron PID* conditions is even better than with *ideal electron PID* it is not necessary to use a stronger definition for *real electron PID* (e.g. a condition that all 3 detectors have to give a positive electron decision), which would further decrease the efficiency.

Owing to the small efficiency an additional comparison to an analysis without any electron PID is shown in Fig. 7.18 c). Here, all negative and positive charged particles are combined. This causes a larger fraction of fake pairs, but due to the cuts on the common vertex, the opening angle, and the invariant mass the purity is still adequate: in this case the photon-signal purity decreases from 81.6% to 69.7%.

The efficiency with *no electron PID* (Fig. 7.19 c)) is as high as for *ideal electron PID* (Fig. 7.19 a)) because when taking all charged tracks, all true e^+e^- pairs from photons are certainly included. The photon efficiency for *real electron PID* (Fig. 7.19 b)) decreases stronger at low p_T because of the electron efficiency in the electron PID detectors. In the real experiment one can compromise on photon-signal purity and efficiency depending on the amount of data that will be recorded. The option of an analysis without any electron PID information is an interesting alternative especially for the measurement of neutral pions described in Chapter 7.5.

7.5 Measurement of Neutral Pions

Due to the large number of potential photon sources and the large multiplicities in heavy-ion collisions, direct-photon identification on an event-by-event basis is not feasible. Instead, they can be measured on a statistical basis. It is possible to compare the inclusive photons on a statistical basis to the expectation from hadron decays, which is determined based on the measurement of π^0 s in the same event sample. By using this method a large fraction of systematic errors, e.g. at normalization and centrality selection, are eliminated.

The measurement of direct photons requires precise knowledge of the contribution from decays (mainly $\pi^0, \eta \rightarrow \gamma\gamma$) to the inclusive photon spectrum. Owing to their larger mass η -mesons are produced less frequently than neutral pions. In addition, the branching ratio of $\eta \rightarrow \gamma\gamma$ is smaller (only 39.3% in comparison to 98.8% in case of the π^0 [Yao06]). Hence, this signal reconstructed by photon conversions is very small and is not investigated in this analysis.

A useful quantity is the double ratio of the yield of photons per π^0 for the measured spectra and the simulation:

$$\frac{N^\gamma/N^{\pi^0}|_{\text{meas}}}{N^\gamma/N^{\pi^0}|_{\text{bkgd}}}. \quad (7.6)$$

An enhancement of photons compared to the expectation from hadron decays is attributed to a direct-photon signal. Moreover, the π^0 measurement employing the same method provides a good cross check for the method of photon measurement.

The identification probability of neutral pions using the photon-conversion method is very low because both decay photons have to convert, and all four originating lepton tracks have to be reconstructed. With a theoretical conversion probability of a photon in the target of about 2.9% the production probability of four leptons from a π^0 is only about 8×10^{-4} . In Fig. 7.20 a), the invariant-mass distribution of the reconstructed π^0 s from 5,000 central Au+Au collisions is shown. Here, the peak extraction has been initially done using the MC information of the photon mothers.

In order to increase the π^0 -signal especially at high p_T a data set is simulated in which 1,000 π^0 s uniformly distributed in $p_T(0 \text{ GeV}/c < p_T < 3 \text{ GeV}/c)$ is included into every UrQMD event. By using this method the pion-reconstruction efficiency can be determined for all interesting p_T regions. The number of 1,000 embedded π^0 s considerably exceeds the overall multiplicity of π^0 s in central Au+Au collisions at 25 AGeV beam energy, which is about 300 per event within the detector acceptance. However, the additional particles do not cause any problems in the reconstruction as the number of charged-particle tracks does not strongly increase because of the small photon-conversion probability. The total number of reconstructed π^0 s increases by a factor of 22 (see Fig. 7.20 b)).

For the purpose of a larger electron acceptance at low p_T a special ‘dilepton setup’ of the STS in conjunction with a reduced magnetic field is also tested. The surface area of the STS stations is increased by a factor of 1.5 and the magnetic field is reduced to 70%. The corresponding invariant-mass distribution of reconstructed π^0 s is presented in Fig. 7.20 c). The ratio of the π^0 -signals measured with the ‘dilepton setup’ and the standard setup is shown in Fig. 7.21. In comparison to the standard setup the π^0 -reconstruction efficiency is increased at low p_T due to the larger acceptance for low momentum electrons in the larger STS stations. But the probability slightly decreases for higher p_T because of the worse dielectron separation in the lower magnetic field.

A further analysis is done with a thicker gold target to increase the photon-conversion probability. The theoretical conversion probability in a 500 μm target is 3.8 times higher than in the 250 μm standard target. In the analysis the thicker target results in a 3.1 times

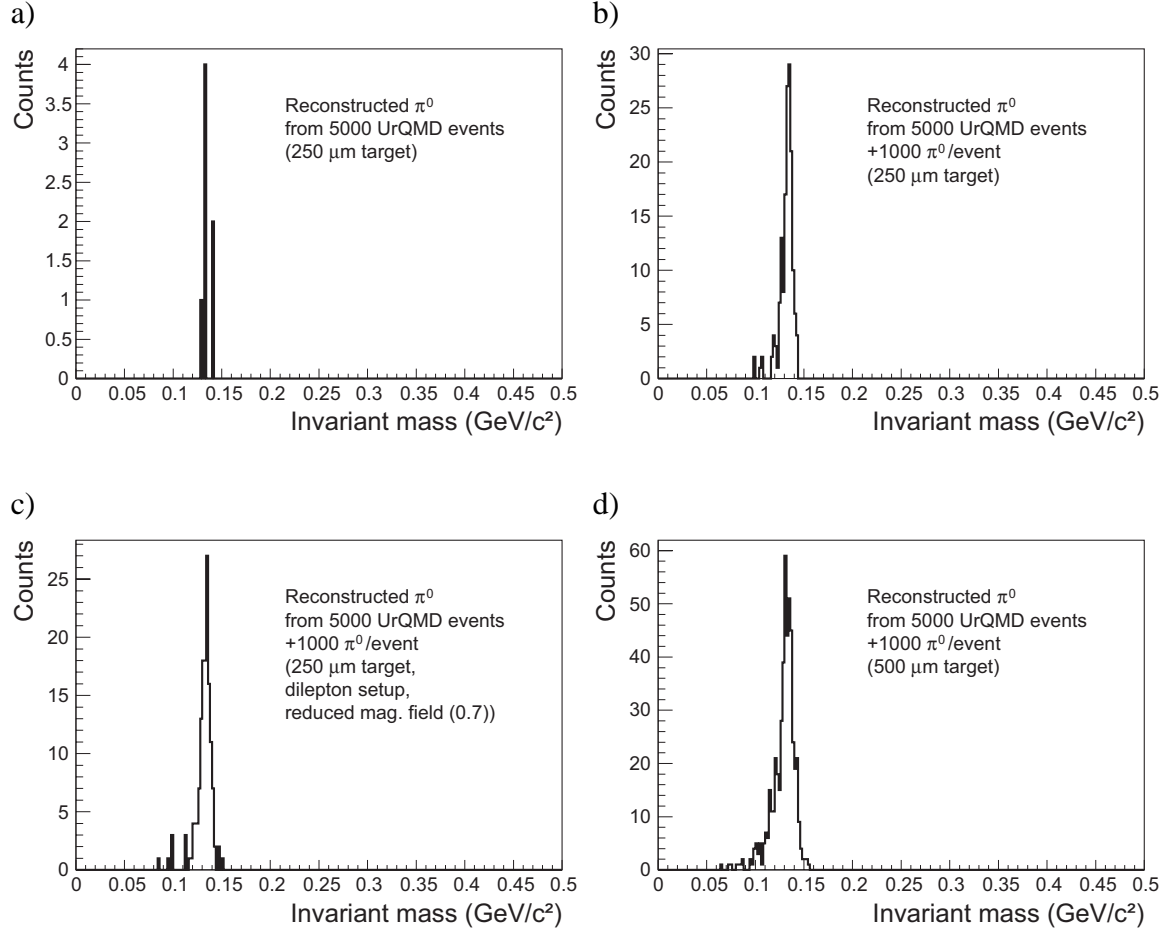


Figure 7.20: Invariant-mass distribution of π^0 s reconstructed via photon conversion from a) 5,000 UrQMD events (central Au+Au collisions at 25 AGeV beam energy) and b) of 5,000 UrQMD and additional 1,000 π^0 s per event, c) using the ‘dilepton setup’ of the STS and, d) using a 500 μm gold target.

higher pion-reconstruction probability. Nevertheless, in the following analysis the standard STS geometry with nominal magnetic field and a standard gold target is used since it is currently the most probable setup for the CBM experiment and also used in many other analyses.

7.5.1 Extraction of the π^0 -Signal

The π^0 -signal can be determined by an invariant-mass analysis of photon pairs. Using the reconstructed photons (see Chapter 7.4.2) the combination of all $\gamma\gamma$ pairs is built (as seen in Fig. 7.22).

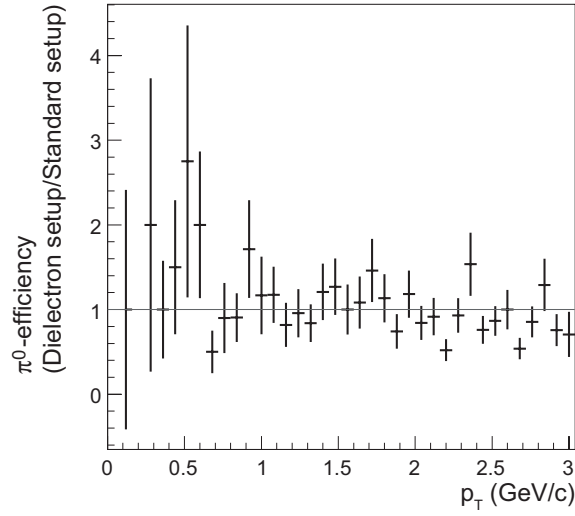


Figure 7.21: Ratio of the amount of reconstructed π^0 s using the ‘dilepton setup’ to reconstructed π^0 s using the standard setup of the STS as function of p_T .

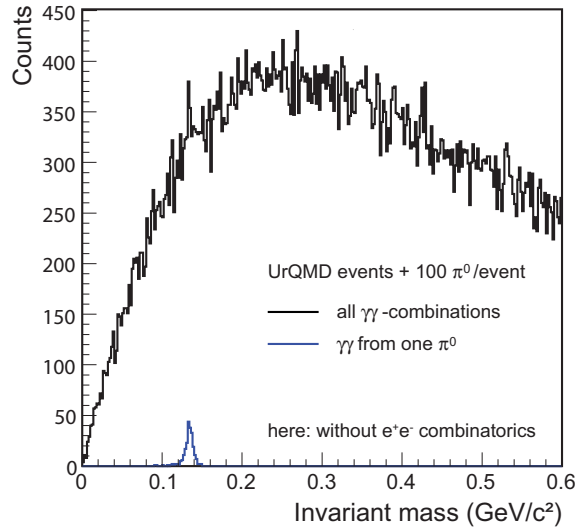


Figure 7.22: Invariant mass of all reconstructed $\gamma\gamma$ pairs, the blue line shows those with true π^0 mothers (obtained from the MC PID information). This analysis is performed only with true e^+e^- pairs (no fake pairs). Here, 20,000 UrQMD events from central Au+Au collisions at 25 AGeV beam energy are analyzed. In addition, 100 π^0 s, uniformly distributed in p_T ($0 \text{ GeV}/c < p_T < 3 \text{ GeV}/c$), are embedded into every event.

Considering all possible photon-photon combinations leads to a large combinatorial background in addition to the π^0 -signal. This background increases quadratically with the multiplicity N . The number of possible pair combinations is

$$N_{\text{pair}} = \frac{N}{2} \cdot (N - 1).$$

The π^0 yield can be determined by subtracting the combinatorial background. For the determination of dN_{π^0}/dp_T distributions the invariant-mass spectra are investigated for different intervals of the transverse momentum.

For the measured photon pairs the combinatorial background can be reduced by using the phase-space distribution of the photons in a π^0 -decay. The probability for a decay photon to carry a fraction x of the pion's energy is the same for all values of x between 0 and β , where β is the velocity of the π^0 in units of c . For sufficiently large momenta, β approaches 1. This is equivalent to the expectation that the *asymmetry* α of the two photon energies, defined by Equation 7.7, has a flat distribution.

$$\alpha = \frac{E_1 - E_2}{E_1 + E_2} \quad (7.7)$$

For random combinations within one event the asymmetry is not flat. Due to the steeply falling energy distribution of all detected particles from a heavy-ion collision, pair combinations containing one hit with lower energy are more probable. Hence, a measured asymmetry distribution increases towards larger values of α . In the measured data the background from uncorrelated photon pairs can be reduced by an asymmetry cut removing pairs with large values of α . In this simulation this is not possible because of the flat p_T input spectrum of the π^0 which is necessary to calculate the efficiency also at higher p_T . However, in an analysis of real data this can be a helpful tool which should be considered.

Determination of Combinatorial Background Using Mixed Events

The combinatorial background of combined particle properties like the invariant mass of a photon pair can be determined through *event mixing*. Here, the result obtained by combining particles within one event is compared to the result for particle combinations from different events, which are by definition not correlated. In this analysis the mixed-events distribution is determined by combining one photon with all other photons of previous events. The number of previous events used for the pair combinations determines the statistical error of the combinatorial background; in this analysis a buffer of three previous events is used for event mixing with the current event. Fig. 7.23 shows the invariant-mass

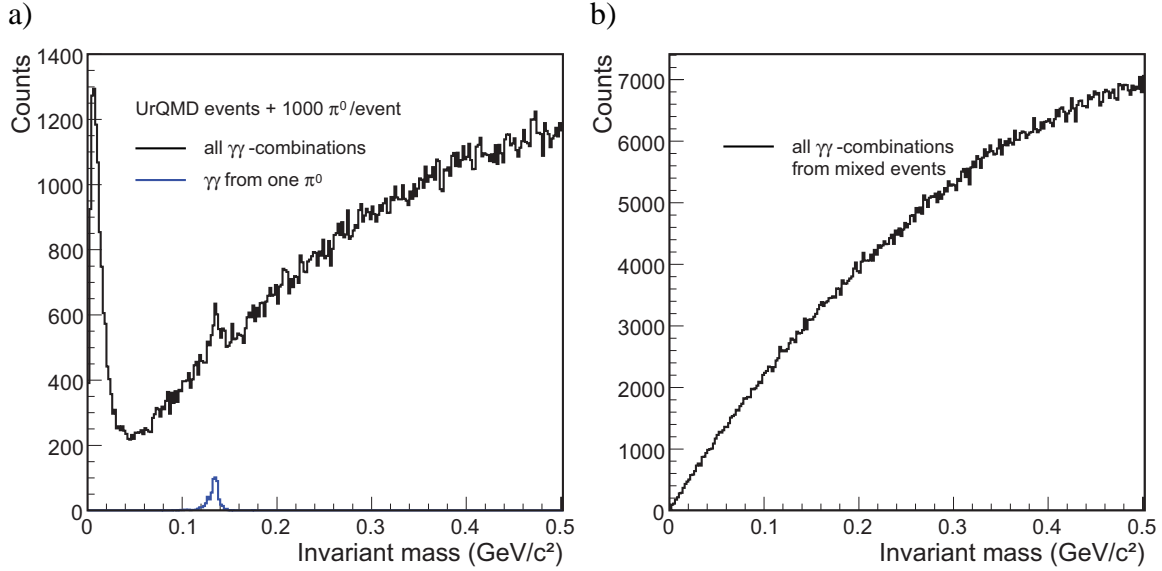


Figure 7.23: Invariant mass of a) all reconstructed $\gamma\gamma$ pairs in the same event and b) from mixed events. This analysis is performed with full e^+e^- combinatorics (true and fake e^+e^- pairs). Here, 20,000 UrQMD events from central Au+Au collisions at 25 AGeV beam energy are analyzed. In addition, 1,000 π^0 s, uniformly distributed in $p_T(0 \text{ GeV}/c < p_T < 3 \text{ GeV}/c)$, are embedded into every event.

distribution of all reconstructed photon pairs a) from the same event and b) from mixed events.

Unlike in Fig. 7.22, where only true e^+e^- pairs having the same mother are considered, now real events with full e^+e^- combinatorics (true and fake e^+e^- pairs) are used for the photon reconstruction. The invariant-mass spectrum of all reconstructed $\gamma\gamma$ pairs is illustrated in Fig. 7.23 a). The additional peak at small invariant masses is due to residual correlations, which are not seen in mixed events (see Fig. 7.23 b)). This peak is caused by fake e^+e^- pairs, which are electrons and positrons originating from different mothers and being misidentified as a dielectron pair and passing the photon identification cuts. In spite of the very efficient Kalman-filter method with all its conditions (e.g. a cut on X^2), there is always a fraction of fake pairs in the dielectron reconstruction caused by electrons and positrons, which are independently produced in close vicinity of each other.

Fig. 7.24 shows the invariant-mass distribution of the fake e^+e^- pairs after application of the cut on the opening angle. It can be seen that the fake e^+e^- pairs are predominantly reconstructed at small invariant masses with a maximum at about $9 \text{ MeV}/c^2$. Thus, the correlation peak also appears in the invariant-mass spectrum when combining all reconstructed $\gamma\gamma$ pairs, which contain these fake e^+e^- pairs. In the analysis, the number of fake

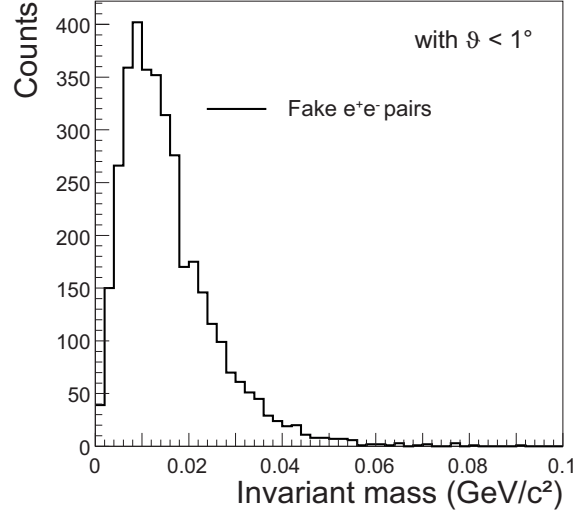


Figure 7.24: Invariant-mass distribution for fake e^+e^- pairs with the application of the cut on the opening angle. Here, 20,000 UrQMD events from central Au+Au collisions at 25 AGeV beam energy are analyzed.

e^+e^- pairs has been reduced by the cut on the invariant mass of the reconstructed e^+e^- pairs (the applied cut is shown in Fig. 7.13c)). With the condition $m_{\text{inv},e^+e^-} < 15 \text{ MeV}/c^2$, the peak in the invariant-mass spectrum of reconstructed $\gamma\gamma$ pairs is sufficiently small and does not disturb the π^0 analysis since it does not reach the mass region of π^0 (as seen in Fig. 7.23 a)).

Before the mixed-event background $M(p_T, m_{\text{inv}})$ can be subtracted from the invariant-mass distribution of real events $R(p_T, m_{\text{inv}})$, it has to be scaled to consider the increased number of pair combinations in the mixed events:

$$M_{\text{scaled}}(p_T, m_{\text{inv}}) = f \cdot M(p_T, m_{\text{inv}}). \quad (7.8)$$

The scaling function f can be determined by dividing the real and the mixed invariant-mass distributions (see Fig. 7.25).

Here, f is obtained by fitting a constant function to the ratio in the range $140 \text{ MeV}/c^2 < m_{\text{inv}} < 1 \text{ GeV}/c^2$. In Fig. 7.26, the resulting normalized background for different p_T is shown together with the invariant-mass distribution from real events.

After subtraction of the background a π^0 -peak can be extracted (see Fig. 7.27). The sigma of a Gaussian fit to the π^0 -peak has a value of about $6 \text{ MeV}/c^2$. The invariant-mass distribution of the real events is integrated in the peak region to obtain the raw π^0 yield in this p_T range. For example, in the p_T region of $1.5 - 2 \text{ GeV}/c$, 90 π^0 s are reconstructed

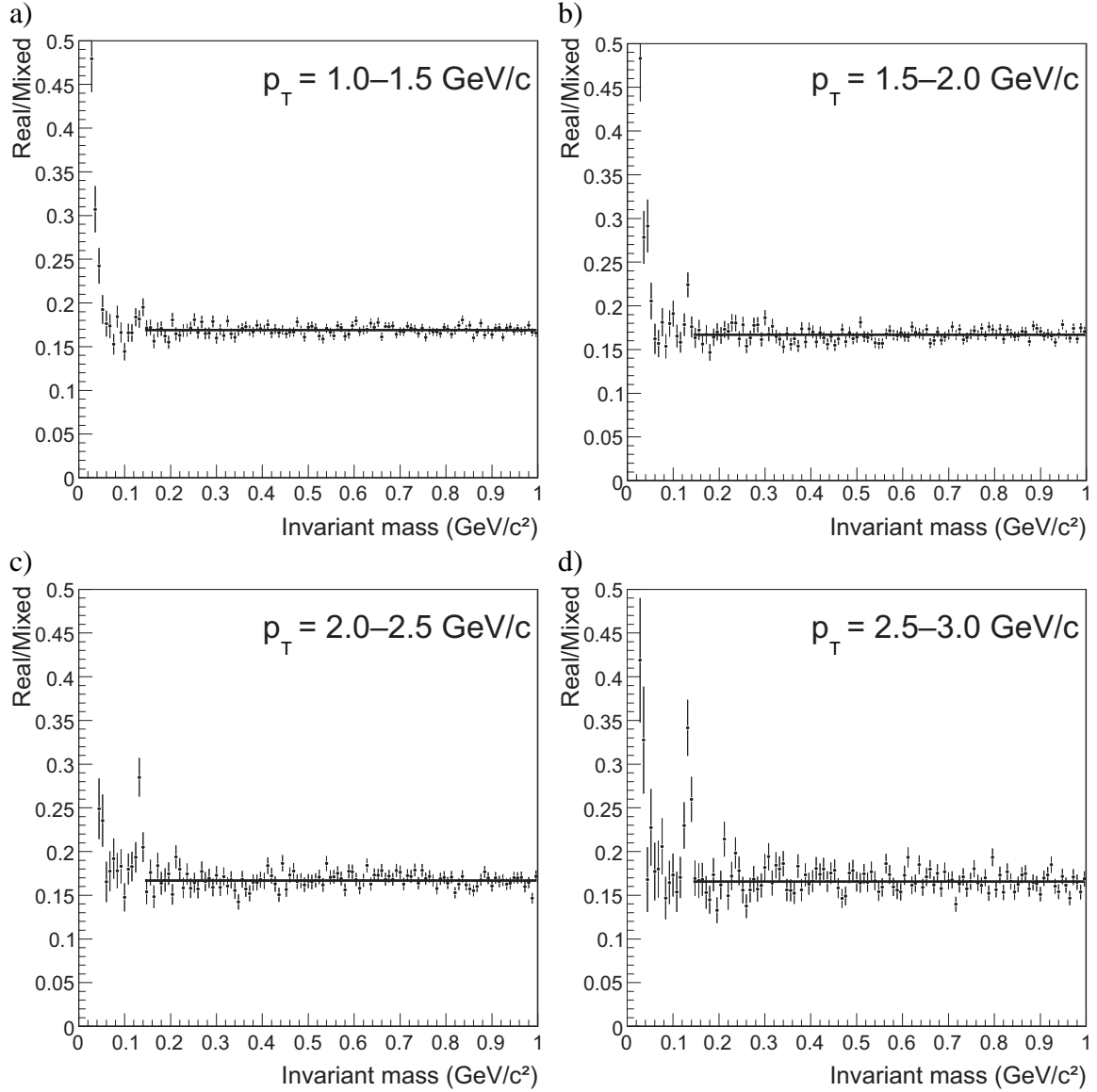


Figure 7.25: The ratio of the invariant-mass distributions of $\gamma\gamma$ pairs from real and mixed events for different p_T bins used to obtain the scaling function f . Here, 20,000 UrQMD events from central Au+Au collisions at 25 AGeV beam energy are analyzed. In addition, 1,000 π^0 s, uniformly distributed in p_T ($0 \text{ GeV}/c < p_T < 3 \text{ GeV}/c$), are embedded into every event. Here, an *ideal electron PID* is applied.

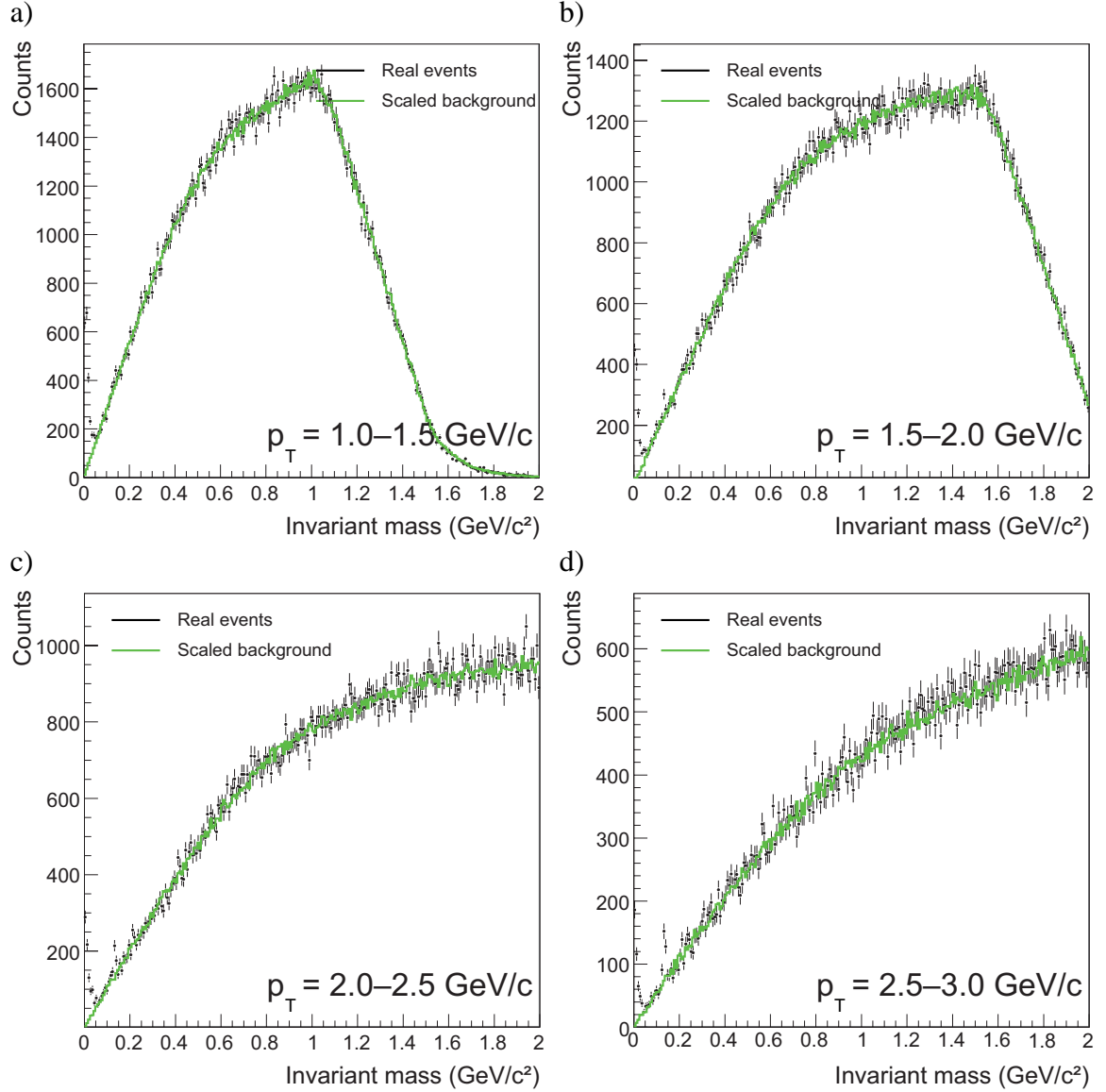


Figure 7.26: Invariant-mass distribution of $\gamma\gamma$ pairs for real events (full circles) and normalized background (green line). Here, 20,000 UrQMD events from central Au+Au collisions at 25 AGeV beam energy are analyzed. In addition, 1,000 π^0 s, uniformly distributed in $p_T(0 \text{ GeV}/c < p_T < 3 \text{ GeV}/c)$, are embedded into every event. Here, an *ideal electron PID* is applied.

from a total of 20,000 UrQMD events (central Au+Au collisions at 25 AGeV beam energy) each with 1,000 embedded π^0 s.

In addition, the S/B ratio is shown for the different p_T regions. It ranges between 4.9% and 36.4% for $1 \text{ GeV}/c < p_T < 3 \text{ GeV}/c$. This S/B ratio is very good, also in comparison to the overall S/B ratio of 0.3% (for all momenta of central Au+Au collisions at 25 AGeV beam energy) obtained with the ECAL measurement. Nevertheless, the measured S/B ratio strongly depends on the number of photons, which is influenced by the input spectrum, the acceptance, and the photon ID cuts. Note that the S/B ratio is calculated for a π^0 input spectrum that has a uniform distribution in p_T ($0 \text{ GeV}/c < p_T < 3 \text{ GeV}/c$), which is not realistic for a nucleus-nucleus collision, where the spectrum is usually exponential with a typical inverse slope of about 185 MeV plus contribution from hydrodynamic expansion (as measured in central Pb+Pb collisions at 158 AGeV [Agg99]).

The efficiency for reconstructing π^0 s by using this method is shown in Fig. 7.28 a). It is calculated by dividing the reconstructed π^0 -signal by the π^0 s from the MC input spectrum in the detectors' acceptance window ($2.5^\circ < \theta < 25^\circ$, $\Delta\eta = 2.3$). The low overall reconstruction efficiency is a consequence of the photon-reconstruction efficiency entering in quadrature. In addition, the efficiency decreases towards lower p_T because of the larger opening angle for photon pairs. This reduces the geometrical acceptance. This efficiency can be used to determine the statistics which will be needed for reconstructing a reasonable π^0 -spectrum. The efficiency is multiplied with the π^0 -signal of an UrQMD spectrum of central Au+Au collisions at 25 AGeV beam energy; the resulting spectrum is presented in Fig. 7.28 b). This spectrum shows the average number of reconstructed π^0 s in one UrQMD event. E.g. one can deduce that $1.39 \cdot 10^8$ UrQMD events lead to 100 π^0 s at 2 GeV/c (with a bin width dp_T of 160 MeV/c).

For an event rate of e.g. 250 kHz, the 10% most central events (selected by the PSD) are recorded. Thus, 25 kHz is the maximum data recording rate for Au+Au collisions without any trigger. With an expected data storage rate of 20 kHz in the experiment, it would take 2 hours of data taking to obtain a π^0 -signal at 2 GeV/c ($dp_T = 160 \text{ MeV}/c$) of the same size as the one which can be seen in Fig. 7.27 b), with decreasing yield towards larger p_T .

The π^0 -signal in the p_T range of 1.5 – 2 GeV/c (see Fig. 7.27 b)) was determined with a statistical error of 41.9%. In order to determine the statistical error of the number of measured π^0 s, the number of the measured $\gamma\gamma$ pairs (N) is used together with the number of correlated (S) and the number of uncorrelated (B) $\gamma\gamma$ pairs in the integration interval of the real-events distribution. The distribution was already shown in Fig. 7.26b).

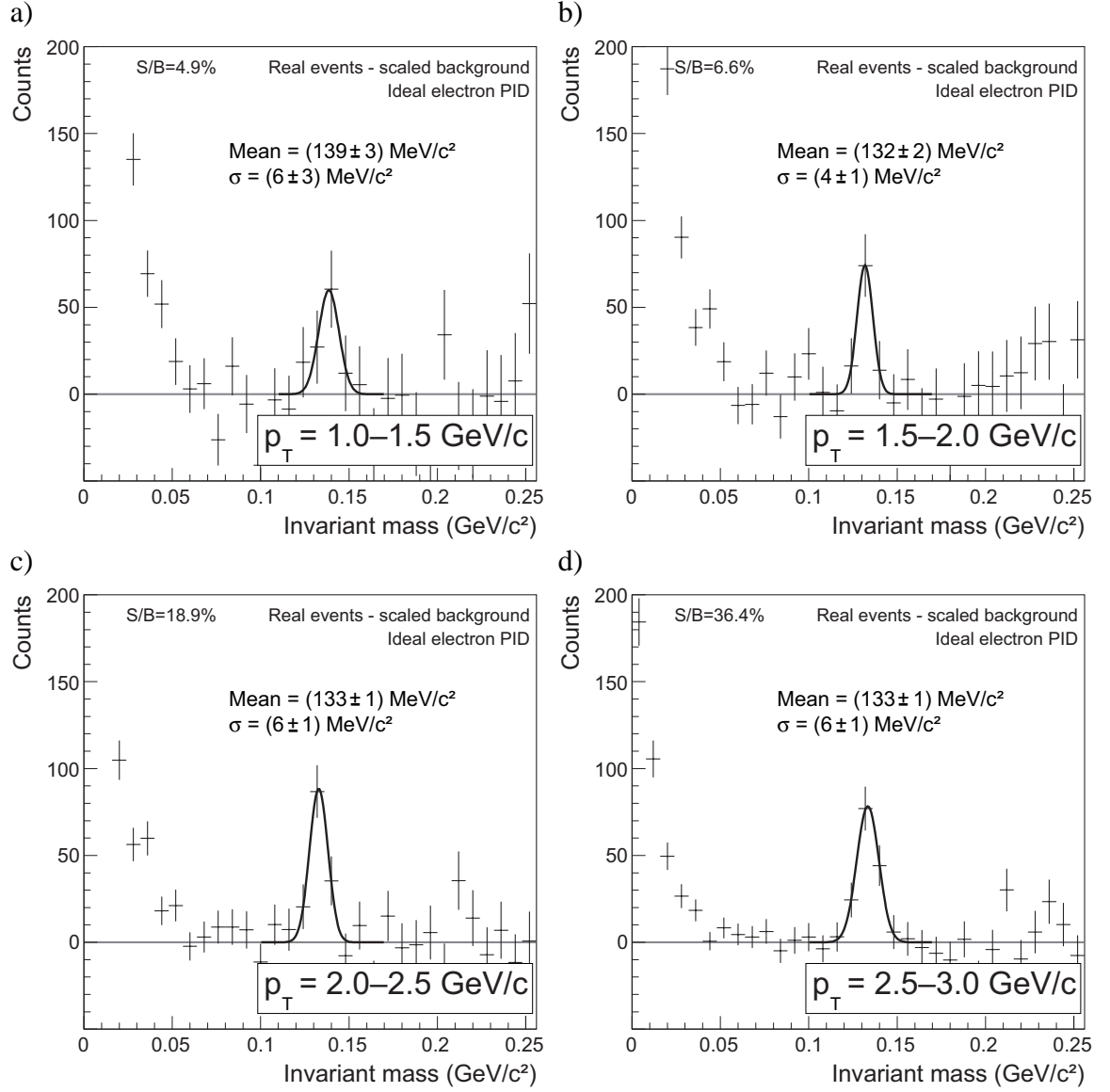


Figure 7.27: Invariant-mass distribution of $\gamma\gamma$ pairs after background subtraction for *ideal electron PID*. Here, 20,000 UrQMD events from central Au+Au collisions at 25 AGeV beam energy are analyzed. In addition, 1,000 π^0 s, uniformly distributed in $p_T(0 \text{ GeV}/c < p_T < 3 \text{ GeV}/c)$, are embedded into every event.

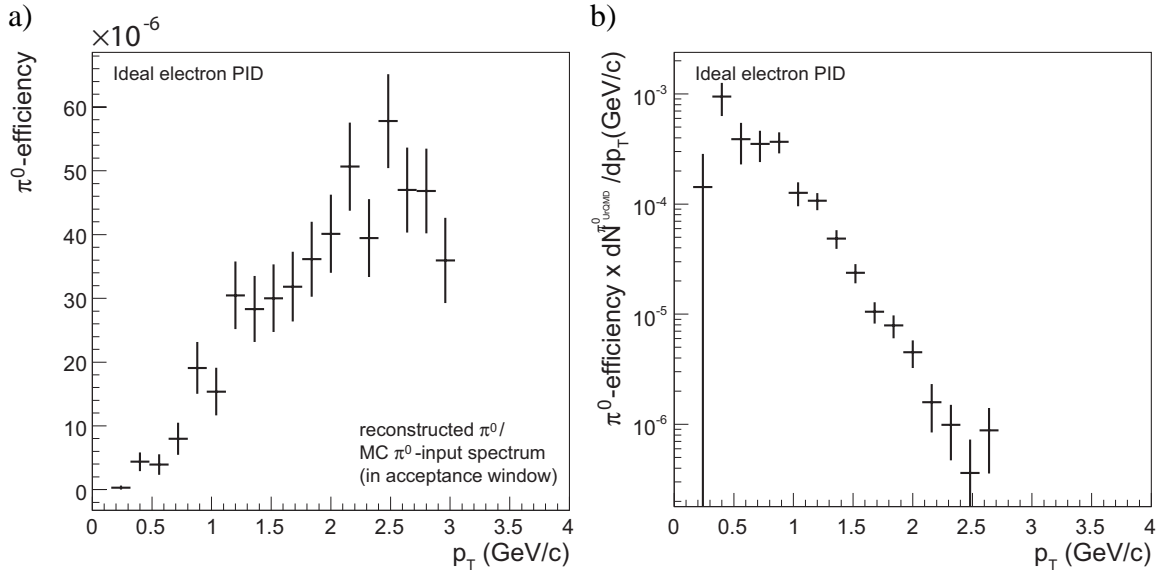


Figure 7.28: a) π^0 -reconstruction efficiency and b) the average number of reconstructed π^0 s as function of p_T in one UrQMD event (central Au+Au events at 25 AGeV beam energy), both for *ideal electron PID*.

The statistical error is approximated to [Bat02]:

$$\sigma^2(S') = S' + B' + \sigma^2(k)M^2 + k^2M, \quad (7.9)$$

where $S' = N - kM$ is the estimated number of correlated photons, and $B' = kM$ is the estimated background of uncorrelated photons determined by the invariant-mass distribution in the same integration interval. Here, M denotes the number of measured $\gamma\gamma$ pairs in the integration interval of the invariant-mass distribution, and k is the scaling factor of the background as shown in Fig. 7.25b). σ is the error with the assumption that N and M are Poisson-distributed. For $\sigma(k)$, the error of the constant fit to the ratio of the invariant-mass distributions of $\gamma\gamma$ pairs from real and mixed events was taken.

One can estimate that the statistical error in the p_T range of $1.5 - 2$ GeV/c can be reduced from 41.9% to $< 6.6\%$ when increasing the data taking time by a factor of 100 (200 hours).

The raw π^0 yield as well as the efficiency of the π^0 reconstruction depend on the electron PID conditions. For an analysis with *real electron PID* (two out of three detectors – RICH, TRD, TOF – have to send a positive electron decision) the π^0 -peak extraction is illustrated in Fig. 7.29. The corresponding efficiency is shown in Fig. 7.30 a). As it is expected, the π^0 -reconstruction efficiency is comparable to the quadratic photon-

reconstruction efficiency whereas it shows a stronger decrease towards lower p_T ($< 1 \text{ GeV}/c$) (compare Fig. 7.30 a) and Fig. 7.19 a)).

It is also multiplied with the π^0 -signal of an UrQMD spectrum of central Au+Au collisions at 25 AGeV beam energy and the resulting spectrum is displayed in Fig. 7.30 b). For the reconstruction of $100 \pi^0$ s at $2 \text{ GeV}/c$ ($dp_T = 160 \text{ MeV}/c$), $5 \cdot 10^8$ UrQMD events are required. With an expected data storage rate of 20 kHz in the experiment this would take 7 hours of data taking.

In order to increase the efficiency the same analysis is done without applying any electron PID conditions. For this analysis the π^0 -peak extraction is presented in Fig. 7.31 and the efficiency is shown in Fig. 7.32 a). In this case the data taking for the π^0 analysis takes as long as for the theoretical *ideal electron PID* case. When comparing the average number of reconstructed π^0 s from one UrQMD event, which is shown for *no electron PID* in Fig. 7.32b), the data taking time can be reduced by a factor of 3.6 in comparison to an analysis with *real electron PID*.

The sigma of a Gaussian fit to the π^0 -peak has a value of about $6 \text{ MeV}/c^2$. With a typical calorimeter photon measurement, e.g. an analysis of Pb+Pb collisions in the WA98 experiment, a π^0 -peak width of $10 \text{ MeV}/c^2$ is obtained for peripheral collisions, and this π^0 -peak width increases to $\sim 13 \text{ MeV}/c^2$ for central collisions [Blu98]. These values were measured in an $(m_T - m_0)$ region of $0.3 - 2 \text{ MeV}/c^2$ for peripheral collisions and $0.3 - 2.9 \text{ MeV}/c^2$ for central collisions. Another calorimeter photon measurement was done in the analysis of p+p collisions in the PHENIX experiment, where a π^0 -peak width of $10 - 15 \text{ MeV}/c^2$ is obtained in the p_T region $0 - 3 \text{ GeV}/c$ [Zau07]. Of course, this is not a straight forward comparison since PHENIX is a collider experiment. In a fixed target experiment (like WA98 and CBM), the Lorentz boost is helpful as for a given p_T the photon energy is much higher and hence the energy resolution is better. For the CBM ECAL, a π^0 -peak width of 9 MeV, integrated over all momenta, is expected from current simulations [CBM09a]. The smaller width of the π^0 -peak reconstructed via photon conversions is due to the good momentum resolution of the electron tracking.

The results encourage a photon and π^0 measurement via conversions with the CBM experiment. Of course, the reconstruction efficiency of photons and in particular for π^0 s using the conversion method is much lower than the one with an ECAL measurement: by simulations with CbmRoot for the CBM ECAL, a reconstruction efficiency of 35 – 40% is expected for photons with $E > 0.5 \text{ GeV}$ [CBM09a]. But since the combinatorial background of photon pairs decreases quadratically, the low efficiency of the conversion method leads to a better S/B ratio between 4.9% and 37.6% for $1 \text{ GeV}/c < p_T < 3 \text{ GeV}/c$ in the π^0 measurement. Moreover, the very good momentum resolution of the photon as well as of the π^0 -reconstruction obtained by using the conversion method provides an

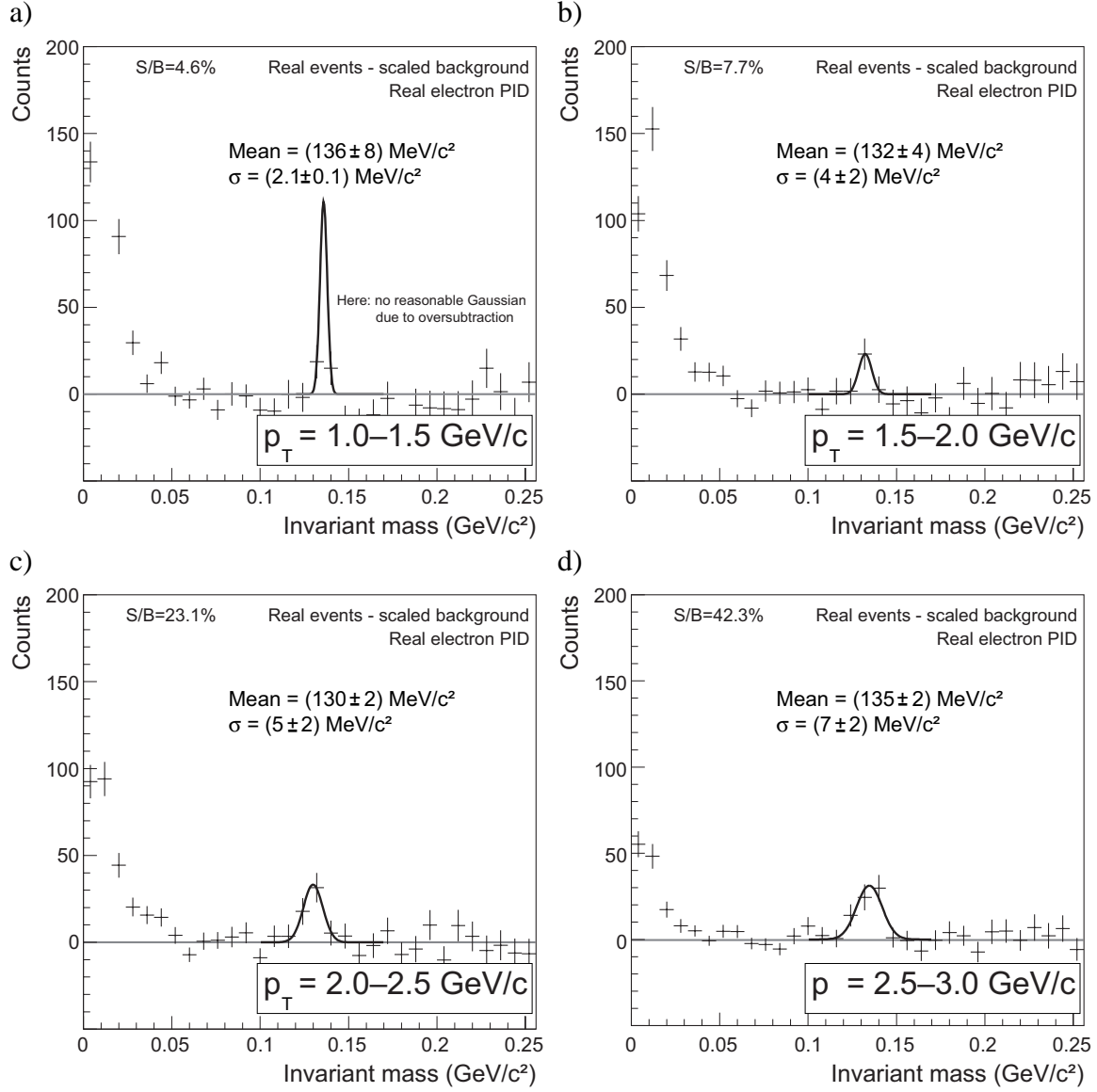


Figure 7.29: Invariant-mass distribution of $\gamma\gamma$ pairs after background subtraction for *real electron PID*. Here, 20,000 UrQMD events from central Au+Au collisions at 25 AGeV beam energy are analyzed. In addition, 1,000 π^0 s, uniformly distributed in $p_T(0 \text{ GeV}/c < p_T < 3 \text{ GeV}/c)$, are embedded into every event.

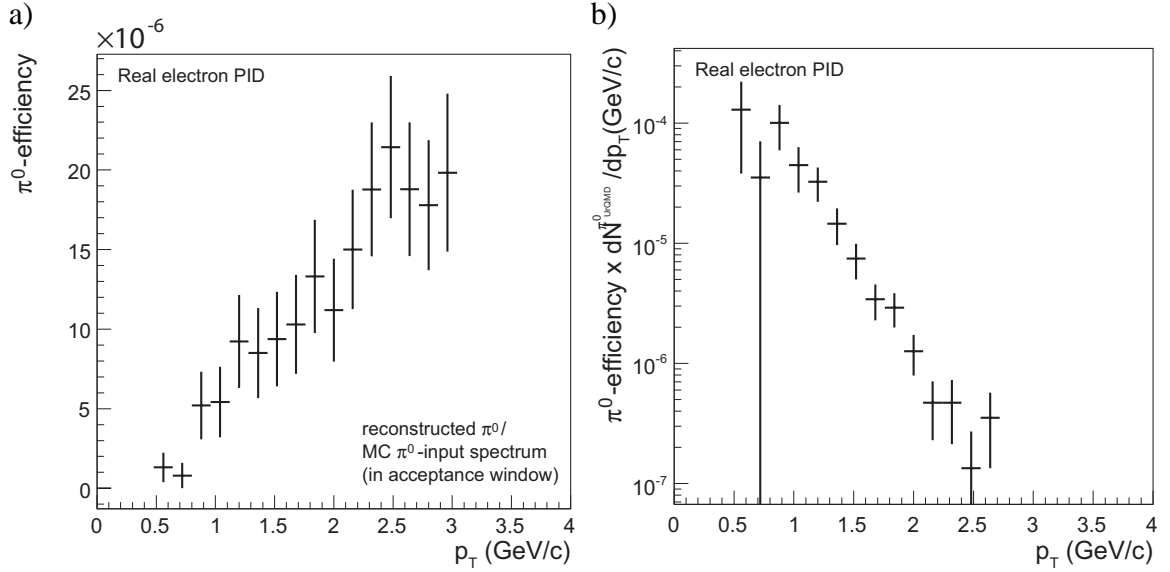


Figure 7.30: a) π^0 -reconstruction efficiency and b) the average number of reconstructed π^0 s as function of p_T in one UrQMD event (central Au+Au events at 25 AGeV beam energy), both for *real electron PID*.

advantage especially at low momenta and both measurements should be done in addition to the ECAL data analysis.

The measurements, which are shown here, can be carried out with the standard detector setup intended for CBM as e.g. designated for the J/ψ measurement (assuming the usage of a segmented target with integrated thickness of 250 μm) and for any ‘inclusive-hadron’ measurement like π , K, p, Δ , Ξ , Ω , including flow. For the photon and π^0 measurement by using the conversion method, no further triggers are required, i.e. they will be feasible with a simple Minimum Bias or centrality trigger.

The efficiency of the photon and thus of the π^0 measurement can be drastically increased by adding some converter material behind the target. This may be an interesting option for single runs in the CBM experiment. Besides the larger efficiency due to the higher photon-conversion probability the photon/ π^0 -Dalitz ratio would be very large in such a measurement. Due to the very short mean life time of $(8.4 \pm 0.6) \times 10^{-17}$ s, the path length of the π^0 is very small ($c\tau = 25.1$ nm) and thus there are no π^0 s behind the target. In the e^+e^- pair reconstruction one could apply a vertex constraint to this converter position and obtain a photon spectrum with a high purity and large statistical accuracy.

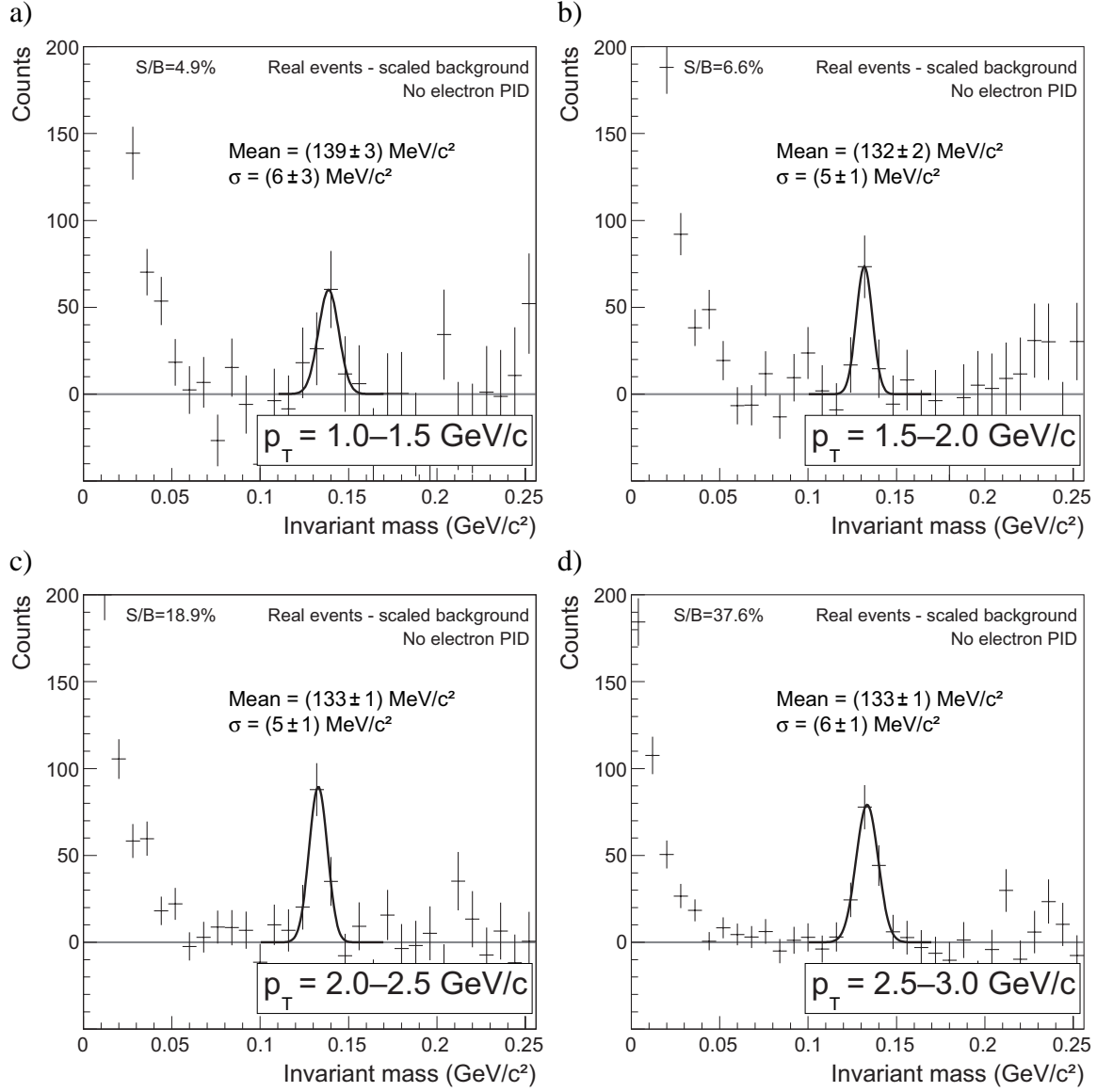


Figure 7.31: Invariant-mass distribution of $\gamma\gamma$ pairs after background subtraction for *no electron PID*. Here, 20,000 UrQMD events from central Au+Au collisions at 25 AGeV beam energy are analyzed. In addition, 1,000 π^0 s, uniformly distributed in $p_T(0 \text{ GeV}/c < p_T < 3 \text{ GeV}/c)$, are embedded into every event.

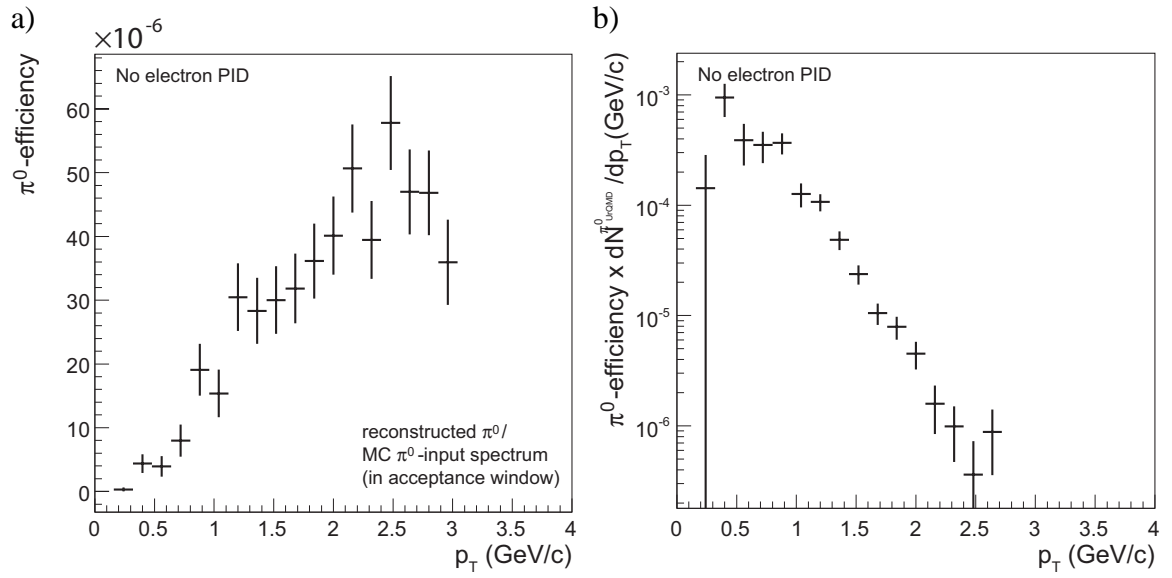


Figure 7.32: a) π^0 -reconstruction efficiency and b) the average number of reconstructed π^0 s as function of p_T in one UrQMD event (central Au+Au events at 25 AGeV beam energy), both for *no electron PID*.

Summary

The focus of this thesis was the development of a Transition Radiation Detector (TRD) for the future CBM experiment at FAIR. The CBM TRD will provide electron identification and – together with a Silicon Tracking System (STS) – will allow tracking of charged particles. In conjunction with the Ring Imaging Cherenkov (RICH) detector and a time-of-flight (TOF) measurement, it will provide sufficient electron identification for the measurements of charmonium and low-mass vector mesons.

The most important and challenging aspect of the TRD design is that the detector has to cope with very high interaction rates of up to 10^7 Hz and large particle multiplicities in CBM. These conditions lead to counting rates of up to 100 kHz/cm^2 in the central part of the TRD (at small polar angles). In this thesis it was confirmed that TRDs consisting of a combination of radiators and simple multiwire proportional chambers (MWPC) with 6 mm gas thickness and multipad readout are good candidates for high-granularity fast detectors. The small gas thickness minimizes drift time and reduces space-charge effects in a high counting-rate environment. However, as shown in this thesis, a reduction of the detector thickness leads to a smaller absorption efficiency for the transition radiation in a single layer of the detector. In order to circumvent this aspect without increasing the number of layers and readout channels, a new TRD architecture was proposed and successfully tested. The configuration is based on a symmetric arrangement of two MWPCs with a common double-sided central pad-readout electrode. The prototypes were designed, built and tested in collaboration with the group of Prof. M. Petrovici from IFIN-HH, Bucharest, Romania. The performance of two identical MB-TRD (Münster-Bucharest TRD) prototypes was investigated using a ^{55}Fe X-ray source of 5.9 keV and mixed electron, pion, and proton beams with rates of up to 200 kHz/cm^2 and momenta of up to $2 \text{ GeV}/c$ provided by a secondary beam line at the SIS 18 accelerator at GSI, Darmstadt.

The performance of the TRD prototypes was investigated in terms of electron/pion discrimination, tracking performance as well as gas-gain and position-resolution stability at high incident particle rates. The position resolution was determined using two identical detectors assuming equal contribution of both chambers for different anode voltages, gas

mixtures, and particularly for different beam intensities. In all measurements a position resolution in anode-wire direction of less than $200\text{ }\mu\text{m}$ was achieved for particle rates of up to 200 kHz/cm^2 . These results conform to the requirements of the CBM TRD. Also, the position resolution of the detectors perpendicular to the anode wires was determined. Due to the geometry of the MB-TRD prototype the position of the charge cluster in this direction can be determined with a resolution of about 1.2 mm . However, the cluster position itself is shifted from the particle-track position towards the next anode wire and can be determined with a resolution of the order of $700\text{ }\mu\text{m}$ (wire spacing (2.5 mm) divided by $\sqrt{12}$). This performance is also fulfilling the CBM requirements. Nevertheless, this very good position resolution in both directions was achieved with a small prototype having a high readout-pad granularity. The position resolution of a real-size TRD has to be as good with a realizable number of readout channels. In order to meet these requirements, an optimized geometry of the readout electrode with rectangular readout pads, which are subdivided into two triangles each, has been developed. This layout should allow for a two-dimensional track reconstruction in one TRD layer.

Using test-beam data, the electron/pion discrimination of the MB-TRD prototypes was estimated. The charge-deposit distributions of electrons and pions were used as probability distributions in simulations aimed at determining the pion rejection factor of the prototypes as a function of number of TRD layers. The pion efficiency was measured for one TRD layer and was subsequently extrapolated to a larger number of layers. The pion efficiency of 1% at an electron efficiency of 90%, like it is envisaged for the CBM-TRD, was achieved for nine layers of the prototypes. This performance was reached by using simple sandwich radiators consisting of foam and fibers. Even less layers will be needed with regular foil radiators or correspondingly larger rejection factors may be achieved.

The results encourage the further development of this new design principle for a TRD for the CBM experiment. Based on the prototype performance demonstrated in this thesis, a next generation of TRD prototype has been developed and is currently under construction. This new device is a real-size prototype being intended as unit cell of a module design of a full TRD layer.

The new TRD geometry was implemented into the simulation framework (CbmRoot) of the CBM experiment. The measured charge-deposit spectra were reproduced by a GEANT3 simulation with appropriate parameters for the transition-radiation simulation in order to provide a realistic input for the TRD in the simulation. CbmRoot provides the possibility to perform feasibility studies for physics measurements, and the further optimization of the detector layout. Hence, the TRD design could also be investigated in conjunction with the other sub-systems within a simulation of the whole CBM detector

setup. This – currently most probable – detector geometry meets all design goals of the TRD.

As a possible application of the TRD in CBM, the measurement of dielectrons from photon conversions in the target was studied in this thesis. For this study, the full event simulation and reconstruction in CbmRoot was used. An Electromagnetic Calorimeter (ECAL) is designated to provide photon identification in CBM. A complementary measurement of dielectrons from photon conversions can be used to increase the precision of the photon measurement. This method is very auspicious especially at low momenta due to the good momentum resolution of the electron tracking. Moreover, it does not suffer much from misidentified charged and neutral hadron background. The electrons and positrons are measured using the charged-particle tracking (with STS and TRD) and electron identification detectors (RICH, TRD, and TOF).

In order to reconstruct photons via conversions into e^+e^- pairs, the lowest invariant-mass region ($< 100 \text{ MeV}/c^2$) of dielectrons was investigated, where the main contribution is due to photon conversions and π^0 -Dalitz decays. Through the application of several cuts, the reconstruction efficiency for photons and neutral pions was optimized. The γ/π^0 -Dalitz ratio was shown to increase from 4.2 to 7.7, and the fraction of photons compared to all (true and fake) reconstructed e^+e^- pairs was shown to increase from 3.2% to 81.3%. This purity of the photon signal and the efficiency of the photon reconstruction was investigated for different PID conditions. Based on these results, one can now adjust the efficiency and purity for photon reconstruction according to the available bandwidth for this reaction channel and the amount of beam time available to the experiment.

In addition, the momentum resolution of the reconstructed photons was determined. It was shown that, especially at low momenta (up to $8 \text{ GeV}/c$), a resolution of better than $\Delta p/p = 2.5\%$ can be obtained. This is considerably better than the expected momentum resolution in a photon measurement using the ECAL. This is achieved because of the good momentum resolution of the charged-particle tracking.

The measurement of direct photons requires precise knowledge of the contribution from decays (mainly $\pi^0, \eta \rightarrow \gamma\gamma$) to the inclusive photon spectrum. An enhancement of photons compared to the expectation from hadron decays can be directly attributed to a direct-photon signal. Moreover, the π^0 -measurement employing the same method provides a useful cross check for the method of photon measurement. Thus, a further analysis of neutral pions using the photon-conversion method was performed.

The π^0 -signal was determined through an invariant-mass analysis of photon pairs. Taking into account all possible photon-photon combinations leads to a large combinatorial background. This was determined using an event-mixing technique. In order to investigate and to increase the statistical accuracy, this analysis was also performed for

different PID conditions. By using the obtained efficiency of reconstructing π^0 s with this method and in comparison to an UrQMD spectrum, the data-taking time that is necessary to obtain a π^0 -signal with the required statistical accuracy was estimated. It was shown that the statistical error in the p_T range of 1.5–2 GeV/ c is of the order of $< 6.6\%$ for a net run time of 200 hours when exhausting the full bandwidth to mass storage.

The resolution of the π^0 's invariant-mass has a value of about 6 MeV/ c^2 in the p_T -region of 0–3 GeV/ c , which is a very good resolution particularly in comparison to known calorimeter measurements.

The results encourage a photon and π^0 -measurement via conversions in the CBM experiment. Of course, the reconstruction efficiency of photons and in particular of π^0 s through the conversion method is much lower than the one for an ECAL measurement. However, since the combinatorial background of photon pairs decreases quadratically, the low efficiency of the conversion method leads to an improved S/B ratio for $1 \text{ GeV}/c < p_T < 3 \text{ GeV}/c$ in the π^0 -measurement. Moreover, the very good momentum resolution of the photon as well as of the π^0 -reconstruction obtained with the conversion method provides an advantage especially at low momenta, and both measurements should be carried out in addition to the ECAL data analysis.

In summary, the new TRD prototype for electron/pion discrimination and tracking of charged particles in high counting rate environments has been developed. It has been demonstrated to fulfill the requirement of the CBM experiment at the future FAIR. Based on the obtained results a real-size prototype with an optimized geometry of the readout electrode in order to provide two-dimensional position information is now being developed. In addition, a feasibility study for the measurement of photons and neutral pions via photon conversions was performed in simulations using the TRD layout developed in hardware. These measurements can be carried out with the standard detector setup intended for CBM and without dedicated triggers.

Zusammenfassung

Der Fokus dieser Arbeit lag auf der Entwicklung eines Übergangsstrahlungsdetektors (TRD) für das zukünftige CBM-Experiment am FAIR-Beschleuniger. Der CBM-TRD wird die Identifizierung von Elektronen und – zusammen mit einem Silicon-Tracking-System (STS) – die Spurrekonstruktion geladener Teilchen ermöglichen. In Verbindung mit einem Ring-Imaging-Cherenkov-Detektor (RICH) und einer Flugzeitmessung (TOF) soll der TRD eine Elektronidentifizierung bieten, die Messungen von Charmonium und Vektormesonen niedriger Masse ermöglicht.

Der wichtigste und anspruchsvollste Aspekt in der Entwicklung des TRD-Designs liegt darin, dass der Detektor bei sehr hohen Wechselwirkungsraten von bis zu 10^7 Hz und hohen Teilchenmultiplizitäten betrieben werden soll. Im zentralen Bereich des TRD (bei kleinen Polarwinkeln) führen diese Bedingungen zu Zählraten von bis zu 100 kHz/cm^2 . In dieser Arbeit wurde bestätigt, dass TRDs bestehend aus einer Kombination von Radiatoren und einfachen Violdraht-Proportionalkammern mit einer Gasdicke von 6 mm und Multipad-Auslese geeignete Kandidaten für schnelle Detektoren mit hoher Granularität sind. Eine kleine Gasdicke verkürzt die Driftzeit und reduziert Raumladungseffekte insbesondere bei hohen Zählraten. Wie in dieser Arbeit gezeigt, führt eine Reduzierung der Detektordicke jedoch zu einer kleineren Absorptionswahrscheinlichkeit für Übergangsstrahlung in einer einzelnen Lage des Detektors. Um diesen Aspekt zu umgehen, ohne gleichzeitig die Anzahl an Lagen und Auslesekanälen zu erhöhen, wurde ein neues TRD-Layout konstruiert und erfolgreich getestet. Es basiert auf einer symmetrischen Anordnung zweier Violdraht-Proportionalkammern mit einer zentralen, doppelseitigen Ausleseelektrode. Die Prototypen wurden in Zusammenarbeit mit der Gruppe von Prof. M. Petrovici vom IFIN-HH in Bukarest entwickelt, gebaut und getestet. Die Performance zweier identischer Münster-Bucharest-TRD-Prototypen (MB-TRD) wurde zunächst mit einer ^{55}Fe -Röntgenquelle von 5,9 keV und anschließend mit gemischten Strahlen aus Elektronen, Pionen und Protonen untersucht. Letztere wurden mit Raten von bis zu 200 kHz/cm^2 und Impulsen von bis zu $2 \text{ GeV}/c$ von einer Sekundärstrahlführung am SIS-18-Beschleuniger an der GSI, Darmstadt, bereitgestellt.

Untersucht wurde das Verhalten der TRD-Prototypen in Bezug auf Elektron/Pion-Separation, Spurrekonstruktion und auf Stabilität der Gasverstärkung sowie der Ortsauflösung bei hohen Zählraten. Die Ortsauflösung konnte unter der Annahme gleicher Beiträge in beiden Kammern mit zwei identischen Detektoren bestimmt werden, welche bei verschiedenen, aber in beiden Kammern identischen, Betriebsparametern wie Anodenspannung, Gasmischung und insbesondere bei unterschiedlichen Teilchenraten betrieben wurden. In allen Messungen wurde eine Ortsauflösung in Anodendrahtrichtung von weniger als $200\text{ }\mu\text{m}$ selbst bei maximalen Teilchenraten von bis zu 200 kHz/cm^2 erreicht. Diese Ergebnisse erfüllen das Design-Ziel für den CBM-TRD. Die Ortsauflösung der Detektoren wurde auch in senkrechter Richtung zu den Anodendrahten bestimmt. Mit der Geometrie des MB-TRD Prototypen kann der Ort des Ladungs-Clusters in dieser Richtung mit einer Auflösung von etwa 1 mm ermittelt werden. Die Position des Clusters selbst ist jedoch von der Teilchenspur in Richtung des nächsten Anodendrahtes verschoben und kann mit einer Auflösung von etwa $700\text{ }\mu\text{m}$ (Anodendrahtabstand ($2,5\text{ mm}$) geteilt durch $\sqrt{12}$) bestimmt werden. Diese Auflösung erfüllt ebenfalls die Bedingungen für CBM. Allerdings wurden die Werte mit einem kleinen Prototypen erreicht, der eine hohe Pad-Granularität aufweist, und müssen auch für einen größeren TRD mit einer realisierbaren Anzahl an Auslesekanälen erzielt werden. Um dies zu gewährleisten, wurde eine optimierte Geometrie der Ausleseelektrode entwickelt, die rechteckige Auslese-Pads aufweist, welche in jeweils zwei Dreiecke unterteilt sind. Dieses Layout soll eine zweidimensionale Spurrekonstruktion in einer TRD-Lage ermöglichen.

Mit den Teststrahldaten wurde auch die Elektron/Pion-Separation der MB-TRD-Prototypen abgeschätzt. Die Verteilungen der deponierten Ladung für Elektronen und Pionen können als Wahrscheinlichkeitsverteilungen in Simulationen genutzt werden, um den Pionenunterdrückungsfaktor der Prototypen als Funktion der Anzahl der TRD-Lagen zu bestimmen. Die Pioneneffizienz wurde mit einer TRD-Lage gemessen und anschließend für eine größere Anzahl an Lagen extrapoliert. Die für den CBM-TRD gewünschte Pioneneffizienz von 1% bei 90% Elektroneneffizienz wurde für 9 Lagen der Prototypen erreicht. Diese Performance wurde mit einfachen Sandwich-Radiatoren erreicht, welche aus Schaum und Fasermatten bestehen. Mit regulären Folienradiatoren werden sogar weniger Lagen benötigt oder es wird ein entsprechend größerer Unterdrückungsfaktor erreicht.

Die Ergebnisse ermutigen zur Weiterentwicklung dieses neuen Design-Prinzips für einen TRD im CBM-Experiment. Basierend auf der Prototyp-Performance, die in dieser Arbeit gezeigt ist, wurde eine nächste Generation von TRD-Prototypen entwickelt, welche aktuell konstruiert werden. Dieses neue Gerät ist ein Prototyp mit realistischen Ab-

messungen, der als einzelne Zelle einer vollen TRD-Lage mit modularem Design geplant ist.

Die neue TRD-Geometrie wurde in die Simulationsumgebung des CBM-Experimentes (CbmRoot) implementiert. Die gemessenen Spektren der deponierten Ladung wurden mit einer GEANT3-Simulation und geeigneten Parametern für die Simulation der Übergangsstrahlung beschrieben, um eine realistische Grundlage für den TRD in der Simulation zu bieten. CbmRoot bietet die Möglichkeit, physikalische Machbarkeitsstudien und weitere Optimierungen des Detektor-Layouts vorzunehmen. Dadurch konnte das TRD-Design auch zusammen mit anderen Subsystemen in einer Simulation des kompletten CBM-Detektoraufbaus untersucht werden. In dieser zur Zeit wahrscheinlichsten Detektorgeometrie erfüllt der TRD alle Design-Ziele.

Als eine mögliche Anwendung des TRD in CBM wurde in dieser Arbeit die Messung von Dileptonen aus Photonkonversionen im Target untersucht. Für diese Studie wurde eine vollständige Simulation und Rekonstruktion in CbmRoot genutzt. Die herkömmliche Messung von Photonen soll in CBM mit einem elektromagnetischen Kalorimeter durchgeführt werden. Eine komplementäre Messung von Dileptonen aus Photonkonversionen kann genutzt werden, um die Präzision der Photonenmessung zu erhöhen. Diese Methode ist besonders bei kleinen Impulsen auf Grund der guten Impulsauflösung der Elektron-Spurrekonstruktion sehr vielversprechend. Außerdem ist sie nicht stark durch den Untergrund aus missidentifizierten geladenen und neutralen Hadronen beeinträchtigt. Die Elektronen und Positronen werden bei der Spurrekonstruktion geladener Teilchen (mit dem STS und TRD) gemessen und mit dem RICH, TRD und TOF identifiziert.

Um Photonen über Konversionen in e^+e^- -Paare zu rekonstruieren, wurden Dileptonen im Bereich niedrigster invarianter Massen ($< 100 \text{ MeV}/c^2$) untersucht, wo der Hauptbeitrag durch Photonkonversionen und π^0 -Dalitz-Zerfälle entsteht. Durch die Anwendung verschiedener Cuts wurde die Rekonstruktionseffizienz für Photonen und neutrale Pionen optimiert. Es wurde gezeigt, dass sich das γ/π^0 -Dalitz-Verhältnis von 4,2 auf 7,7 und der Anteil der Photonen im Vergleich zu allen (richtigen und falschen) rekonstruierten e^+e^- -Paaren von 3,2% auf 81,3% erhöht. Die Reinheit des Photonsignals sowie die Effizienz der Photonrekonstruktion wurden mit unterschiedlichen PID-Bedingungen untersucht. Basierend auf diesen Ergebnissen kann nun im Experiment die Effizienz und Reinheit der Photonrekonstruktion entsprechend der vorhandenen Bandbreite für diesen Reaktionskanal und der zur Verfügung stehenden Strahlzeit gewählt werden.

Darüber hinaus wurde die Impulsauflösung der rekonstruierten Photonen bestimmt. Es konnte gezeigt werden, dass besonders bei kleinen Impulsen (bis zu $8 \text{ GeV}/c$) eine Auflösung von besser als $\Delta p/p = 2,5\%$ erreicht wird, welche deutlich besser als die er-

wartete Auflösung einer Photonenmessung mit dem ECAL ist. Die Ursache liegt in der guten Impulsauflösung bei der Spurrekonstruktion geladener Teilchen.

Zur Messung direkter Photonen wird eine präzise Kenntnis des Beitrags aus Zerfällen (hauptsächlich $\pi^0, \eta \rightarrow \gamma\gamma$) zum inklusiven Photonenspektrum benötigt. Eine Erhöhung der Photonenausbeute verglichen mit der Erwartung für den Beitrag aus hadronischen Zerfällen kann direkt einem Signal direkter Photonen zugeschrieben werden. Darüber hinaus bietet die π^0 -Messung mit derselben Methode eine nützliche Gegenprobe für die Methode der Photonenmessung. Deshalb wurde eine weitere Analyse neutraler Pionen mit der Photonkonversionsmethode durchgeführt.

Das π^0 -Signal wurde mit einer Analyse invarianter Massen von Photonenpaaren bestimmt. Wenn alle möglichen Photon-Photon-Kombinationen berücksichtigt werden, führt dies zu einem großen kombinatorischen Untergrund. Dieser wurde mit einer Mixed-Event-Technik bestimmt. Um die statistische Genauigkeit zu untersuchen und zu erhöhen, wurde diese Analyse auch mit unterschiedlichen PID-Bedingungen durchgeführt. Mit Hilfe der Effizienz der π^0 -Rekonstruktion unter Verwendung dieser Methode und einem Vergleich mit einem UrQMD-Spektrum wurde die Datennahmezeit abgeschätzt, die nötig ist, um ein π^0 -Signal mit der benötigten statistischen Genauigkeit zu erhalten. Es wurde gezeigt, dass bei Ausschöpfung der vollen Bandbreite zum Massenspeicher der statistische Fehler im p_T -Bereich von 1,5–2 GeV/c bei einer Netto-Datennahmezeit von 200 Stunden kleiner als 6,6% wird.

Die Auflösung der invarianten Masse des π^0 hat einen Wert von etwa 6 MeV/c² im p_T -Bereich von 0–3 GeV/c, was eine sehr gute Auflösung insbesondere im Vergleich zu bekannten Kalorimetermessungen darstellt.

Die Ergebnisse ermutigen zu einer Photonen- und π^0 -Messung über Konversionen im CBM-Experiment. Natürlich ist die Rekonstruktionseffizienz für Photonen und insbesondere für π^0 s mit der Konversionsmethode sehr viel kleiner als die mit einer ECAL-Messung. Doch da der kombinatorische Untergrund der Photonenpaare quadratisch wächst, führt die kleine Effizienz der Konversionsmethode zu einem verbesserten Signal-zu-Untergrund-Verhältnis im Bereich $1 \text{ GeV}/c < p_T < 3 \text{ GeV}/c$ bei der π^0 -Messung. Darüber hinaus bietet die sehr gute Impulsauflösung der Photon- sowie der π^0 -Rekonstruktion unter Verwendung der Konversionsmethode vor allem bei kleinen Impulsen einen Vorteil und beide Messungen sollten zusätzlich zur ECAL-Analyse durchgeführt werden.

Zusammenfassend wurde ein neuer TRD-Prototyp zur Elektron/Pion-Separation und Spurrekonstruktion geladener Teilchen bei hohen Zählraten entwickelt und es wurde gezeigt, dass er die Anforderungen des CBM-Experimentes am zukünftigen FAIR-Beschleuniger erfüllt. Basierend auf den Ergebnissen wurde ein Prototyp realer Größe mit

einer optimierten Geometrie der Ausleselektrode entwickelt, mit der eine zweidimensionale Ortsinformation erhalten werden kann. Darüber hinaus wurde eine Machbarkeitsstudie zur Messung von Photonen und neutralen Pionen mit Simulationen durchgeführt, in denen das TRD-Layout benutzt wurde, welches in Hardware entwickelt wurde. Diese Messungen können mit dem Standard-Detektoraufbau, wie er für CBM geplant ist, und ohne bestimmte Trigger durchgeführt werden.

A. Run summary of the test beam in 2006 at GSI

Run	$U(V)$	$p(\text{GeV}/c)$	Spill(s)	Size(MB)	Comments
041	1700	1.5 -	10	207	Xe(85%)CO ₂ (15%), sandwich radiators in front of MB-TRD1/MB-TRD2
042	1700	1.5 -	4(?)	200	Foil radiators in front of MB-TRD1
043	1700	1.5 -	4	120	Sandwich radiators in front of MB-TRD1 and MB-TRD2
044	1700	1.5 -	4	263	
047	1800	1.5 -	4	202	
048	1800	1.5 -	4	202	
049	1800	1.0 -	4	170	Pbgl thr -> 60mV, TDC implemented
050	1800	1.0 -	4	200	Pbgl thr -> 70mV
051	1800	1.0 -	4	200	
052	1800	1.0 +	2	200	Switch to positive particles
053	1800	1.0 +	2	135	Low rate
054	1800	1.5 +	2	217	Low rate
055	1800	1.5 +	2	163	Low rate
056	1800	1.5 +	1	129	Pbgl thr -> 120 mV
057	1800	1.5 +	1	241	
058	1800	1.5 +	10	146	
061	1800	1.5 +	1	200	S2 and Pbgl realigned
062	1800	1.5 +	1		Noticed different gain for B1 and M1
063	1800	1.5 +	1	290	Beam not stable; removed Si
064	1800	1.5 +	1	229	Dubna change HV
065	1800	1.5 +	2	362	
066	1800	1.5 +	5	400	Si back to beam
067	1800	1.5 +	0.7	410	Si removed
068	1800	1.5 +	0.5	363	HV of B1 not stable; problem with ion source
069	1800	1.5 +	0.5		Very low intensity
070	1800	1.5 +	0.5		Rate vary very strong
071	1800	1.5 +	4	98	M1 no radiator

Table A.1: Run summary of the test beam in 2006 at GSI.

Run	$U(V)$	$p(\text{GeV}/c)$	Spill(s)	Size(MB)	Comments
072	1800	1.5 +	4	157	Beam fluctuations, Pbgl off from trigger
073	1800	2.0 +	10	225	
074	1800	2.0 +	10	200	
075	1800	2.0 +	5	202	
076	1800	2.0 +	5	159	Low rate
077	1800	2.0 +	5	210	
078	1800	2.0 +	2	198	
079	1800	2.0 +	2	202	
080	1600	2.0 +	2	201	change voltages
081	1600	2.0 +	2	200	
082	1600	2.0 +	5	200	
083	1600	2.0 +	5	206	
084	1600	2.0 +	10	201	
085	1600	2.0 +	10	210	
086	1600	2.0 +	2	203	Si off from DAQ
087	1700	2.0 +	2	94	Xe(90%)CO ₂ (10%), low rate
088	1700	2.0 +	2	200	Dubna change HV
089	1700	2.0 +	2	200	
090	1700	2.0 +	5	201	
091	1700	2.0 +	5	212	
092	1700	2.0 +	10	201	
093	1700	2.0 +	10	205	
094	1500	2.0 +	10		Test file for HV (B1,M1,B2)
095	1550	2.0 +	10	204	
096	1550	2.0 +	10	204	
097	1550	2.0 +	5	201	
098	1550	2.0 +	5	201	
099	1550	2.0 +	2	214	
110	1650	2.0 +	5	200	Xe(80%)CO ₂ (20%)
111	1650	2.0 +	2	200	

Table A.2: Run summary of the test beam in 2006 at GSI.

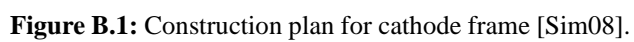
Run	$U(\text{V})$	$p(\text{GeV}/c)$	Spill(s)	Size(MB)	Comments
113	1850	2.0 +	2	239	change HV
114	1850	2.0 +	2	200	
115	1650	2.0 +	2		
116	1650	2.0 +	2		
117	1850	2.0 +	5	251	change HV
118	1850	2.0 +	5	200	
119	1850	2.0 +	10		Change angles to 30 deg
120	1850	2.0 +	10	340	
121	1800	2.0 +	10	133	
122	1800	2.0 +	10	258	
123	1800	2.0 +	10	187	Remove B1 and B2; GSI at 20 deg
124	1800	2.0 +	2	258	
125	1800	2.0 +	2	204	
126	1800	2.0 +	2	204	
127	1800	2.0 +	10	214	GSI at 10 deg
128	1800	2.0 +	10	200	
129	1800	2.0 +	2	211	
130	1800	2.0 +	2	200	
131	1800	2.0 +	10	207	GSI back to 0 deg, start with GEM scan
132	1800	2.0 +	10	216	
133	1800	1.5 +	10	210	
134	1800	1.5 +	10	204	
135	1800	1.5 +	10	208	
136	1800	1.5 +	5		
137	1800	1.5 +	5	200	
138	1800	1.5 +	5	226	
139	1800	1.5 +	5	200	
140	1800	1.5 +	5	206	
141	1800	1.5 +	5	226	
142	1800	1.5 +	5	203	

Table A.3: Run summary of the test beam in 2006 at GSI.

Run	$U(\text{V})$	$p(\text{GeV}/c)$	Spill(s)	Size(MB)	Comments
143	1800	1.5 +	5	203	
144	1800	1.5 +	5	218	
145	1800	1.5 +	5	204	
146	1800	1.5 +	5	201	
147	1800	1.5 +	10	207	
148	1800	1.5 +	10	205	
149	1800	1.5 +	10	205	
150	1800	1.5 +	10	203	
151	1800	1.5 +	10	201	
152	1800	1.5 +	10	150	
153	1800	1.5 +	2	513	End GEM scan
154	1800	1.5 +	2	266	
155	1800	1.5 +	2		Pbgl back in trigger
156	1600	2.0 +	10		Ar(85%)CO ₂ (15%) remove radiators
157	1610	2.0 +	10	278	
158	1610	2.0 +	10	244	
159	1610	2.0 +	5	265	Low intensity
160	1610	2.0 +	5	320	
161	1610	2.0 +	2	206	
162	1610	2.0 +	2	204	
163	1610	2.0 +	2	234	
164	1700	1.5 +	2	19	Xe(85%)CO ₂ (15%) M1 0 deg, M1 with foil radiator
165	1700	1.5 +	0.5	87	
166	1700	1.5 +	0.5	202	
167	1700	1.5 +	0.5	205	
168	1700	1.5 +	0.75	205	
169	1700	1.5 +	0.75	205	
170	1700	1.5 +	0.75	215	

Table A.4: Run summary of the test beam in 2006 at GSI.

B. Technical Drawings



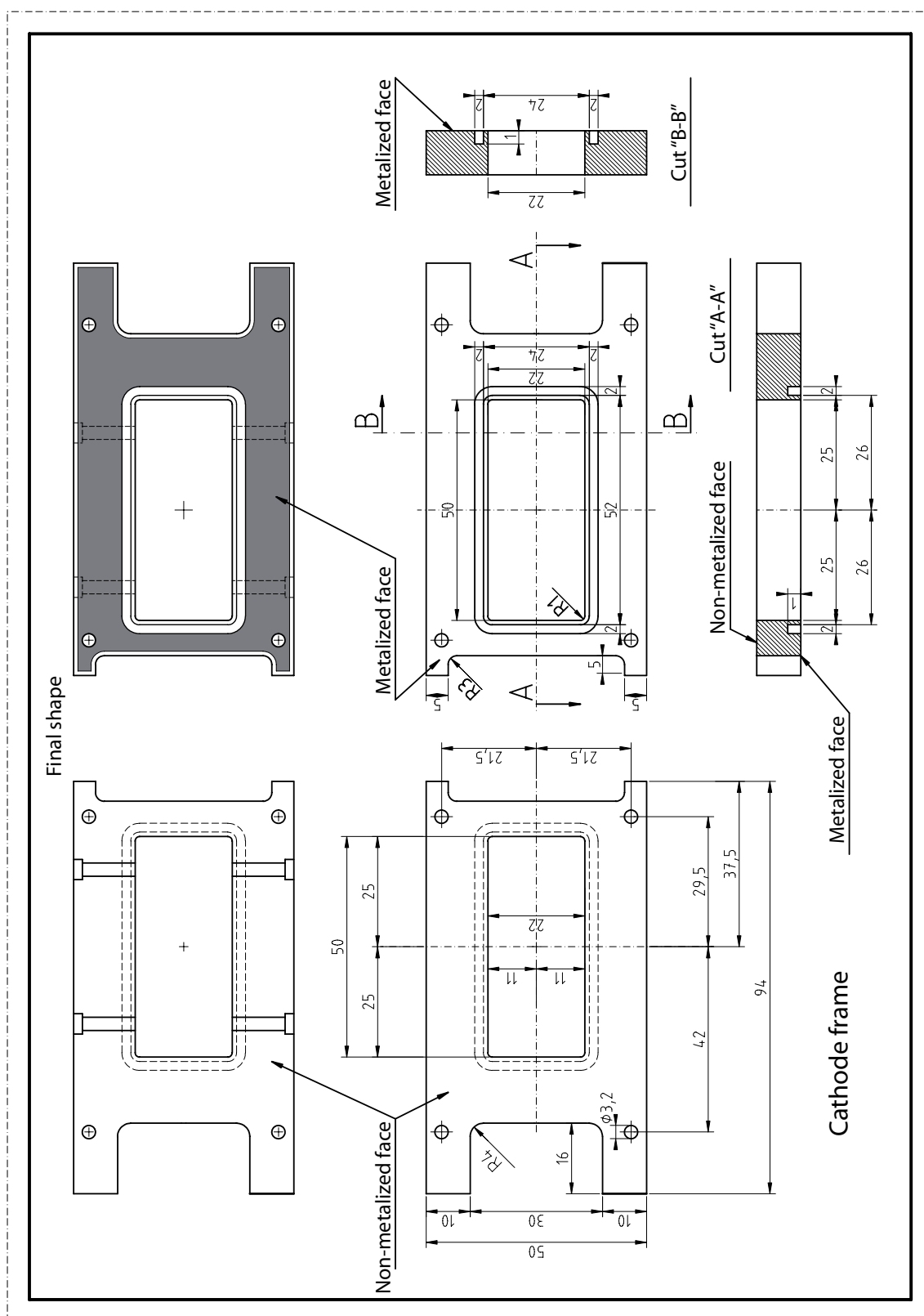


Figure B.2: Construction plan for cathode frame (overview) [Sim08].

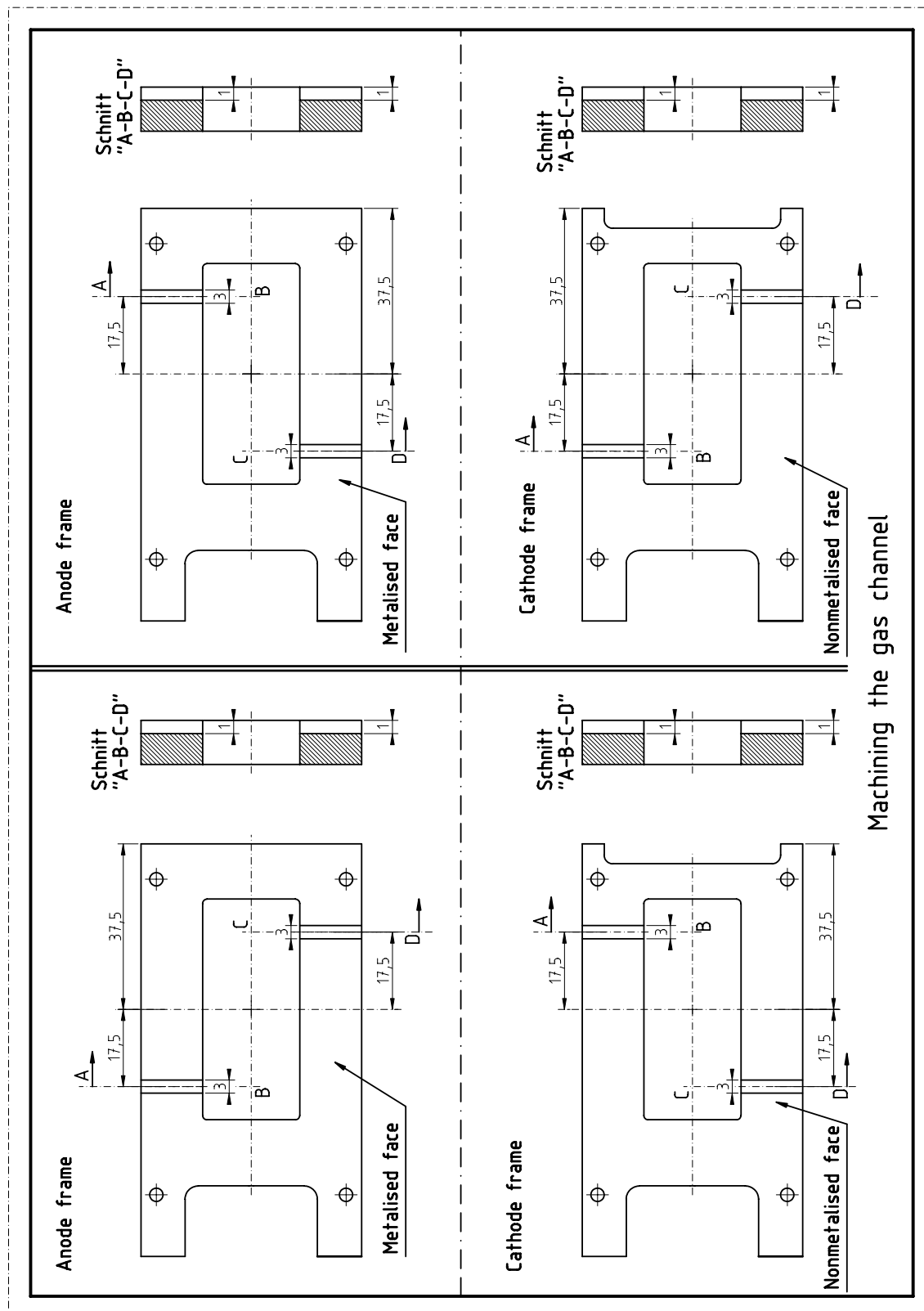


Figure B.3: Construction plan for matching the gas channel [Sim08].

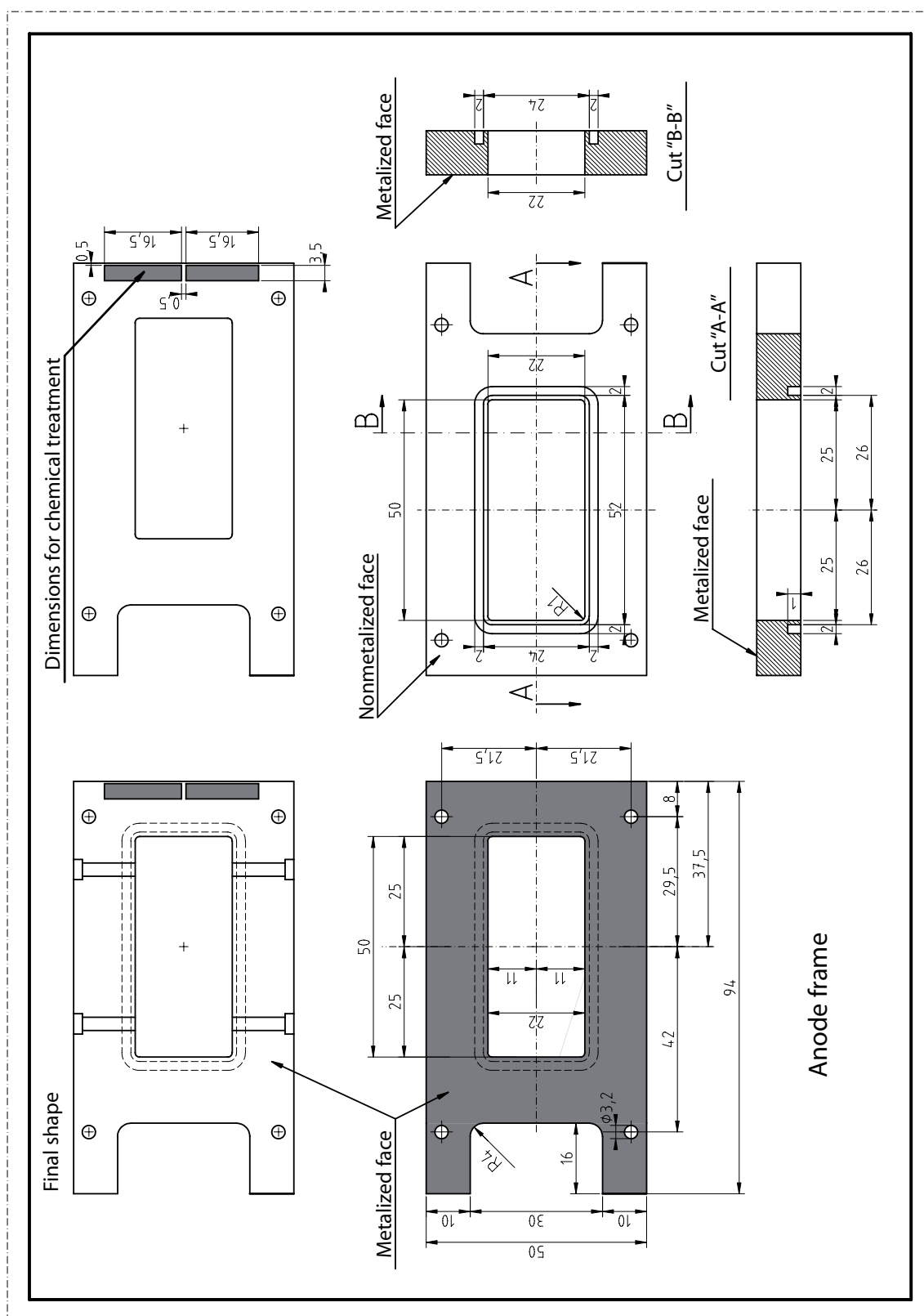
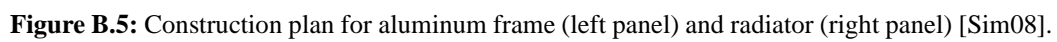


Figure B.4: Construction plan for anode frame [Sim08].



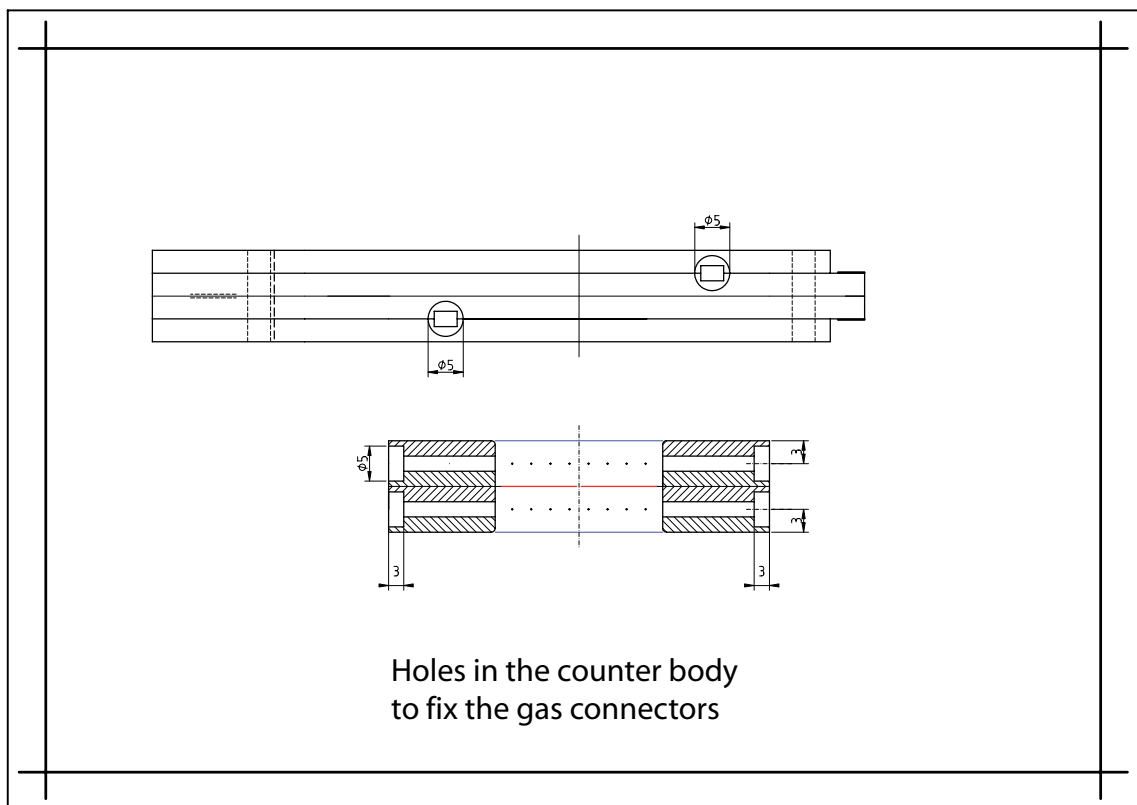
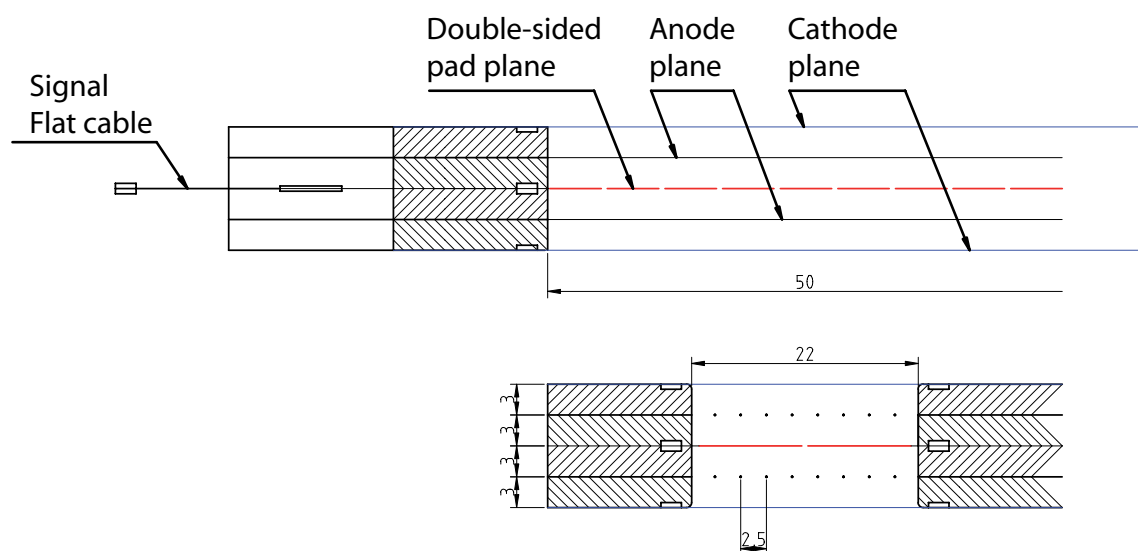


Figure B.6: Construction plan for hole in the counter frame to fix the gas connectors [Sim08].



Pad plane: 25 μm Kapton + 0.3 μm copper structure on both sides

Anode plane: 20 μm Wo+Au wire

Cathode plane: Al covered 25 μm Kapton

Frames: 3 mm pc board

Figure B.7: Schematic drawing of the counter [Sim08].

Bibliography

- [Abr00] M. C. Abreu *et al.*, *Phys. Lett.* **B477** (2000) 28.
- [Abr01] M. C. Abreu *et al.*, *Phys. Lett.* **B521** (2001) 195.
- [Ada08] A. Adare *et al.*, *Enhanced Production of Direct Photons in Au+Au Collisions at $\sqrt{s_{NN}} = 200$ GeV*, arXiv:0804.4168 [nucl-ex], 2008.
- [Ada09] A. Adare *et al.*, *Phys. Lett.* **B670** (2009) 313.
- [Adl05] S. S. Adler *et al.*, *Phys. Rev. Lett.* **94** (2005) 232301.
- [Adl07] S. S. Adler *et al.*, *Phys. Rev. Lett.* **98** (2007) 012002.
- [Afa07] S. Afanasiev *et al.*, *Enhancement of the Dielectron Continuum in $\sqrt{s_{NN}} = 200$ GeV Au+Au Collisions*, arXiv:0706.3034 [nucl-ex], 2007.
- [Aga95] G. Agakishiev *et al.*, *Phys. Rev. Lett.* **75** (1995) 1272.
- [Aga07] G. Agakishiev *et al.*, *Phys. Rev. Lett.* **98** (2007) 052302.
- [Aga08] G. Agakishiev *et al.*, *Phys. Lett.* **B663** (2008) 43.
- [Agg99] M. M. Aggarwal *et al.*, *Phys. Rev. Lett.* **83** (1999) 926.
- [Agg00a] M. M. Aggarwal *et al.*, *Direct Photon Production in 158 AGeV $^{208}\text{Pb} + ^{208}\text{Pb}$ Collisions*, arXiv:0006007 [nucl-ex], 2000.
- [Agg00b] M. M. Aggarwal *et al.*, *Phys. Rev. Lett.* **85** (2000) 3595.
- [Aki07] A. Akishina *et al.*, *Nucl. Instrum. Meth.* **A572** (2007) 676.
- [Aki08] E. P. Akishina, T. P. Akishina, V. V. Ivanov, *et al.*, *Phys. Part. Nucl. Lett.* **5** (2008) 116.

-
- [Ale05] B. Alessandro *et al.*, *Eur. Phys. J.* **C39** (2005) 335.
- [Alf01] M. G. Alford, *Ann. Rev. Nucl. Part. Sci.* **51** (2001) 131.
- [Alf08] M. G. Alford, A. Schmitt, K. Rajagopal, *et al.*, *Rev. Mod. Phys.* **80** (2008) 1455.
- [ALI01] *ALICE Technical Design Report of the Transition Radiation Detector (TRD)*, 2001, cERN-LHCC-2001-021.
- [Alt08] C. Alt *et al.*, *Energy Dependence of Particle Ratio Fluctuations in Central Pb+Pb Collisions from $\sqrt{s_{NN}} = 6.3$ to 17.3 GeV*, arXiv:0808.1237 [nucl-ex], 2008.
- [Ams08] C. Amsler *et al.*, *Phys. Lett.* **B667** (2008) 1.
- [And01] A. Andronic *et al.*, *IEEE Trans. Nucl. Sci.* **48** (2001) 1259.
- [And06a] A. Andronic, *Nucl. Instrum. Meth.* **A563** (2006) 349.
- [And06b] A. Andronic *et al.*, *Nucl. Instrum. Meth.* **A558** (2006) 516.
- [And07a] A. Andronic *et al.*, *Electron/Pion Identification with Fast TRD Prototypes*, CBM Progress Report 2006, 2007.
- [And07b] A. Andronic *et al.*, *Research and Development of Fast TRD Readout Chambers*, CBM Progress Report 2006, 2007.
- [And07c] A. Andronic *et al.*, *Research and Development of Fast TRD Readout Chambers*, 2007, jINR-2007-061.
- [Arn06] R. Arnaldi *et al.*, *Phys. Rev. Lett.* **96** (2006) 162302.
- [Arn07] R. Arnaldi *et al.*, *Phys. Rev. Lett.* **99** (2007) 132302.
- [Arn08] R. Arnaldi *et al.*, *Phys. Rev. Lett.* **100** (2008) 022302.
- [Arn09a] R. Arnaldi, *J/ ψ Production in p+A and A+A Collisions at Fixed Target Experiments*, Talk given on the 21st International Conference on Ultra-Relativistic Nucleus-Nucleus Collisions in Knoxville, 2009.
- [Arn09b] R. Arnaldi *et al.*, *Eur. Phys. J.* **C59** (2009) 607.
- [Ars07] I. C. Arsene *et al.*, *Phys. Rev.* **C75** (2007) 034902.

-
- [Bal82] D. Ballard and C. Brown, *"The Hough Method for Curve Detection" Section in Computer Vision*, Prentice Hall, 1982.
- [Bar77] B. C. Barrois, *Nucl. Phys.* **B129** (1977) 390.
- [Bas98] S. A. Bass *et al.*, *Prog. Part. Nucl. Phys.* **41** (1998) 255.
- [Bat02] S. Bathe, *Impulsfluktuationen und Produktion neutraler Pionen in ultrarelativistischen Schwerionenreaktionen*, Doctoral thesis, Institut für Kernphysik, Münster, 2002.
- [Bec04] F. Becattini, M. Gaździcki, A. Keränen, *et al.*, *Phys. Rev. C* **69** **2** (2004) 024905.
- [Ber10] C. Bergmann, *Development of the CBM TRD*, Diploma thesis, Institut für Kernphysik, Münster, to be submitted in 2010.
- [Blu94] W. Blum and L. Rolandi, *Particle Detection with Drift Chambers*, Springer-Verlag, 1994.
- [Blu98] C. Blume, *Produktion neutraler Mesonen in heißer hadronischer Materie*, Doctoral thesis, Institut für Kernphysik, Münster, 1998.
- [Blu05] C. Blume, *J. Phys.* **G31** (2005) S685.
- [Blu08] W. Blum and L. Rolandi, *Particle Detection with Drift Chambers*, Springer-Verlag, 2008.
- [BM01a] P. Braun-Munzinger, *Nucl. Phys.* **A681** (2001) 119.
- [BM01b] P. Braun-Munzinger, D. Magestro, K. Redlich, *et al.*, *Phys. Lett.* **B518** (2001) 41.
- [BM04] P. Braun-Munzinger, J. Stachel, and C. Wetterich, *Phys. Lett.* **B596** (2004) 61.
- [Boc98] R. Bock, *The Particle Detector Brief Book*, Springer-Verlag, 1998.
- [Bri07] G. Britvich *et al.*, *Prototype of the Fine-Sampling Electromagnetic Calorimeter*, CBM Progress Report 2006, 2007.
- [Bru97] R. Brun and F. Rademakers, *Nucl. Instrum. Meth.* **A389** (1997) 81.

- [Bru04] G. E. Bruno, *J. Phys.* **G30** (2004) S717.
- [Cas01] W. Cassing, E. L. Bratkovskaya, and A. Sibirtsev, *Nucl. Phys.* **A691** (2001) 753.
- [CBM05] *CBM Technical Status Report*, <http://www.gsi.de/documents/DOC-2005-Feb-447.html>, 2005.
- [CBM09a] *CBM Physics Book*, to be published in 2009.
- [Cbm09b] *CbmRoot Simulation and Analysis Framework*, <http://cbmroot.gsi.de>, 2009.
- [Cha68] G. Charpak, R. Bouclier, T. Bressani, *et al.*, *Nucl. Instrum. Meth.* **62** (1968) 262.
- [Cho74] A. Chodos, R. L. Jaffe, K. Johnson, *et al.*, *Phys. Rev.* **D9** (1974) 3471.
- [Chu03] P. Chung *et al.*, *Phys. Rev. Lett.* **91** (2003) 202301.
- [Cio01] M. Ciobanu and V. Catanescu, *Preamplifier/Shaper for ALICE TRD*, IFIN-HH Scientific Report 2000, ISSN 1454-2714, 2001.
- [Com93] A. S. G. Computing and C. Networks Division, *GEANT Detector description and simulation tool*, <http://wwwasd.web.cern.ch/wwwasd/geant/>, 1993.
- [Dol93] B. Dolgoshein, *Nucl. Instrum. Meth.* **A326** (1993) 434.
- [Dub08] A. Dubey *et al.*, *R&D with GEMs and THGEMs Towards Developing a Muon Tracker for CBM*, CBM Progress Report 2007, 2008.
- [Ehe96] W. Ehehalt and W. Cassing, *Nucl. Phys.* **A602** (1996) 449.
- [Ein05] A. Einstein, *Ann. Phys. (Leipzig)* **17** (4) (1905) 549.
- [FAI06] *FAIR Baseline Technical Report*, <http://www.gsi.de/documents/DOC-2006-Dec-94-1.pdf>, 2006.
- [Fan79] D. Fancher and A. C. Schaffer, *IEEE Trans. Nucl. Sci.* **NS-26** (1979) 150.
- [Fod04] Z. Fodor and S. D. Katz, *JHEP* **04** (2004) 050.
- [Fri08] V. Friese *et al.*, *The CBM Experiment at FAIR*, CBM Progress Report 2007, 2008.

- [Frö07] I. Fröhlich *et al.*, *PoS ACAT2007* (2007) 076.
- [Gal08] T. Galatyuk *et al.*, *Di-Electron Spectroscopy in CBM*, CBM Progress Report 2007, 2008.
- [Gat79] E. Gatti, A. Longoni, P. Semenza, *et al.*, *Nucl. Instrum. Meth.* **163** (1979) 83.
- [GD08] D. González-Díaz *et al.*, *Progress in the CBM-TOF Wall, R&D and Simulation*, GSI Report 2007-1, 2008.
- [Gor07] S. Gorbunov and I. Kisel, *Reconstruction of Decayed Particles Based on the Kalman Filter*, <http://www.gsi.de/documents/DOC-2007-May-14-1.pdf>, 2007.
- [Gre00] D. Green, *The Physics of Particle Detectors*, Cambridge University Press, 2000.
- [Gro73] D. J. Gross and F. Wilczek, *Phys. Rev. Lett.* **30** (1973) 1343.
- [Hen93] B. Henke *et al.*, *X-ray Interactions: Photoabsorption, Scattering, Transmission, and Reflection at $E=50-30000$ eV, $Z=1-92$* , http://henke.lbl.gov/optical_constants, 1993.
- [Heu07] J. M. Heuser, *Nucl. Instrum. Meth.* **A582** (2007) 910.
- [Höh08a] C. Höhne, *J. Phys.* **G35** (2008) 104160.
- [Höh08b] C. Höhne *et al.*, *Nucl. Instrum. Meth.* **A595** (2008) 187.
- [Irm94] D. Irmischer, *Nucl. Phys.* **A566** (1994) 347c.
- [Iva06] Y. B. Ivanov, V. N. Russkikh, and V. D. Toneev, *Phys. Rev.* **C73** (2006) 044904.
- [Iva09] A. Ivashkin, *Projectile Spectator Detector in CBM setup at SIS300*, Talk given on the 1st CBM-Russia-JINR Collaboration Meeting in Dubna, 2009.
- [Jac75] J. Jackson, *Classical Electrodynamics*, John Wiley & Sons, Inc., 1975.
- [Jor05] C. Joram, *Particle Detectors – Principles and Techniques*, Academic Training Lecture For Postgraduate Students at CERN, Geneva, 2005.

-
- [KB05] C. Klein-Bösing, *Production of Neutral Pions and Direct Photons in Ultra-Relativistic Au+Au Collisions*, Doctoral thesis, Institut für Kernphysik, Münster, 2005.
- [KB08] M. Klein-Bösing *et al.*, *Nucl. Instrum. Meth.* **A585** (2008) 83.
- [Kha08] Y. Kharlov, *Particle Identification in ECAL*, Talk given on the CBM Collaboration Meeting in Dubna, 2008.
- [Kis08a] I. Kisel *et al.*, *Fast SIMDized Kalman filter Based Track Fit*, CBM Progress Report 2007, 2008.
- [Kis08b] S. M. Kiselev, *Direct Photons in Nuclear Collisions at FAIR Energies*, arXiv:0801.1425 [hep-ph], 2008.
- [Kli09] M. Kliemant, *Analysis of ALICE-TRD Test-Beam Data*, Talk given on the DPG Spring Meeting in Bochum, 2009.
- [Kre09] D. Kresan and C. Höhne, *Event-by-Event Fluctuations of the K/π Yield Ratio in the CBM Experiment*, CBM Progress Report 2008, 2009.
- [Kri09] F. Krizek, *Inclusive Di-Electron Production in Ar+KCl Collisions at 1.76 AGeV with HADES*, Talk given on the 21st International Conference on Ultra-Relativistic Nucleus-Nucleus Collisions in Knoxville, 2009.
- [KY05] T. H. K. Yagi and Y. Miake, *Quark-Gluon Plasma*, Cambridge University Press, 2005.
- [Leb07] S. Lebedev *et al.*, *Ring Recognition in the RICH Detector of CBM*, CBM Progress Report 2006, 2007.
- [Leb08] S. Lebedev and G. Ososkov, *Ring Reconstruction in the CBM RICH Detector*, CBM Progress Report 2007, 2008.
- [Leo87] W. Leo, *Techniques for Nuclear and Particle Physics Experiments*, Springer-Verlag, 1987.
- [Let02] J. Letessier and J. Rafelski, *Hadrons and Quark-Gluon Plasma*, Cambridge University Press, 2002.
- [Mat86] T. Matsui and H. Satz, *Phys. Lett.* **B178** (1986) 416.
- [Mat88] E. Mathieson, *Nucl. Instrum. Meth.* **A270** (1988) 602.

- [McL85] L. D. McLerran and T. Toimela, *Phys. Rev.* **D31** (1985) 545.
- [NA606] *NA60 status report*, 2006, cERN/SPSC 2006-024.
- [Pes06] V. Peshekhonov, *TRD Straw Tracker*, Talk given on the CBM Collaboration Meeting in Strasbourg, 2006.
- [Pet07] M. Petrovici *et al.*, *Nucl. Instrum. Meth.* **A579** (2007) 961.
- [Phi08] O. Philipsen, *Prog. Theor. Phys. Suppl.* **174** (2008) 206.
- [Pol73] H. D. Politzer, *Phys. Rev. Lett.* **30** (1973) 1346.
- [Pov99] Povh, Rith, Scholz, *et al.*, *Teilchen und Kerne*, Springer-Verlag, 1999.
- [Raf82] J. Rafelski and B. Muller, *Phys. Rev. Lett.* **48** (1982) 1066.
- [Rey04] K. Reygers, *Die Suche nach dem Quark-Gluon-Plasma mit dem PHENIX-Experiment am RHIC*, Professorial dissertation, Institut für Kernphysik, Münster, 2004.
- [Rey07] K. Reygers, *AIP Conf. Proc.* **892** (2007) 413.
- [Roe96] B. P. Roe, *Particle Physics at the New Millenium*, Springer-Verlag, New York, 1996.
- [Sau77] F. Sauli, *Principles of Operation of Multiwire Proportional and Drift Chambers*, 1977, cERN-77-09.
- [Sen09] P. Senger, *Status of the CBM Experiment at FAIR*, CBM Progress Report 2008, 2009.
- [Sha06] R. Shahoyan *et al.*, *Nucl. Phys.* **A774** (2006) 677.
- [Shu78] E. V. Shuryak, *Phys. Lett.* **B78** (1978) 150.
- [Shu80] E. V. Shuryak, *Phys. Rept.* **61** (1980) 71.
- [Sim08] V. Simeon, *Private communications*, Drawing by V. Simeon, IFIN-HH Bucharest, Romania, 2008.
- [Sjo06] T. Sjostrand, S. Mrenna, and P. Skands, *JHEP* **05** (2006) 026.

-
- [Sol07] H. K. Soltveit *et al.*, *Fast TRD Pre-Amplifier Shaper for the CBM Experiment*, GSI Report 2006-1, 2007.
- [TG08] Tomasi-Gustafsson *et al.*, *Estimation of Charm Particles Elementary Cross Sections Relevant to GSI-CBM Project*, arXiv:0810.4250 [hep-ph], 2008.
- [Tho01] A. Thompson *et al.*, *X-Ray Data Booklet*, Lawrence Berkeley National Laboratory, University of California, 2001.
- [Toi07] A. Toia, *PoS CPOD07* (2007) 037.
- [Tsa74] Y.-S. Tsai, *Rev. Mod. Phys.* **46** (1974) 815.
- [Uhl08] F. Uhlig, *TRD Layout Studies and Energy Loss Simulations*, CBM Progress Report 2007, 2008.
- [UrQ02] *Animations: Physics Simulation Performed by Ultra-Relativistic Quantum Molecular Dynamics (UrQMD)*, <http://th.physik.uni-frankfurt.de/urqmd>, 2002.
- [Won94] C.-Y. Wong, *Introduction to High-Energy Heavy-Ion Collisions*, World Scientific, Singapore, 1994.
- [Yao06] W.-M. Yao *et al.*, *Journal of Physics G* **33**.
- [Zau07] O. Zaudtke, *Measurement of Direct-Photon Production and Neutral Pion Double Helicity Asymmetry in Ultra-Relativistic $p+p$ Collisions*, Doctoral thesis, Institut für Kernphysik, Münster, 2007.
- [Zin09] A. Zinchenko *et al.*, *Feasibility Evaluation of the Straw Tube Detector Option for the CBM Muon System*, CBM Progress Report 2008, 2009.

Danksagung

Anschließend möchte ich mich bei all denen bedanken, die zum Gelingen dieser Arbeit beigetragen haben.

Herrn Prof. Dr. Johannes P. Wessels danke ich für die interessante und abwechslungsreiche Aufgabenstellung, die Unterstützung und Betreuung meiner Arbeit, die hervorragenden Arbeitsbedingungen am Institut für Kernphysik sowie für die Ermöglichung der Teilnahme an zahlreichen nationalen und internationalen Konferenzen und Arbeitsaufenthalten. Insbesondere bin ich ihm sehr dankbar dafür, dass ich einen Teil meiner Arbeit zwecks Familienzusammenführung am CERN schreiben durfte.

Neben Herrn Prof. Dr. Johannes P. Wessels möchte ich auch Herrn PD Dr. Alfons Khoukaz für die Begutachtung dieser Dissertation ganz herzlich danken.

Ein besonderes Dankeschön geht an Dr. Christian Klein-Bösing, der mit seinen Ideen und Diskussionen einen großen Anteil zum Gelingen dieser Arbeit beigetragen hat. Ich danke ihm dafür, dass ich ihn zu jeder Zeit und Unzeit um Rat fragen durfte und diesen auch stets erhalten habe. Sein Interesse an meiner Arbeit war entscheidend für deren Erfolg.

Bei Alexander Wilk bedanke ich mich für die gemeinsamen Strahlzeiten und die außergewöhnliche Zusammenarbeit während unseres ganzen Studiums und der Promotion.

Für die sehr fruchtbare Zusammenarbeit und die Betreuung meiner Arbeit in den verschiedenen Themenbereichen bedanke ich mich bei Dr. Claudia Höhne, Dr. Mariana Petris, Prof. Dr. Mihai Petrovici und Dr. Florian Uhlig. Ihre Diskussionsbereitschaft, die zahlreichen Anregungen und die Hilfestellung bei physikalischen und technischen Fragen haben diese Arbeit entscheidend voran gebracht.

Innerhalb der CBM-Kollaboration möchte ich außerdem Dr. Anton Andronic, Dr. Chilo Garabatos und Estela Jimenez danken, die mir mit ihrer langjährigen Erfahrung auf dem Gebiet der Gasdetektoren immer wieder hilfsbereit zur Seite standen.

Aber auch in Münster bekam ich unter anderem im Gruppentreffen viel Unterstützung durch gute Ideen und Ratschläge. Hierfür danke ich vor allem Dr. Tom Dietel, Dr. Christian Klein-Bösing, PD Dr. Klaus Reygers und Prof. Dr. Rainer Santo. Darüber hinaus

danke ich mit Cyrano Bergmann meinem bislang einzigen CBM-Kollegen in Münster, der meine Arbeit nach seiner Einarbeitung sehr schnell und hilfreich unterstützt hat.

Bei Norbert Heine, Helmut Baumeister, Cyrano Bergmann, André Braem, Rui de Oliveira und Victor Simeon bedanke ich mich für ihren Einsatz beim Aufbau der Prototypen und die gute Zusammenarbeit. Ohne sie wäre ein großer Teil dieser Arbeit so nicht möglich gewesen.

Für die angenehme Arbeitsatmosphäre und ihre Unterstützung gilt mein Dank der gesamten CBM-Kollaboration, darunter insbesondere der Arbeitsgruppe von Prof. Dr. Mihai Petrovici, außerdem den TRD-Kollegen aus der ALICE-Kollaboration sowie allen aktuellen und ehemaligen Mitgliedern meiner Arbeitsgruppe: B. Albrecht, J. Anielski, J. Auffenberg, B. Bathen, C. Baumann, C. Bergmann, K. Büscher, Dr. T. Dietel, H. Gatz, R. Glasow, H. Gottschlag, Dr. J.-F. Große-Oetringhaus, H. Grimm, M. Heide, N. Heine, H. Hünteler, Dr. M. Kalisky, S. Klamor, Dr. C. Klein-Bösing, S. Korsten, M. Kowalik, A. Kumpmann, R. Luchtenborg, J.-F. Pietschmann, F. Poppenborg, M. Rammler, PD Dr. K. Reygers, B. Sahlmüller, Prof. Dr. R. Santo, E. Sicking, A. Sperling, W. Verhoeven, D. Vernekohl, M. Walter, U. Westerhoff, A. Wilk, S. Wulff und O. Zaudtke.

Für die kritische Durchsicht der Arbeit danke ich Dr. Anton Andronic, Cyrano Bergmann, Dr. Tom Dietel, Dr. Jan-Fiete Große-Oetringhaus, Dr. Claudia Höhne, Mareike Hoppe, Dr. Matus Kalisky, Dr. Christian Klein-Bösing, Dr. Mariana Petris, Markus Rammler, PD Dr. Klaus Reygers, Dr. Marcus Schäfer, Eva Sicking, Corinna Siemeit, Dr. Florian Uhlig und Dres. Anja und André Wenning.

Ein besonderes Dankeschön geht an meine Verwandten, Freunde und Studienkollegen, die mich auch außerhalb der Physik begleitet haben und dabei immer wieder viel Verständnis für meine Arbeitszeiten aufbrachten.

Zu guter Letzt möchte ich mich bei meiner Familie bedanken, insbesondere noch einmal bei meinem Mann Dr. Christian Klein-Bösing, neben den oben zahlreich erwähnten Beiträgen zu meiner Arbeit auch für seine unendliche Geduld und Motivation. Auch bei unserem Töchterchen möchte ich mich bedanken, das mir mit der Ankündigung der Geburt die wohl schönste und beste Motivation für eine zeitnahe Abgabe meiner Doktorarbeit geliefert hat.

Lebenslauf und Bildungsgang

Name: Melanie Klein-Bösing, geb. Hoppe
geb.: 06.12.1977 in Telgte
Staatsangehörigkeit: deutsch
Eltern: Alfons Hoppe
Maria Hoppe, geb. Schmülling
Familienstand: verheiratet mit Dr. Christian Klein-Bösing
Schulbildung: Grundschule: 1984 – 1988
Kardinal-von-Galen-Grundschule
Drensteinfurt
Gymnasium: 1988 – 1997
Immanuel-Kant-Gymnasium
Münster
Allgemeine Hochschulreife: am 22.5.1997 in Münster
Studium: Okt. 1997 – Mär. 2004
Diplomstudiengang Physik an der
Westfälischen Wilhelms-Universität Münster
Prüfungen: Vordiplom: 20.10.2000
Diplom: 30.03.2004
Tätigkeiten: Okt. 2001 – Mär. 2004 stud. Hilfskraft,
Apr. 2004 – Mai 2004 wiss. Hilfskraft,
seit Juni 2004 wiss. Mitarbeiterin
Beginn der Dissertation: 01.04.2004
am Institut für Kernphysik bei
Prof. Dr. J. P. Wessels

